Momentum-space correlations in the depletion of weakly interacting lattice Bose gases

Antoine Ténart

université
PARIS-SACLAY

Momentum-space correlations in the depletion of weakly interacting Bose gases

Corrélations en impulsion dans les gaz de Bose sur réseaux faiblement interagissant

Thèse de doctorat de l'université Paris-Saclay

École doctorale n°527 Ondes et Matière (EDOM)
Spécialité de doctorat : Physique
Graduate School : Physique Référent : Institut d'Optique

Thèse préparée dans l'unité de recherche **LCF (Université Paris-Saclay, Institut d'Optique Graduate School, CNRS)**, sous la direction de **David CLEMENT**, Maître de conférence

Thèse soutenue à Paris-Saclay, le 09 Décembre 2021, par

Antoine TENART

Composition du Jury

Jacqueline BLOCH Directrice de recherche, Université Paris-Saclay	Présidente
Jérôme BEUGNON Maître de conférence, Ecole Normale Supérieure	Rapporteur & Examinateur
David GUERY-ODELIN Professeur, Université Toulouse III-Paul Sabatier	Rapporteur & Examinateur
Anna MINGUZZI Directrice de recherche, Université Grenoble Alpes	Examinatrice
Aurélien PERRIN Chargé de recherche, Université Sorbonne Paris Nord	Examinateur
David CLEMENT Maître de conférence, Université Paris-Saclay	Directeur de thèse

THESE DE DOCTORAT

NNT : 2021UPASP128

"I have no idea where this will lead us, but I have a definite feeling it will be a place both wonderful and strange."

Dale Cooper in Twin Peaks (Mark Frost & David Lynch)

Contents

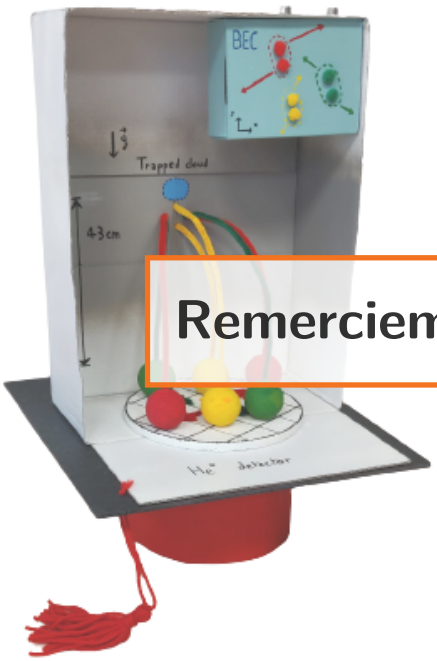

Remerciements

Durant mes quelques modestes années passées dans le monde de la recherche, il m'est souvent arrivé de parcourir des manuscrits de thèse comme celui-ci à la recherche de l'information essentielle qui sauverait ma journée. Ce faisant, j'aimais toujours beaucoup jeter un coup d'oeil à la section remerciements qui laisse souvent entrevoir ce que l'on ne trouve pas écrit dans le reste du manuscrit mais pourtant d'une grande importance : l'ambiance d'un labo, des blagues d'initiés, les personnes qui ont compté bref, les éléments essentiels de la vie du thésard et qui conditionnent beaucoup la réussite d'une thèse. C'est donc non sans une certaine émotion que je me lance moi aussi dans cet exercice, en espérant que ces lignes trouveront toutes les personnes que j'aimerais remercier pour avoir fait de moi un thésard très privilégié durant ces 3 années qui n'auraient pas pu mieux se passer, ou qu'elles apporteront un peu de distraction dans la journée d'un lecteur de passage à la recherche d'un waist ou d'une valeur de désaccord.

Les premières personnes que je souhaiterais remercier sont naturellement les membres de l'équipe Hélium sur réseaux. L'équipe est probablement un des éléments les plus importants dans le travail du physicien moderne, et j'ai eu l'immense chance de tomber dans une équipe formidable. Mon premier merci va évidemment à David Clément, le créateur de cette expérience et mon maître de thèse, tout d'abord pour m'avoir choisi et fait confiance pour m'occuper de cette super manip'. Merci pour ta qualité d'encadrement hors du commun, ta grande sympathie, ta grande disponibilité, ta motivation et ta passion sans faille et très communicative de la physique, ainsi que ton indulgence face aux (plus ou moins) petites bêtises en salle de manip'. Tu as toujours su créer une excellente ambiance de travail, motiver et tirer le meilleur de nous, et j'ai vraiment le sentiment d'avoir énormément progressé à ton contact, que ce soit en compréhension pure de la physique mais aussi dans la façon de raconter et d'expliquer les choses. Pour quelqu'un comme moi qui se destine à l'enseignement, je pense vraiment que toutes ces choses me seront extrêmement précieuses dans le futur. Un très grand merci pour tout !

Mon second merci va à tous mes co-thésards et post-docs avec qui j'ai eu le plaisir de tourner des vis et sonder les mystères de la physique quantique pendant ces 3 ans. J'aimerais remercier tout d'abord les "anciens" : Marco, que je n'ai croisé que brièvement mais qui m'a tout appris de l'art des tables optiques de refroidissement laser, Hugo, pour

m'avoir transmis son savoir et pour ses éminents conseils cinématographiques, et enfin Cécile, elle aussi pour avoir pris le temps de former le bébé thésard que j'étais, sa force de travail inébranlable et pour sa grande contribution à la bonne ambiance dans l'équipe, des gâteaux d'anniversaire jusqu'aux super soirées à la coloc' de Massy. J'aimerais vous adresser un très grand merci pour toute l'énergie et le travail que vous avez dépensé pour améliorer et faire marcher cette expérience. J'ai eu la grande chance d'hériter grâce à vous d'une manip' très bien construite, robuste et résistante à tous les tracas de la physique expérimentale, c'est grâce à vous si j'ai pu étudier cette belle physique pendant ma thèse et je vous en suis grandement reconnaissant. J'aimerais maintenant remercier le H et le B avec qui je formais l'équipe HBT pour Hercé-Bureik-Ténart (non sans rapeller les illustres Hanbury-Brown et Twiss, pionniers de l'étude des corrélations quantiques) Gaétan et JP. Un très grand merci à Gaétan pour ta bonne humeur inattaquable et ton dévouement, pour avoir gardé le sourire même face aux pires pièges que nous réservait la manip', et pour avoir rendu les séances obligatoires de tournage de vis bien plus agréables en blastant les plus grands tubes de Maître Gims, Jenifer ou même des Vengaboys. Un très grand merci également à JP, tout d'abord pour m'avoir montré la lumière en programmation (demain promis j'arrête Matlab, mais juste un dernier script), pour ta grande sympathie et pour toutes les discussions de bureau, en espérant que tu m'aies pardonné mes quelques blagues inoffensives sur un certain Bayern-PSG. J'aimerais également remercier Alexandre qui nous accompagnés quelques mois en tant que post-doc pour son aide précieuse, tant dans la rédaction d'articles que dans l'élaboration de nouveaux codes d'analyse ou pendant le déménagement, ainsi que tous les stagiaires qui sont venus nous prêter main forte. Ces remerciements ne seraient pas complets sans une mention au membre le plus important de cette équipe, à savoir la manip'. La physique expérimentale est une activité qui rend pour le moins superstitieux, c'est pourquoi je tiens à remercier l'esprit de la manip' pour sa grande clémence en lui pardonnant ses facéties parfois très imaginatives, en espérant qu'il veille et prenne soin des futurs thésards pour de nombreuses années.

J'aimerais également remercier tous les membres du groupe Gaz Quantiques, à commencer par les permanents, Chris, Denis, Marc, Isabelle, Thomas, Vincent et Alain, ainsi que tous les thésards et post-docs que j'ai eu la chance de rencontrer dont la liste serait trop longue à dresser. Le groupe Gaz Quantiques est un groupe où règne une excellente ambiance et où l'on trouve toujours une porte à laquelle frapper en quête d'un bon conseil ou d'une monture de miroir manquante. Vous côtoyer et travailler avec vous a été un vrai plaisir !

Je remercie aussi tous les gens qui ont pu collaborer avec nous, que ce soit en théorie ou en rédaction d'articles, avec en tête Tommaso Roscilde dont les calculs QMC et les idées nous ont été inestimables, Hepeng Yao et Laurent Sanchez-Palencia pour leur collaboration sur le sujet des gaz 1D, ainsi que Iacopo Carusotto, Salvatore Butera et encore une fois Thomas Bourdel et Alain Aspect. Etant ancien élève de l'IOGS (dans lequel j'aurais bientôt passé 7 ans soit l'équivalent d'un collège-lycée !), ce fut un grand plaisir pour moi de passer de l'autre côté et de rejoindre l'équipe enseignante pour dispenser quelques TDs/TPs. Un grand merci donc à tous les gens avec qui j'ai pu enseigner, dont la liste est elle aussi un peu longue. J'aimerais finalement remercier l'ensemble du personnel du laboratoire Charles Fabry et particulièrement son directeur, Patrick Georges, pour sa grand gentillesse et son écoute, ainsi que les services généraux et techniques, particulièrement Florence Nogrette, Marc Apfel, Frédéric Moron, Mondher Besbes, Patrick Roth, Jean-René Rullier, Fabrice Cartier et Fabien Siffrit qui nous ont tous donné un coup de main salvateur à un moment ou l'autre de ma thèse.

Pour finir, j'aimerais remercier ceux qui m'ont aidé à survivre à ces dernières années remplies d'événements pour le moins inattendus, à savoir mes amis. Merci pour commencer à Sylvain et Nicolas qui ont toujours été là et ce depuis de nombreuses années, que ce soit autour d'un poutine ou d'une bière (souvent les deux), pendant la coloc' éphémère à la VillaDuChato du confinement numéro 2, ou encore à distance durant les longues soirées d'hiver sous couvre-feu, un immense merci à vous deux. J'aimerais bien entendu remercier toute la troupe du Shitstorm, Alice, Anaïs, Baptiste, Benjamin, Cécile, Colin, Coraline, Elise, Laura, Marc, Paul, Solène et Vincent qui ont tous joué un rôle inestimable dans la réussite de cette thèse, pour tous les Skypéros et autres soirées du dimanche après-midi au coeur des différentes vagues du Covid, pour toutes les soirées à Clamart, Alésia, dans une crêperie de Montparnasse ou évidemment au POP (dont je devrais probablement aussi remercier l'équipe vu le temps qu'on y a passé) à disserter de sujet très sérieux (*e.g.* Muse ou Star Wars) ou plus légers (*e.g.* la politique), sans oublier les supers vacances ponctuées des meilleures jam sessions, parties de pétanque, mario kart ou tarot que l'on ait connu. Merci pour tout, vous êtes vraiment trop cool. J'aimerais aussi avoir un mot pour Marie, qui aura elle aussi joué un très grand rôle malgré tout. Merci également à Alexandre pour son aide avec les illustrations des paires d'atomes corrélées. Mon dernier mot sera pour ma famille, ma soeur et mes parents, pour leur soutien inconditionnel depuis toujours, pour m'avoir transmis le goût des sciences et de l'enseignement et pour avoir toujours tout fait pour que j'en arrive là aujourd'hui.

Introduction

In our quest to describe and understand the world with physics, our intuition tells us to start with the small and the simple before working our way up to larger scales and more complex problems. This is the path we follow when we are first taught about atomic physics and start with the smallest existing atom, Hydrogen. Even before we know about quantum mechanics, we are often taught how to use simple Newtonian mechanics to calculate the circular movement of the Hydrogen electron around the nucleus in the historical Rutherford model. If we now aim at describing a slightly more complex atom, let us say Carbon for instance, we need to consider the electrostatic forces exerted by the nucleus on each of the 6 electrons as well as between each of the electrons. We are then quickly overcome by a feeling of helplessness at the sight of the equations we would have to solve.

This kind of problem is obviously not restricted to the description of atoms and is actually found in many areas of physics. Would we want to study an ensemble of celestial objects orbiting around a star, electrons in a copper wire, molecules in a gas, atoms in a solid or even how a crowd behaves, a thorough description of these systems would require to account for the motions of all the individual bodies and the interactions between each one of them, leaving us with an enormous amount of degrees of freedom and equations to solve. This is even more so true as the number of particles gets very large in these problems: a good order of magnitude is the Avogadro number $\mathcal{N}_A = 6.02 \times 10^{23}$, giving the number of Carbon 12 atoms in only 12g of Carbon! These problems are regrouped under the denomination "**many-body** problems".

Actually, many-body problems are not entirely impossible to approach theoretically. To do so, we need to go against our intuition to decompose the system into its elementary components and rather see it as a whole to study some kind of **averaged** behavior. This idea is for instance at the core of the field of Thermodynamics which aims to describe macroscopic properties of large numbers of particles, such as its temperature, pressure, entropy etc. representing ensemble averages independent from the dynamics of the individual components of the system. Another famous approach that relies on averaging to study interacting many-body systems is the **mean-field approximation**. The idea is to approximate the action of every particle of the system on a single one as an averaged

effect, reducing the many-body problem to an effective one body problem that we may be able to solve.

Quantum physics

When we study many-body problems where the individual constituents are the (almost) smallest brick of matter, namely electrons and atoms, we enter the realm of **quantum mechanics**. The key concept to understand when a system requires a quantum treatment is the de Broglie wavelength. In 1923 [48], the french physicist Louis de Broglie took the hypothesis of M. Planck and A. Einstein that light could have a corpuscular aspect and turned it around by postulating that matter could behave as a wave with a wavelength λ_{dB} equal to:

$$\lambda_{\mathrm{dB}} = \frac{h}{m\boldsymbol{v}} \tag{1}$$

where $m\boldsymbol{v}$ is the momentum of the particle that also writes $\hbar\boldsymbol{k}$ in quantum mechanics. Strictly speaking, $\boldsymbol{k}$ designs a wave vector but we will identify it to the momentum in the rest of this manuscript. Translating this concept to many-body physics, when taking an ensemble of particles at temperature T, one can define the average de Broglie wavelength, also known as the thermal de Broglie wavelength as:

$$\lambda_{\mathrm{dB}} = \frac{h}{\sqrt{2\pi m k_{\mathrm{B}} T}} \tag{2}$$

If the typical inter-particle distance in the many-body ensemble is much larger than the thermal de Broglie wavelength, *i.e* $\lambda_{\mathrm{dB}}^3 n \ll 1$ with n the density of particles, the wave character of the particles hardly plays a role as the different matter waves do not overlap and the system is properly described using classical physics. On the other hand, when $\lambda_{\mathrm{dB}}^3 n \sim 1$, the system shows quantum wave-like behavior. This regime is known as the **quantum degeneracy** regime. Importantly, this condition is most often met when considering the physics of electrons in condensed matter systems even at room temperature, due to their small mass $m_e = 9.1 \times 10^{-31}$ kg and the high densities of electrons in solids of the order of 10^{29} m^{-3}.

The wave-like nature of the particles, as well as the effect of quantum statistics and quantum fluctuations observed in the quantum degeneracy regime brings out a large variety of fascinating and "intuition-defying" phenomena of which many are still not understood to this day, especially in many-body systems. For these reasons, quantum physics constitutes an exciting and leading area of modern day physics.

Interactions in quantum systems

While approximate methods like the mean-field approach have been used with great success in the past to study quantum many-body problems, they nevertheless fail to characterize

more strongly interacting systems for which beyond mean-field approaches are required [114, 102, 121]. To properly describe these systems, it is then necessary to consider the dynamics of the individual components of the system [85, 139, 164]. As a result, the modern day term "many-body physics" usually refers to beyond mean-field approaches that account for the presence of **correlations** between the individual components of the system. Importantly, these correlation patterns get increasingly more complex and contain more information as the interactions are strong. Consequently, a large part of quantum many-body physics is dedicated to studying how correlations emerge from the interplay between the inter-particle interactions and the quantum fluctuations and what they tell us of the physics of the system. This field of physics remains to this day a largely open field with a lot of unresolved questions concerning systems ranging from solid state physics to neutron stars, but that already found some great successes. We can mention the notable example of low temperature superconductivity studied by Bardeen-Cooper-Schrieffer [7] (BCS) in 1957 that described the superconducting current as a superfluid of Cooper pairs [42], where a Cooper pair is a pair of electrons bound by an effective attractive interaction (in this case the exchange of phonons). The existence of high temperature superconductors remains however unexplained to this day and constitutes a particularly interesting question of many-body physics.

Cold atoms and quantum simulation

Even though we have understood that exact analytical approaches are almost always impossible to pursue in the case of quantum many-body systems, we could however think of using numerical techniques and the calculation power of modern-day super computers. Nevertheless, if we wish to consider all kinds of correlations between the particles, the size of the associated Hilbert space grows exponentially with the number of particles. This exponential growth considerably limits the number of particles that can be simulated, roughly to a hundred with modern day computers. In a famous paper of 1982 [59], R. Feynman introduced the concept of **quantum simulation** by suggesting that quantum phenomena could be simulated using actual quantum components instead of classical computers. The idea is to simulate a system or an Hamiltonian of interest with a quantum platform on which one can (*i*) precisely control all the relevant parameters and (*ii*) measure the observables of interest. The technological developments of the past decades have made Feynman's idea come to life with increasingly more precise and efficient simulators implemented on a variety of platforms such as ions, superconducting qubits or ultracold gases. We will focus in this manuscript on this latter example.

Contrary to condensed matter systems, ultracold gases are a dilute state of matter in the sense that they typically contain $10^5 - 10^7$ atoms in large volumes, resulting in much lower densities than those found in solids. As a result, at room temperature, these gases are far from being quantum degenerate. To reach the regime of quantum degeneracy, the gas must be cooled down to very low temperatures $\sim \mu$K to increase λ_{dB} until $\lambda_{\mathrm{dB}}^3 n$ reaches unity. When the atoms are indistinguishable bosons, under a critical temperature associated with $\lambda_{\mathrm{dB}}^3 n \sim 1$, a macroscopic number of atoms occupy the lowest energy state of the system, forming a new state of matter called the **Bose-Einstein Condensate (BEC)**. Importantly, all the condensed atoms then form a single, **coherent** matter-wave.

The field of ultracold atoms was born thanks to the discovery of laser cooling techniques

[38, 44, 127] that allowed to reach such low temperatures and led to the observations of the first BECs by the teams of E. Cornell [2] and W. Ketterle [47] in 1995. From this day, ultracold atoms and Bose-Einstein Condensates have been the subject of many experiments and brought a large variety of important results and several Nobel prizes.

Ultracold atoms are actually perfectly suited to study condensed matter as it is relatively easy to create all sorts of potentials to trap the atoms using laser light, with the notable example of optical lattices [12] that reproduces the crystalline structure of solids. Another interesting properties of ultracold atoms is that the strength of the interactions of some atomic species[1] can be tuned using Feshbach resonance [37, 58]. One may thus have a system in which one controls the number of particles, the properties of the crystal-like potential such as its geometry and the distance between the sites and finally the strength of interactions. Such quantum gas platforms fulfill the first condition for them to be an adequate quantum simulator of famous condensed matter models such as the Fermi- and Bose-Hubbard models for fermions and bosons respectively, or the Ising model. This level of control on the parameters of the simulated Hamiltonian would of course be useless if it were impossible to measure the properties of the system. One other significant asset of ultracold atoms in optical lattices systems is that they are actually relatively easy to probe.

Probing the momentum degree of freedom

Recent optical lattices experiments can be categorized according to the kind of probes they use to study the many-body problem. A first technique consists in probing the excitations of the system, *i.e* how the system respond when extra energy or momentum is deposited in the system, to obtain information about the many-body states. This probe was developed in analogy to condensed matter approaches such as angle-resolved photoemission spectroscopy [45] or neutron scattering [4]. For ultracold atoms systems, the excitations of the system can be probed using radio-frequency (RF) spectroscopy [151], Raman spectroscopy [46], amplitude modulations of a 2D lattice revealing Higgs mode excitations [53] or Bragg spectroscopy [146, 148]. Finally, the properties of the excitations can also be accessed by studying the out-of-equilibrium properties of the system [92, 159].

Ultracold atoms platforms have brought up new ways to probe many-body systems differently from the techniques used in condensed matter experiments. It is notably possible to probe the position or spin degree of freedom using quantum gases microscopes [6, 35, 54, 141] capable of detecting the fluorescence of individual atoms trapped in the different sites of an optical lattice. These techniques allow to characterize many-body systems through the study of position and spin correlations between individual particles.

Finally, the same idea can be extended to the momentum degree of freedom. The momentum-space can be accessed through Time-Of-Flight (TOF) techniques [77, 147, 166] that consist in measuring the positions of the atoms after a time t_{TOF} of free expansion. In a very simple picture with classical particles that do not interact during the TOF, this position gives information about the in-trap momentum of the particle through the simple **ballistic relation**:

[1] This is however not the case for metastable Helium-4 that we will study in this manuscript

$$\hbar \boldsymbol{k} = \frac{m\boldsymbol{r}}{t_{\mathrm{TOF}}} \tag{3}$$

The situation is actually more complex when accounting for the wave nature of the particles, as we will discuss later, but we can keep for now this simple picture. The combination of a TOF and a single-atom resolved detection technique allows to study momentum-space correlations between individual particles from which meaningful information about many-body systems can be obtained. The experiment that we will describe in this manuscript belongs to this last category that will be our main point of focus.

There are many motivations to measure the momentum distribution to study ultracold gases and many-body physics as a whole. One of the main advantages of the momentum distribution is to reveal the **coherence** properties of the system, that are themselves greatly influenced by the interactions and the induced correlations between the particles [77]. Indeed, the wave-function in momentum-space $\psi(\boldsymbol{k})$ is linked to the spatial wave-function $\phi(\boldsymbol{r})$ by the Fourier transform:

$$\psi(\boldsymbol{k}) \propto \int \mathrm{d}\boldsymbol{r} e^{i\boldsymbol{k}\cdot\boldsymbol{r}} \phi(\boldsymbol{r}) \tag{4}$$

As the momentum density $\rho(\boldsymbol{k})$ writes $\rho(\boldsymbol{k}) = |\psi(\boldsymbol{k})|^2$, we obtain [129]:

$$\rho(\boldsymbol{k}) \propto \int \mathrm{d}\boldsymbol{R} e^{i\boldsymbol{k}\cdot\boldsymbol{R}} \int \mathrm{d}\boldsymbol{r} \phi^*(\boldsymbol{r})\phi(\boldsymbol{r}+\boldsymbol{R}) \propto \mathrm{FT}[g^{(1)}(\boldsymbol{R})] \tag{5}$$

which tells us that the momentum distribution is obtained from the Fourier transform of the first order correlation function $g^{(1)}$ which contains information about the coherence properties of the system. This is quite reminiscent of Optics in which far-field interference experiments are used to characterize the spatial and temporal coherence properties of a light source. With ultracold atoms, the light waves are replaced by matter-waves and the far-field regime of observation analog to the momentum distribution of the gas.

The momentum distribution was historically [2] used to detect the presence of Bose-Einstein Condensation as illustrated on Fig.-1. As the BEC is a fully coherent matter-wave, it manifests itself by the presence of sharp peak around zero momentum with a small width set by Heisenberg uncertainty principle as the atoms are spatially localized. The momentum distribution can also be used to study excitations, complementary to the methods cited earlier, signaled in momentum-space by the dispersion relation from which a variety of information can be obtained [39, 120, 136].

Last but not least, the momentum distribution also contains signatures of more complex interaction-induced correlation patterns between several individual particles. One of the most simple and famous example of such correlations are pairing mechanism inducing opposite momentum correlations. This is notably the case for two electrons belonging to a Cooper pair as discussed earlier, as well as for the **quantum depletion** of a BEC. The quantum depletion is the fraction of atoms removed from the condensate by the effect of inter-particle interactions and quantum fluctuations at zero temperature. It is an emblematic and conceptually simple example of a many-body effect. While the quantum depletion has already been observed [33, 106, 166], there have been no direct observation

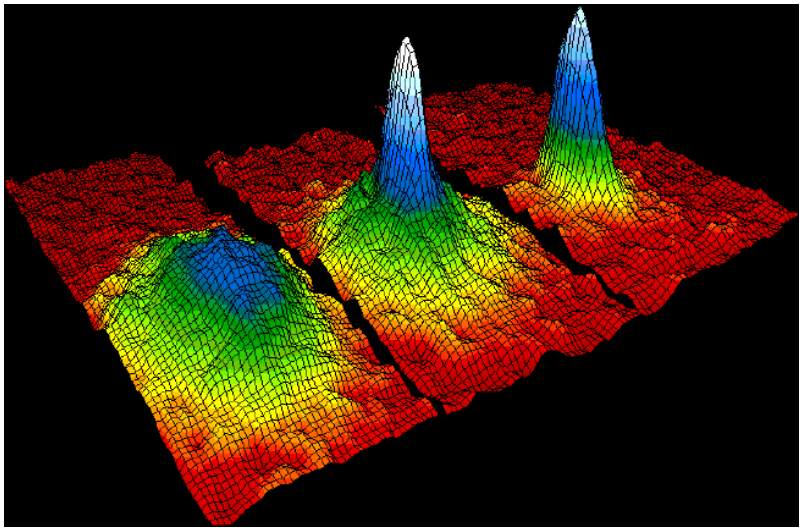

Figure 1: Bose-Einstein Condensation. As temperature diminishes, the momentum distribution gets increasingly peaked around zero momentum. (JILA team, NIST USA)

of pairing at opposite momentum expected for quantum depleted atoms. Obtaining this result will be the main point of focus of this manuscript.

Metastable Helium and electronic detection

In order to detect such pairing correlations (or more complex correlation patterns with more than 2 particles that might be present in strongly interacting systems), a detection technique capable of resolving the momentum of each individual atoms of the gas is needed. Indeed, the idea behind correlation measurements is to measure the probability of **simultaneous** detection of several particles at specific momenta (for instance $\boldsymbol{k}$ and $-\boldsymbol{k}$). Many experimental efforts have been made in this direction in the past decades [118]. While optical imaging techniques typically only allow to measure the **momentum density** of the gas rather than the full **momentum distribution**, some experiments such as the one led by S. Jochim in Heidelberg [140] or by J. Schmiedmayer in Vienna [19] have adapted the quantum microscope technology to detect the fluorescence of single atoms after a TOF, thus obtaining a single-atom resolution in the momentum-space. However, the performances of these setups are somewhat limited by the properties of the imaging system, that requires the number of atoms to be kept relatively low so that the fluorescence patterns of the different atoms do not overlap for them to be resolved.

An alternative to optical probing is to use **electronic** detection techniques. In the early 2000s, the team lead by D. Boiron, C. Westbrook and A. Aspect at Institut d'Optique pioneered a new detection scheme exploiting the properties of the metastable state of the Helium atom that they managed to bring to quantum degeneracy in 2001 [133]. A great advantage of this method lies in its **3D** single-atom resolution as well as the possibility to implement it for systems with larger atom numbers of the order of $10^3 - 10^5$ (this must be nuanced by the fact that the detector saturates if the atomic flux is too high). In addition, this method allows to use large Times-Of-Flight to properly access the far-field regime of expansion in which the interferences are well resolved, in analogy to the Fraunhofer regime

of diffraction[2].

As we will see in this manuscript, a major drawback of this technique is that it only works with noble gases with a metastable state. To this day, Helium is the only noble gas that has been brought to quantum degeneracy (even though Neon, Argon and Krypton have been laser cooled [91, 142]), limiting the use of this detection technique to this single atomic species. To this day, there are actually only a few metastable Helium experiments in the world: Canberra led by A. Truscott [1], Vienna led by A. Zeilinger [93], Amsterdam formerly led by W. Vassen [111] with the fermionic isotope of Helium ^{3}He and two in Palaiseau, the historical one led by D. Boiron, C. Westbrook and A. Aspect and a second one led by D. Clément. This second metastable Helium experiment was built at Institut d'Optique starting in 2011, with the observation of Bose-Einstein condensation in 2015 [16]. This new experiment implemented a new cooling sequence allowing to produce a BEC in $\sim$ 6s instead of $\sim$ 30s on the historical experiment, thus significantly speeding up the data acquisition time for the measurement of momentum correlations.

Optical lattices and the superfluid-to-Mott insulator transition

The other specificity of this second experiment at Institut d'Optique is the use of optical lattices, from which the name of the team "Helium Lattice" derives. Optical lattices are particularly suited to study many-body, strongly interacting systems as the lattice potential locally increases the density and in turn the interactions, making phenomenon like quantum depletion even more pronounced than in regular harmonic traps. In addition, the Bose-Hubbard model predicts the existence of a phase transition from a superfluid phase to an insulating phase when the depth of the lattice potential increases, known as the superfluid-to Mott insulator transition, first observed with cold atoms in 2002 [77] following the proposal of [89]. Studying momentum correlations all across the superfluid-to Mott insulator transition sets the general frame of the work presented in this manuscript, and conducted during my time as an intern and then as a PhD student in the Helium Lattice team that I had the chance to join in 2018.

Outline of the manuscript

The manuscript is organized in five chapters. All chapters but the final one are centered around the common topic of the $\boldsymbol{k}/-\boldsymbol{k}$ correlations in the quantum depletion of weakly-interacting lattice Bose gas.

- The first chapter is dedicated to presenting the proper formalism to study quantum correlations. The concept of correlation functions is first introduced in the context of Quantum Optics and then extended to Atomic Physics. We then detail the main lines of the Bogoliubov theory of the homogeneous weakly-interacting Bose gas. We present what the quantum depletion is and where does the $\boldsymbol{k}/-\boldsymbol{k}$ pairing comes from. Finally, we discuss some recent numerical calculations [23] of the correlations in the Bogoliubov theory for trapped systems, before presenting the essential experimental ingredients to observe the $\boldsymbol{k}/-\boldsymbol{k}$ pairs.

[2]This point will be discussed in details in this manuscript

- The second chapter is also a theoretical one and discusses the Bose-Hubbard model of bosons trapped in a 3D optical lattice. We explain what the superfluid-to-Mott insulator transition is and discuss the conditions under which the in-trap momentum distribution of the gas can be properly measured using a TOF technique, as well a the observability of the $\boldsymbol{k}/-\boldsymbol{k}$ pairs of the quantum depletion in this system.
- The third chapter describes our experimental apparatus, namely the sequence used to produce a BEC of metastable Helium and the detection technique. In a second stage, we present two experimental measurements aimed at proving the points raised in Chapter 2: one proving that we are able to adiabatically prepare an arbitrary state of the Bose-Hubbard model; a second one measuring beyond-mean field two-body collision effects happening during the TOF to prove that they are negligible in usual experimental conditions (therefore not detrimental to our measurement of the momentum distribution).
- The fourth chapter details our experimental observation of the $\boldsymbol{k}/-\boldsymbol{k}$ pairs of the quantum depletion. We describe the numerical procedure to analyze the data and study the characteristics of the experimental correlation signals in light of Bogoliubov theory: width, amplitude and dependency to temperature. We then perform complementary analysis of the data to obtain results leading towards probing the presence of entanglement in our system: we observe a relative number squeezing measurement between modes $\boldsymbol{k}$ and $-\boldsymbol{k}$, as well as a violation of the Cauchy-Schwarz inequality. Finally, we discuss some preliminary results on the evolution of the correlation signals with momentum k.
- The fifth and last chapter is separate from the rest of this manuscript and concerns a different project that was led during this thesis, the measurement of Tan's contact in 1D gases. We first introduce Tan's contact as well as the main results of a recent theoretical study [170] of the contact for trapped 1D bosons. We then present the procedure used to extract the contact from the raw experimental data and discuss the first preliminary results and their discrepancy with theory.

$$G^{(2)}(\boldsymbol{k},\boldsymbol{k'}) = \langle \hat{a}^\dagger_{\boldsymbol{k}} \hat{a}^\dagger_{\boldsymbol{k'}} \hat{a}_{\boldsymbol{k}} \hat{a}_{\boldsymbol{k'}} \rangle$$

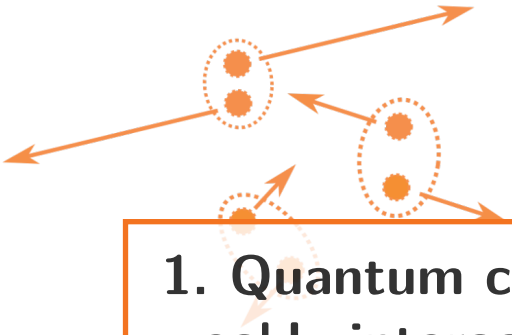

Chapter 1

1. Quantum correlations in the weakly-interacting Bose gas

The main challenge of quantum many-body physics is to understand how ensembles of interacting individual particles behave. Towards this aim, many meaningful information can be obtained by studying how the interactions between the different particles induce **correlations** in the degrees of freedom of the particles, *e.g.* their position, their momentum or their spin. To understand and quantify these correlations, physicists have used the mathematical formalism of **correlation functions** that we will introduce in this chapter.

Historically, the first field of physics that developed and made an extensive use of correlation functions was the field of Optics, and more specifically Quantum Optics in the 50s-60s. The interest for correlation functions was sparked by the Hanbury Brown and Twiss experiment of 1954 measuring intensity correlations in the light emitted by a star between two separate photo-detectors. Trying to provide an explanation of these experiments in terms of the detection of individual photons led R. J. Glauber to develop his theory of photodetection [74] using correlation functions in a seminal paper of 1963. This theory was then later adapted to study more complex systems where the particles, for instance atoms, interact.

One of the conceptually simplest example of such an interacting many-body system is the weakly-interacting homogeneous Bose gas, which describes an ensemble of bosons with weak contact and repulsive interactions in an homogeneous box potential. This system shows the great advantage that it can be theoretically described with a fairly great accuracy at the price of a few approximations that were suggested by N. Bogoliubov in 1947 [14]. One of the great success of this theory was to predict the existence of the quantum depletion that was later showed to be made of $\boldsymbol{k}/-\boldsymbol{k}$ correlated pair of atoms by Lee Huang and Yang [103] in 1957.

An experimental realisation of such a system proves to be rather difficult because of the **homogeneous** aspect of the theory that is hard to reproduce experimentally. Only recently were Bose gases realized in box traps in Cambridge [67] and the quantum depletion studied in this homogeneous configuration [106]. But experiments often rely on an harmonic potential to trap the atoms in one place, therefore breaking the homogeneity of the system and making theoretical approaches more complicated. However, recent

works [23, 110, 156] have aimed at characterizing correlation functions within the frame of Bogoliubov theory for inhomogeneous trapped systems to provide theoretical ground for comparison with experiments.

In this chapter, we will first introduce the concept of correlation functions by studying the historical and founding experiments of Optics and Quantum Optics. In a second stage, we will show how this formalism can be extended to atomic physics and apply it to the Bogoliubov theory of the homogeneous weakly-interacting Bose gas of which we will present the main lines. Finally, we will present some of the principal results of the work [23] extending the Bogoliubov theory to inhomogeneous systems produced with our experiment and discuss the experimental criteria to experimentally observe the $\boldsymbol{k}/-\boldsymbol{k}$ correlations of the quantum depletion.

1.1 Correlation functions in Classical and Quantum Optics

In the most general sense, correlation functions are a mathematical object characterizing the statistical correlations between random variables. They are defined from the concept of statistical average or expected value of a random variable in Mathematics which is intuitively understood as the value that we will get on average if we measure the random variable a large number of occurences. In the following, the statistical average of a random variable X is denoted $\langle X \rangle$.

The simplest correlation function correlating two random variables X_1 and X_2 that we take to be real for this simple introduction writes:

$$\mathrm{Corr}(X_1, X_2) = \langle X_1 X_2 \rangle \tag{1.1}$$

Interestingly, if X_1 and X_2 are independent and therefore uncorrelated, one has:

$$\langle X_1 X_2 \rangle = \langle X_1 \rangle \langle X_2 \rangle \tag{1.2}$$

meaning that the expected value of the product $X_1 X_2$ is simply the product of the expected values of X_1 and X_2. However, if X_1 and X_2 are correlated, the probability distribution of X_2 changes if we already know the realisation of X_1, preventing us to write the simple equation 1.2. The value of $\langle X_1 X_2 \rangle$ thus quantifies the degree of correlation of the two random variables. The concept of correlation function can be generalized up to any order to involve several random variables. We also note that in physics, the random variables are often dependent from time, space etc.. In all generality, the correlation function correlating n random variables writes:

$$\mathrm{Corr}^{(n)}(X_1(s_1), X_2(s_2), ..., X_i(s_i), ..., X_n(s_n)) = \langle X_1(s_1) X_2(s_2) ... X_i(s_i) ... X_n(s_n) \rangle \tag{1.3}$$

where s_i is the proper set of parameters describing the variable X_i.

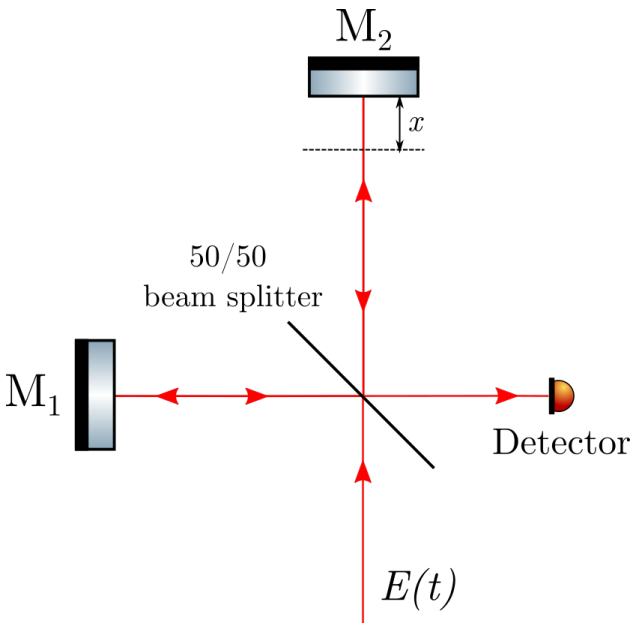

Figure 1.1: Principle of the Michelson interferometer.

1.1.1 First order correlation function of classical light

Having seen the general definition of correlation functions, let us now illustrate how they can be used in Physics with the simple example of the classical description of light. Correlation functions of light were introduced in connection with the notion of **coherence** that characterizes the possibility for waves to interfere. A light field is said to be coherent when there is a fixed phase relationship for the electric field at different positions (spatial coherence) and different times (time coherence).

To illustrate where correlation functions come from, we will first look at time coherence in the emblematic Michelson interferometer (see Fig.-1.1). For simplicity sake, we will not yet discuss spatial coherence effects and will thus consider a point source producing a complex, linearly-polarized light field $E(t)$ that enters the interferometer. The intensity measured by the detector writes[1]:

$$I = \langle |E(t) + E(t-\tau)|^2 \rangle \tag{1.4}$$

with $\tau = \frac{2x}{c}$ the delay between the two interfering waves induced by the optical path difference between the two arms of the interferometer. In Optics, the notation $\langle ... \rangle$ denotes the time averaging made by the detector. Developing equation 1.4 we get:

$$I = \langle |E(t)|^2 \rangle + \langle E(t-\tau)^2 \rangle + 2\mathrm{Re}\langle E(t)E^*(t-\tau) \rangle \tag{1.5}$$

For simplicity sake, we assume that the source is stationary to write $\langle |E(t)|^2 \rangle = \langle |E(t-\tau)|^2 \rangle = I_0$, we then obtain :

[1] While we write here an equal sign for clarity, we strictly speaking only have $I \propto \langle |E(t) + E(t-\tau)|^2 \rangle$

$$I = 2I_0\Big(1 + \mathrm{Re}\Big[g^{(1)}(\tau)\Big]\Big) \ , \ g^{(1)}(\tau) = \frac{\langle E(t)E^*(t-\tau)\rangle}{\langle |E|^2\rangle} \tag{1.6}$$

We have introduced the **normalized first-order correlation function** $g^{(1)}$ that characterizes the interference term. If $E(t)$ and $E(t-\tau)$ are independent random variables and thus uncorrelated, $\langle E(t)E^*(t-\tau)\rangle = \langle E(t)\rangle\langle E^*(t-\tau)\rangle = 0$ and interference are not observed. On the other hand, if there is a **correlation** between these two quantities, an interference phenomenon can be observed.

To illustrate what kind of information are contained in this first-order correlation function, we compute it for the simple case of a monochromatic light source of frequency ω_0. The light field writes:

$$E(t) = E_0 e^{i\omega_0 t} \tag{1.7}$$

Such a light source is perfectly coherent. From this, we calculate the first-order correlation function:

$$g^{(1)}(\tau) = \frac{|E_0|^2\langle e^{i\omega_0 t}e^{-i\omega_0(t-\tau)}\rangle}{|E_0|^2} = e^{i\omega_0\tau} \tag{1.8}$$

The detected intensity is thus a perfect sinusoidal function of τ that is scanned by changing the position of the second mirror and thus the value of x:

$$I(x) = 2I_0\Big(1 + \cos\Big(\omega_0\frac{2x}{c}\Big)\Big) \tag{1.9}$$

Measuring the intensity pattern as a function of x thus gives a measurement of ω_0. This model is however very idealized and does not exist in reality. To make it more plausible, we introduce a random phase $\phi(t)$:

$$E(t) = E_0 e^{i(\omega_0 t + \phi(t))} \tag{1.10}$$

To keep things simple, we will take $\phi(t)$ uniformly distributed on $[0, 2\pi)$ and assume phase "jumps" from a value to another with a time-independent probability. This is the so-called wave packet model. Between two times t and $t+dt$, the probability for the phase to change writes:

$$\mathrm{d}P = \frac{\mathrm{d}t}{\tau_c} \tag{1.11}$$

with τ_c a time constant called the **coherence time**.

The first-order correlation function is now:

$$g^{(1)}(\tau) = \langle e^{i(\phi(t)-\phi(t-\tau))}\rangle e^{i\omega_0\tau} \tag{1.12}$$

We therefore need to evaluate $\langle e^{i(\phi(t)-\phi(t-\tau))}\rangle$. If the phase has not changed between $t-\tau$ and t, we simply have $\langle e^{i(\phi(t)-\phi(t-\tau))}\rangle = 1$. On the contrary, if the phase has changed in this time interval, $\langle e^{i(\phi(t)-\phi(t-\tau))}\rangle = 0$ as the phase jumps are independent. We therefore need to determine the probability $P_0(t)$ that no phase jump occurs between $t = 0$ and a time t. The probability for the phase to stay constant up to a time $t + \mathrm{d}t$ writes:

$$P_0(t + \mathrm{d}t) = P_0(t)\left[1 - \frac{\mathrm{d}t}{\tau_c}\right] \tag{1.13}$$

from which we get the differential equation:

$$\frac{\mathrm{d}P_0(t)}{\mathrm{d}t} + \frac{P_0(t)}{\tau_c} = 0 \tag{1.14}$$

whose solution is (with $P_0(0) = 1$):

$$P_0(t) = e^{-t/\tau_c} \tag{1.15}$$

The first-order correlation function then writes:

$$g^{(1)}(\tau) = (1 \times e^{-\tau/\tau_c} + 0 \times (1 - e^{-\tau/\tau_c}))e^{i\omega_0\tau} = e^{-\tau/\tau_c}e^{i\omega_0\tau} \tag{1.16}$$

The visibility of the interference pattern therefore decays exponentially on the scale set by τ_c. We can keep complexifying the problem and consider a source with two monochromatic components ω_1 and ω_2. The new light field is now:

$$E(t) = E_1 e^{i(\omega_1 t+\phi_1(t))} + E_2 e^{i(\omega_2 t+\phi_2(t))} \tag{1.17}$$

We take $\phi_1(t)$ and $\phi_2(t)$ to be uncorrelated random variables described by the same probability law characterized by the coherence time τ_c. The numerator of the first-order correlation function now writes:

$$\begin{aligned}\langle E(t)E^*(t-\tau)\rangle = {} & e^{-\tau/\tau_c}(I_1 e^{i\omega_1\tau} + I_2 e^{i\omega_2\tau}) \\ & + \langle E_1 E_2^* e^{i\omega_2\tau} e^{i(\omega_1-\omega_2)t} e^{i(\phi_1(t)-\phi_2(t-\tau))}\rangle \\ & + \langle E_2 E_1^* e^{i\omega_1\tau} e^{i(\omega_2-\omega_1)t} e^{i(\phi_2(t)-\phi_1(t-\tau))}\rangle\end{aligned} \tag{1.18}$$

where the two last terms are null as $\phi_1(t)$ and $\phi_2(t)$ are uncorrelated. If we consider the simple case where $I_1 = I_2$, the normalized first-order correlation function writes:

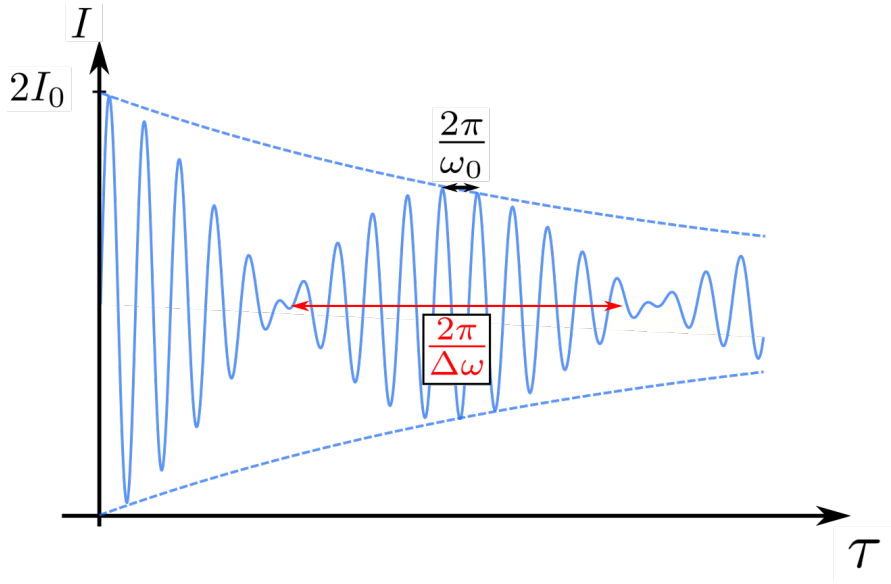

Figure 1.2: Intensity pattern for a light source with two monochromatic component of frequencies ω_1 and ω_2. The fast oscillation of frequency $\omega_0 = (\omega_1 + \omega_2)/2$ is modulated by a slow oscillation of frequency $\Delta\omega = |\omega_1 - \omega_2|$ and an exponential decay $e^{-\tau/\tau_c}$.

$$g^{(1)}(\tau) = \frac{1}{2} e^{-\tau/\tau_c} (e^{i\omega_1 \tau} + e^{i\omega_2 \tau}) \tag{1.19}$$

We simply get the sum of the contribution of the two frequencies. The intensity pattern as a function of x is thus the sum of two cosine functions with different frequencies. Using trigonometric identities, we find that the intensity pattern consists of a "fast" oscillation of frequency $\omega_0 = (\omega_1 + \omega_2)/2$, modulated by a "slow" oscillation of frequency $\Delta\omega = |\omega_1 - \omega_2|$ as well as an exponential decay $e^{-\tau/\tau_c}$, reducing the visibility of the interference pattern (see Fig.-1.2).

Through this very simple example, we understand that the observed interference pattern strongly depends on the spectrum of the source. For a source with an arbitrary spectrum $S(\omega)$, under the assumption that every spectral components are independent and do not interfere with one another, the overall intensity pattern results of the sum of the contribution of each spectral component:

$$I = \int_{-\infty}^{\infty} 2S(\omega)[1 + \cos(\omega\tau)]\mathrm{d}\omega \tag{1.20}$$

Writing $\int_{-\infty}^{\infty} S(\omega)\mathrm{d}\omega = I_0$ and $s(\omega) = S(\omega)/I_0$, we obtain

$$I = 2I_0 \left[1 + \int_{-\infty}^{\infty} s(\omega)\cos(\omega\tau)\mathrm{d}\omega\right] \tag{1.21}$$

As $S(\omega) = |\mathrm{FT}[E(t)]|^2$ where FT denotes the Fourier transform, $s(\omega)$ is real allowing us to write [108]:

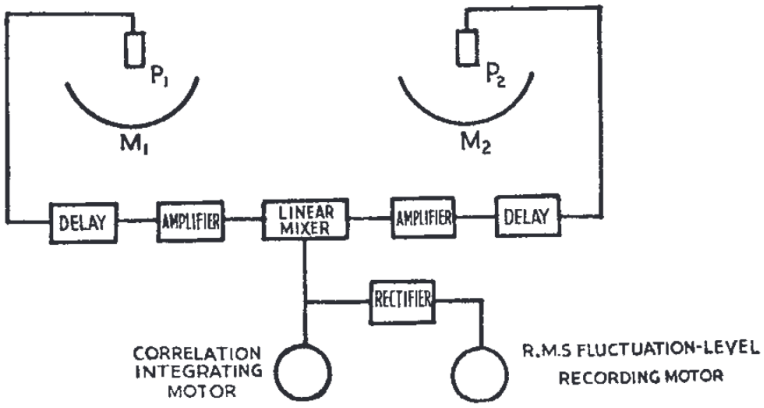

Figure 1.3: Diagram of the historical Hanbury Brown and Twiss apparatus, taken from [17]. The novelty of this apparatus was to use two detectors, P_1 and P_2, to measure the second-order correlation function.

$$I = 2I_0 \left[1 + \mathrm{Re}\left(\int_{-\infty}^{\infty} s(\omega)\cos(\omega\tau)\mathrm{d}\omega\right)\right] \tag{1.22}$$

From which we get, using equation 1.5:

$$g^{(1)}(\tau) = \int_{-\infty}^{\infty} s(\omega)\mathrm{e}^{\mathrm{i}\omega\tau}\mathrm{d}\omega \tag{1.23}$$

where we recognize the definition of the Fourier transform. This is the **Wiener-Khintchine** theorem. The first-order correlation function, measurable with an interferometric measurement, thus contains information about the spectrum of the light source.

In this introductory paragraph, we have seen a concrete and evocative example of how correlation functions can be used to obtain meaningful information about a given system, here a light source, with the simplest correlation function there is, correlating two values of the light field. This idea can be extended to higher order of correlations like intensity correlations, involving four values of the light field. This was at the core of the approach developed by Hanbury Brown and Twiss to improve the resolution of the Michelson interferometer to measure the size of the stars and avoid the deterrent effect of turbulences from the atmosphere in their celebrated 1954 article [18]. This experiment was of particular importance as its interpretation in terms of individual particles, the photons, gave birth to the field of Quantum Optics.

1.1.2 Second order correlation function of light: Hanbury Brown and Twiss experiment

The scheme proposed by Hanbury Brown and Twiss relies on the measurement of cross-correlations between the intensities measured by two independent photodetectors (see Fig-1.3), *i.e* a measurement of the **second-order correlation function**. To understand how it works, we will follow the complementary approach to the one developed in the last paragraph and look at the spatial properties of the light source.

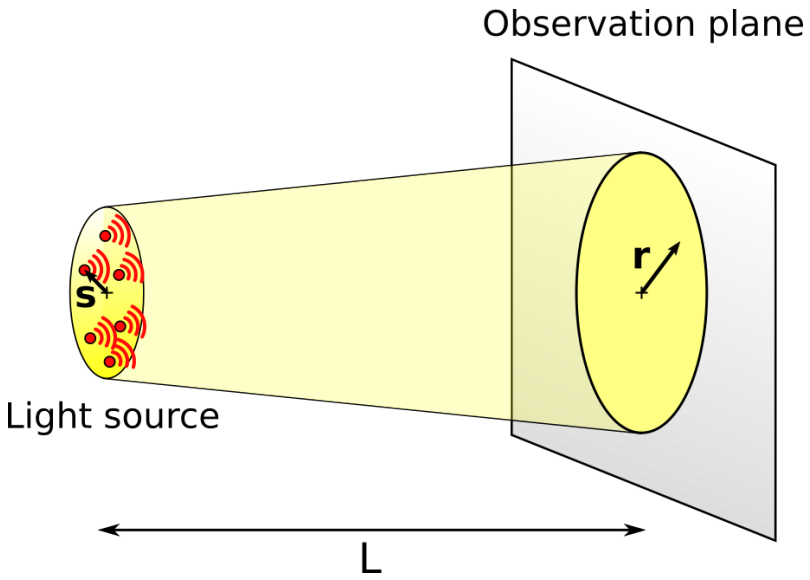

Figure 1.4: Schematic of an extended light source. The small red dots represent the different incoherent elementary emitters of the source.

A star is described as an incoherent, extended light source that we approximate to be monochromatic (wavelength λ) for simplicity (in practice, filters can be used to obtain a quasi-monochromatic source). We write S the surface of the source seen from the Earth. We model this source of light as an ensemble of elementary, point-like and independent emitters and note their spatial location $\boldsymbol{s}$. The field amplitude at a point $\boldsymbol{r}$ in an observation plane situated at distance L, far-away from the source so that we are in the Fraunhofer regime $L \gg \lambda, r, s$, writes (see Fig-.1.4):

$$E(\boldsymbol{r}) \propto \int_S e(\boldsymbol{s}) e^{\frac{i\pi}{\lambda L}|\boldsymbol{r}-\boldsymbol{s}|^2} d\boldsymbol{s} \tag{1.24}$$

The second-order correlation function correlates the values of the intensity of the light field at two different points of space $\boldsymbol{r}_1$ and $\boldsymbol{r}_2$. In terms of field amplitude, it corresponds to the four-term correlator:

$$G^{(2)}(\boldsymbol{r}_1, \boldsymbol{r}_2) = \langle E^*(\boldsymbol{r}_1) E(\boldsymbol{r}_1) E^*(\boldsymbol{r}_2) E(\boldsymbol{r}_2) \rangle \tag{1.25}$$

All the elementary emitters are incoherent and thus each have a random phase value, determined by an uniform probability law defined on the interval $[0, 2\pi)$. They thus form a set of **independent** random variables with the **same statistics**. We can therefore apply the Central Limit Theorem to the sum of their contributions $E(\boldsymbol{r})$ and find that it follows Gaussian statistics [75]. The fact that E is a classical Gaussian variable allows us to simplify the four-term correlator into:

$$G^{(2)}(\boldsymbol{r}_1, \boldsymbol{r}_2) = \langle I(\boldsymbol{r}_1) \rangle \langle I(\boldsymbol{r}_2) \rangle + \langle E^*(\boldsymbol{r}_1) E(\boldsymbol{r}_2) \rangle \langle E(\boldsymbol{r}_1) E^*(\boldsymbol{r}_2) \rangle \tag{1.26}$$

We recognize in the second term the spatial counterpart of the temporal first-order correlation function discussed in the previous paragraph. Using equation 1.24, we obtain:

$$G^{(1)}(\boldsymbol{r}_1,\boldsymbol{r}_2) = \langle E^*(\boldsymbol{r}_1)E(\boldsymbol{r}_2)\rangle \propto \iint_S \langle e^*(\boldsymbol{s}_1)e(\boldsymbol{s}_2)\rangle\, e^{-\frac{i\pi}{\lambda L}\left(|\boldsymbol{r}_1-\boldsymbol{s}_1|^2-|\boldsymbol{r}_2-\boldsymbol{s}_2|^2\right)}\mathrm{d}\boldsymbol{s}_1\mathrm{d}\boldsymbol{s}_2 \quad (1.27)$$

Since the source is incoherent, $\langle e^*(\boldsymbol{s}_1)e(\boldsymbol{s}_2)\rangle = I(\boldsymbol{s}_1)\delta_{\boldsymbol{s}_1,\boldsymbol{s}_2}$, leading to

$$G^{(1)}(\boldsymbol{r}_1,\boldsymbol{r}_2) \propto \int_S I(\boldsymbol{s}_1)e^{-\frac{2i\pi}{\lambda L}(\boldsymbol{r}_1-\boldsymbol{r}_2)\boldsymbol{s}_1}\mathrm{d}\boldsymbol{s}_1 \quad (1.28)$$

In analogy with what we showed in the last paragraph for the temporal coherence, the first-order spatial correlation function is the Fourier transform of the spatial intensity profile. This is known as the **Van Cittert-Zernike** theorem [75]. For a homogeneous intensity distribution of the source, the first-order correlation function decays on a length scale called the **correlation length** l_c proportional to the inverse of the source size L_{source}, $l_c \sim \lambda L/L_{\text{source}}$.

In a nutshell, the second-order normalized correlation function takes the simple expression:

$$g^{(2)}(\boldsymbol{r}_1,\boldsymbol{r}_2) = \frac{\langle I(\boldsymbol{r}_1)\rangle\langle I(\boldsymbol{r}_2)\rangle + \langle E^*(\boldsymbol{r}_1)E(\boldsymbol{r}_2)\rangle\langle E(\boldsymbol{r}_1)E^*(\boldsymbol{r}_2)\rangle}{\langle I(\boldsymbol{r}_1)\rangle\langle I(\boldsymbol{r}_2)\rangle} = 1 + |g^{(1)}(\boldsymbol{r}_1,\boldsymbol{r}_2)|^2 \quad (1.29)$$

Depending on the positions of the detectors $\boldsymbol{r}_1$ and $\boldsymbol{r}_2$ we have (see Fig.-1.5):

- $g^{(2)}(\boldsymbol{r}_1,\boldsymbol{r}_2) = 2$ for $\boldsymbol{r}_1 = \boldsymbol{r}_2$
- $1 \leq g^{(2)}(\boldsymbol{r}_1,\boldsymbol{r}_2) \leq 2$ for $|\boldsymbol{r}_1 - \boldsymbol{r}_2| \lesssim l_c$
- $g^{(2)}(\boldsymbol{r}_1,\boldsymbol{r}_2) = 1$ for $|\boldsymbol{r}_1 - \boldsymbol{r}_2| \gg l_c$

The size of the source can thus be measured by progressively increasing the distance between the two detectors and measuring the length scale on which the second order correlation function decreases. This was done successfully by Hanbury Brown and Twiss [17] to measure the size of Sirius in 1956.

While the calculations are rather straightforward in a classical model where light is described as a wave, the interpretation of the Hanbury Brown and Twiss experiment in terms of individual particles, *i.e* from a Quantum Optics point of view, sparked many debates that lead to a deeper understanding of the phenomena involved. If we take a look at what happens for $\boldsymbol{r}_1 = \boldsymbol{r}_2$, we see that a peculiar phenomenon occurs. The normalized second-order correlation function can be interpreted as the probability to detect simultaneously two photons on the detector located at $\boldsymbol{r}_1$ and $\boldsymbol{r}_2$, normalized by the probability to detect them independently. Therefore, since $g^{(2)}(\boldsymbol{r}_1,\boldsymbol{r}_2) = 2$ for $\boldsymbol{r}_1 = \boldsymbol{r}_2$, the probability to detect two photons at the same position is twice as high as it is to detect them independently! It was only after a few years that an explanation was suggested by Fano in 1961 [56]. Considering a pair of source points A and B in the star and two detectors 1 and 2 on Earth, Fig-.1.6 illustrates the two possibilities for a joint detection of two photons on the couple of detectors. For indistinguishable photons, the paths amplitudes interfere constructively resulting in a joint detection probability higher

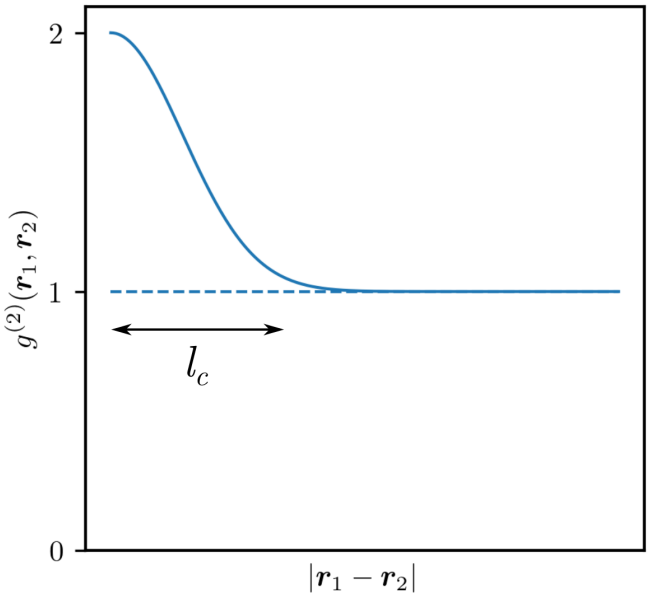

Figure 1.5: Second-order normalized correlation function for the Hanbury Brown and Twiss effect.

than that for independent events. While the interference effect is averaged out considering all the possible pairs of elementary emitters in the source, it can be observed when the distance between the two detectors is very close to zero, as observed by Hanbury Brown and Twiss. Interestingly, the interferences are destructive for fermions, resulting in a reduced probability of joint detection, also referred as **anti-bunching**, an effect than cannot be explained classically contrary to the Hanbury Brown and Twiss effect.

Because it will be a crucial point in the following of this thesis, we stress that the key ingredient to observe bosonic bunching is the **chaotic** character of the source. The theoretical development that we have just presented relies on the application of the Central Limit Theorem for the source made of a large number of independent elementary emitters, each with a random phase. This is notably not the case for laser light that we will discuss in the next paragraph.

To summarize, we have seen in this paragraph an example of a second-order correlation effect, the Hanbury Brown and Twiss effect, and its classical description with a chaotic light source. We also have an insight of how this effect can be understood when considering individual particles, here photons, laying the grounds to study more complex systems with correlations between interacting quantum particles. The observations of Hanbury Brown and Twiss sparked interest in the community and lead to the development of the new formalism of Quantum Optics [74] with quantized light fields or light particles, *i.e.* photons, with the great success that we know of today. In the next paragraphs, we will study the main elements of the theory of Quantum Optics through a few examples of increasing complexity as a mean to understand and conceptualize correlations at the single particle level.

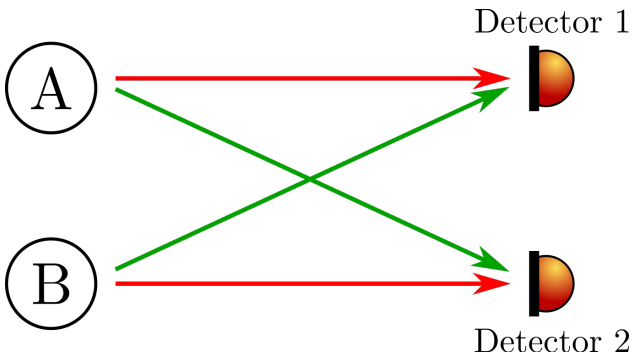

Figure 1.6: Quantum interpretation of the Hanbury Brown and Twiss effect. For two source points A and B, a joint detection occurs if a photon produced by A is detected in 1 and a photon produced by B is detected in 2 (red arrows), or the other way around A $\rightarrow$ 2 and B $\rightarrow$ 1 (green arrows). Interferences of the paths amplitudes explain the Hanbury Brown and Twiss effect.

1.1.3 Second quantization and correlations between individual particles

The first quantum descriptions, such as the one developed by Planck to describe black-body radiation, were in fact semi-classical theories in the sense that only the energy of the atoms is quantized, while the radiation fields are still described classically. While semi-classical theories found great success, the observations of Hanbury Brown and Twiss, as well as the development of laser light called for a theory accounting for the corpuscular aspect of light. This gave birth to the Quantum Optics theory whose core element is to push further the idea of quantization by quantizing the radiation fields. While the term is most often associated with atomic physics as we will see later on, we can speak here of **second quantization**, the first quantization being the one of the energy.

The general idea behind the quantization of the light field is to describe light as a collection of independent quantum harmonic oscillators for the different modes of the field. For a field defined in a box of volume $V = L^3$ with periodic boundary conditions, the field can be described as a superposition of plane waves with a wave vector $k = \frac{2\pi}{L}n$ with $n \in \mathbb{N}$ each described by a harmonic oscillator [162]:

$$\hat{\boldsymbol{E}}(\boldsymbol{r},t) = \sum_l i\boldsymbol{\epsilon}_l \sqrt{\frac{\hbar\omega_l}{2\varepsilon_0 V}} \left[e^{i(\boldsymbol{k}_l\cdot\boldsymbol{r}-\omega_l t)}\hat{a}_l - e^{-i(\boldsymbol{k}_l\cdot\boldsymbol{r}-\omega_l t)}\hat{a}_l^\dagger\right] = \hat{\boldsymbol{E}}^{(+)}(\boldsymbol{r},t) + \hat{\boldsymbol{E}}^{(-)}(\boldsymbol{r},t) \quad (1.30)$$

where $\boldsymbol{\epsilon}_l$ denotes the polarisation of mode l. We have introduced the two mutually adjoint operators $\hat{a}_l$ and $\hat{a}_l^\dagger$, analog to the creation and annihilation operators of the quantum harmonic oscillator. In the formalism of the quantum harmonic oscillator, these operators respectively destroy or create a quanta of energy, which in our case corresponds to a photon in mode l. Since photons are bosons, $\hat{a}_l$ and $\hat{a}_l^\dagger$ follow the commutation relations:

$$\left[\hat{a}_l, \hat{a}_{l'}^\dagger\right] = \delta_{ll'} \quad [\hat{a}_{l'}, \hat{a}_l] = 0 \quad (1.31)$$

To show the effect of $\hat{a}_l$ and $\hat{a}_l^\dagger$, we introduce the **number states** or **Fock states**

$|n_l\rangle$, eigenstates of the number operator $\hat{N}_l = \hat{a}_l^\dagger \hat{a}_l$ with n_l representing the number of photons in mode l. The Fock state corresponding to the absence of the photons is called the vacuum state and denoted $|0\rangle$. The action of the creation and annihilation operators on the Fock states writes:

$$\hat{a}_l^\dagger |n_l\rangle = \sqrt{n_l + 1}\, |n_l + 1\rangle \tag{1.32}$$

$$\hat{a}_l |n_l\rangle = \sqrt{n_l}\, |n_l - 1\rangle \tag{1.33}$$

From this, we see that every Fock state can be obtained by applying the creation operator on the vacuum state the right amount of times:

$$|n_l\rangle = \frac{1}{\sqrt{n_l!}} \left(\hat{a}_l^\dagger\right)^{n_l} |0\rangle \tag{1.34}$$

Finally we can write the Hamiltonian of the collection of independent quantum harmonic oscillators as:

$$\hat{H} = \sum_l \hbar\omega_l \left(\hat{N}_l + \frac{1}{2}\right) \tag{1.35}$$

with $\hbar\omega_l$ being the energy of a photon in mode l.

n-th order correlation functions

As discussed in the previous paragraphs, there is a strong connection between correlation functions and the notion of coherence. Motivated by the measurements of Hanbury Brown and Twiss, Roy J. Glauber introduced [74] the notion of n-th order coherence in the formalism of Quantum Optics and linked it to n-th order correlation functions, as we will recall now.

We have discussed so far correlation functions up to the second order. Correlation functions can be extended to higher order n describing the probability of joint detection of n photons at a set of positions and times $\{(\boldsymbol{r}_1, t_1), (\boldsymbol{r}_2, t_2), ..., (\boldsymbol{r}_n, t_n)\}$:

$$G^{(n)}(\boldsymbol{r}_1, t_1, ..., \boldsymbol{r}_n, t_n) = \left\langle \hat{\boldsymbol{E}}^{(-)}(\boldsymbol{r}_1, t_1) ... \hat{\boldsymbol{E}}^{(-)}(\boldsymbol{r}_n, t_n)\, \hat{\boldsymbol{E}}^{(+)}(\boldsymbol{r}_n, t_n) ... \hat{\boldsymbol{E}}^{(+)}(\boldsymbol{r}_1, t_1) \right\rangle \tag{1.36}$$

Note that the order of the operators is important with all the terms in $\hat{E}^{(-)}$ (and thus $\hat{a}^\dagger$) on the left and terms in $\hat{E}^{(+)}$ (and thus $\hat{a}$) on the right. This is called **normal ordering** and ensures that the expectation value of the combination of the operators is zero for the vacuum state.

Likewise, we introduce the normalized $n-$th order correlation function.

$$g^{(n)}\left(\boldsymbol{r}_1, t_1, ..., \boldsymbol{r}_n, t_n\right) = \frac{G^{(n)}\left(\boldsymbol{r}_1, t_1, ..., \boldsymbol{r}_n, t_n\right)}{\prod_{j=1}^{n} G^{(1)}\left(\boldsymbol{r}_1, t_1, ..., \boldsymbol{r}_n, t_n\right)} \tag{1.37}$$

Coherent states

From this definition, we define a fully coherent field as a field that verifies, for any value of $n \in \mathbb{N}^*$ [74]:

$$g^{(n)}\left(\boldsymbol{r}_1, t_1, ..., \boldsymbol{r}_n, t_n\right) = 1 \tag{1.38}$$

This means that for a fully coherent field, we have the simple relation:

$$G^{(j)}\left(\boldsymbol{r}_1, t_1, ..., \boldsymbol{r}_j, t_j\right) = \prod_{i=1}^{j} G^{(j)}(\boldsymbol{r}_i, t_i) \tag{1.39}$$

Interestingly, we note that if the field was in a state $|\alpha\rangle$ that would be an eigenstate of $\hat{\boldsymbol{E}}^{(+)}$, $\hat{\boldsymbol{E}}^{(+)}|\alpha\rangle = \alpha|\alpha\rangle$, and an eigenstate of $\hat{\boldsymbol{E}}^{(-)}$, $\langle\alpha|\hat{\boldsymbol{E}}^{(-)} = \langle\alpha|\alpha^*$, the conditions 1.38 and 1.39 would be automatically verified. For simplicity sake, we consider a single mode and use the fact that $\hat{\boldsymbol{E}}^{(+)} \propto \hat{a}$ and $\hat{\boldsymbol{E}}^{(-)} \propto \hat{a}^\dagger$. We are thus looking for the state $|\alpha\rangle$ which is an eigenstate of $\hat{a}$. It can be shown that in the basis of the number states, $|\alpha\rangle$ writes [73]:

$$|\alpha\rangle = e^{-\frac{1}{2}|\alpha|^2} \sum_{n=0}^{\infty} \frac{\alpha^n}{\sqrt{n!}} |n\rangle \tag{1.40}$$

The state $|\alpha\rangle$ is called a **coherent state** or Glauber state. We thus find that a coherent state writes as a sum of number states and that the probability to find n photons follows a Poissonian law (see Fig.-1.7). A well-known example of coherent state is laser light.

Let us now close the parenthesis on the coherent state and come back to the Hanbury Brown and Twiss effect described in the last sub-section, characterized by $g^{(2)}(\boldsymbol{r}_1, t_1, \boldsymbol{r}_2, t_2) = 2$ for $\boldsymbol{r}_1 = \boldsymbol{r}_2$ and $t_1 = t_2$. As we have just seen, it would be impossible to observe this effect with a fully coherent light as $g^{(2)}(\boldsymbol{r}_1, t_1, \boldsymbol{r}_2, t_2) = 1$ by definition. Let us rewrite the second order correlation function in the formalism of Quantum Optics to see if it tells us something new. For $\boldsymbol{r}_1 = \boldsymbol{r}_2$ and $t_1 = t_2$, the expression writes:

$$g^{(2)}\left(\boldsymbol{r}_1, t_1, \boldsymbol{r}_2 = \boldsymbol{r}_1, t_2 = t_1\right) = \frac{\left\langle \hat{a}^\dagger \hat{a}^\dagger \hat{a} \hat{a} \right\rangle}{\left\langle \hat{a}^\dagger \hat{a} \right\rangle^2} \tag{1.41}$$

Using the commutation relation, we write:

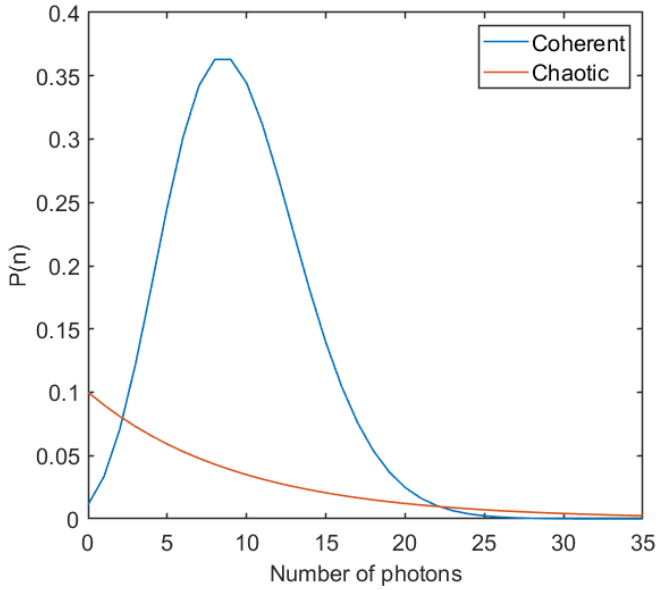

Figure 1.7: Probability distribution of the number of photons for coherent and chaotic light sources for a fixed value of $|\alpha^2|$.

$$g^{(2)}\left(\boldsymbol{r}_1, t_1, \boldsymbol{r}_2 = \boldsymbol{r}_1, t_2 = t_1\right) = \frac{\left\langle \hat{a}^\dagger(\hat{a}\hat{a}^\dagger - 1)\hat{a} \right\rangle}{\left\langle \hat{a}^\dagger \hat{a} \right\rangle^2} = \frac{\langle \hat{N}^2 \rangle - \langle \hat{N} \rangle}{\left\langle \hat{a}^\dagger \hat{a} \right\rangle^2} = 1 + \frac{\sigma_N^2 - \langle \hat{N} \rangle}{\left\langle \hat{a}^\dagger \hat{a} \right\rangle^2} \tag{1.42}$$

where we introduce σ_N the standard deviation of the number of photons N. We see that the value of $g^{(2)}$ depends on the statistics of the source. For the case of laser light where N follows a Poissonian law, $\sigma_N^2 = \langle \hat{N} \rangle$ and we retrieve $g^{(2)}\left(\boldsymbol{r}_1, t_1, \boldsymbol{r}_2 = \boldsymbol{r}_1, t_2 = t_1\right) = 1$.

Thermal chaotic states

To understand how the Hanbury Brown and Twiss effect arises, we need to introduce the concept of **mixed states**, in opposition to **pure states**. In most cases, our limited knowledge of the system requires to describe it as a statistical mixture of pure states. This is what we call a mixed state. For such states, we use the formalism of the **density matrix** which is defined as:

$$\hat{\rho} = \sum_i p_i \left|\Psi_i\right\rangle \left\langle\Psi_i\right| \tag{1.43}$$

where p_i is the probability for the system to be in the pure state $|\Psi_i\rangle$. The expectation value of an operator $\hat{O}$ is obtained through:

$$\langle \hat{O} \rangle = \mathrm{Tr}(\hat{\rho}\hat{\mathrm{O}}) \tag{1.44}$$

This formalism is particularly useful to describe light sources made of a large number of independent individual emitters. Let us say that the first emitter brings the field in

state $|\alpha_1\rangle$, the second emitter in state $|\alpha_2\rangle$ etc.. It can be shown ([73]) that for a large number of individual emitters j, the probability distribution for the complex amplitude $\alpha = \alpha_1 + \alpha_2 + ... + \alpha_j$ follows a Gaussian law:

$$P(\alpha) = \frac{1}{\pi\langle n\rangle} e^{-\frac{|\alpha|^2}{\langle n\rangle}} \tag{1.45}$$

where $\langle n\rangle$ is the mean value of $|\alpha|^2$ and represents the number of energy quanta in the mode. From this, we use equation 1.40 to write the density matrix of the system in the basis of the number states:

$$\hat{\rho} = \frac{1}{1+\langle n\rangle} \sum_{m=0}^{\infty} \left(\frac{\langle n\rangle}{1+\langle n\rangle}\right)^m |m\rangle\langle m| \tag{1.46}$$

The probability to find m photons then writes (see Fig.-1.7):

$$P(m) = \frac{1}{1+\langle n\rangle} \left(\frac{\langle n\rangle}{1+\langle n\rangle}\right)^m \tag{1.47}$$

A light source with these statistics is called a **chaotic** light source. This is notably the case of thermal light, described by the Planck's distribution with $\langle n\rangle = 1/(e^{h\nu/k_B T} - 1)$. From equation 1.47, we find that the variance of the photon number N writes:

$$\sigma_N^2 = \langle N\rangle^2 + \langle N\rangle \tag{1.48}$$

Injecting this result into equation 1.42, we find that for a chaotic light source, $g^{(2)}(\boldsymbol{r}_1, t_1, \boldsymbol{r}_2, t_2) = 2$ for $\boldsymbol{r}_1 = \boldsymbol{r}_2$ and $t_1 = t_2$, that is the bosonic bunching observed by Hanbury Brown and Twiss!

In fact, this result can be obtained through a complementary approach that relies on the application of the Wick's theorem [66].

Wick's theorem

Wick's theorem

When a system is characterized by a Gaussian density matrix [66] $\hat{\rho} \propto \exp\left(\sum_i (\alpha_i \hat{a}_i^\dagger \hat{a}_i + \beta_i \hat{a}_i^2 + \gamma_i \hat{a}_i^{\dagger 2})\right)$ and $\forall i, \langle \hat{a}_i\rangle = \langle \hat{a}_i^\dagger\rangle = 0$, the high-order products of of creation and annihilation operators can be factorized into all possible products of only two operators. For bosonic particles, this writes:

$$\langle \hat{A}_1 ... \hat{A}_{2m}\rangle = \sum_\sigma \langle \hat{A}_{i_1}\hat{A}_{i_2}\rangle\langle \hat{A}_{i_3}\hat{A}_{i_4}\rangle ... \langle \hat{A}_{i_{2m-1}}\hat{A}_{i_{2m}}\rangle$$

where σ denotes all possible permutations changing the order $1, 2, ..., 2m$ to $i_1, i_2, ..., i_{2m}$, and $\hat{A}_i$ is any creation or annihilation operator.

As shown in equations 1.45 and 1.46, the density matrix of a chaotic light source is Gaussian, it is therefore possible to use Wick's theorem to simplify the second-order correlation function

$$g^{(2)}\left(\boldsymbol{r}_1, t_1, \boldsymbol{r}_2 = \boldsymbol{r}_1, t_2 = t_1\right) = \frac{\langle \hat{a}^\dagger \hat{a}^\dagger \rangle \langle \hat{a}\hat{a} \rangle + 2\langle \hat{a}^\dagger \hat{a} \rangle^2}{\langle \hat{a}^\dagger \hat{a} \rangle^2} \tag{1.49}$$

For a thermal chaotic state where the number of photons is well-defined, the averages $\langle \hat{a}^\dagger \hat{a}^\dagger \rangle$ and $\langle \hat{a}\hat{a} \rangle$ are null as they do not conserve the number of photons. We thus retrieve that $g^{(2)}\left(\boldsymbol{r}_1, t_1, \boldsymbol{r}_2 = \boldsymbol{r}_1, t_2 = t_1\right) = 2$. Actually, this procedure can be extended up to any order to show that the n-th order correlation function can be simplified to a linear combination of first-order correlation functions. This means that the entirety of the information is contained in the first-order correlation function. The normalized probability of joint detection of n photons then writes:

$$g^{(n)}(\boldsymbol{r}_1, ..., \boldsymbol{r}_n, t_1, ..., t_n) = n! \text{ for } \boldsymbol{r}_1 = \boldsymbol{r}_2 = ... = \boldsymbol{r}_n \text{ and } t_1 = t_2 = ... = t_n \tag{1.50}$$

which is a generalisation of the two particles bosonic bunching, seen previously, for n particles. Importantly, the situation is very different with a coherent state $|\alpha\rangle$ as we have $\langle \hat{a} \rangle, \langle \hat{a}^\dagger \rangle, \langle \hat{a}\hat{a} \rangle, \langle \hat{a}^\dagger \hat{a}^\dagger \rangle \neq 0$ (because the well-defined phase implies that the photon number is not defined). While the Wick's theorem still applies, its expression is more complicated and not helpful as the second order correlation function is much easier to compute:

$$g^{(2)}\left(\boldsymbol{r}_1, t_1, \boldsymbol{r}_2 = \boldsymbol{r}_1, t_2 = t_1\right) = \frac{\langle \alpha | \, \hat{a}^\dagger \hat{a}^\dagger \hat{a}\hat{a} \, | \alpha \rangle}{\langle \alpha | \, \hat{a}^\dagger \hat{a} \, | \alpha \rangle^2} = \frac{|\alpha|^4}{|\alpha|^4} = 1 \tag{1.51}$$

This proves that coherent states do not show bosonic bunching.

We have thus seen how the Hanbury Brown and Twiss effect writes in the formalism of Quantum Optics and shown the differences between a coherent and chaotic light source. We will keep this result in the back of our minds as it will be of primary importance when we will study second order correlation functions with interacting atoms a little further down the line.

1.1.4 The non-degenerate parametric amplifier

We will now increase the complexity by adding non-linearity in the systems we study as a means to induce additional correlations between different modes. The most emblematic example of such a system in Quantum Optics is the **non-degenerate parametric amplifier**. Through the interaction with a non-linear optical medium, a pump photon at frequency 2ω can be converted into two photons in two modes at frequency ω_1 and ω_2, the signal and idler mode that we name mode 1 and mode 2, with $2\omega = \omega_1 + \omega_2$. Using a few approximations (see [162]), the Hamiltonian of the system may be written as:

$$H = \hbar\omega_1 \hat{a}_1^\dagger \hat{a}_1 + \hbar\omega_2 \hat{a}_2^\dagger \hat{a}_2 + i\hbar\chi(\hat{a}_1^\dagger \hat{a}_2^\dagger e^{-2i\omega t} - \hat{a}_1 \hat{a}_2 e^{2i\omega t}) \tag{1.52}$$

where χ is a coupling constant. The particularity of the two photons produced from the pump photon is that they are emitted in a correlated manner as a **pair**. The system will thus feature **cross-correlations** between the modes 1 and 2.

This time-dependent problem is best solved in the interaction picture, *i.e.* where the time dependence is carried by both operators and states. The interaction Hamiltonian then writes:

$$\hat{H}_I(t) = i\hbar\chi(\hat{a}_1^\dagger(t)\hat{a}_2^\dagger(t) - \hat{a}_1(t)\hat{a}_2(t)) \tag{1.53}$$

The counterpart to the Schrödinger equation in the interaction picture is the Heisenberg equation of motion:

$$\frac{\mathrm{d}\hat{a}_1}{\mathrm{d}t} = \frac{1}{i\hbar}[\hat{a}_1, \hat{H}_I] = \chi\hat{a}_2^\dagger \tag{1.54}$$

$$\frac{\mathrm{d}\hat{a}_2^\dagger}{\mathrm{d}t} = \frac{1}{i\hbar}[\hat{a}_2^\dagger, \hat{H}_I] = \chi\hat{a}_1 \tag{1.55}$$

The solution of these coupled equations are:

$$\hat{a}_1(t) = \hat{a}_1(0)\mathrm{cosh}\chi t + \hat{a}_2^\dagger(0)\mathrm{sinh}\chi\mathrm{t} \tag{1.56}$$

$$\hat{a}_2(t) = \hat{a}_2(0)\mathrm{cosh}\chi t + \hat{a}_1^\dagger(0)\mathrm{sinh}\chi\mathrm{t} \tag{1.57}$$

From this, we can derive a few interesting results. First, we write the quantum state $|\Psi(t)\rangle$ generated by the parametric amplification process. To do so, we write the interaction picture evolution operator:

$$\hat{U}(t) = \exp\left[\chi t\left(\hat{a}_1^\dagger\hat{a}_2^\dagger - \hat{a}_1\hat{a}_2\right)\right] \tag{1.58}$$

At the price of a few lines of calculations (see [138]), this operator can be re-written in a factored form:

$$\hat{U}(t) = \frac{1}{(\cosh\chi t)} e^{\hat{a}_1^\dagger\hat{a}_2^\dagger \tanh\chi t} e^{-\left(\hat{a}_1^\dagger\hat{a}_1 + \hat{a}_2^\dagger\hat{a}_2 + 1\right)\ln(\cosh\chi t)} e^{-\hat{a}_1\hat{a}_2\tanh\chi t} \tag{1.59}$$

While this expression is a bit daunting, it becomes way simpler if we consider the initial state to be the vacuum:

$$|\Psi(t)\rangle = \frac{1}{(\cosh\chi t)} e^{\hat{a}_1^\dagger\hat{a}_2^\dagger\tanh\chi t}|0\rangle \tag{1.60}$$

We obtain easily from this the expression of $|\Psi(t)\rangle$ in the number states basis:

$$|\Psi(t)\rangle = \frac{1}{(\cosh \chi t)} \sum_{n=0}^{\infty} (\tanh \chi t)^n \, |n\rangle_1 \, |n\rangle_2 \tag{1.61}$$

The state thus writes as a superposition of number states with the same number of photons in modes 1 and 2. The populations in modes 1 and 2 are therefore **perfectly correlated**. If we now look at the reduced state corresponding to mode 1 for instance, the reduced density matrix writes:

$$\hat{\rho}_1(t) = \mathrm{Tr}_2 \left[|\Psi(t)\rangle \langle \Psi(t)| \right] = \frac{1}{\cosh^2 \chi t} \sum_{n=0}^{\infty} \tanh^{2n} \chi t \, |n\rangle_1 \langle n|_1 \tag{1.62}$$

Using the properties of hyperbolic functions, we get:

$$\hat{\rho}_1(t) = \frac{1}{1 + \sinh^2 \chi t} \sum_{n=0}^{\infty} \left(\frac{\sinh^2 \chi t}{1 + \sinh^2 \chi t} \right)^n |n\rangle_1 \langle n|_1 \tag{1.63}$$

where we recognize the form of the chaotic density matrix defined in equation 1.46 with $\langle n \rangle = \sinh^2 \chi t$. This result tells us that if we look only at one of the two modes and ignore the paired photons in the other mode, we observe bosonic bunching [172] $g^{(2)}(1,1) = g^{(2)}(2,2) = 2$.

Amplitude of cross-correlations

We have seen that the pairing process induces the presence of cross-correlations between modes 1 and 2 that can once again be characterized with the second-order correlation function. To look for a signature of these correlations, we compute the two-body correlator $G^{(2)}(1,2) = \langle \hat{a}_1^\dagger(t) \hat{a}_2^\dagger(t) \hat{a}_2(t) \hat{a}_1(t) \rangle$ which describes the probability to detect simultaneously a photon in mode 1 and a photon in mode 2. As explained in the last paragraph, we apply Wick's theorem and use equations 1.56 and 1.57 to get:

$$\begin{aligned} \langle \hat{a}_1^\dagger(t) \hat{a}_2^\dagger(t) \hat{a}_1(t) \hat{a}_2(t) \rangle = \langle \hat{a}_1^\dagger(t) \hat{a}_2^\dagger(t) \rangle \langle \hat{a}_1(t) \hat{a}_2(t) \rangle + \langle \hat{a}_1^\dagger(t) \hat{a}_1(t) \rangle \langle \hat{a}_2^\dagger(t) \hat{a}_2(t) \rangle \\ + \langle \hat{a}_1^\dagger(t) \hat{a}_2(t) \rangle \langle \hat{a}_2^\dagger(t) \hat{a}_1(t) \rangle \end{aligned} \tag{1.64}$$

Working with initial vacuum conditions, we compute the different correlators:

$$\begin{aligned} \langle \hat{a}_1(t) \hat{a}_2(t) \rangle = \cosh(\chi t) \sinh(\chi t) (\langle \hat{a}_1(0) \hat{a}_1^\dagger(0) \rangle + \langle \hat{a}_2^\dagger(0) \hat{a}_2(0) \rangle) + \cosh^2(\chi t) \langle \hat{a}_1(0) \hat{a}_2(0) \rangle \\ + \sinh^2(\chi t) \langle \hat{a}_2^\dagger(0) \hat{a}_1^\dagger(0) \rangle \end{aligned} \tag{1.65}$$

which gives:

$$\langle \hat{a}_1(t)\hat{a}_2(t)\rangle = \langle \hat{a}_1^\dagger(t)\hat{a}_2^\dagger(t)\rangle = \cosh(\chi t)\sinh(\chi t) \tag{1.66}$$

Likewise,

$$\langle \hat{a}_1^\dagger(t)\hat{a}_1(t)\rangle = \langle \hat{a}_2^\dagger(t)\hat{a}_2(t)\rangle = \sinh^2(\chi t) \tag{1.67}$$

$$\langle \hat{a}_1^\dagger(t)\hat{a}_2(t)\rangle = \langle \hat{a}_2^\dagger(t)\hat{a}_1(t)\rangle = 0 \tag{1.68}$$

Now that we have evaluated $G^{(2)}(1,2)$, we can write the normalized second-order correlation function:

$$\begin{aligned} g^{(2)}(1,2) &= \frac{\langle \hat{a}_1^\dagger(t)\hat{a}_2^\dagger(t)\hat{a}_2(t)\hat{a}_1(t)\rangle}{\langle \hat{a}_1^\dagger(t)\hat{a}_1(t)\rangle\langle \hat{a}_2^\dagger(t)\hat{a}_2(t)\rangle} \\ &= 1 + \frac{\cosh^2(\chi t)\sinh^2(\chi t)}{\sinh^4(\chi t)} \\ &= 1 + \frac{(1+\sinh^2(\chi t))\sinh^2(\chi t)}{\sinh^4(\chi t)} \end{aligned} \tag{1.69}$$

from which we finally get:

$$\boxed{g^{(2)}(1,2) = 2 + \frac{1}{\langle \hat{n}_1(t)\rangle}} \tag{1.70}$$

where $\hat{n}_1(t)$ is the number of photons in mode 1. We see that the amplitude of the correlation function scales linearly with the inverse average mode occupation. Interestingly, we notice that this amplitude is higher than the bosonic bunching correlations within a single mode $g^{(2)}(1,1) = g^{(2)}(2,2) = 2$. In fact, this is quite an important result as we will now discuss.

1.1.5 Violation of the Cauchy-Schwarz inequality and Busch-Parentani criterion

The celebrated Cauchy-Schwarz inequality has seen countless applications in Mathematics and Physics. What will most interest us here is its formulation in the framework of probability theory. In classical Physics, with two fluctuating quantities I_1 and I_2, the Cauchy-Schwarz inequality writes:

$$\langle I_1 I_2\rangle \leq \sqrt{\langle I_1^2\rangle\langle I_2^2\rangle} \tag{1.71}$$

This inequality can be rewritten with creation/annihilation operators to work with two-body correlation functions. With the notations $G^{(2)}(i,j) = \langle \hat{a}_i^\dagger \hat{a}_j^\dagger \hat{a}_i \hat{a}_j\rangle$ we have used so far, the Cauchy-Schwarz inequality becomes [162]:

$$G^{(2)}(1,2) \leq \sqrt{G^{(2)}(1,1)G^{(2)}(2,2)} \tag{1.72}$$

In the symmetrical case with $\langle \hat{a}_1^\dagger \hat{a}_1 \rangle = \langle \hat{a}_2^\dagger \hat{a}_2 \rangle$ (valid for the non-degenerate parametric amplifier), we obtain $G^{(2)}(1,1) = G^{(2)}(2,2)$ and finally:

$$g^{(2)}(1,2) \leq \sqrt{g^{(2)}(1,1)g^{(2)}(2,2)} \iff g^{(2)}(1,2) \leq g^{(2)}(1,1), g^{(2)}(2,2) \tag{1.73}$$

Therefore, the Cauchy-Schwarz inequality states that the cross-correlation amplitude cannot exceed the amplitude of the auto-correlation with a classical model. The result of equation 1.70 violates this inequality and is therefore the signature of a quantum phenomenon, as observed experimentally in [176]. Actually, violating the Cauchy-Schwarz inequality was at the core of different landmark Quantum Optics experiments [132] aiming to identify light sources that could not be described with classical optics.

In fact, violating the Cauchy-Schwarz inequality can be enough to demonstrate entanglement in some situations. The work [22] devises the Busch-Parentani criterion for a state to be entangled that writes:

$$\langle \hat{n}_1 \hat{n}_2 \rangle - |\langle \hat{a}_1^\dagger \hat{a}_2^\dagger \rangle|^2 < 0 \tag{1.74}$$

From equation 1.64, we get

$$\langle \hat{a}_1^\dagger \hat{a}_2^\dagger \hat{a}_1 \hat{a}_2 \rangle = |\langle \hat{a}_1^\dagger \hat{a}_2^\dagger \rangle|^2 + \langle \hat{n}_1 \hat{n}_2 \rangle + \langle \hat{a}_1^\dagger \hat{a}_2 \rangle \langle \hat{a}_2^\dagger \hat{a}_1 \rangle \tag{1.75}$$

where the last term is zero in the non-degenerate parametric amplifier problem as shown before. Injecting 1.74, we get:

$$\langle \hat{a}_1^\dagger \hat{a}_2^\dagger \hat{a}_1 \hat{a}_2 \rangle > 2 \langle \hat{n}_1 \hat{n}_2 \rangle \tag{1.76}$$

Dividing by $\langle \hat{n}_1 \hat{n}_2 \rangle$, we obtain:

$$g^{(2)}(1,2) > 2 \iff g^{(2)}(1,2) > g^{(2)}(1,1), g^{(2)}(2,2) \tag{1.77}$$

which is strictly equivalent to violating the Cauchy-Schwarz inequality, therefore proving that the emitted photon pairs form an entangled state. Note that this development holds only if (i) the statistics of the system are Gaussian so that we can apply Wick's theorem and have $g^{(2)}(1,1) = g^{(2)}(2,2) = 2$, (ii) $\langle \hat{a}_1^\dagger \hat{a}_2 \rangle \langle \hat{a}_2^\dagger \hat{a}_1 \rangle = 0$ which is true here but not in general. The effect described in this paragraph is also known as **spontaneous parametric down conversion** and is in fact one of the simplest way to obtain entangled states of light and has been used in many landmarks experiments [21, 82, 131].

We have thus seen so far a few examples of historical Quantum Optics results through which we have familiarized ourselves with the concept of correlation functions and the kind

of information they contain. However, we are still overlooking one of the key ingredient of the problem we wish to study, namely **interactions**. Indeed, photons are essentially massless, non-interacting particles. In order to add interactions into these famous Quantum Optics problems, physicists naturally turned to atoms. As a matter of fact, the Quantum Optics formalism can be extended quite easily to matter and atoms and gives an incentive to reproduce famous Quantum Optics effects with massive particles.

1.2 Bogoliubov theory of the homogeneous weakly-interacting gas

We will now use the formalism of correlation functions to study one of the most simple many-body problem, the weakly-interacting homogeneous Bose gas, *i.e.* an ensemble of bosonic particles with weak contact interactions in a box of volume V. This approach is a nice compromise: while it accounts for interactions between individual particles that may give rise to interesting correlations phenomena, the system can be described theoretically at the price of a few approximations as stated in the introduction to this chapter. This theory has been developed by Nikolay Bogoliubov in his celebrated 1947 article [14]. In this section, we will remind the main lines of Bogoliubov's approach and see what it tells us in terms of correlation functions.

1.2.1 Second quantization in atomic physics

Before diving into the specifics of Bogoliubov theory, we briefly remind the formalism of second quantization in atomic physics that will allow us to use the results obtained in the last paragraph for Quantum Optics. Interestingly, the idea of second quantization of Quantum Optics can be extended to treat the quantum many-body problem in a more efficient and intuitive way. Indeed, calculations get quite complex when considering many-body systems of indistinguishable particles as the many-body wave-function must be (anti-)symmetrized in the case of bosons (fermions), a problem that the second quantization formalism aims to resolve.

The key point is to switch things around by counting the number of particles in each state instead of the usual approach which would be to determine in which state each particle is. To this end, the many-body state is represented as a set of occupation numbers:

$$|\{n_\beta\}\rangle = |n_1, n_2, ..., n_\beta, ...\rangle \tag{1.78}$$

where n_β denotes the number of particles in state β. For fermions, this number is either 0 or 1 because of the Pauli exclusion principle, whereas it can be any integer value for bosons. We recognize the states $|\{n_\beta\}\rangle$ as the **Fock states** described in the last paragraph. As for Quantum Optics, we introduce creation and annihilation operators $\hat{a}^\dagger_\beta$ and $\hat{a}_\beta$ respectively creating or destroying a particle in state β. For bosons on which this thesis will be focused:

$$\hat{a}^\dagger_\beta |n_\beta\rangle = \sqrt{n_\beta + 1}\, |n_\beta + 1\rangle \tag{1.79}$$

$$\hat{a}_\beta |n_\beta\rangle = \sqrt{n_\beta}\, |n_\beta - 1\rangle \tag{1.80}$$

Just as for photons, the Fock states are constructed by applying the creation operators the right amount of times on the vacuum state. For bosonic particles, the commutation relation is the same as for photons:

$$\left[\hat{a}_\beta, \hat{a}^\dagger_{\beta'}\right] = \delta_{\beta\beta'} \quad \left[\hat{a}_{\beta'}, \hat{a}_\beta\right] = 0 \tag{1.81}$$

This has the advantage that the symmetric properties are taken care of by the commutation relations, avoiding complex symmetrization calculation.

1.2.2 Bogoliubov approximation

We now describe the weakly-interacting Bose gas of N_{bec} atoms with contact interactions. In the second quantization formalism, the Hamiltonian of the system writes [14]:

$$\hat{H} = \int \left(\frac{\hbar^2}{2m}\nabla\hat{\psi}^\dagger(\mathbf{r})\nabla\hat{\psi}(\mathbf{r})\right) \mathrm{d}\mathbf{r} + \frac{g}{2}\int \hat{\psi}^\dagger(\mathbf{r})\hat{\psi}^\dagger\left(\mathbf{r}'\right)\delta\left(\mathbf{r}-\mathbf{r}'\right)\hat{\psi}(\mathbf{r})\hat{\psi}\left(\mathbf{r}'\right)\mathrm{d}\mathbf{r}'\mathrm{d}\mathbf{r} \tag{1.82}$$

with $\delta\left(\mathbf{r}-\mathbf{r}'\right)$ the contact interaction potential and $g = \dfrac{4\pi\hbar^2 a_s}{m}$ the strength of the interactions with a_s the s-wave scattering length [101] with $a_s = 7.5$ nm for He^*. The approximation of contact interactions is reasonable in the case where the scattering length is much smaller than the distance between atoms, $|a_s|n^{1/3} \ll 1$, as it is the case in our experiment. For a homogeneous gas contained within a box of volume V, the field operator $\hat{\psi}$ can be written in the plane wave basis:

$$\hat{\psi}(\boldsymbol{r}) = \frac{1}{\sqrt{V}}\sum_{\boldsymbol{k}} \hat{a}_{\boldsymbol{k}} e^{i\boldsymbol{k}\cdot\boldsymbol{r}} \tag{1.83}$$

$$\hat{\psi}^\dagger(\boldsymbol{r}) = \frac{1}{\sqrt{V}}\sum_{\boldsymbol{k}} \hat{a}^\dagger_{\boldsymbol{k}} e^{-i\boldsymbol{k}\cdot\boldsymbol{r}} \tag{1.84}$$

with $\hat{a}_{\boldsymbol{k}}$ the operator destroying a particle of momentum k. The Hamiltonian can then be rewritten

$$\hat{H} = \sum_{\boldsymbol{k}} \frac{\hbar^2 k^2}{2m}\hat{a}^\dagger_{\boldsymbol{k}}\hat{a}_{\boldsymbol{k}} + \frac{g}{2V}\sum_{\boldsymbol{k}_1,\boldsymbol{k}_2,\boldsymbol{k}_3} \hat{a}^\dagger_{\boldsymbol{k_1}+\boldsymbol{k_3}}\hat{a}^\dagger_{\boldsymbol{k_2}-\boldsymbol{k_3}}\hat{a}_{\boldsymbol{k_1}}\hat{a}_{\boldsymbol{k_2}} \tag{1.85}$$

The interaction term is written so that the momentum is conserved as the scattering process is elastic. At $T = 0$, all the atoms are in the ground state of the system. In order to simplify this Hamiltonian, we use the Bogoliubov approximation that assumes the interactions to be weak so that the fraction of atoms removed from the BEC by interactions is small. This has two consequences:

- We treat $\hat{a}_{\mathbf{0}}$ and $\hat{a}_{\mathbf{0}}^\dagger$ as ordinary numbers and replace them by $\sqrt{N_{\text{bec}}}$ where N_{bec} is the number of condensed atoms.
- The effect of the interactions is treated perturbatively by writing the field operator as [14]:

$$\hat{\psi}(\boldsymbol{r}) = \frac{\hat{a}_{\mathbf{0}}}{\sqrt{V}} + \theta, \;\; \theta = \frac{1}{\sqrt{V}} \sum_{\boldsymbol{k}\neq\mathbf{0}} \hat{a}_{\boldsymbol{k}} e^{i\boldsymbol{k}\cdot\boldsymbol{r}} \tag{1.86}$$

  considering θ as a correction term and neglecting all terms of order 2 and superior of θ in equation 1.82.

With these approximations, the simplified Hamiltonian writes:

$$H_{\text{bogo}} = \sum_{\boldsymbol{k}\neq\mathbf{0}} \frac{\hbar^2 k^2}{2m} \hat{a}_{\boldsymbol{k}}^\dagger \hat{a}_{\boldsymbol{k}} + \frac{gn}{2} \sum_{\boldsymbol{k}\neq\mathbf{0}} (\hat{a}_{\boldsymbol{k}}^\dagger \hat{a}_{-\boldsymbol{k}}^\dagger + \hat{a}_{\boldsymbol{k}} \hat{a}_{-\boldsymbol{k}}) + \frac{gnN_{\text{bec}}}{2} \tag{1.87}$$

with $n = N_{\text{bec}}/V$. Importantly, this Hamiltonian can be diagonalized. This is achieved through the linear Bogoliubov transformation where we introduce a new quasi-particle operator:

$$\hat{b}_{\boldsymbol{k}} = u_{\boldsymbol{k}} \hat{a}_{\boldsymbol{k}} + v_{-\boldsymbol{k}} \hat{a}_{-\boldsymbol{k}}^\dagger \tag{1.88}$$

To determine the expression of the coefficients $u_{\boldsymbol{k}}$ and $v_{\boldsymbol{k}}$, we impose that the new operator $\hat{b}_{\boldsymbol{k}}$ follows the bosonic operator commutation rule:

$$[\hat{b}_{\boldsymbol{k}}, \hat{b}_{\boldsymbol{k}'}^\dagger] = \delta_{\boldsymbol{k},\boldsymbol{k}'} \tag{1.89}$$

This gives $u_{\boldsymbol{k}}^2 - v_{-\boldsymbol{k}}^2 = 1$. We can therefore write $u_{\boldsymbol{k}} = \cosh(\alpha_{\boldsymbol{k}})$ and $v_{-\boldsymbol{k}} = \sinh(\alpha_{\boldsymbol{k}})$ and look to determine $\alpha_{\boldsymbol{k}}$. For the Hamiltonian to be diagonal, this value must be chosen so that the coefficients of the terms in $\hat{b}_{\boldsymbol{k}}^\dagger \hat{b}_{-\boldsymbol{k}}^\dagger$ and $\hat{b}_{\boldsymbol{k}} \hat{b}_{-\boldsymbol{k}}$ vanish. We obtain an additional equation:

$$\frac{gn}{2} \left(u_{\boldsymbol{k}}^2 + v_{-\boldsymbol{k}}^2 \right) + \left(\frac{\hbar^2 k^2}{2m} + gn \right) u_{\boldsymbol{k}} v_{-\boldsymbol{k}} = 0 \tag{1.90}$$

from which we finally obtain after a few lines of calculation using the properties of hyperbolic functions:

$$u_{\boldsymbol{k}}, v_{-\boldsymbol{k}} = \pm \left(\frac{\hbar^2 k^2/2m + gn}{2\varepsilon(k)} \pm \frac{1}{2} \right)^{1/2} \tag{1.91}$$

with

$$\varepsilon(k) = \sqrt{\frac{\hbar^2 k^2}{2m} \left(\frac{\hbar^2 k^2}{2m} + 2gn \right)} \tag{1.92}$$

the famous Bogoliubov dispersion relation. The Hamiltonian has now been diagonalized and writes:

$$\hat{H}_B = \sum_{\boldsymbol{k}} \varepsilon(k) \hat{b}^\dagger_{\boldsymbol{k}} \hat{b}_{\boldsymbol{k}} + E_0 \tag{1.93}$$

The system of interacting particles has thus been transformed into a system of non-interacting Bogoliubov quasi-particles associated to creation and annihilation operators $\hat{b}^\dagger_{\boldsymbol{k}}$ and $\hat{b}_{\boldsymbol{k}}$ with a dispersion relation $\varepsilon(k)$. The prediction of this excitation spectrum is one of the key results of Bogoliubov theory that we will now discuss in further details.

1.2.3 Spectrum of excitations

The Bogoliubov dispersion relation has two clear asymptotic trends for small and high momentum values. For low values of k, using $\frac{\hbar^2 k^2}{2m} \ll 2gn$, we obtain:

$$\varepsilon(k) \underset{k\to 0}{=} \hbar k \sqrt{\frac{gn}{m}} \tag{1.94}$$

The dispersion relation takes a phonon-like linear form where the sound velocity is $c = \sqrt{\frac{gn}{m}}$. In this regime, the Bogoliubov quasi-particles are phonons corresponding to a coherent superposition of a forward and backward propagating waves $\hat{b}_{\boldsymbol{k}} = u_{\boldsymbol{k}} \hat{a}_{\boldsymbol{k}} + v_{-\boldsymbol{k}} \hat{a}^\dagger_{-\boldsymbol{k}}$ with $|u_{\boldsymbol{k}}| \simeq |v_{-\boldsymbol{k}}|$.

On the other hand, at high values of k, the dispersion relation becomes that of free particles:

$$\varepsilon(k) \underset{k\to+\infty}{=} \frac{\hbar^2 k^2}{2m} \tag{1.95}$$

In terms of operators, $v_k \underset{k\to+\infty}{=} 0$ and $u_k \underset{k\to+\infty}{=} 1$ so $\hat{b}_{\boldsymbol{k}} \underset{k\to+\infty}{=} \hat{a}_{\boldsymbol{k}}$, a quasi-particle is equivalent to a particle.

The transition between the two regimes occurs when $\frac{\hbar^2 k^2}{2m} \simeq gn$, it thus convenient to define a characteristic length associated to this momentum range:

$$\xi = \sqrt{\frac{\hbar^2}{2mgn}} \tag{1.96}$$

This length is called the **healing length**. Its name comes from the fact the ξ represent the length scale on which a local perturbation of the density is "healed" back to the bulk density.

[2] E_0 is not simple to calculate and was the subject of the famous work [103] that we will discuss later on.

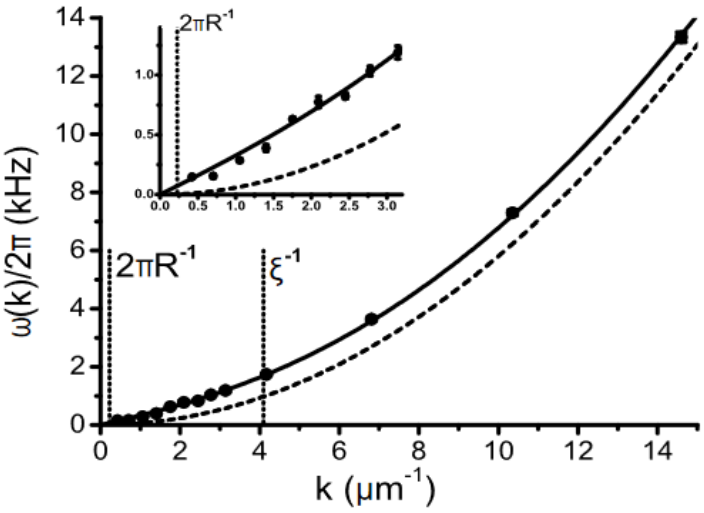

Figure 1.8: Experimental observation of the Bogoliubov excitation spectrum (Steinhauer *et al.* [148]). The phononic and free particle parts are clearly identifiable. The inset shows a zoom on the linear part of the spectrum and the dashed line the free particle spectrum. ξ is the healing length of the condensate.

The Bogoliubov spectrum of excitations provides a support for the superfluid properties and has been a very successful theoretical prediction observed experimentally in a large variety of systems [63, 112, 119, 148, 150]. This is not however all that is predicted by Bogoliubov theory. As we will discuss below, this theory also describes the many-body **ground-state** of the system.

1.2.4 Many-body ground state and quantum depletion

The Bogoliubov approach describes the excitations of the weakly-interacting Bose gas as non-interacting quasi-particles. These quasi-particles therefore behave as ideal bosons and are populated by the finite temperature with the Bose distribution:

$$\langle b_{\boldsymbol{k}}^\dagger b_{\boldsymbol{k}} \rangle = \frac{1}{e^{\varepsilon(k)/(k_B T)} - 1} \tag{1.97}$$

At $T = 0$, the population of quasi-particles is null: $\langle \hat{b}_{\boldsymbol{k}}^\dagger \hat{b}_{\boldsymbol{k}} \rangle_{T=0} = 0$. What can we say about real particles? By using the Bogoliubov transform, one can express the population of particles for a given momentum $k \neq 0$:

$$\langle \hat{a}_{\boldsymbol{k}}^\dagger \hat{a}_{\boldsymbol{k}} \rangle = (|u_k|^2 + |v_k|^2) \langle \hat{b}_{\boldsymbol{k}}^\dagger \hat{b}_{\boldsymbol{k}} \rangle + |v_k|^2 \tag{1.98}$$

The blue term corresponds to the Bogoliubov excitations populated by temperature. The fraction of particles removed from the condensate this way is called the **thermal depletion**. This fraction vanishes at $T = 0$. Interestingly, an additional term $|v_k|^2$ is present that results from the non-commutation of the bosonic creation and annihilation operators, the signature of an essentially quantum phenomenon. This term implies that $\langle \hat{a}_{\boldsymbol{k}}^\dagger \hat{a}_{\boldsymbol{k}} \rangle_{T=0} \neq 0$,

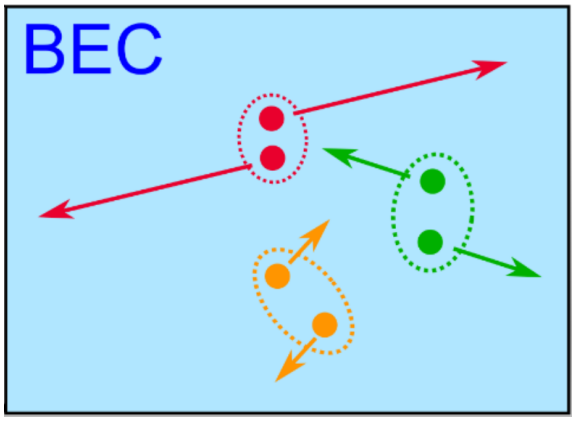

Figure 1.9: Illustration of the $\boldsymbol{k}/-\boldsymbol{k}$ pairing of the quantum depleted atoms in the BEC (light blue).

meaning that there is a fraction of atoms outside of the BEC with a non-zero momentum in the ground state! Under the interplay between interactions and quantum fluctuations, some atoms are removed from the BEC and promoted to non-zero momentum states. This fraction is called the **quantum depletion**.

1.2.5 Pairing mechanism in the quantum depletion

We now look to build a microscopical, physically meaningful picture of how the quantum depletion emerges. We remind that a key ingredient of the Bogoliubov theory is that the only considered interaction processes are the ones involving two particles of the BEC or two particles outside of the BEC being brought into it. From this consideration, we understand that the atoms belonging to the quantum depletion were initially in the BEC and were removed from it after undergoing a two-body interaction process. The interaction process populating the quantum depletion thus involves two atoms in the BEC with a momentum value $k \simeq 0$. To conserve the overall momentum, the two atoms leaving the BEC then have opposite momenta $\boldsymbol{k}$ and $-\boldsymbol{k}$ and form a momentum correlated pair. This falls exactly into the kind of signal we are interested in, namely correlations between several particles, here two, caused by a quantum, interaction-induced effect.

The common factor with quantum effects is that they usually defy our intuition built on our observation of the everyday world, well described by classical physics. In this case, the "quantum weirdness" comes from the fact this process seems to violate the conservation of energy. Initially, the two atoms belong to the **at-rest** BEC, their total kinetic energy is then zero. After the collision process, they acquire momenta $\boldsymbol{k}$ and $-\boldsymbol{k}$ meaning that the total kinetic energy is $2(\hbar^2 k^2/2m)$. The important aspect is that $\boldsymbol{k}$ can be arbitrarily large, making the kinetic energy of the pair larger than the available interaction energy. Naturally, the conservation of energy is still well respected here. The apparent contradiction comes from the fact that it is conceptually wrong to isolate two atoms in the BEC. Every atom of the ground state belongs to the same quantum state, which exhibits non-zero momentum components at large momenta. Because the pairs are created by the interaction term of the Hamiltonian, the pair creation is a coherent process. The many-body ground state is thus a superposition of the BEC and the pairs and writes:

$$|\psi_B\rangle \sim \exp\left(\sqrt{N_0}a_0^\dagger + \sum_{\boldsymbol{k}\neq 0}(v_k/u_k)a_{-\boldsymbol{k}}^\dagger a_{\boldsymbol{k}}^\dagger\right)|0\rangle \tag{1.99}$$

which is of the same form of the ground-state of the Bardeen-Cooper-Schrieffer theory of supraconductivity [7].

The energy of the many-body ground state of the weakly-interacting Bose gas thus contains a small correction that corresponds to the presence of the $\boldsymbol{k}/-\boldsymbol{k}$ pairs of the quantum depletion. This small correction is called the Lee-Huang-Yang correction, named after the authors of the seminal 1957 article [103] that first predicted the presence of the $\boldsymbol{k}/-\boldsymbol{k}$ pairs.

This pairing effect is quite reminiscent of the spontaneous parametric down conversion photon pairing effect that we saw in 1.1.4. The analogy between the non-degenerate parametric amplifier and the Bogoliubov Hamiltonian, replacing modes 1 and 2 by modes $\boldsymbol{k}$ and $-\boldsymbol{k}$ will in fact allow us to re-use the majority of the results derived in 1.1.4 for the $\boldsymbol{k}/-\boldsymbol{k}$ pairs. There is however one crucial difference, which is that the non-degenerate parametric amplifier is an **out-of-equilibrium**, **time-dependent** problem contrary to the **equilibrium** weakly-interacting Bose gas. This is in fact the fascinating aspect of the $\boldsymbol{k}/-\boldsymbol{k}$ pairs of the quantum depletion whose existence can only be explained by the effect of quantum fluctuations.

We are thus looking at a system which falls into our general area of interest described in the introduction of this thesis, namely many-body systems with interactions displaying quantum behaviors. The weakly-interacting Bose gas shows the advantage to be one of the conceptually simplest many-body systems for which a theory can be derived as we just have shown. We will now build a bridge with the first part of this chapter by discussing what are the relevant correlation functions to study the weakly-interacting Bose gas.

1.3 Two-body correlations in the homogeneous weakly-interacting Bose gas

Now that we have identified the $\boldsymbol{k}/-\boldsymbol{k}$ pairing mechanism in the quantum depletion, it is natural to look for a signature of it in the second order correlation function that characterizes the correlations between two particles [23, 110, 156]. We start by describing the general case of the two-body correlator between two modes $\boldsymbol{k}$ and $\boldsymbol{k'}$:

$$G(\boldsymbol{k},\boldsymbol{k'}) = \langle \hat{a}_{\boldsymbol{k}}^\dagger \hat{a}_{\boldsymbol{k'}}^\dagger \hat{a}_{\boldsymbol{k}} \hat{a}_{\boldsymbol{k'}} \rangle \tag{1.100}$$

As we have seen in the previous section, the Bogoliubov Hamiltonian is diagonal in the quasi-particle basis, meaning that all quantum states have Gaussian statistics in this basis. As the Bogoliubov transformation is linear and therefore conserves Gaussianity, the statistics are Gaussian in the particle basis as well [23]. We can then apply Wick's theorem (see 1.1.3) to simplify the correlator:

$$G(\boldsymbol{k},\boldsymbol{k}') = \langle \hat{a}^\dagger_{\boldsymbol{k}} \hat{a}^\dagger_{\boldsymbol{k}'} \rangle \langle \hat{a}_{\boldsymbol{k}} \hat{a}_{\boldsymbol{k}'} \rangle + \langle \hat{a}^\dagger_{\boldsymbol{k}} \hat{a}_{\boldsymbol{k}} \rangle \langle \hat{a}^\dagger_{\boldsymbol{k}'} \hat{a}_{\boldsymbol{k}'} \rangle + \langle \hat{a}^\dagger_{\boldsymbol{k}} \hat{a}_{\boldsymbol{k}'} \rangle \langle \hat{a}^\dagger_{\boldsymbol{k}'} \hat{a}_{\boldsymbol{k}} \rangle \tag{1.101}$$

We end up with three different terms:

- The first term that equals $|\langle \hat{a}^\dagger_{\boldsymbol{k}} \hat{a}^\dagger_{\boldsymbol{k}'} \rangle|^2$.
- We recognize in the second term the product of the momentum densities $\rho(\boldsymbol{k})\rho(\boldsymbol{k}')$.
- The third term that equals $|\langle \hat{a}^\dagger_{\boldsymbol{k}} \hat{a}_{\boldsymbol{k}'} \rangle|^2$.

We regroup the two last terms in the function $G^{(2)}_N(\boldsymbol{k},\boldsymbol{k}') = \rho(\boldsymbol{k})\rho(\boldsymbol{k}') + |\langle \hat{a}^\dagger_{\boldsymbol{k}} \hat{a}_{\boldsymbol{k}'} \rangle|^2$ that we call the **normal** correlation function as the operators are normally ordered (see 1.1.3). In opposition, we introduce for the last term the function $G^{(2)}_A(\boldsymbol{k},\boldsymbol{k}') = |\langle \hat{a}^\dagger_{\boldsymbol{k}} \hat{a}^\dagger_{\boldsymbol{k}'} \rangle|^2$ that we call the **anomalous** correlation function. Interestingly, this term is non-zero only if there exists interactions coupling different modes, in our case $\boldsymbol{k}$ and $-\boldsymbol{k}$.

We must now determine which atoms participate to which correlation signal. We have seen in 1.2.4 that the depletion of the condensate is divided between the **quantum** and the **thermal** depletion. As we have shown in 1.2.5, we expect that the quantum depleted atoms contribute to the anomalous $\boldsymbol{k}/-\boldsymbol{k}$ correlation signal due to the microscopic mechanism describing how the quantum depletion is populated. In fact, it is also possible for the thermal depletion to contribute to the anomalous correlation signal. Indeed, as discussed in 1.2.3, for low k values such as $k\xi \ll 1$, the Bogoliubov quasi-particles have a strong phononic character $\hat{b}_{\boldsymbol{k}} = u_{\boldsymbol{k}} \hat{a}_{\boldsymbol{k}} + v_{-\boldsymbol{k}} \hat{a}^\dagger_{-\boldsymbol{k}}$ with $|u_{\boldsymbol{k}}| \simeq |v_{-\boldsymbol{k}}|$ and exhibits non-negligible $\boldsymbol{k}/-\boldsymbol{k}$ correlations. This is an issue as if we were to observe $\boldsymbol{k}/-\boldsymbol{k}$ correlations, we would not be able to unambiguously attribute them to the quantum depletion as they could come from phonons of the thermal depletion. To quantify this contribution, we use Bogoliubov's transformation to rewrite equation 1.101 in its normalized form in terms of quasi-particle operators and Bogoliubov coefficients u_k and v_k [23, 110].

$$g^{(2)}(\boldsymbol{k},\boldsymbol{k}') = \frac{|u_k v_k (1 + 2\langle \hat{b}^\dagger_{\boldsymbol{k}} \hat{b}_{\boldsymbol{k}} \rangle)|^2}{\left((|u_k|^2 + |v_k|^2) \langle \hat{b}^\dagger_{\boldsymbol{k}} \hat{b}_{\boldsymbol{k}} \rangle + |v_k|^2 \right)^2} \delta_{\boldsymbol{k},-\boldsymbol{k}'} + \delta_{\boldsymbol{k},\boldsymbol{k}'} + 1 \tag{1.102}$$

The function $g^{(2)}(\boldsymbol{k},-\boldsymbol{k})$ is plotted on Fig.-1.10 for both quantum ($T = 0$) and thermally depleted atoms. As $k\xi$ increase, the density of quantum depleted atoms decreases, meaning that their contribution to $g^{(2)}(\boldsymbol{k},-\boldsymbol{k})$ increases following from the analogy with the non-degenerate parametric amplifier and the result of equation 1.70. On the contrary, the contribution of the thermally depleted atoms decreases with $k\xi$ as the phononic character of the quasi-particles disappears, and becomes negligible for $k\xi \geq 1$. This gives us a nice workaround: if we restrict our measurement of $\boldsymbol{k}/-\boldsymbol{k}$ correlations to large k, we could safely attribute them to the quantum depletion.

Let us now take a look at normal correlations, *i.e* bosonic bunching. We get from equation 1.102 and the plots of Fig.-1.10 that we have perfect bosonic bunching independently of k for both quantum and thermally depleted atoms. As we have seen in 1.2.3 and 1.2.4, the Bogoliubov quasi-particles of the thermal depletion follow the Bose distribution and therefore have thermal chaotic statistics, explaining the presence of bosonic bunching. On the other hand, the $\boldsymbol{k}/-\boldsymbol{k}$ pairs of the quantum depletion form a pure coherent state (see equation 1.99) for which we would then not expect bosonic bunching as explained in

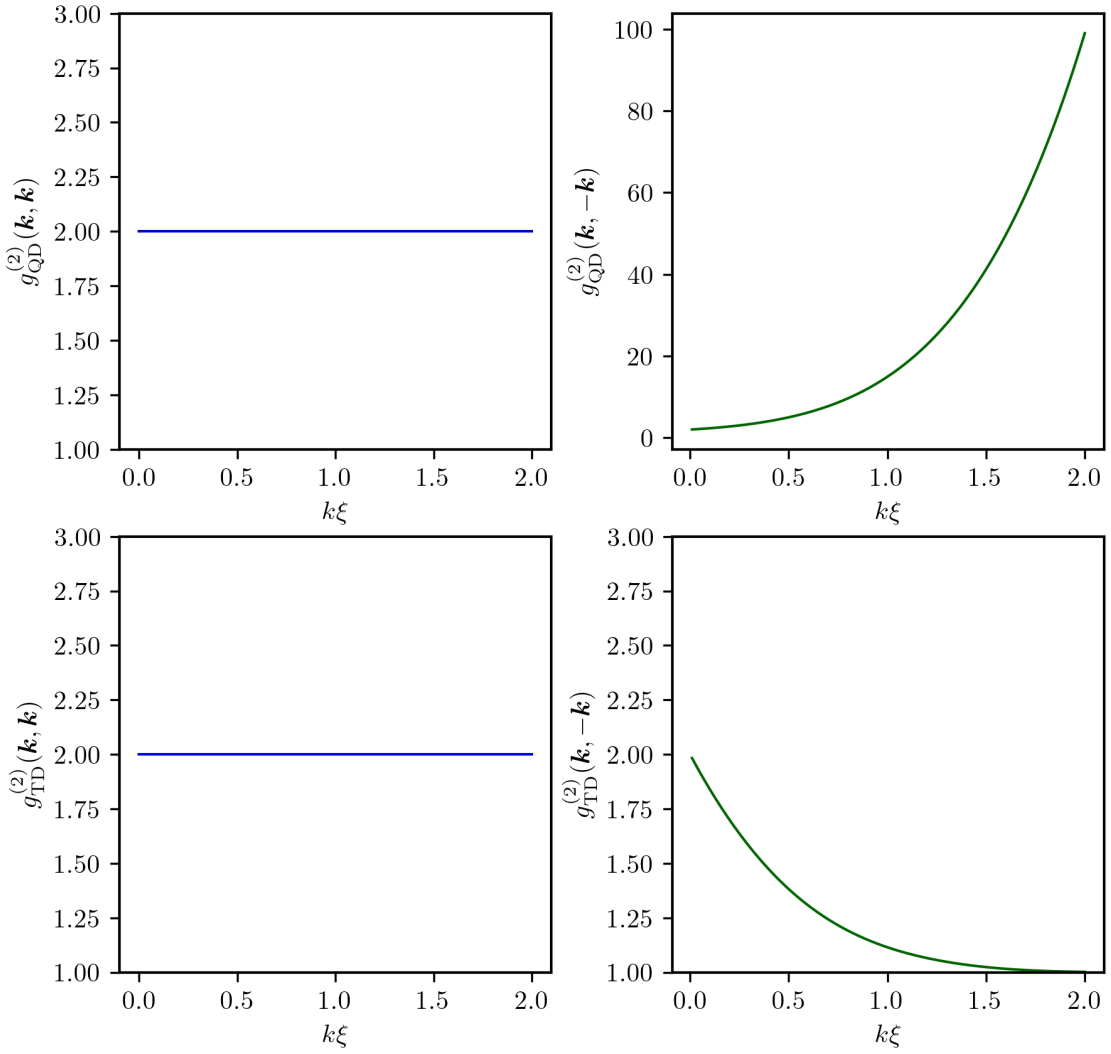

Figure 1.10: Second order correlation function for normal $\boldsymbol{k}/\boldsymbol{k}$ correlations (blue) and anomalous $\boldsymbol{k}/-\boldsymbol{k}$ correlations (green) with quantum (subscript QD) and thermally depleted (subscript TD) atoms (resp. top and bottom row) as a function of $k\xi$. These results are obtained from the Bogoliubov theory of the weakly-interacting, homogeneous, 1D Bose gas with a chemical potential $\mu = h \times 1.5$ kHz and temperature $T = 60$ nK.

1.1.3. The situation is however a bit more subtle than that. In direct analogy with the non-degenerate parametric amplifier, when we look for same mode $\boldsymbol{k}/\boldsymbol{k}$ correlations, we do so between atoms belonging to two different pairs. We retrieve a density matrix with a chaotic character [172] by tracing over the second atom of the pair that we ignore, as proven in 1.1.4. This means that we should observe bosonic bunching with the quantum depletion as well [23]!

In a nutshell, we have two correlation features of interest well separated in momentum-space and containing very different types of information. On the one hand, the normal correlations correspond to close-by correlations and bosonic bunching revealing the chaotic statistics of the system, coming from either the thermal statistics of the thermal depletion, or the partial trace over the second atom of the pair destroying the quantum coherence for the quantum depletion. On the other hand, the anomalous correlations correspond to $\boldsymbol{k}/-\boldsymbol{k}$ correlations and reveal the quantum coherences of the many-body ground state, provided that we probe them in the region $k\xi \geq 1$. While our main goal will be to measure the anomalous $\boldsymbol{k}/-\boldsymbol{k}$ correlations for the reasons mentioned earlier, it will also be of great interest to measure the normal correlations to contrast their behaviour with the anomalous correlations as a means to illustrate the different physical origins of the two signals.

1.4 Effects of an external trapping potential

The weakly-interacting **homogeneous** Bose gas Hamiltonian does not actually faithfully represent our experiment as we use an external harmonic potential $V(\boldsymbol{r})$ to trap the atoms, making the system not homogeneous anymore. This makes the theoretical approach significantly more difficult, but still manageable through numerical calculations as it was recently done in [23] to evaluate the correlation functions in the trapped case.

In this section, we will summarize the main results of [23] to show how the spatial size of the system affects the widths of the correlation signals and obtain estimates for comparison with experimental data. Indeed, as we have seen in the Hanbury Brown and Twiss experiment aiming to measure the size of Sirius through the measurement of the second order correlation function, the width of the correlation function is inversely proportional to the spatial size of the source.

1.4.1 Normal correlations

As discussed in the last paragraph for the homogeneous case, we expect a perfect bosonic bunching $g^{(2)}(\boldsymbol{k},\boldsymbol{k}) = 2$ for both the thermal and the quantum depletion. This feature is actually the same in the trapped case as shown in [23] where the numerical calculations also give a perfect bosonic bunching, independently of the temperature and thus of the balance between the thermally and quantum depleted atoms. The width of the correlation peak shows however quite interesting dependencies on the momentum value k and the temperature.

At $T = 0$ or very low temperatures, the RMS width σ_k of the normal correlations is dominated by the contribution of the quantum depletion. As the quantum depletion is non-existent outside of the BEC, its spatial size is the one of the BEC, meaning that the width of the normal correlations at $T = 0$ should be $\sim 1/L_{\mathrm{BEC}}$ with L_{BEC} the spatial

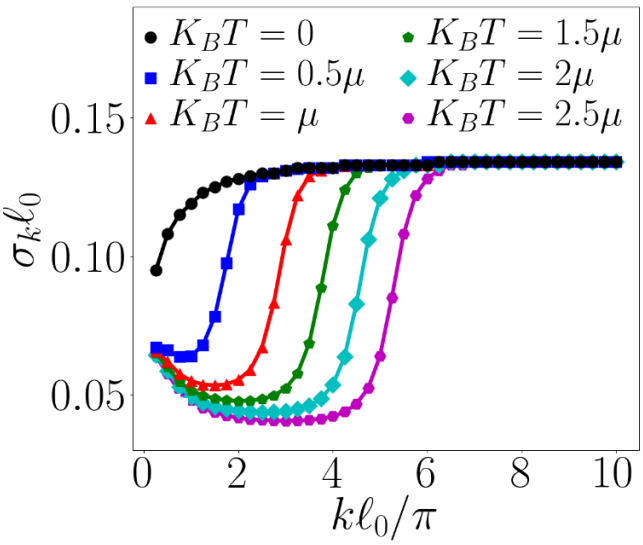

Figure 1.11: Evolution of the normal correlations width $\sigma_k l_0$ as a function of kl_0/π with $l_0 = \sqrt{\hbar/2m\omega}$ where ω is the trapping frequency for different values of the temperature. Taken from [23].

size of the BEC, and so independently of k. This is what we observe on Fig.-1.11 from [23], with however a small increase of the width with k that the authors attribute to a stronger localisation of the highly-excited Bogoliubov modes associated to the quantum depletion. For $T \neq 0$ however, the dependency of the normal correlations width with k is non-monotonic. At large k, we retrieve the same width than for $T = 0$. Indeed, the thermal energy is not sufficient to populate such high k values. The depletion is thus fully quantum and the width $\sim 1/L_{\mathrm{BEC}}$. As k decreases, we progressively reach a momentum region where the depletion is mainly thermal. As the spatial size of the thermal excitations is larger than that of the BEC because of the increased kinetic energy, σ_k is reduced. We then enter a plateau region that starts for higher values of k and stabilizes around lower values of σ_k as T increases as shown on Fig.-1.11. The plateau region ends for very low values of k as σ_k slightly increases with decreasing k that the authors of [23] attribute to the phononic character of the thermal excitations in this k region.

1.4.2 Anomalous correlations

The situation is more straightforward for the anomalous correlations related to the quantum depletion that is not affected by the temperature. The width of the anomalous correlations is therefore almost insensitive to temperature and independent from k, apart from a small increase at low k in the same fashion than for normal correlations at $T = 0$ (see Fig.-1.12).

1.5 Towards the experimental detection of k/-k pairs

Now that we have formed a clear picture of the kind of correlation functions we want to measure and have understood their essential features, we need to identify the key

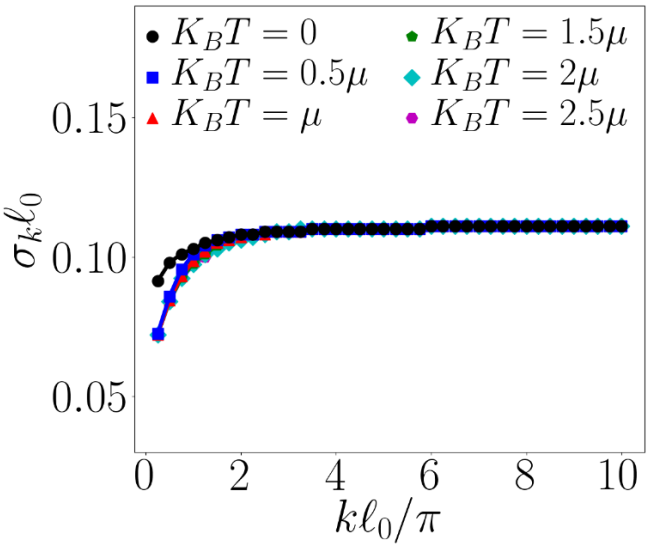

Figure 1.12: Evolution of the anomalous correlations width $\sigma_k l_0$ as a function of kl_0/π for different values of the temperature. Taken from [23].

experimental ingredients necessary to observe such signals. The principal one is to have an experiment capable of measuring the momentum of individual atoms in momentum-space and not only the momentum density as in most cold atoms experiment. This will be the subject of Chapter 3.

In addition, there are several key features of the $\boldsymbol{k}/-\boldsymbol{k}$ correlation signal that we need to understand to design an experimental scheme where the $\boldsymbol{k}/-\boldsymbol{k}$ correlation signal can be properly detected.

1.5.1 Separating the BEC from its depletion

A crucial aspect of studying the correlations in the depletion is the ability to separate the depleted atoms from the condensed ones. As a matter of fact, the BEC is a fully coherent state with macroscopic occupation of a single mode. In analogy with laser light in Optics, the statistics of the BEC are not chaotic and no bosonic bunching can therefore be observed. In addition, no $\boldsymbol{k}/-\boldsymbol{k}$ correlations are expected for atoms belonging to the condensate. Furthermore, in the weakly-interacting BEC, the number of condensed atoms is much larger than the number of depleted atoms. This has a direct consequence for our measurement: if we are unable to remove condensed atoms from the analysis, they will entirely drown out the correlation signals of the depletion.

Fortunately, the BEC and the depletion extents in momentum-space are very different. As for the width of the first-order correlation functions, the typical size of the momentum mode of the BEC is $1/L_{\mathrm{BEC}}$ [149]. On the other hand, the typical momentum width of the quantum depletion is $1/\xi$. Since $\xi \ll L_{\mathrm{BEC}}$, $1/\xi \gg 1/L_{\mathrm{BEC}}$ meaning that the quantum depletion extends on a much larger momentum area than the BEC. Likewise, for the typical temperatures accessible in our experiment, the momentum width of the thermal depletion is significantly larger than for the BEC. This effect is illustrated on Fig.-1.13. This provides us with a natural way to separate the condensate from its depletion and defines one of the

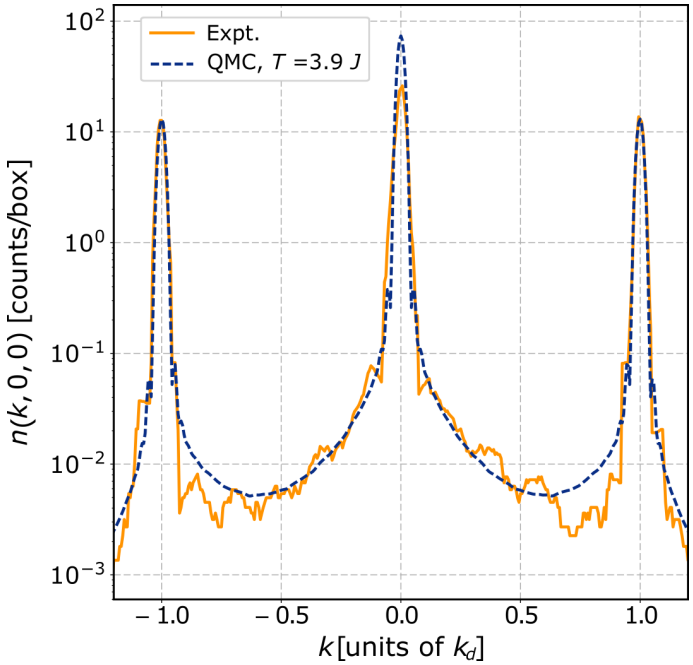

Figure 1.13: Experimental momentum density illustrating the different momentum extents of the BEC and the depletion. The condensed atoms correspond to the sharp and narrow peaks, as opposed to the wide background between the peaks that correspond the depletion. Note that the presence of several condensed peaks is linked to the presence of an optical lattice, as it will be explained in Chapter 2. Taken from [29].

experimental ingredients: we need an experimental setup capable of resolving the different regions of momentum-space so that the region around $\boldsymbol{k} = \boldsymbol{0}$ corresponding to the BEC can be removed from the analysis. In addition, while removing the BEC region we also remove the low k part of the momentum-space in which the Bogoliubov quasi-particles have a strong phononic character (see Chapter 4 for experimental numbers) and thus $\boldsymbol{k}/-\boldsymbol{k}$ correlations between particles, fulfilling the requirement described in 1.3.

1.5.2 Finite temperature effects

Another parameter that we must be very careful of is the temperature. In an ideal situation, we would conduct the experiment at zero temperature where the depletion is entirely quantum and all atoms consequently $\boldsymbol{k}/-\boldsymbol{k}$ paired. Obviously this is impossible to do in practice and the experiment will always be conducted at finite temperature.

Temperature is an absolutely crucial parameter when measuring $\boldsymbol{k}/-\boldsymbol{k}$ correlations as it sets the population of the thermal depletion, *i.e.* the population of the Bogoliubov quasi-particles (see equation 1.97). Indeed, as we have just seen, thermally depleted atoms show no $\boldsymbol{k}/-\boldsymbol{k}$ correlations in the momentum range that we wish to probe. If the temperature is too high, the thermally depleted atoms will significantly outnumber the quantum depleted ones and it will then be impossible to detect the $\boldsymbol{k}/-\boldsymbol{k}$ correlations. In order to quantify the effect of temperature, we compare the typical thermal energy $k_B T$ to the chemical potential of the condensate μ quantifying the effect of interactions. We aim to be in an experimental regime where $k_B T \ll \mu$, *i.e.* where interactions effects dominate

temperature effect. The first idea that comes to mind is then to reduce the temperature as much as possible. We however quickly hit a brick wall: the lowest temperature in ultracold experiments are obtained through evaporative cooling. This process will be detailed in Chapter 3 but we can quickly give here the main idea, which is to selectively remove the atoms of the gas with the highest thermal energy to let the other thermalize at a colder temperature. We quickly see the problem here: when the energy is dominated by the interaction energy $\sim \mu$ with μ the chemical potential, the atoms are removed randomly with respect to their thermal energy and there is thus no cooling anymore. This method allows us to typically reach $k_B T \sim 0.75\mu$ [33] which is not sufficient to ensure the proper detection of $\boldsymbol{k}/-\boldsymbol{k}$ correlations.

We are thus left with one only possible solution which is to increase the interactions. To this end, we will use a **3D optical lattice**. As a brief overview, a 3D optical lattice is formed by interference of 3 pairs of counter-propagating beams, one for each direction of space. The interferences create a sinusoidal potential trapping the atoms at the maximum of the light intensity profile, *i.e.* in periodically arranged wells, mimicking a condensed matter crystal. Interestingly, the density increases inside of the individual wells as a result of higher local trapping frequencies, increasing the strength of interactions and thus the likelihood to observe $\boldsymbol{k}/-\boldsymbol{k}$ correlations.

1.6 Conclusion

In this chapter, we have shown that correlation functions are an important and powerful tool that was first developed to describe classical effects of the light such as interferences. The experiment of Hanbury Brown and Twiss introduced the use of second-order correlation functions and revealed the existence of bosonic bunching. This observation later gave birth to the Quantum Optics formalism and the extended theory of coherence developed by R. J. Glauber with higher order correlation functions. This formalism was then adapted to atomic physics where correlation functions are of great interest to characterize **many-body interacting** systems. We made the proposition to study one of the simplest many-body system, the weakly-interacting Bose gas described by the Bogoliubov theory that we detailed the main lines of. We have shown that the Bogoliubov theory predicts the existence of the quantum depletion, a fraction of atoms removed from the condensate through the interplay between interactions and quantum fluctuations, and that we expect these atoms to form $\boldsymbol{k}/-\boldsymbol{k}$ correlated pairs that we will aim to detect by measuring second-order correlation functions. To this end, we have devised that our experimental setup should:

- Detect single atoms in momentum-space.
- Isolate the contribution of the depletion from the one of condensed atoms.
- Be in the low-temperature regime where interactions dominate temperature effects $k_B T \ll \mu$.

We decided for this last point to use 3D optical lattices that we will discuss in details in the next chapter of this thesis.

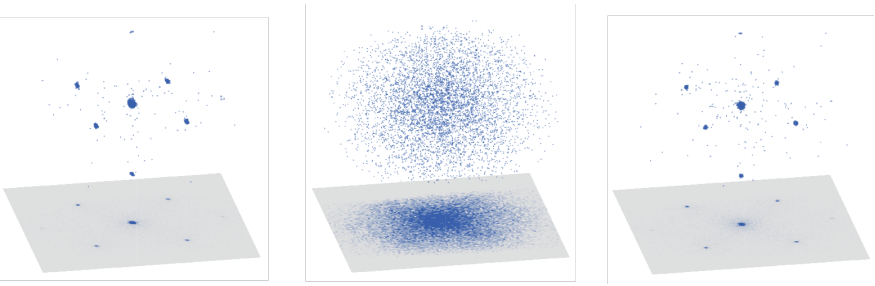

Chapter 2

2. Optical lattices and the Bose-Hubbard model

Quantum gases loaded in optical lattices (lattice gases for short) are one of the paramount examples of Quantum Simulation systems. The periodical trapping potential indeed well reproduces the crystal structure of condensed matter system and allows one to study relatively simple Hamiltonians such as the Bose- and Fermi-Hubbard Hamiltonians or the Ising model [12] that however account for interactions and show strong correlations effects. The main advantages of this experimental platform is that the different parameters of the Hamiltonians can be set and controlled, while information about the system can be accessed using a variety of experimental techniques as described in the introduction to this manuscript. Following the proposition of [89], the experimental observation of the superfluid to Mott insulator transition in 2002 [77] sparked interest in the community and lead to the development of the field from the early 2000s up until this day.

In this chapter, we expose the main elements of the Bose-Hubbard theory of lattice gases and briefly study the superfluid to Mott insulator transition. We then show how and under which conditions the in-trap momentum distribution of the gas can be accessed through Time-Of-Flight measurements, before drawing the connection with the Bogoliubov theory exposed in Chapter 1. The goal of this chapter is to give all the essential points necessary to obtain a system in which the $\boldsymbol{k}/-\boldsymbol{k}$ pairs of the quantum depletion can be experimentally observed, rather than providing a detailled description of Bose-Hubbard physics. For a more thorough study of the superfluid to Mott insulator transition with our experimental apparatus, we refer the reader to the manuscript of Cécile Carcy [25].

2.1 The Bose-Hubbard Model

We consider a 3D lattice potential with cubic symmetry and spacing d:

$$V(\boldsymbol{r}) = V_0 \left[\sin^2\left(\frac{k_d}{2}x\right) + \sin^2\left(\frac{k_d}{2}y\right) + \sin^2\left(\frac{k_d}{2}z\right) \right] + V_{\text{ext}}(x,y,z) \tag{2.1}$$

where $k_d = \frac{2\pi}{d}$ is the associated wave-vector and V_0 the lattice depth. For convenience, V_0 is usually expressed in units of recoil energy $V_0 = sE_\mathrm{r}$ with $E_r = h^2/8md^2$. In most experiments, such a potential is created with counter-propagating pairs of Gaussian laser beams. The term $V_\mathrm{ext}(x, y, z)$ denotes the additional harmonic potential that results from the Gaussian shape of the beams. For simplicity of calculations, we will first treat here the homogeneous case $V_\mathrm{ext}(x, y, z) = 0$.

We consider an ensemble of N bosons that interact with one another with the potential $U_\mathrm{int}(\boldsymbol{r}_1, \boldsymbol{r}_2)$ loaded in the lattice potential $V(\boldsymbol{r})$. The Hamiltonian of the system writes:

$$\hat{H} = \sum_{i=1}^{N} \frac{\boldsymbol{p}_i^2}{2m} + \sum_{i=1}^{N} V(\boldsymbol{r}_i) + \sum_{i}^{N} \sum_{j>i}^{N} U_\mathrm{int}(\boldsymbol{r}_i, \boldsymbol{r}_j) \tag{2.2}$$

Non-interacting lattice gas

To begin with, we consider that the atoms are non-interacting and study the simplified Hamiltonian:

$$\hat{H}_0 = \sum_{i=1}^{N} \frac{\boldsymbol{p}_i^2}{2m} + \sum_{i=1}^{N} V(\boldsymbol{r}_i) \tag{2.3}$$

As the Hamiltonian is separable along the 3 directions of space and the gas of atoms is non-interacting, we can simply work with the one-dimensional, single particle Hamiltonian:

$$\hat{H}_\mathrm{1D} = \frac{p_x^2}{2m} + \sin^2\left(\frac{k_d}{2}x\right) \tag{2.4}$$

To find the eigenstates of this Hamiltonian, we use the Bloch's theorem [4]:

Bloch's theorem

The eigenstates of a Hamiltonian corresponding to a spatially periodic potential $V(\boldsymbol{r})$ on a lattice $\mathcal{B}$ are Bloch waves $\psi_{\boldsymbol{q}}(\boldsymbol{r})$, product of a plane-wave $e^{i\boldsymbol{r}.\boldsymbol{q}}$ and a periodical function on $\mathcal{B}$, $u_{\boldsymbol{q}}(\boldsymbol{r})$.

We therefore look for eigenstates of the form:

$$\psi_{n,q}(x) = e^{iqx} u_{n,q}(x) \tag{2.5}$$

with $n \in \mathbb{N}$ and $q \in \mathbb{R}$ the **quasi-impulsion**. In order to determine the functions $u_{n,q}(x)$ and the energy $E_n(q)$, we inject equation 2.5 in the eigenvalue equation to find that they must verify:

$$\left[\frac{(p_x + \hbar q)^2}{2m} + V_0 \sin^2\left(\frac{k_d}{2}x\right)\right] u_{n,q}(x) = E_n(q) u_{n,q}(x) \tag{2.6}$$

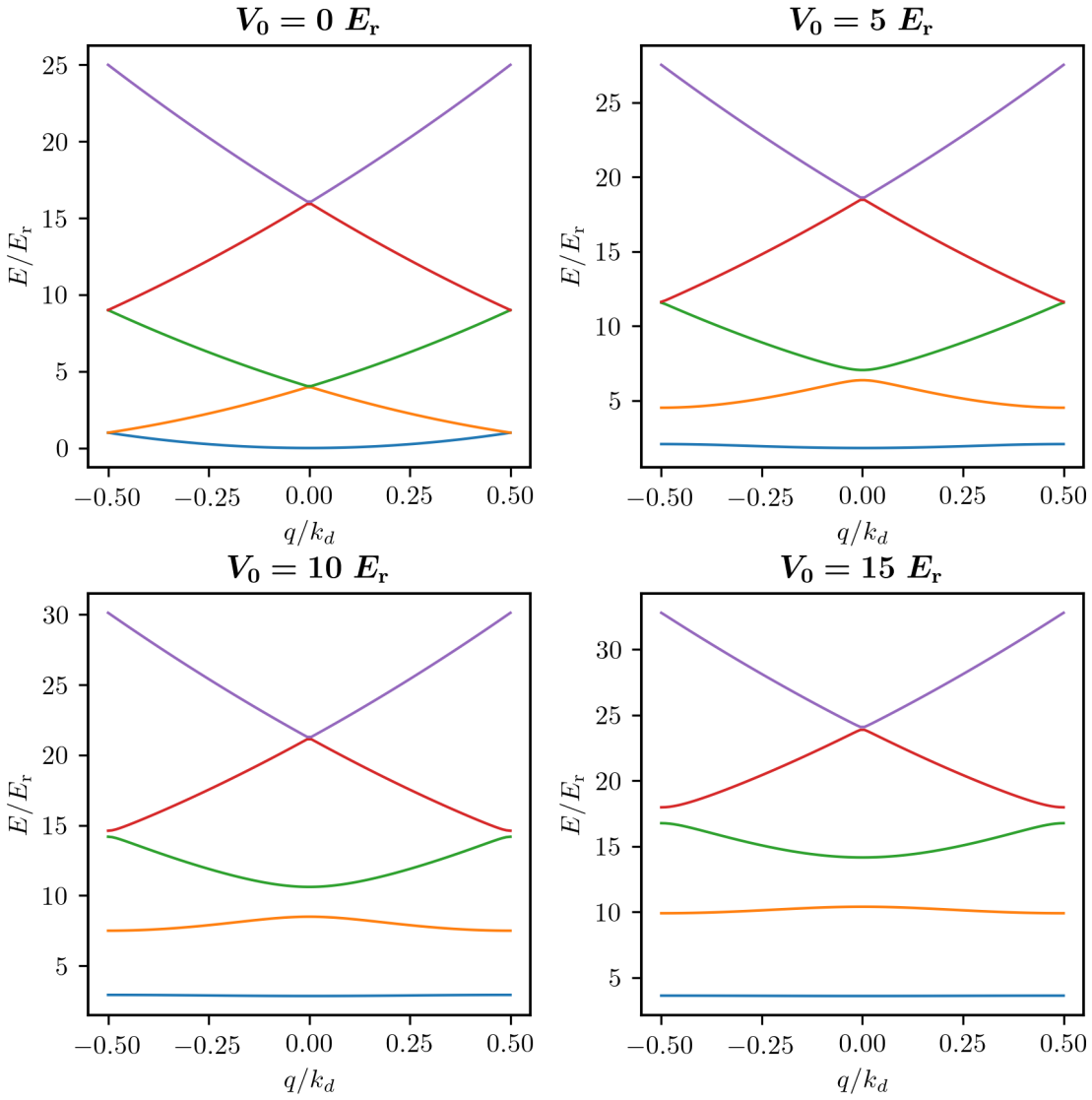

Figure 2.1: First five Bloch energy bands for various lattice amplitudes V_0. The gap between the first bands increases as V_0 increases.

As $E_n(q)$ is periodic $E_n(q + k_d) = E_n(q)\ \forall(n, q)$, we can restrict the definition interval of q to $[-k_d/2, k_d/2)$ which is called the **first Brillouin zone**. This equation can be easily numerically solved to obtain $u_{n,q}(x)$ and $E_n(q)$. We plot on Fig.-2.1 the first five energy bands as a function of q in the first Brillouin zone for various values of the lattice amplitude V_0. Interestingly, we see that a gap appears between the different bands as we increase V_0. For a 3D lattice, the total energy is the sum of the energies along each direction of the lattice. The first excited band then corresponds to two 1D lowest energy bands and one 1D excited band. In order for the gap to appear, the lattice amplitude must be above $V_0 \simeq 2.2\ E_r$, whereas it is present at all values of V_0 in the 1D case.

In addition to the Bloch waves, it is possible to define a new kind of functions called the **Wannier functions** [163] that are localized near the lattice sites. They are defined from the Bloch waves by:

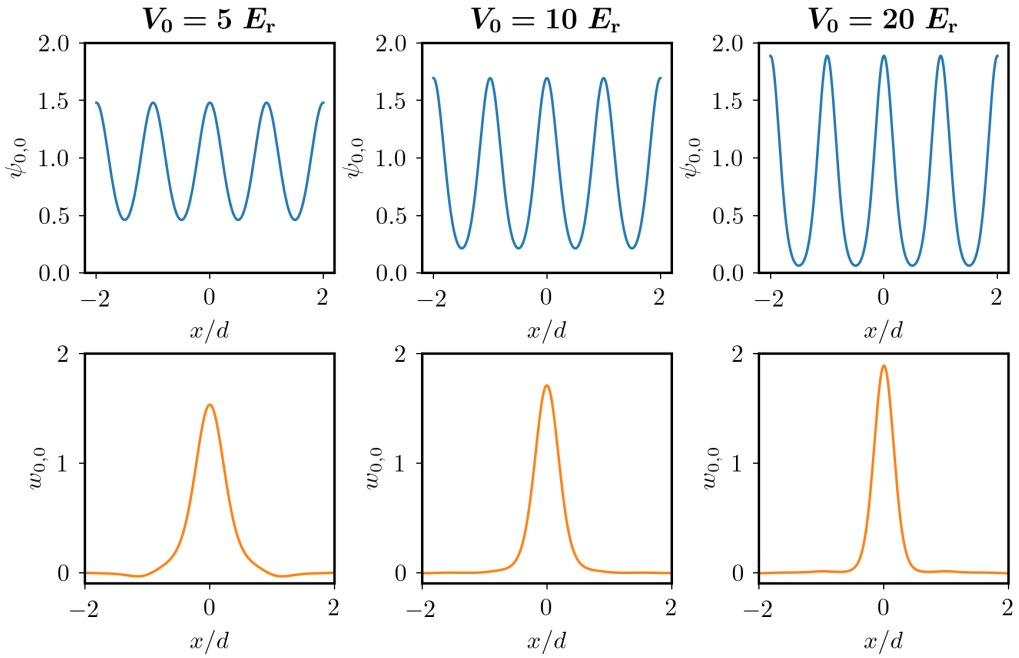

Figure 2.2: Real parts of the Bloch and Wannier functions for various lattice depths. When the lattice depth increases, the Bloch function is increasingly peaked around the lattice sites and the Wannier function gets narrower.

$$w_{n,j}(x) = \sqrt{\frac{d}{2\pi}} \int_{\mathrm{BZ}} \psi_{n,q}(x) e^{-ijqd}\, \mathrm{d}q, \quad j \in \mathbb{Z} \tag{2.7}$$

with BZ denoting an integration over the first Brillouin zone and where j can be interpreted as the index of a lattice site. Actually, we have from equation 2.7 the simple relation:

$$w_{n,0}(x - jd) = w_{n,j}(x) \tag{2.8}$$

The Bloch waves can then be re-written with the definition of the Wannier functions and write:

$$\psi_{n,q}(x) = \left(\frac{d}{2\pi}\right)^{1/2} \sum_j w_{n,j}(x) e^{-ijdq} \tag{2.9}$$

The Bloch waves are the sum of the localized Wannier functions $w_{n,j}$ that can be interpreted as the wave-functions of a particle located in lattice site j. The Bloch and Wannier functions for various lattice depths are represented on Fig.-2.2.

We can now re-write the Hamiltonian of the system with the newly introduced Wannier functions. To do so, we start by writing it in the Bloch waves basis with the second quantization formalism, introducing the operator $\hat{c}_{n,q}$ that destroys a particle in the Bloch wave $\psi_{n,q}$.

$$\hat{H}_{1\mathrm{D}} = \sum_n \int_{\mathrm{BZ}} E_n(q)\hat{c}^\dagger_{n,q}\hat{c}_{n,q}\ \mathrm{d}q \tag{2.10}$$

To change into the Wannier function basis as defined in 2.9, we introduce the operator $\hat{b}_{n,j}$ destroying a particle in the Wannier function $w_{n,j}$ and defined such as:

$$\hat{c}_n(q) = \sqrt{\frac{d}{2\pi}} \sum_j \hat{b}_{n,j} e^{ijdq} \tag{2.11}$$

Injecting equation 2.11 in equation 2.10, we get:

$$\hat{H}_{1\mathrm{D}} = \sum_n \sum_{j,j'} J_n\left(j - j'\right) \hat{b}^\dagger_{n,j'} \hat{b}_{n,j} \tag{2.12}$$

This Hamiltonian has a nice physical meaning: it describes the tunneling process by which a particle in site j can "hop" to another lattice site j' with the tunneling amplitude $J_n(j - j')$ that writes:

$$J_n\left(j - j'\right) = \frac{d}{2\pi} \int_{\mathrm{BZ}} e^{i(j-j')qd} E_n(q)\mathrm{d}q \tag{2.13}$$

This expression tells that the probability for a particle to tunnel from lattice site j to j' is reduced as the distance between the two sites j and j' increases and as the potential barrier, *i.e* the lattice depth, increases.

As for the rest of this thesis, we will focus on the ground-state properties of the system and therefore assume that the lowest energy band is the only one populated. This assumption is valid as long as $V_0 \geq 2.2\ E_\mathrm{r}$ at which the gap is opening and the typical excitation energy ΔE is smaller than the gap $\Delta = E_1 - E_0$. In addition, for $V_0 \geq 5\ E_\mathrm{r}$ [71], we can use the tight-binding approximation for which only the tunneling events between adjacent sites are non-negligible. We thus simplify the Hamiltonian 2.12 by replacing $J_n\left(j - j'\right)$ by a constant J denoting the probability to tunnel between adjacent lattice sites,

$$J = -J_0(1) \tag{2.14}$$

so that J is positive. Finally, we obtain the first term of the Bose-Hubbard Hamiltonian:

$$\hat{H}_{1\mathrm{D}} = -J \sum_{\langle i,j \rangle} \hat{b}^\dagger_i \hat{b}_j \tag{2.15}$$

where $\langle i, j \rangle$ denotes the ensemble of all adjacent lattice sites i and j. In the 3D case, the expression of the Hamiltonian remains the same.

Interaction term

We now turn to studying the interaction term that we had left out in the full Hamiltonian of equation 2.2. In the formalism of second quantification, the short-range, s-wave, 1D interaction Hamiltonian writes:

$$\hat{H}_{\text{int}} = \frac{1}{2}\int dx \int dx' U_{\text{int}}\left(x, x'\right) \hat{\Psi}^{\dagger}(x)\hat{\Psi}^{\dagger}\left(x'\right) \hat{\Psi}\left(x'\right) \hat{\Psi}(x) \tag{2.16}$$

with $\hat{\Psi}(x)$ the operator destroying a particle at position x that we write in terms of Wannier functions as:

$$\hat{\Psi}(x) = \sum_j w_j(x)\hat{b}_j = \sum_j w_0(x - x_j)\hat{b}_j \tag{2.17}$$

Note that we dropped the energy band number n as we are considering only the lowest energy band. We approximate the interactions to be contact, repulsive interactions so that:

$$U_{\text{int}} = g\delta(x_1 - x_2) \tag{2.18}$$

with $g = \dfrac{4\pi\hbar^2 a_s}{m}$ the strength of the interactions. The interaction Hamiltonian can then be re-written:

$$\hat{H}_{\text{int}} = \frac{g}{2}\sum_{j_1}\sum_{j_2}\sum_{j_3}\sum_{j_4} \hat{b}^{\dagger}_{j_4}\hat{b}^{\dagger}_{j_3}\hat{b}_{j_2}\hat{b}_{j_1}\int w^*_{j_4}(x)w^*_{j_3}(x)w_{j_2}(x)w_{j_1}(x)\ \mathrm{d}x \tag{2.19}$$

which is still a fairly complicated expression. We can however greatly simplify it by considering that the Wannier functions become narrower as the lattice depth increases. The overlap between the Wannier functions of the different lattice sites then becomes increasingly negligible. This means that the integral of equation 2.19 is non-zero only if $j_1 = j_2 = j_3 = j_4$, *i.e* if we only consider on-site interactions. This approximation is at the core of the tight-binding regime. In the end, the interaction Hamiltonian writes:

$$\hat{H}_{\text{int}} = \frac{U_{\text{1D}}}{2}\sum_j \hat{n}_j(\hat{n}_j - 1) \tag{2.20}$$

where we have introduced the on-site energy $U_{\text{1D}} = g\int |w_{0,0}(x)|^4\,\mathrm{d}x$, easily generalized to the 3D case with $U = g(\int |w_{0,0}(x)|^4\,\mathrm{d}x)^3$.

Combining this Hamiltonian to the non-interacting Hamiltonian of equation 2.15, we obtain the celebrated **Bose-Hubbard Hamiltonian** (see Fig.-2.3):

$$\hat{H}_{\text{BH}} = -J\sum_{\langle i,j\rangle}\hat{b}^{\dagger}_i\hat{b}_j + \frac{U}{2}\sum_j \hat{n}_j(\hat{n}_j - 1) \tag{2.21}$$

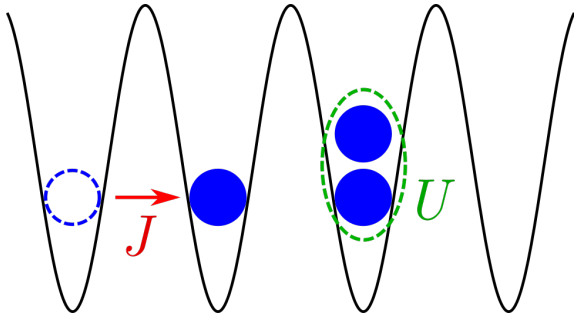

Figure 2.3: Representation of the Bose-Hubbard model. The physics of the system are set by the tunneling coefficient J and the on-site interaction energy U.

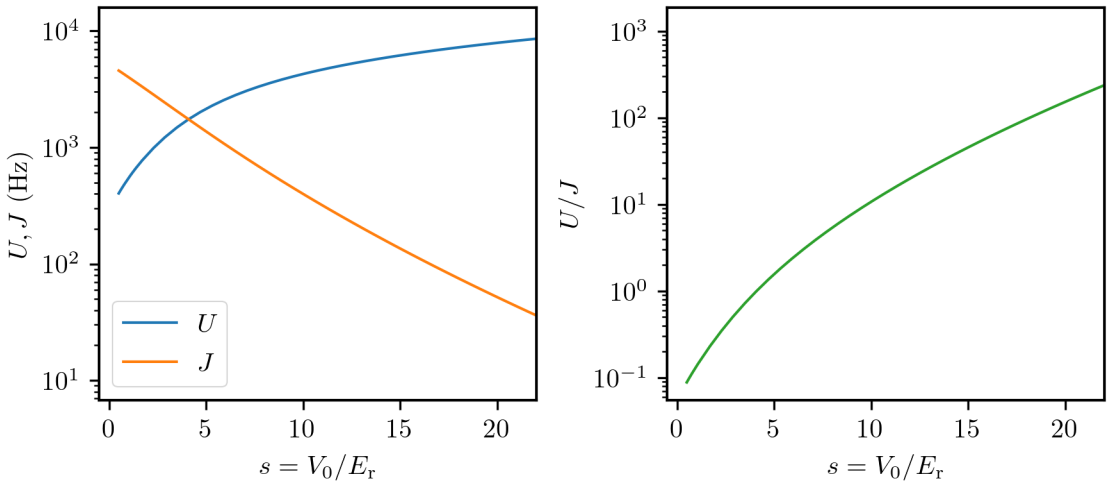

Figure 2.4: Evolution of U, J and the ratio U/J as a function of the lattice depth in log-scale from a numerical calculation with Wannier functions.

The physics of the homogeneous ground-state depends only from the two parameters J and U as we will see in the next paragraph. Interestingly, the ratio $u = U/J$ depends from the lattice depth V_0 as illustrated on Fig-2.4. The parameter u is therefore easily controllable in an experiment over orders of magnitude, for instance by changing the power of the laser beams used to produce the lattice potential.

2.2 The superfluid to Mott insulator transition

We discuss in this section the properties of the Bose-Hubbard Hamiltonian ground-state for N particles spread over M sites with filling $\bar{n} = N/M$. To begin, we describe the extreme cases $u \to 0$ and $u \to \infty$, which are the only cases for which the Hamiltonian can be analytically solved.

2.2.1 Extreme cases

Perfect superfluid (SF) phase $u \to 0$

In this case, the particles are non-interacting. In these conditions, the ground-state $|\Psi_0\rangle$ of the N particles system is simply the product of the single particle ground state wave-functions, *i.e* the Bloch wave-functions for $q = 0$ [13]:

$$|\Psi_0\rangle_{\mathrm{SF}} = \frac{1}{\sqrt{N!}}(\hat{c}^\dagger(\boldsymbol{q}=0))^N |0\rangle = \frac{1}{\sqrt{N!}}\left(\frac{1}{\sqrt{M}}\sum_{j=1}^{M}\hat{b}_j^\dagger\right)^N |0\rangle \tag{2.22}$$

The ground-state is an ideal Bose-Einstein condensate with a condensed fraction equal to 1. In the thermodynamic limit with $N \to \infty$, $M \to \infty$, it is possible to show at the price of a few lines of complex calculations [71] that the probability to find n_i atoms at a given site i is:

$$p\left(n_i\right) \approx e^{-\bar{n}}\frac{\bar{n}^{n_i}}{n_i!} \tag{2.23}$$

We recognize the same Poissonian distribution that we obtained for a bosonic coherent state in Chapter 1. We therefore write:

$$|\Psi_0\rangle_{\mathrm{SF}} \approx |\Psi\rangle_{\mathrm{coh}} = \mathcal{N}e^{\sqrt{N}\hat{c}^\dagger(\boldsymbol{q}=0)}|0\rangle = \mathcal{N}\prod_i e^{\sqrt{\bar{n}}\hat{b}_i^\dagger}|0\rangle = \prod_i \mathcal{N}_i \sum_{n_i=0}^{\infty}\frac{\alpha_i^{n_i}}{\sqrt{n_i!}}|n_i\rangle_i \tag{2.24}$$

with $\alpha_i = \sqrt{\bar{n}}\ \forall i \in \mathbb{Z}$ and the normalization factor $\mathcal{N}_i = e^{-|\alpha_i|^2/2}$. We thus find that the ground state can be described as a product of local coherent states associated to the different lattice sites.

As in Chapter 1, we write the first-order correlation function between two different lattice sites i and j to characterize the coherence properties of the ground-state:

$$G^{(1)}(i,j) = \langle \hat{b}_i^\dagger \hat{b}_j \rangle \tag{2.25}$$

In the limit $u \to 0$, $G^{(1)}(i,j)$ is easy to calculate and writes:

$$G^{(1)}(i,j) = {}_{u\to 0}\langle\Psi_0|\,\hat{b}_i^\dagger\hat{b}_j\,|\Psi_0\rangle_{u\to 0} = \alpha_i^*\alpha_j = \bar{n} \tag{2.26}$$

We see that the result does not depend from the chosen lattice sites i and j and thus from the distance between them, indicating an infinite range coherence.

Perfect Mott insulator (MI) phase $u \to \infty$

In the opposite extreme limit, one can consider that the tunneling probability goes to zero ($J = 0$) so that each of the lattice sites are independent from one another. The Hamiltonian reduces to:

$$\hat{H}_{\mathrm{BH}} = \frac{U}{2} \sum_j \hat{n}_j(\hat{n}_j - 1) \tag{2.27}$$

Because of the strong repulsive interactions, the atoms localize on the lattice sites and cannot hop from site to site as $J = 0$. The ground-state is then reached by distributing the particles among the different sites of the lattice so that the number of particles per site is as low as possible to minimize the interaction energy. This corresponds to putting $\bar{n} = N/M$ particles in each of the M available lattice sites. For simplicity sake, we assume here that the filling is commensurate, *i.e* $\bar{n}$ is an integer. The ground-state then has the simple expression of a Fock state:

$$|\Psi_0\rangle_{\mathrm{MI}} = \frac{1}{\sqrt{N!}} \prod_{j=1}^{M} \left(\hat{b}_j^\dagger\right)^{\bar{n}} |0\rangle \tag{2.28}$$

This state is called the **Mott insulator** state [60]. The first-order correlation function now writes

$$G^{(1)}(i,j) = {}_{u\to\infty}\langle\Psi_0|\, \hat{b}_i^\dagger \hat{b}_j \,|\Psi_0\rangle_{u\to\infty} = \delta_{i,j}\bar{n} \tag{2.29}$$

and is zero when we consider any pair of different lattice sites with $i \neq j$. In the limit $J \to 0$, the system is therefore fully incoherent.

2.2.2 The zero-temperature Mott phase transition

What can then be said for intermediates values of $u = U/J$? If we start from the case $J = 0$ and progressively increase J, it becomes possible for the atoms to hop from site to site. When an atom hops to an adjacent site, the occupancy is increased, increasing the energy by U. When the gain in kinetic energy J is smaller than U, this process is unfavorable and the atoms remain localized on the lattice sites. However, when J is much larger than U, the gain in kinetic energy outweighs the effect of the interactions and the atoms hop through the different sites of the lattice. The ground-state of the Bose-Hubbard then undergoes a phase transition as U/J varies from an **insulating phase** to a **superfluid phase** with very different properties (see Fig.-2.5).

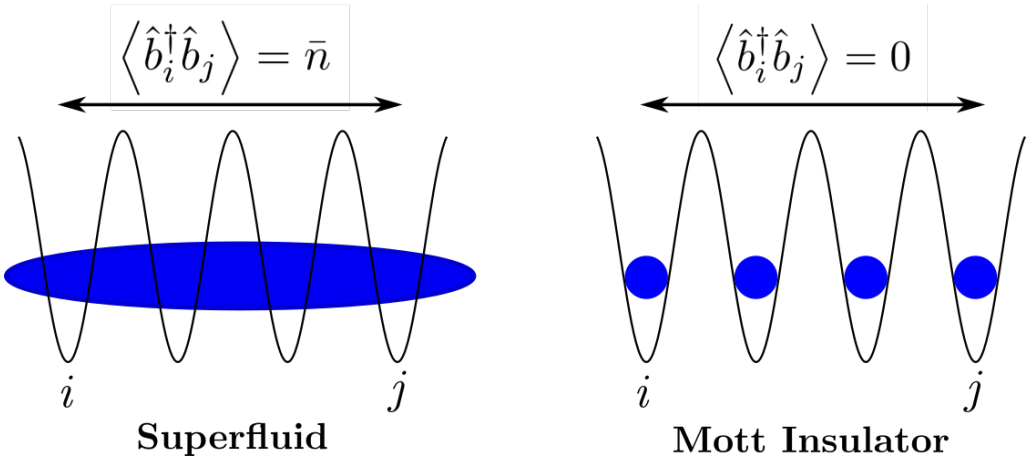

Figure 2.5: Schematic of the superfluid to Mott insulator transition. In the superfluid phase, the atoms are delocalized and the system shows long range coherence, contrary to the Mott insulator phase where the atoms are well localized on the lattice sites, making the system incoherent.

Superfluid phase

- The atoms are delocalized over the entire lattice.
- The condensed fraction is non-zero.
- The system shows long range coherence, *i.e* the phase is fixed.
- The on-site number of atoms is fluctuating.
- For low values of u (far from the transition), the effect of interaction is small, so that we can use the Bogoliubov approximation (detailled later in this chapter). We find that the excitation spectrum is gapless and phonon-like at low q.

Insulating phase

- The atoms are localized on the lattice sites.
- The condensed fraction is zero.
- The system is incoherent, the phase is fluctuating.
- The on-site number of atoms is well defined and non-fluctuating.
- The excitation spectrum is gapped, with the excitations consisting of particle-hole modes that can restore short-range coherence.

Phase diagram

In the homogeneous case, the properties of the system thus change dramatically when $u = U/J$ crosses the **Quantum Critical Point** (QCP) u_c. To discuss the value of u_c, we slightly complexify our model where we had only considered commensurate fillings, thus fixing the chemical potential that we now set to be a free parameter. We plot on Fig.-2.6 the full phase diagram function of μ/U, set by the filling in the Mott insulator phase $\bar{n}$ and J/U. As the system is homogeneous, the filling $\bar{n}$ is independent of u. The grey dashed lines correspond to iso-filling lines for a given value of $\bar{n}$. For commensurate fillings, the iso-filling lines cross the Mott stability lobes at the critical ratio u_c that increases as the filling increases. If the filling is however incommensurate (line $n = 1 + \varepsilon$), we notice that the system remains in the superfluid phase as long as $J \neq 0$. This is due to the fact that a small fraction of the atoms can delocalize over the whole lattice without being blocked

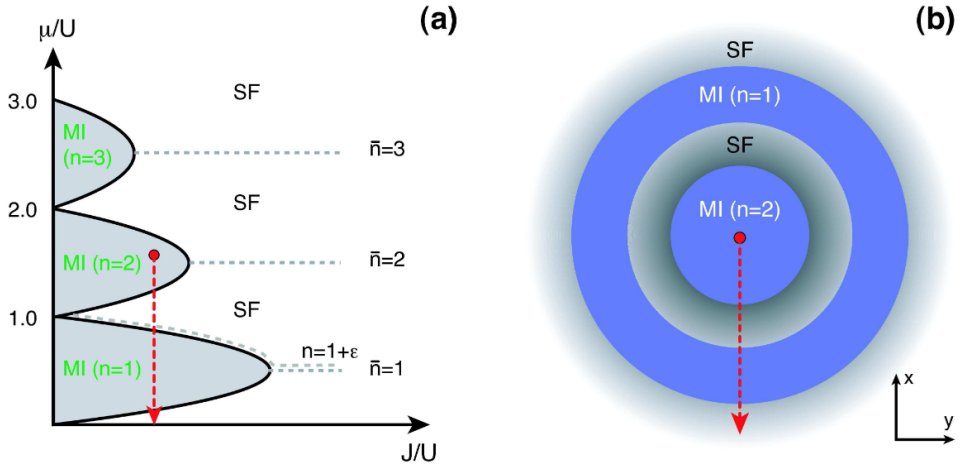

Figure 2.6: (a) Homogeneous phase diagram as a function of μ/U and J/U. The dashed lines are iso-filling lines. We observe a superfluid to Mott insulator phase transition for commensurate fillings. (b) Wedding-cake structure for the trapped gas. The red arrow illustrate how μ_{eff} varies and the corresponding phases as the distance from the center of the trap increases. Taken from [13].

by the interactions U as there will never be two of these particles in the same site as a consequence of the fact that the filling is incommensurate.

The value of u_c was first calculated with mean-field theories giving out the general formula holding for any dimension $u_c = 5.8z$ for $\bar{n} = 1$ and $u_c = 4\bar{n}z$ for $\bar{n} \gg 1$, with z being the number of nearest neighbors (6 in 3D, 4 in 2D and 2 in 1D). Later on, Quantum Monte Carlo (QMC) calculations [24] simulating the 3D system for a filling $\bar{n} = 1$ found $u_c = 29.3(2)$, *i.e* slightly lower than the mean-field prediction $u_c = 34.8$. For more details on this aspect, we refer the reader to the works of our team [25, 83] studying the value of u_c in our experiment.

2.2.3 Trapping effects

In practice, the system is often not homogeneous because of the external harmonic potential $V_{\text{ext}}(\boldsymbol{r})$ mentioned in 2.1. The properties of the trapped system can be linked to the properties of the homogeneous system by applying the Local Density Approximation[1] [11] and replacing the chemical potential by an effective one:

$$\mu_{\text{eff}} = \mu - V_{\text{ext}}(\boldsymbol{r}) \tag{2.30}$$

This means that the effective chemical potential, and thus the lattice filling, varies with the distance from the center of the trap. A typical situation is illustrated by the red arrow on the phase diagram of Fig.-2.6 where J/U is small enough for Mott phases to exist and the center of the trap corresponds to a filling $\bar{n} = 2$. As we get away from the center of the trap towards regions of low μ_{eff} following the red arrow, we exit the first Mott

[1] Valid as long as the trapping potential varies slowly from site to site and the system is at thermal equilibrium. This approximation may however fail at the quantum critical point [130].

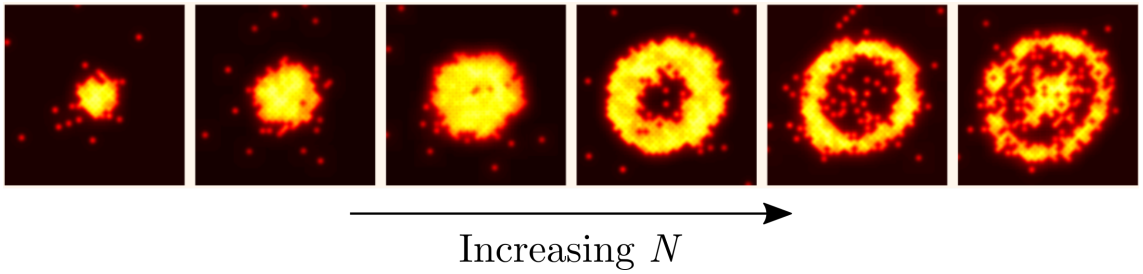

Figure 2.7: Visualisation of the wedding cake structure with a quantum microscope experiment. The imaging technique used here allows to detect the fluorescence of atoms trapped in a single site of an optical lattice, only if the number of atoms in the site is odd. We observe that as N increases, the wedding cake structure appears. Taken from [141].

region $\bar{n} = 2$ to enter a superfluid region where the filling decreases continuously up to a second Mott region with filling $\bar{n} = 1$ and finally reach a last superfluid region at the edge of the trap at vanishing values of μ_{eff}. The Mott phases are incompressible, meaning that the density remains constant even though the external trapping potential is rising, differentiating them from the superfluid region. This results in the famous "wedding-cake" density profile as illustrated on panel (b) of Fig.-2.6 and Fig.-2.7.

Actually, the external harmonic potential is quite important for experiments. If the system is homogeneous and the entropy constant, when the lattice depth is increased thus going deeper in the Mott phase, the increase of the energy gap makes it increasingly difficult for excitations to be created meaning that the temperature must increase to keep the entropy constant. In the presence of a trap however, the entropy is concentrated in the superfluid shells that can also turn to a normal gas phase, preventing the temperature of the system from increasing too much.

In the remainder of this manuscript for clarity sake, the system will be said to be in the Mott insulator phase as long as a Mott plateau exists, *i.e* when $u > u_c$ where u_c is the critical point for the corresponding homogeneous system.

2.2.4 Finite temperature effects

If we finally consider the effect of temperature, we obtain the complete phase diagram of Fig.-2.8 function of T/J and u with the apparition of an additional phase, the normal (thermal) gas. For $u \leq u_c$, the transition between the normal gas phase and the superfluid phase driven by the temperature is similar to the well-known BEC transition. This transition is induced by the thermal fluctuations and is then called classical, in opposition to the $T = 0$ Mott transition which is driven by variations of physical parameters of the Hamiltonian in the presence of quantum fluctuations and therefore is a quantum transition.

On the other hand, the Mott insulator phase also goes to the normal gas phase as the temperature increases, but with a smooth crossover. When T increases, excitations are created preferably near the edges of the Mott plateaus, progressively smoothing out the sharp density profile of the Mott insulator phase. A Mott-like region survives until $T^* \sim 0.2\ U/k_B$ [70] also called the "melting temperature" of the Mott phase.

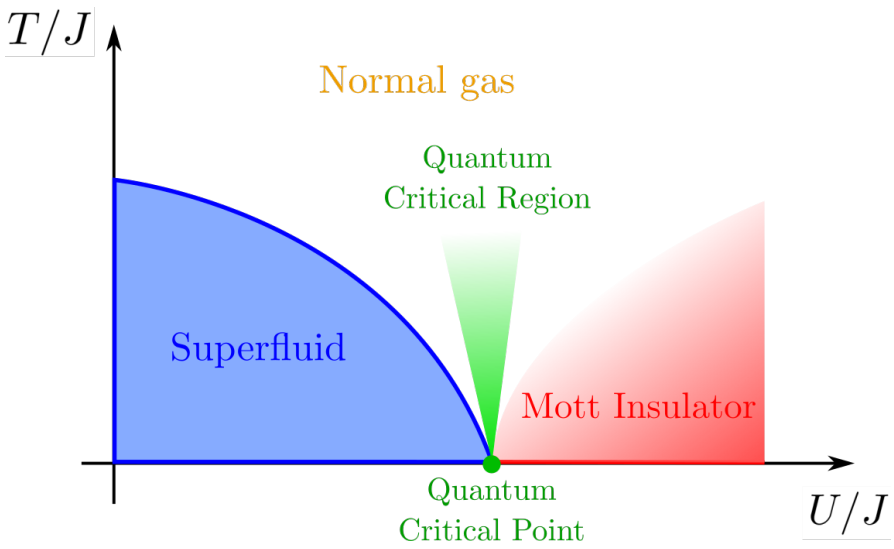

Figure 2.8: Bose-Hubbard phase diagram function of T/J and U/J. We identify three phases, the Superfluid, Mott Insulator, and Normal Gas. The green area indicates the region in which critical point quantum effects could be observable in spite of the finite temperature.

Interestingly, the superfluid to Mott insulator transition subsists at low temperature. At $T = 0$ and at the QCP of the transition, the ground-state undergoes a macroscopic rearrangement characterized by the apparition of critical quantum fluctuations and complex correlation patterns. Importantly, the physics of the QCP affect a signficant part of the finite temperature phase diagram as signaled by the green area on Fig.2.8. In this region, some observables such as the momentum density indeed show critical behavior, *i.e* a power law scaling with temperature with an exponent set by the critical exponents of the QCP. While the physics of the QCP are a very interesting and trending topic, they fall out of the scope of this thesis and we refer the reader to the works [25, 64, 135] for more informations on this aspect.

2.2.5 The Gutzwiller method

To conclude this section, we present an approximate theoretical approach to treat the Bose-Hubbard Hamiltonian, the Gutzwiller method. This method takes its name from its author who introduced it in [80] to study strongly correlated Fermi systems. It was later adapted to characterize the ground-state of the Bose-Hubbard Hamiltonian in [134]. This method is particularly useful to evaluate the density profile and therefore the size of the lattice gas with good accuracy all across the Mott transition, apart from the region close to the critical point. Although this is a ground-state, $T = 0$ method that does not faithfully represent the reality of experiments, its predictions remain fairly accurate and will be quite valuable to understand the correlation signals that we will present in this thesis.

The method revolves around the Gutzwiller ansatz that consists in writing the many-body ground-state as a product of on-site wave-functions $|\phi_i\rangle$:

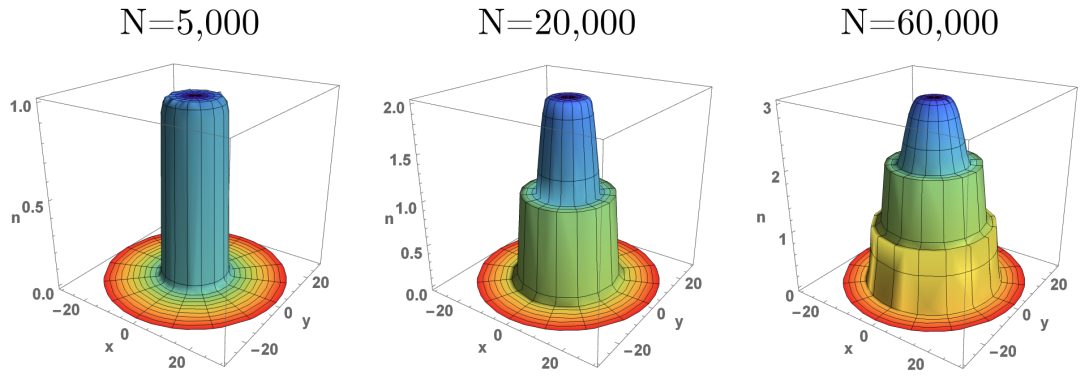

Figure 2.9: Gutzwiller density profiles for various atom numbers at $s = 18$ with n the number of atoms per site and x,y the positions in units of lattice spacing.

$$|\Psi_G\rangle = \prod_{i}^{\text{sites}} |\phi_i\rangle \tag{2.31}$$

The on-site wave-functions are then developed on the Fock-state basis:

$$|\phi_i\rangle = \sum_{n_j=0}^{\infty} f(n_j)\,|n_j\rangle \tag{2.32}$$

This ansatz is motivated by the fact that it matches the exact ground-state for the extreme cases:

- For $u \to 0$, the ground-state is a coherent state (see equation 2.24) so that $f(n_j) = \mathcal{N}_j(\alpha_j^{n_j})(\sqrt{n_j!})$ with $\alpha_j = \sqrt{\bar{n}}$ and $\mathcal{N}_i = e^{-|\alpha_i|^2/2}$.
- For $u \to \infty$, the ground-state is already a Fock state (see equation 2.28) so that $f(n_j) = \delta_{n_j,\bar{n}}$.

The Gutzwiller method is a **variational** approach, meaning that the ground-state is determined by finding the coefficients $f(n_j)$ that minimizes the free energy defined as:

$$G = \langle H_{\text{BH}}\rangle_{|\Psi_G\rangle} - \mu\langle N\rangle_{|\Psi_G\rangle} = -J\sum_{\langle i,j\rangle}\alpha_i^*\alpha_j + \sum_j\sum_{n_j=0}^{\infty}\left[\frac{U}{2}n_j\left(n_j-1\right) - \mu n_j\right]\left|f\left(n_j\right)\right|^2 \tag{2.33}$$

with the condition $\langle n_j\rangle = \sum_{n_j=0}^{\infty}\left|f_j\left(n_j\right)\right|^2 n_j = \bar{n}$. The coefficients $f(n_j)$ can be found through numerical calculations. Interestingly, following the arguments of 2.2.3, μ can be replaced by the effective μ_{eff} to account for the effect of the external trapping potential present in our experiment. We show on Fig.-2.9 wedding cake density profiles for various atom numbers at $s = 18$ with our experimental parameters computed with the Gutzwiller method.

2.3 Accessing the in-trap momentum distribution in a Time-Of-Flight experiment

Now that we have laid down the main elements of lattice gases physics, we need to determine the proper experimental tools to characterize the system. As developed in Chapter 1, the main focus of this thesis will be on the **momentum-space** correlations, requiring us to devise a technique to effectively measure the momentum distribution of a lattice gas. The most natural idea for momentum-space measurements is to use the well-known and widely used **Time-Of-Flight** (TOF) technique. This technique consists in suddenly turning off the trapping potential to let the atoms fall under the effect of gravity and measure their positions $\boldsymbol{r}$ after a given TOF t_{TOF}. In a very simple picture with classical and non-interacting particles, the position $\boldsymbol{r}$ gives information about the in-trap momentum of the particle through the simple **ballistic relation**:

$$\hbar \boldsymbol{k} = \frac{m\boldsymbol{r}}{t_{\mathrm{TOF}}} \tag{2.34}$$

The validity of this simple relation is however far from being obvious for the quantum gases released from optical lattice. We will describe in this section the TOF dynamics of an atomic gas released from an optical lattice to identify the conditions under which a TOF measurement can be used to properly measure the in-trap momentum of the gas.

2.3.1 Expansion from the lattice and far-field regime

We start our calculations with the simplified case for which we neglect the effects of interactions during the TOF. In this configuration, the problem is very similar to the diffraction of a light wave by a grating in optics, in which a diffraction interference pattern results from the coherent sum of the contribution of many source points associated to each of the diffraction grating holes. For the lattice gas, the source points correspond to the lattice sites associated to Wannier functions that will be able to interfere if the system is coherent. For simplicity sake, we will only consider the 1D case from which the 3D case can be easily obtained as the non-interacting Hamiltonian is separable.

At time $t = 0$, right before the lattice potential is turned off, the atomic field operator writes (see 2.17)

$$\hat{\Psi}(x) = \sum_j w_0(x - x_j)\hat{b}_j \tag{2.35}$$

The expression of the Wannier functions is rather complex and very hard to handle in calculations. However, we can approximate the lattice potential near a minimum to its second-order Taylor expansion, *i.e* approximate it to a harmonic potential of frequency $\omega_L = 2\sqrt{s}(E_{\mathrm{r}}/\hbar)$ [156]. As illustrated in Fig.-2.10, the Wannier function is well approximated by the Gaussian wave-function of the harmonic oscillator ground state for amplitudes $V_0 \gtrsim 10\ \mathrm{E_r}$ (note however that this does not approximate tunelling well as a Gaussian function does not show the same small oscillations as the Wannier function):

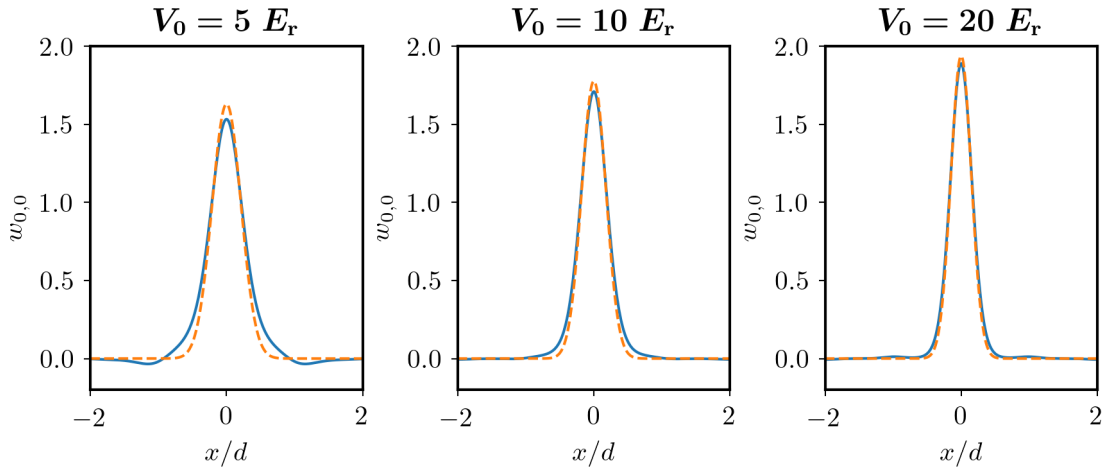

Figure 2.10: Comparison between the Wannier functions (blue) and and the Gaussian wave-function of the ground state of the harmonic oscillator of frequency ω_L (orange) for various lattice depths.

$$w_0(x) \simeq \frac{1}{\pi^{1/4}\sqrt{x_0}} \exp\left(\frac{-x^2}{2x_0^2}\right) \tag{2.36}$$

with $x_0 = \sqrt{\hbar/m\omega_L}$.

When the lattice potential is turned off, each of the lattice sites wave-functions expand freely following the harmonic oscillator dynamics [156]:

$$w\left(x - x_j, t\right) = \frac{1}{\pi^{1/4}\sqrt{W(t)}} \exp\left(-\frac{\left(x - x_j\right)^2}{2W(t)^2}\right) \exp\left(-i\frac{\left(x - x_j\right)^2}{2W(t)^2}\frac{ht}{mx_0^2}\right) \tag{2.37}$$

with $W(t) = x_0\sqrt{1 + \left(\hbar t/mx_0^2\right)^2}$ the width of the Gaussian envelope.

The far-field regime

In practice, as ω_L is high ($\sim 10^5 - 10^6$ Hz), $W(t)$ increases very quickly. For instance, with $s = 5$, $W(t)$ is multiplied by ~ 600 after 1 ms of expansion and is thus much larger than the size of the lattice L. For $t > 1$ ms, we can make the approximation $W(t) \simeq \hbar t/mx_0$ as well as neglect the dependency on the initial site x_j in the amplitude term as long as $|x| \ll W(t)$ so that we can write:

$$\exp\left(-\frac{\left(x - x_j\right)^2}{2W(t)^2}\right) \simeq \exp\left(-\frac{x^2}{2W(t)^2}\right) \tag{2.38}$$

This is equivalent to the paraxial approximation of the Fraunhofer diffraction regime in Optics.

Building up on the diffraction analogy, we would like to define an analog Fraunhofer distance where the dependency of the phase factor on the quadratic analog Fresnel term in x_j can be neglected. Using $W(t) \simeq \hbar t/mx_0$, we obtain $\frac{(x-x_j)^2}{2W(t)^2}\frac{ht}{mx_0^2} \simeq \frac{(x-x_j)^2}{2x_0W(t)}$ from which we derive the condition $\frac{x_j^2}{2x_0W(t)} \ll 1, \forall j$ that we rewrite [72, 156]:

$$t \gg t_{\mathrm{FF}} = \frac{mL^2}{2\hbar} \tag{2.39}$$

This condition defines the **far-field regime** after which the interference pattern is well developed, in analogy to the Fraunhofer regime of diffraction. We note the far-field regime is accessed for smaller times for lighter particles. Using one of the lightest atom, ^{4}He, thus makes it easier to fulfill the far-field regime condition in the experiment.

Combining the different approximations, we simplify 2.37 to:

$$w\left(x-x_j,t\right) = \sqrt{\frac{m}{\hbar t}}\tilde{w}_0[Q(x,t)]\exp\left(-i\frac{\hbar Q(x,t)^2}{2m}\right)\exp\left(iQ(x,t)x_j\right) \tag{2.40}$$

with $Q(x,t) = \frac{mx}{\hbar t}$ and $\tilde{w_0}$ the Fourier transform of the Wannier function.

Now that we have the general expression of $w\left(x-x_j,t\right)$, we generalize it to the 3D case and inject it in equation 2.35 to obtain the sum of the contribution of each site:

$$\hat{\Psi}(\boldsymbol{r},t) = \left(\sqrt{\frac{m}{\hbar t}}\right)^3 \tilde{w}_0[\boldsymbol{Q}(\boldsymbol{r},t)]\exp\left(-i\frac{\hbar \boldsymbol{Q}(\boldsymbol{r},t)^2}{2m}\right)\sum_j e^{i\boldsymbol{Q}(\boldsymbol{r},t).\boldsymbol{r}_j}\hat{b}_j \tag{2.41}$$

From this expression, we finally obtain the atomic density $\rho_{\mathrm{TOF}}(\boldsymbol{r},t) = \langle\hat{\Psi}^\dagger(\boldsymbol{r},t)\hat{\Psi}(\boldsymbol{r},t)\rangle$ at position $\boldsymbol{r}$ and a long TOF t:

$$\rho_{\mathrm{TOF}}(\boldsymbol{r},t) = \left(\frac{m}{\hbar t}\right)^3 |\tilde{w}_0(\boldsymbol{Q}(\boldsymbol{r},t))|^2 \sum_{i,j} e^{i\boldsymbol{Q}(\boldsymbol{r},t).(\boldsymbol{r}_j-\boldsymbol{r}_i)}\langle\hat{b}_i^\dagger\hat{b}_j\rangle \tag{2.42}$$

The density $\rho_{\mathrm{TOF}}(\boldsymbol{r},t)$ then consists of a smooth envelope $|\tilde{w}_0(\boldsymbol{Q}(\boldsymbol{r},t))|^2$ set by the Fourier transform of the Wannier function and an interference term $\sum_{i,j} e^{i\boldsymbol{Q}(\boldsymbol{r},t).(\boldsymbol{r}_j-\boldsymbol{r}_i)}\langle\hat{b}_i^\dagger\hat{b}_j\rangle$ that characterizes the coherence properties of the system. A numerical simulation of $\rho_{\mathrm{TOF}}(\boldsymbol{r},t)$ is plotted on Fig.-2.11 at various expansion time for $s = 5$ corresponding to the superfluid phase, illustrating how the interference pattern develops in time.

Relation to the momentum distribution

The main purpose of the TOF technique is to obtain information on the momentum distribution of the gas. To this end, we must find the relation between the measured quantity $\rho_{\mathrm{TOF}}(\boldsymbol{r},t)$ and the in-trap momentum distribution $\rho(\boldsymbol{k})$. To do so, we introduce the operator $\hat{a}_{\boldsymbol{k}}$ destroying a particle in mode $\boldsymbol{k}$:

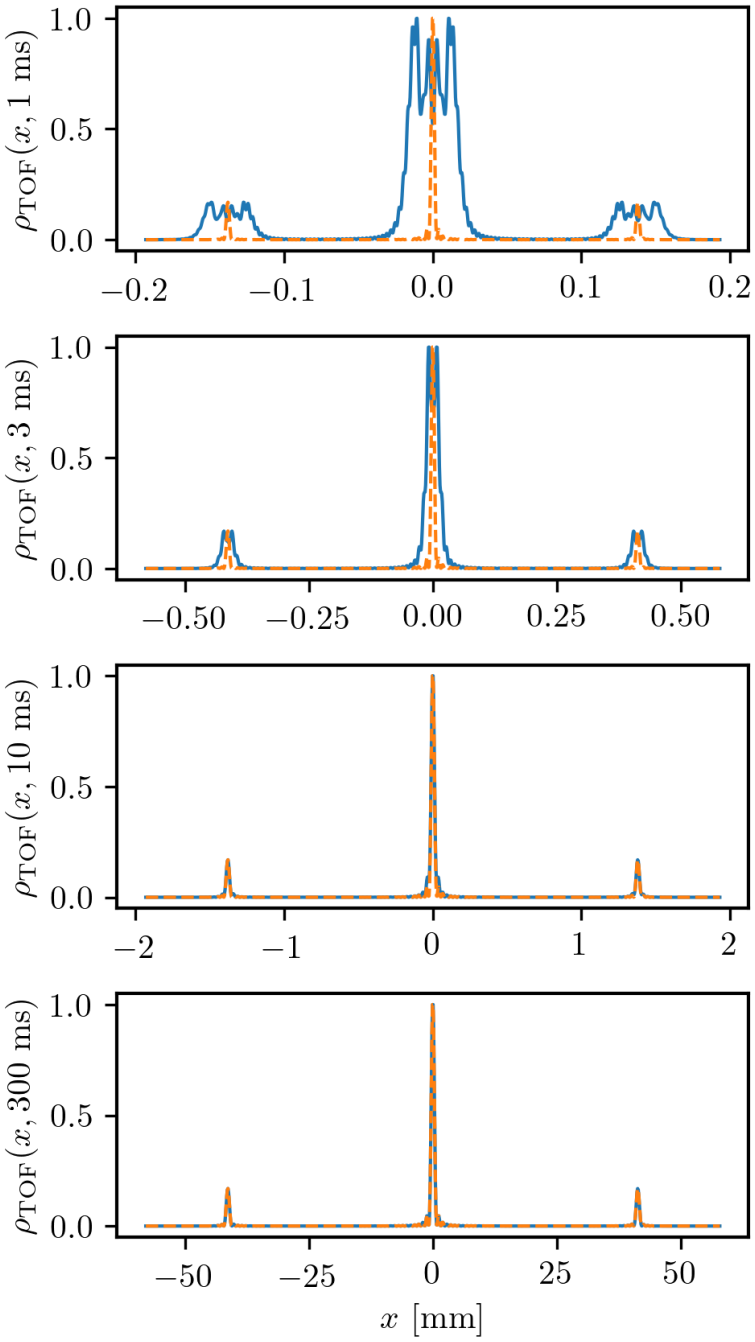

Figure 2.11: Numerical simulation of the atomic density $\rho_{\mathrm{TOF}}(x, t)$ after various expansion times from a 1D lattice of 50 sites with $s = 5$. The orange dashed line serves as a point of comparison with the asymptotic distribution for high TOF times representing the momentum distribution.

$$\hat{a}_{\boldsymbol{k}} = \frac{1}{\sqrt{V}} \sum_j e^{i\boldsymbol{k}\cdot\boldsymbol{r}_j} \hat{b}_j \tag{2.43}$$

where V is the quantization volume set to be the in-trap volume of the gas. The momentum density then writes:

$$\rho(\boldsymbol{k}) = \left\langle \hat{a}^\dagger_{\boldsymbol{k}} \hat{a}_{\boldsymbol{k}} \right\rangle = \frac{1}{V} \sum_{j,i} e^{-i\boldsymbol{k}\cdot(\boldsymbol{r}_j - \boldsymbol{r}_i)} \left\langle \hat{b}^\dagger_i \hat{b}_j \right\rangle \tag{2.44}$$

If the particle are non-interacting, the ballistic relation gives $\boldsymbol{k} = m\boldsymbol{r}/\hbar t_{\mathrm{TOF}}$. From equation 2.42, we obtain:

$$\rho(\boldsymbol{k}) = \frac{\rho_{\mathrm{TOF}}(\boldsymbol{r} = \hbar t \boldsymbol{k}/m, t)}{V \left(\frac{m}{\hbar t}\right)^3 |\tilde{w}_0(\boldsymbol{k})|^2} \tag{2.45}$$

In conclusion, under the conditions that there are no interactions during the TOF and $t_{\mathrm{TOF}} \gg t_{\mathrm{FF}}$ to be in the far-field regime, the TOF distribution maps the in-trap momentum distribution.

Momentum distribution across the Mott transition

As discussed previously, the momentum distribution is strongly dependent on the coherence properties of the system and in turn of the lattice depth.

- In the superfluid phase $u \to 0$, the system is coherent $G^{(1)}(i,j) = \bar{n}$. From equation 2.44, we get that the momentum distribution consists of sharp analog diffraction peaks located at $\boldsymbol{k} = jk_d\boldsymbol{e}_i$ with $j \in \mathbb{Z}$ and $\boldsymbol{e}_i$ the unitary vector in direction $i = x, y, z$. In terms of $\rho_{\mathrm{TOF}}(\boldsymbol{r}, t)$, the amplitude of the different peaks is set by the Fourier transform of the Wannier function.
- In the Mott insulator phase $u \to \infty$ the system is totally incoherent $G^{(1)}(i,j) = \delta_{i,j}\bar{n}$. The momentum distribution is then constant, meaning that $\rho_{\mathrm{TOF}}(\boldsymbol{r}, t)$ simply reflects the Fourier transform of the Wannier function, *i.e* a Gaussian-like function.
- For intermediate values of u, the visibility of the interference pattern progressively decreases as u increases. In addition, as V_0 increases, the Wannier function is more and more localized so that the width of its Fourier transform increases. As a result, the population of the diffracted peaks increases with the lattice depth.

The experimental quantity $\rho_{\mathrm{TOF}}(\boldsymbol{r}, t)$ is therefore a powerful tool to characterize the phase of the system across the Mott transition. This is illustrated on Fig-2.12 of the first experimental observation of the Mott transition with cold atoms [77], on which we can clearly see the visibility of the interference pattern decreasing with V_0 (note that these images are not taken deep in the far-field regime, meaning that some details of the interference pattern are not resolved).

Importantly, a characteristic of the superfluid to Mott insulator transition is that even though the system is incoherent in the insulating phase, the coherence can be restored by ramping down the lattice depth to the superfluid phase. The standard procedure to

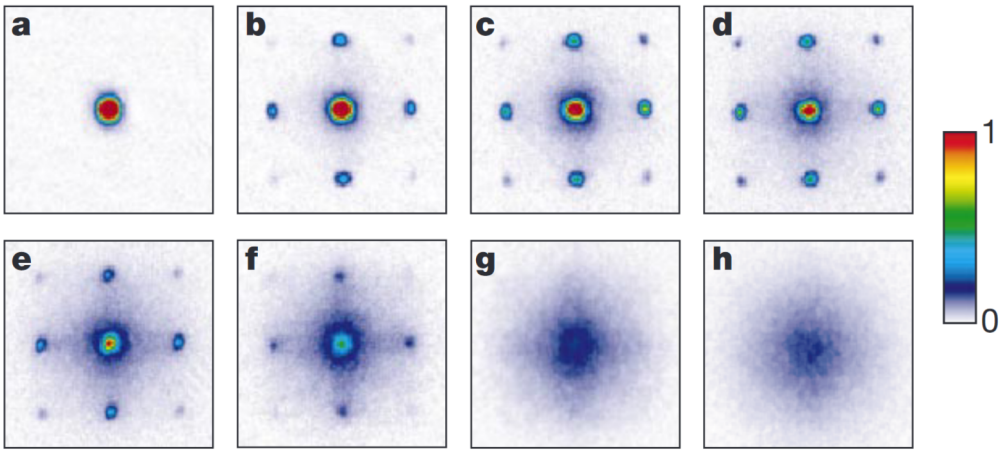

Figure 2.12: Absorption images of Rubidium atoms taken 15 ms after the atoms are released from a 3D cubic lattice. Note that the far-field regime condition is not fulfilled here. **a)** s=0. **b)** s=3. **c)** s=7. **d)** s=10. **e)** s=13. **f)** s=14. **g)** s=16. **h)** 20. Taken from [77].

characterize the presence of the Mott transition is then to set V_0 to be in the superfluid region, ramp up it up to see that the interference pattern disappears, and ramp it down to find back the interference pattern. This allows to certify that the loss of coherence is indeed an effect of the competition between U and J and not an experimental artifact, such as unwanted heating of the cloud.

2.3.2 Mean-field interactions

The experimental technique described in the last paragraph holds if there are no interactions between the particles during the TOF. If it were otherwise, the interactions would affect the TOF dynamics of the gas, preventing us to use the ballistic relation and to map the TOF distribution $\rho_{\mathrm{TOF}}(\boldsymbol{r}, t)$ to the in-trap momentum $\rho(\boldsymbol{k})$. As interactions cannot be effectively turned off by means of a Feshbach resonance, experimentally inaccessible for ^{4}He*, it is crucial to determine whether interactions during the TOF can be neglected or not and under which conditions.

As mentioned in the introduction to this manuscript, describing the interactions between each of the individual particles would be impossible, even for numerical methods for which the calculation time would be prohibitive. To circumvent this issue, the problem can be simplified using the **mean-field approximation** (also explained in the introduction).

To quantify the effect of the interactions treated at the mean-field level, we introduce the interaction energy $U_{\mathrm{int}} \sim gn$ with g the strength of the interactions and n the atomic density. To determine whether the interactions are affecting the expansion of the gas released from the lattice, U_{int} must be compared to the zero point energy of the ground-state of the approximate harmonic oscillator associated to a single lattice site, $\hbar\omega_L$. In typical experimental conditions, $U_{\mathrm{int}}/h \approx 10^3$ Hz $\ll \omega_{\mathrm{L}}/2\pi \approx 10^5 - 10^6$ Hz, meaning that the initial expansion is driven by the zero point energy of the lattice site and not the released interaction energy. In addition, after a small expansion time, the Wannier functions of the different sites overlap as their widths become of the order of the lattice

spacing d and might then interact. However, on this time scale, the atomic density is reduced by a factor $(x_0/d)^3 \approx 10^2$ (for $s = 10$), meaning that this interaction effect should also be negligible [72], provided that the initial density is not too high. This point will be discussed in further details in light of experimental data in Chapter 3.

As developed in [100], the interactions can also induce a dephasing between the different sites. As a matter of fact, the time evolution of the phase of the wave-function associated to a lattice site depends on its initial energy, and therefore of U_{int}. If the lattice sites have different lattice fillings, which typically is the case in the superfluid phase where the on-site atom number fluctuations are large, the different interfering wave-functions can be dephased from one another, reducing the visibility of the interference pattern. This effect is however also negligible [72, 100] in the case of our 3D lattice where $a_s \ll x_0$, provided that the filling is not too high.

2.3.3 Beyond mean-field interactions

While the mean-field approximation is efficient to obtain a first understanding on how the interactions might affect the TOF, it is inherently limited as it does not consider interaction effects between several particles. One clearly identifiable beyond mean-field effect happening during the TOF is the presence of scattering halos between the diffraction peaks [76]. These scattering halos signal the presence of s-wave collisions between the atoms of the different diffraction peaks, *i.e* with significantly different velocities, happening during the first moments of the TOF as they separate. This effect is analog to the scattering halos observed between two colliding condensates [95, 123, 175].

We have conducted a thorough experimental study of the s-wave two-body collisions during the TOF to determine whether they would affect our measurement of the momentum distribution [154]. This study will be detailed in Chapter 3.

2.4 Extension of the Bogoliubov theory to lattice gases

So far, we have focused on the description of the lattice Hamiltonian under the scope of Wannier functions, culminating in the Bose-Hubbard Hamiltonian describing the physics of the Mott transition. We now wish to go back to the central point developed in Chapter 1, namely the $\boldsymbol{k}/-\boldsymbol{k}$ correlations in the quantum depletion predicted by the Bogoliubov theory of the weakly-interacting, homogeneous Bose gas. We concluded by saying that using an optical lattice would be a solution to efficiently increase the interactions as a means to reach the low temperature regime dominated by the interactions $\mu \gg k_{\text{B}}T$ for which we expect the pair correlation signal to be experimentally detectable. This however requires that we extend the method of the Bogoliubov theory to the case of the lattice gas to identify the condition under which the $\boldsymbol{k}/-\boldsymbol{k}$ pairs should be observable.

2.4.1 Effect of the lattice amplitude

As developed in 1.2.2, the central point of the Bogoliubov approximation for the weakly-interacting homogeneous Bose gas resides in the fact that the interactions are **weak**. This means that the system can be described as a BEC from which only a **small fraction** of

the atoms, the depletion, are removed by the effect of interactions.

For the lattice gas, the condensed atoms correspond to the sharp diffraction peaks of the momentum distribution, while the depleted atoms in high quasi-momentum states correspond to the diffuse background between the diffraction peaks that increases as u and therefore the strength of interactions increases, as illustrated by Fig.-2.12. We thus need to be in the shallow lattice regime to use the Bogoliubov approximation, *i.e* at low values of the lattice depth such as $u \ll u_c$. This corresponds to the superfluid phase where the condensed fraction is close to 1 and the fraction of depleted atoms is small. We will typically use $u = 5 \ll u_c \approx 30$ for the $\boldsymbol{k}/-\boldsymbol{k}$ correlations experiments presented in this manuscript (the value of the fraction of depleted atoms will be discussed in Chapter 4).

2.4.2 Dispersion relation and effective mass

For the remainder of this section, we will assume that we are in the shallow lattice regime so that the Bogoliubov approximation can be used. To begin, we remind the Hamiltonian for weakly interacting atoms without the lattice potential, as first introduced in Chapter 1:

$$\hat{H} = \sum_{\boldsymbol{k}} \frac{\hbar^2 k^2}{2m} \hat{a}^\dagger_{\boldsymbol{k}} \hat{a}_{\boldsymbol{k}} + \frac{g}{2V} \sum_{\boldsymbol{k_1},\boldsymbol{k_2},\boldsymbol{k_3}} \hat{a}^\dagger_{\boldsymbol{k_1}+\boldsymbol{k_3}} \hat{a}^\dagger_{\boldsymbol{k_2}-\boldsymbol{k_3}} \hat{a}_{\boldsymbol{k_1}} \hat{a}_{\boldsymbol{k_2}} \tag{2.46}$$

We now add the lattice potential but still neglect the external harmonic trapping potential and write the new Hamiltonian in the Bloch wave basis. In fact, we have already seen the expression of the non-interacting term in the Bloch wave basis in equation 2.10. As we have done throughout this chapter, we consider that only the lowest energy band $n = 0$ is populated. The full Hamiltonian writes [43]:

$$\hat{H} = \sum_{\boldsymbol{q}} E_0(\boldsymbol{q}) \hat{c}^\dagger_{\boldsymbol{q}} \hat{c}_{\boldsymbol{q}} + \frac{g}{2} \sum_{\boldsymbol{q}_1,\boldsymbol{q}_2,\boldsymbol{q}'_1,\boldsymbol{q}'_2} C\left(\boldsymbol{q}_1, \boldsymbol{q}_2, \boldsymbol{q}'_1, \boldsymbol{q}'_2\right) c^\dagger_{\boldsymbol{q}'_1} c^\dagger_{\boldsymbol{q}'_2} c_{\boldsymbol{q}_2} c_{\boldsymbol{q}_1} \tag{2.47}$$

with $\hat{c}_{\boldsymbol{q}}$ the operator destroying a particle in the Bloch wave $\psi_{0,q}$ and

$$C\left(\boldsymbol{q}_1, \boldsymbol{q}_2, \boldsymbol{q}'_1, \boldsymbol{q}'_2\right) = \int_0^V \psi^*_{0,\boldsymbol{q}'_1}(\boldsymbol{r}) \psi^*_{0,\boldsymbol{q}'_2}(\boldsymbol{r}) \psi_{0,\boldsymbol{q}_1}(\boldsymbol{r}) \psi_{0,\boldsymbol{q}_2}(\boldsymbol{r}) \mathrm{d}\boldsymbol{r} \tag{2.48}$$

The non-interacting term $\sum_{\boldsymbol{q}} E_0(\boldsymbol{q}) \hat{c}^\dagger_{\boldsymbol{q}} \hat{c}_{\boldsymbol{q}}$ is quite similar to its equivalent in the homogeneous case $\sum_{\boldsymbol{k}} \frac{\hbar^2 k^2}{2m} \hat{a}^\dagger_{\boldsymbol{k}} \hat{a}_{\boldsymbol{k}}$. In fact, as we can see on Fig-2.13, the function $E_0(\boldsymbol{q})$ can be well approximated by a parabolic function at low values of q. We then rewrite $E_0(\boldsymbol{q})$ as:

$$E_0(\boldsymbol{q}) \approx \frac{\hbar^2 q^2}{2m^*}, \text{ with } \frac{1}{m^*} = \frac{1}{\hbar^2} \frac{\mathrm{d}^2 E_0}{\mathrm{d}q^2} \tag{2.49}$$

where we have introduced the notion of effective mass m^* defined from the curvature of the Bloch energy band, actually very useful to study the dynamics of particles in a lattice

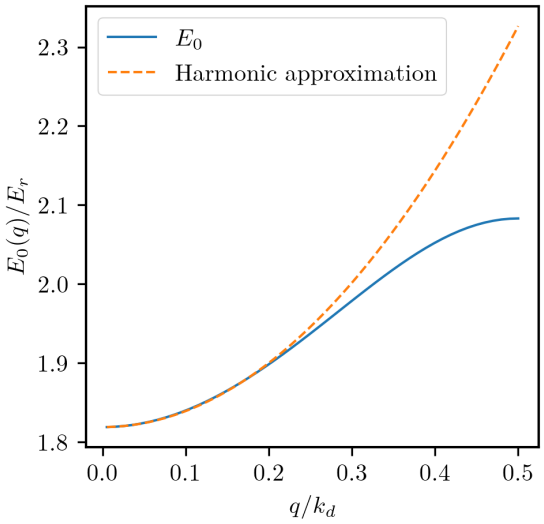

Figure 2.13: Harmonic approximation of the dispersion relation of the first energy band E_0 for $s = 5$.

potential [43, 98]. Under this form, the non-interacting term of the lattice Hamiltonian is then of the exact same form as for the homogeneous Hamiltonian, the effect of the lattice being contained in the new effective mass m^*.

In the case of non-homogeneous harmonically trapped system, the trapping frequency ω is replaced by the effective trapping frequency ω^* as well to account for the effect of the lattice. The effective frequency is defined from the effective mass by [98]:

$$\omega^* = \sqrt{\frac{m}{m^*}}\omega \tag{2.50}$$

2.4.3 The rescaled interaction strength

We turn to calculating the interaction term in equation 2.47. First, like in the homogeneous case, the conservation of momentum gives the relation:

$$\boldsymbol{q_1} + \boldsymbol{q_2} = \boldsymbol{q}'_1 + \boldsymbol{q}'_2 \tag{2.51}$$

allowing us to reduce the sum on $\boldsymbol{q}_1, \boldsymbol{q}_2, \boldsymbol{q}'_1, \boldsymbol{q}'_2$ to a sum on three quasi-momenta $\boldsymbol{q}_1, \boldsymbol{q}_2$ and $\boldsymbol{q}_3$. Using the Bloch function form $\psi_{n,q}(x) = e^{iqx}u_{n,q}(x)$ and assuming that only the states at the bottom of the band are populated, we can finally approximate the Hamiltonian 2.47 to [43]:

$$\hat{H} \approx \sum_q \frac{\hbar^2 q^2}{2m^*}\hat{c}^\dagger_q \hat{c}_q + \frac{g'}{2V}\sum_{\boldsymbol{q_1},\boldsymbol{q_2},\boldsymbol{q_3}} \hat{c}^\dagger_{\boldsymbol{q_1}+\boldsymbol{q_3}}\hat{c}^\dagger_{\boldsymbol{q_2}-\boldsymbol{q_3}}\hat{c}_{\boldsymbol{q_1}}\hat{c}_{\boldsymbol{q_2}} \tag{2.52}$$

with g' the rescaled interaction strength defined as:

$$g' = g\left(d\int_0^d |w_{0,0}(x)|^4 \mathrm{d}x\right)^3 \tag{2.53}$$

that rewrites as:

$$g' = g\left(\frac{\sqrt{\pi/2}s^{1/4}}{\mathrm{Erf}\left[\pi s^{1/4}/2\right]}\right)^3 \tag{2.54}$$

As long as $V_0 > 0$, we have $g' > g$ signaling that the lattice indeed increases the strength of the interactions. Importantly, g' increases with V_0 as the atoms become increasingly localized in smaller region of spaces, increasing the strength of the interactions.

In conclusion, we obtain an Hamiltonian of the same form than the homogeneous case, with two notable differences:

- We have replaced the mass m by the effective mass m^* in the dispersion relation.
- The interaction strength g has been replaced by the rescaled and higher interaction strength g'.

We have then achieved the objective set at the beginning of this chapter, namely obtain a system with $\boldsymbol{k}/-\boldsymbol{k}$ paired quantum depleted atoms as described by the Bogoliubov theory of the weakly-interacting Bose gas, but with increased interactions so that we should be able to reach the low temperature regime dominated by interactions $k_\mathrm{B}T \ll \mu$ for which the $\boldsymbol{k}/-\boldsymbol{k}$ correlation signal should be detectable.

Importantly, the predictions of the Bogoliubov theory detailled in Chapter 1 should not be taken at face value for the much more complicated system of the inhomogeneous lattice gas. In fact, there are no clear experimental studies testing the validity of the Bogoliubov approach for this kind of system. It will then be of great interest to compare the predictions of the simple homogeneous case to the experimental data as a means to detect whether the Bogoliubov approach fails or not and under which conditions.

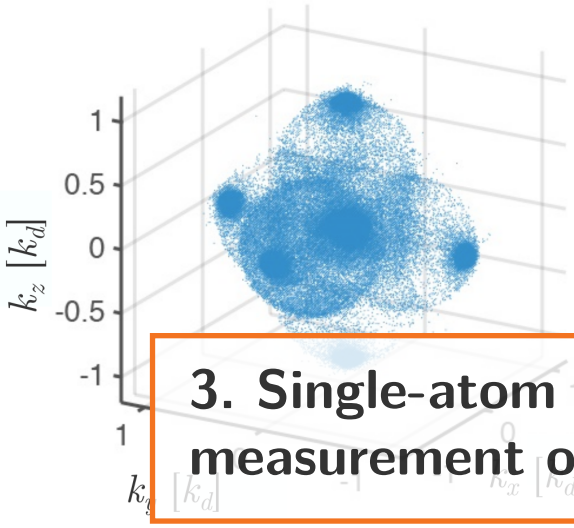

Chapter 3

3. Single-atom resolved momentum measurement of lattice Bose gas

The first chapters of this thesis have laid out the motivations to study the momentum-space correlations between individual particles in ultracold lattice gases. To do so, we need an experimental apparatus capable of measuring the momentum of **single atoms** in 3D. As mentioned in the introduction, while it is possible to use single atom resolved optical imaging techniques [19, 140], they are inherently limited to study systems with small number of atoms. To overcome these limitations, we will exploit the fascinating properties of **metastable Helium** for which a special electronic detection technique can be implemented.

This chapter will be dedicated to the description of all the experimental aspects required to obtain the in-trap momentum distribution of an ultracold lattice Bose gas of metastable Helium. First, we will describe the experimental apparatus and the sequence used to reach quantum degeneracy before explaining how the detection part of the experiment works. In a second stage, we will show how we are able to adiabatically prepare an equilibrium state of the Bose-Hubbard Hamiltonian and experimentally study interaction effects happening during the TOF to validate the hypotheses presented in the section 2.3 of the previous chapter.

3.1 Helium in optical lattices

3.1.1 Metastable Helium

Metastable Helium, noted He*, is kind of an odd atom in the ensemble of species that we know how to bring to quantum degeneracy. Its most important feature, which is actually the reason why we chose this atom to measure correlation functions in momentum-space, is the existence of the metastable state $2\,^3S_1$. This excited state is called metastable for its very long lifetime of the order of 8×10^3 s, far larger than what is required for experiments. Very interestingly, as Helium is a noble gas, the amount of energy required to excite Helium into its metastable state is quite large, 19.8 eV. This large energy is sufficient for a metastable Helium atom to extract an electron from a metallic surface. This opens

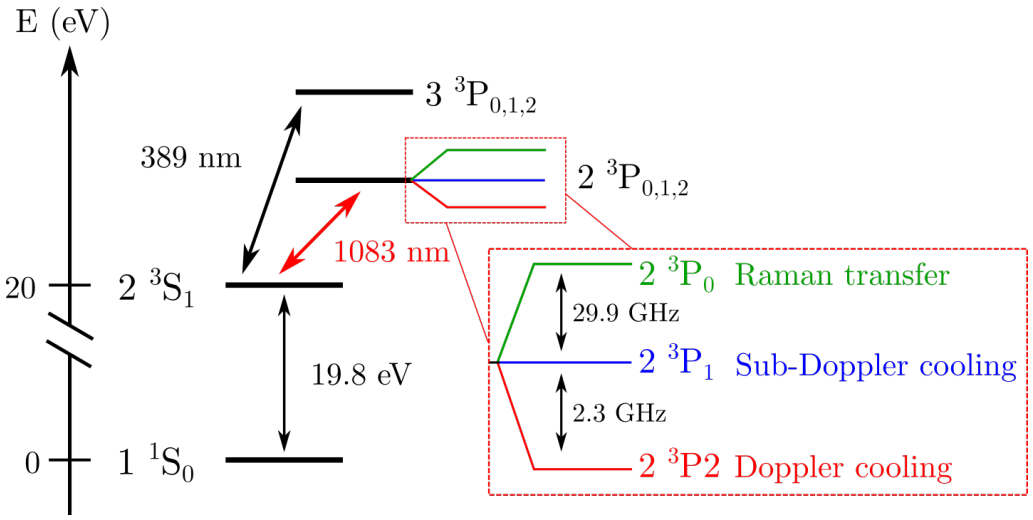

Figure 3.1: Energy levels of the Helium atom. The metastable state is the triplet state $2\ ^3S_1$ that we will call the ground state of the metastable Helium atom. Laser cooling is performed on the optical transition $2\ ^3S_1 \rightarrow 2\ ^3P$ of wavelength $\lambda_0 \simeq 1083$ nm. More specifically, we address the transition to $2\ ^3P_2$ or $2\ ^3P_1$ depending on the cooling scheme (respectively Doppler and sub-Doppler), as well as the transition to $2\ ^3P_0$ to perform two-photon Raman transfer as we will detail later on.

the way for **electronic detection** techniques that allows for **single-atom detection** as we will see in this chapter. In addition, the energy levels structure (see Fig.-3.1) is well adapted to laser cooling with a transition in the near-infrared around $\lambda_0 \simeq 1083$ nm for which reliable laser sources are available. Metastable Helium was actually amongst the first atoms to be brought to quantum degeneracy with the first BEC of He* being obtained in 2001 simultaneously at the Institut d'Optique [133] and Laboratoire Kastler Brossel [49] in France. Helium also has the advantage to have a stable, albeit very rare and expensive fermionic isotope ^{3}He* that has also been brought to quantum degeneracy at the Amsterdam LaserLab in 2006 [111].

In spite of all these advantages, He* comes with a few experimental difficulties that explain why they are actually quite few He* experiments over the world. Firstly, Helium is a very light atom and this comes with some very practical difficulties like the need to pre-cool the atomic source with liquid nitrogen and quite long Zeeman slowers. Secondly, He* is subject to Penning collisions that bring back an atom to the ground state to ionize the other [50]:

$$\mathrm{He}^* + \mathrm{He}^* \rightarrow \mathrm{He} + \mathrm{He}^+ + \mathrm{e}^- \tag{3.1}$$

Such a reaction thus results in the loss of two atoms and must be avoided. The probability for a Penning collision to occur is increased in presence of light [8] but is however greatly reduced when the atomic gas is polarized in the same spin state [57]. This two considerations add additional constraints to the design of the cooling sequence.

In the following, we will detail the different experimental steps used to bring a gas of metastable Helium to quantum degeneracy.

3.1.2 The source

To begin the experimental sequence, we first need to excite Helium atoms in the metastable state. As the energy difference between the ground-state and the metastable state is very large, it is impossible to excite the atoms optically. We therefore rather do it through a plasma discharge. The setup is illustrated on Fig.-3.2. The plasma forms between a metallic needle connected to a high voltage power supply ($\sim$ 2.8 kV) and the grounded skimmer. The needle is held in a glass tube that is glued to a **Boron-Nitride (BN)** piece in which a small hole is pierced for atoms to flow through. The piece is inserted into a larger copper piece cryogenically cooled with liquid nitrogen. The role of the Boron-Nitride piece is twofold. First, the good thermal properties of the Boron-Nitride allow the piece to be cooled via the contact with the copper piece, cooling down in turn the atoms. This is necessary to preliminary reduce the speed of the atoms before laser cooling as we will discuss in the next paragraph. Second, the piece isolates the high voltage needle from the grounded copper to avoid plasma formation in unwanted places.

The source is a quite sensitive part of the experimental apparatus and was often subject to problems during the span of this thesis. Here are a few things that we learned through the different repairs that need to be checked when troubleshooting the source:

- The needle has the tendency to deteriorate over time. When this happens, some metallic particles fall from the needle and end up clogging the small hole in Boron-Nitride, preventing the atoms to flow through. We replaced the needle with a standard metallic cylinder, hoping that it would not deteriorate as fast. While we still could form the plasma without the needle shape, the cylinder still deteriorates, requiring regular operations every few months to unclog the Boron-Nitride piece.
- The diameter of the Boron-Nitride piece needs to be very well adapted to the inner diameter of the copper piece to ensure a good thermal contact and to prevent the Boron-Nitride from moving when temperature changes. This also helps to stabilize the current of the power supply to $\sim$ 11 mA at which the plasma is much more stable.
- The glue holding the glass tube in the Boron-Nitride can contract at low temperatures and add mechanical constraints on the glass tube, sometimes breaking it and causing unwanted atom leakage. The solution is to use an "elastic" glue that can deform when temperature changes without adding too much stress on the tube.

We now move on the next experimental step, laser cooling.

3.1.3 Laser cooling

Our experimental cooling sequence uses two types of laser cooling: Doppler and sub-Doppler cooling. Doppler cooling revolves around the absorption of resonant, counter-propagating photons by a two-level atom, reducing its momentum. The absorbed photons are re-emitted spontaneously in a random direction of space, meaning that after a large number of absorption/emission cycles, the variation of momentum induced by spontaneous emission averages out. The only contribution is thus the one of absorption contributing to slow the atom down. The name Doppler cooling descends from the fact that the detuning δ of the laser beam is set to compensate the Doppler effect $\delta = \boldsymbol{k}\cdot\boldsymbol{v}$, with $\boldsymbol{k}$ the momentum of the laser photons and $\boldsymbol{v}$ the speed of the atoms. This has the advantage that the atoms

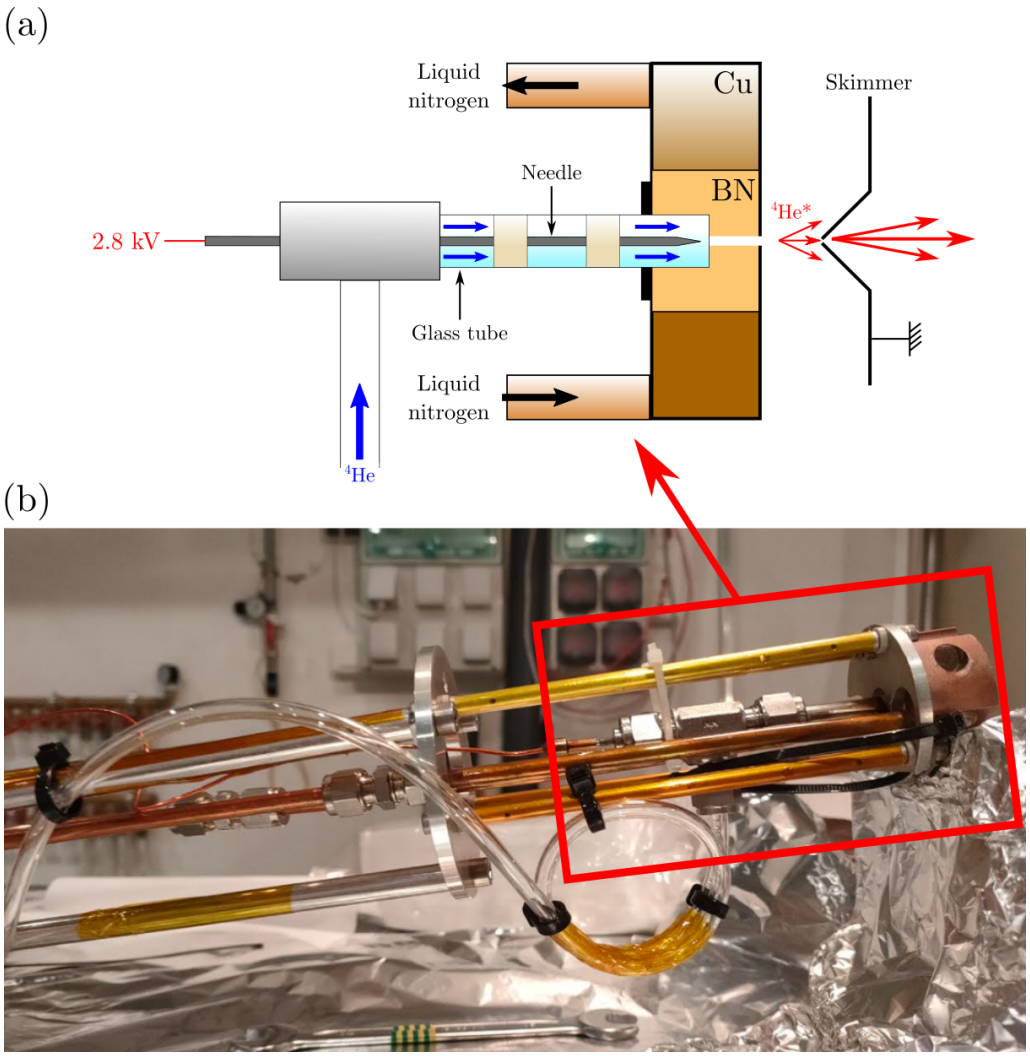

Figure 3.2: Metastable helium source. (a) Drawing of the source apparatus. Helium atoms (blue arrows) are sent into a glass tube glued into a pierced boron-nitride (BN) piece. A plasma forms between the high voltage needle and the grounded skimmer, exciting the atoms in the metastable state (red arrows). The boron nitride is cooled by thermal contact with a copper (Cu) piece in which liquid nitrogen flows, allowing to significantly reduce the speed of the atoms. (b) Photograph of the source apparatus. The red square illustrates what is represented on the drawing.

that have already been cooled cannot resonantly absorb photons anymore, preventing them from being re-heated. The lowest temperature accessible with Doppler cooling T_{D} is set by the number of absorption/emission cycles per unit of time, *i.e* by the linewidth of the excited state Γ [32]:

$$T_{\mathrm{D}} = \frac{\hbar\Gamma}{2k_B} \tag{3.2}$$

On the other hand, sub-Doppler cooling designs a variety of cooling techniques revolving around multi-level atomic structures. These techniques allow to reach lower temperatures than Doppler cooling, at the expense of small velocity captures, nevertheless attainable with prior Doppler cooling.

As shown on Fig.-3.1, we use the $2\ ^3S_1 \rightarrow 2\ ^3P_2$ transition for Doppler cooling. The state $2\ ^3S_1$ has three sub-states $m_J = \{-1, 0, +1\}$ whereas the state $2\ ^3P_2$ has 5 $m_J = \{-2, -1, 0, +1, +2\}$. By using circularly polarised light allowing transitions that increase or decrease m_J by 1, the transition between these two-states can be equated to an effective two-level transition after a few cycles of absorption/emission, making it well suited for Doppler cooling. For sub-Doppler cooling, we use the transition $2\ ^3S_1 \rightarrow 2\ ^3P_1$ where the excited state also has three sub-states, implementing an effective 3-level lambda structure with circularly polarized light as the transition between the sub-states with $m_J = 0$ is a forbidden one. The natural line-width of the $2\ ^3P$ state is $\Gamma = 2\pi \times 1.6$ MHz.

We will not explain here all the details of how laser cooling works, but rather briefly show the main cooling steps of the experimental sequence and give typical experimental numbers. For further details, we refer the reader to previous theses [15, 28, 87].

Zeeman slower

As in many cold atoms experiments, the cooling sequence starts with a Zeeman slower. The general idea is to exploit the Zeeman effect with a variating magnetic field to compensate the Doppler shift that reduces as the atoms get slower. This procedure allows to reduce the speed of the atoms of several order of magnitudes, from roughly $1,200$ m/s when they exit the source to 50 m/s, a speed at which they can be captured in a Magneto-Optical Trap. Note that as Helium is very light, our Zeeman slower is quite long compared to other cold atom experiments with a length of ~ 2.5 m. This also explains the need for liquid nitrogen cooling of the source, without which we would need an absurdly long Zeeman slower.

Magneto-Optical Trap

While reducing the speed of the atoms is necessary to reach quantum degeneracy, it is also necessary to spatially trap the atoms and increase their density. This is achieved by adding a quadrupole magnetic field in order to exploit the Zeeman effect combined to laser cooling. This is the idea behind the **Magneto-Optical Trap** (MOT), the cornerstone of every cold atom experiment. A MOT is made of 3 pairs of counter-propagating red-detuned laser beams, one for each direction of space, on which we add a quadrupole magnetic field. In our case, the magnetic field is produced by two coils centered on the x-axis in anti-Helmoltz configuration. The current is 16 A, resulting in a gradient of 25 G/cm at

the center of trap.

To load the MOT, we use an intensity of roughly $15\ I_{\text{sat}}$ per beam and a large detuning $\delta = -60$ MHz. This serves two purposes: it ensures a large capture velocity, making the loading of the trap efficient, and also keeps the level of light-assisted Penning losses low. We load typically $N \simeq 2 \times 10^9$ atoms in ~ 1.5 s. In a second stage, we compress the gas to increase the atomic density by reducing the detuning to $\delta = -12$ MHz. To avoid major light-assisted Penning losses, we conjointly reduce the total intensity from $90\ I_{\text{sat}}$ to $0.7\ I_{\text{sat}}$. This compressed-MOT phase increases the density by a factor ~ 10.

At the end of the MOT phase, we obtain a gas of $N \simeq 2 \times 10^9$ atoms at $T = 1.2$ mK of density $n = 6.3 \times 10^9$ cm^{-3}.

Red molasses

The magnetic field is then switched off to go back to regular Doppler cooling. To further cool the atoms, the detuning is significantly reduced to $\delta = -1.5$ MHz (approaching the Doppler limit), while the total intensity is reduced to $0.33\ I_{\text{sat}}$ to keep the rate of Penning losses low. The goal is not to reach the lowest possible temperature, but rather to reach a temperature inferior to that of the velocity capture of sub-Doppler cooling effects. After 5 ms of red molasses, we reach $T \simeq 100\ \mu$K with $N \simeq 1.8 \times 10^9$ atoms.

Grey molasses

Grey molasses are a sub-Doppler cooling scheme [40] that works in our case with 3 pairs of $\sigma_+ - \sigma_-$ polarized counter-propagating beams on the $2\ ^3S_1 \rightarrow 2\ ^3P_1$ transition, giving a lambda configuration with two ground states $|g_1\rangle$ and $|g_2\rangle$ and one excited state $|e\rangle$. Through a change of a basis, it is possible to describe the system as a **dark state**, written as a superposition of $|g_1\rangle$ and $|g_2\rangle$ that does not interact with the light, and bright state. The name "grey" molasses comes from the mix between this two kinds of states. Because of the interferences between the counter-propagating beams, the light shift of the bright state is modulated. If the atoms are moving, a motional coupling allows for atoms in the dark state to be transferred into the bright state. For positive detunings, the light shift is positive and increases with the light intensity so that the bright and the dark state are closer at the bottom of the potential "hill" seen be the bright state. This means that an atom in the dark state can be transferred into the bright state at the bottom of the hill, climb it to convert its kinetic energy into potential energy that is then dissipated when the atom is pumped back into the dark state at the top of the hill, effectively cooling the atom (see Fig.-3.3). The atom then goes through the same cycle, just like Sisyphus who was condemned to relentlessly push his rock to the top of a mountain in the ancient Greece mythology, hence the name Sisyphus cooling. Interestingly, it is possible for the atom to be trapped indefinitely in the dark state and stop interacting with light if its speed is low enough. This effect is called velocity-selective coherent population trapping [5].

The grey molasses stage is implemented with blue detuned $\delta = 8$ MHz beams with a total power of $28\ I_{\text{sat}}$. This stage lasts 5 ms after which we obtain $N \simeq 1.7 \times 10^9$ atoms

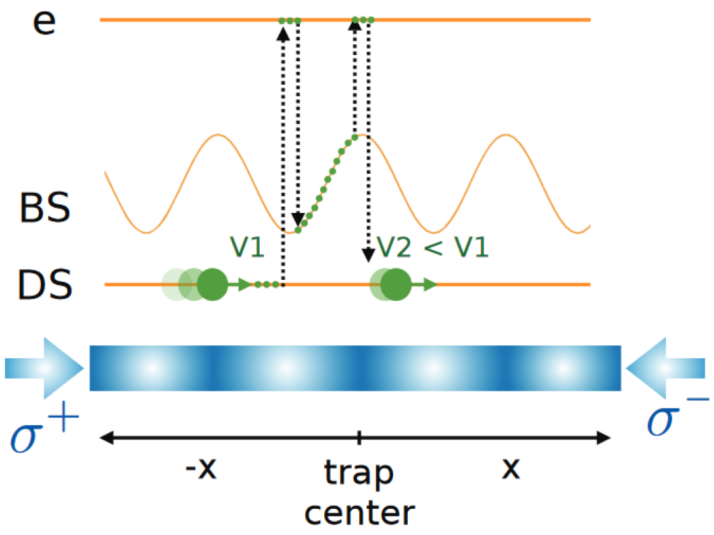

Figure 3.3: Principle of the grey molasses in 1D. The energy of the bright state is modulated because of the interference of the two counter-propagating beams. An atom in the dark state (DS) can couple to the bright state (BS) near the bottom of the potential hill that it will then climb, losing kinetic energy, before being put back in the dark state at the top the hill, resulting in a loss of energy. Taken from [28].

at $T \simeq 15\ \mu K$. While this temperature is already quite low, the cooling steps we have described so far are not enough to reach the kinds of temperatures and densities required to reach quantum degeneracy. Indeed, at this point, we only have $\lambda_{\mathrm{dB}}^3 n = 3.0 \times 10^{-4}$. We thus need another non-optical cooling technique for the last steps of the experiment.

3.1.4 Evaporative cooling

Evaporative cooling was derived from the simple idea that if one is able to selectively remove the more energetic particles of an ensemble, the remaining ones will thermalize at a lower temperature (assuming that the collision rate is large enough to ensure thermalization). This is exactly what we do when we blow on a cup of coffee, removing the more energetic coffee molecules vaporized above the surface to cool down the entire cup of coffee. Evaporative cooling therefore requires to find a way to remove only the more energetic atoms while ensuring that the collision rate amongst the remaining atoms is high enough for a proper thermalization.

There are two main ways to implement evaporative cooling depending on the kind of trap from which we will remove the atoms. The historical one is called **radio-frequency (RF) evaporation** [50, 94, 133] and is performed with magnetic traps. Let us illustrate it with the example of atoms with 3 magnetic sub-states, $m_J = \{-1, 0, 1\}$. If we put these atoms inside a quadrupole magnetic field forming a magnetic gradient, we find that one of the sub-states is trapped, let us say $m_J = 1$, the sub-state $m_J = 0$ does not interact with the magnetic field and is therefore not trapped, just like the sub-state $m_J = -1$ which is anti-trapped. Because of the Zeeman effect, the energy difference between the different sub-states depends on the value of the magnetic field and therefore on the position of the atoms in the trap. The hottest atoms are the ones with the larger kinetic energy and that

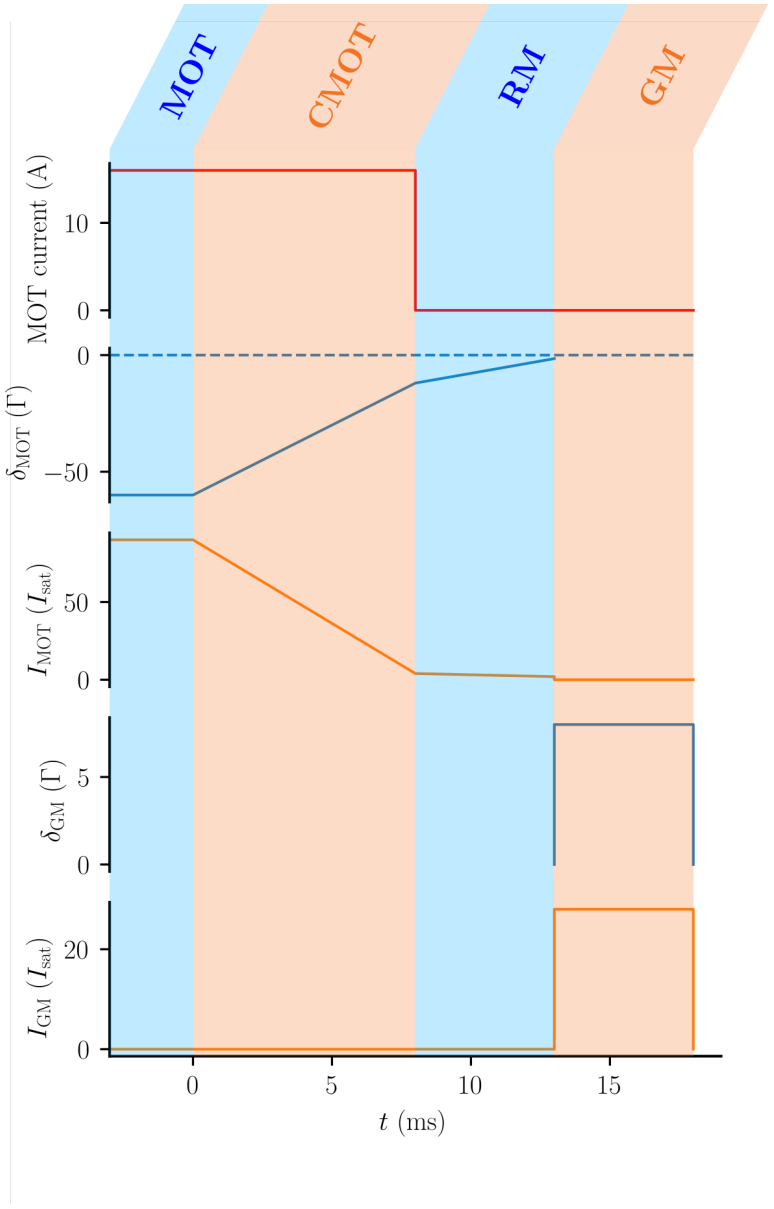

Figure 3.4: Laser cooling sequence. The time $t = 0$ corresponds to the beginning of the compressed MOT step, preceded by the MOT step that lasts 1.5 s. The initials RM and GM corresponds to Red Molasses and Grey Molasses respectively. Current values are represented in red, light frequencies in blue and light intensities in orange. Note that the values of I_{MOT} have been slightly modified for visibility purpose.

therefore reach positions farther away from the center of the trap. The idea is then to use a radio-frequency wave to drive the transition between the trapped and non-trapped sub-states and carefully choose its frequency so that the process is resonant only for the regions farther from the center of the trap, effectively removing the more energetic atoms. The frequency of the RF wave is then progressively reduced to be more and more selective on the energy for which atoms are removed, thus progressively cooling down the gas. An important point is that the frequency must be ramped down slow enough for the gas to have enough time to thermalize. The duration of RF evaporation is thus inherently limited by the collisions properties of the gas, and therefore its density.

The second way to implement evaporative cooling is **optical evaporation** used in optical traps. With high intensity, far-detuned laser beams, the electric field is strong enough to induce a dipole moment in the atom, causing them to be attracted to the maximum intensity of the field (for red-detuned light), effectively trapping them. The depth of the trap is then set by the intensity of the laser light [79]. In this case, evaporation is quite simple: decreasing the intensity decreases the depth of the trap, allowing atoms with a high kinetic energy to escape the trap. Evaporation is then performed by ramping down the intensity of the laser light. Interestingly, optical traps allow to reach higher trapping frequencies than magnetic trap, resulting in higher densities and thus better collision rates, meaning that evaporation can be done much faster. However, one significant disadvantage of optical evaporation that must be considered is that the collision rate decreases as the evaporation progresses since the trapping frequencies decrease with decreasing laser light intensity. This is not the case for RF evaporation as the trapping frequencies remain constant and the density increases as the gas gets colder, thus ensuring at all times a proper thermalization of the cloud.

For our experimental purpose, we need to devise what kind of trap to use. An optical trap would first seem to be the obvious answer as evaporation can be done way quicker, reducing the experimental cycle time and thus making data taking more efficient. This solution is actually used to bring different atomic species to quantum degeneracy such as Rubidium [9], Potassium [137] or Sodium [88]. An all-optical scheme is however very hard to implement for He^* mainly because of Penning collisions. Indeed, during laser cooling, the gas is unpolarized meaning that the inelastic collisions limit the accessible range of density to values too low to ensure proper loading of an optical trap. We thus opted for an hybrid configuration where the atoms are first loaded in a magnetic quadrupole trap, thus polarizing the gas and reducing the Penning collision rate by several orders of magnitude [143]. A first evaporation stage is then performed up to temperatures and densities for which the gas can be efficiently loaded in a optical trap in which we perform a final evaporation stage to reach Bose-Einstein condensation.

Magnetic trap

Before loading, the atomic gas is optically pumped into the trapped state $m_J = 1$. To do so, we create a bias field oriented along the z-axis to set the quantification axis and shine σ_+ resonant polarized light unto the atoms for 700 μs. We then create a magnetic quadrupole field with the same coils used for the MOT to produce an initial gradient of ~ 5 G/cm and load $N \simeq 1.7 \times 10^9$ atoms into the trap. As the Penning collision rate is highly reduced for a spin-polarized gas, we safely go to higher densities by compressing the trap, increasing the gradient to ~ 35 G/cm. The evaporative cooling is performed

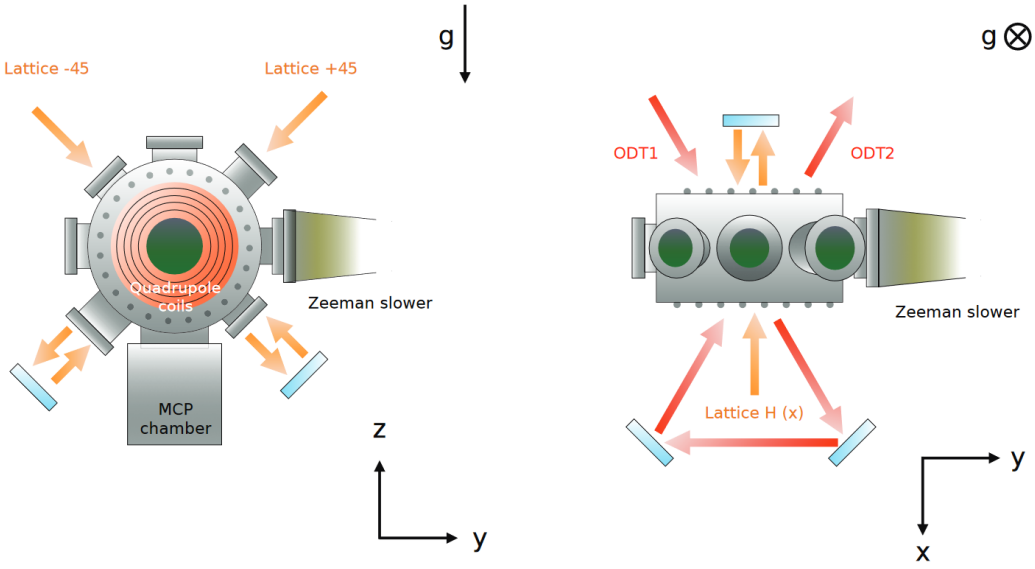

Figure 3.5: Orientation of the ODT and lattice beams in the experiment. Taken from [28].

in 3 s by ramping down the frequency of a RF wave from 40 MHz to 6 MHz, reducing the number of atoms to a typical $N = 120 \times 10^6$. The final temperature is $T \simeq 70\mu K$ and the final density $n = 6.6 \times 10^{11}$ cm^{-3}. Note that while this temperature is higher than what we had at the end of laser cooling as the gas is heated up when loaded in the magnetic trap, we have significantly increased the density to properly load the optical trap. After this first evaporation stage, we obtain $n\lambda_{\mathrm{dB}}^3 = 7.5 \times 10^{-4}$.

Crossed Optical Dipole trap

The Optical Dipole Trap (ODT) is made with two crossing far-detuned 1550nm laser beams whose intensity is stabilized with PID locking. We label these two beams ODT1 and ODT2, the second beam being obtained from the first one in a butterfly-like shape (see Fig.-3.5). Their respective waists are 133 μm and 63 μm and the maximum power for ODT1 is 18 W on the atoms. The ODT is loaded by ramping up the laser power while ramping down the current in the quadrupole coils. The overlap between the two traps is finely adjusted thanks to magnetic biases fields. As the ODT is very narrow, we typically only load $N \simeq 8 \times 10^6$ but reduce the temperature by a factor 2 while increasing the density by two orders of magnitude. The final evaporation stage is done by exponentially ramping down the laser power in 600 ms. We adapt the final laser power to chose the number of atoms in the BEC, from a few thousands to roughly $N \simeq 10^6$ at maximum. The trapping frequencies depend from the chosen final power with typical values $(\omega_x, \omega_y, \omega_z)/2\pi = (81, 352, 320)$ Hz for $N_{\mathrm{bec}} \simeq 6 \times 10^5$ and $(\omega_x, \omega_y, \omega_z)/2\pi = (41, 173, 180)$ Hz for $N_{\mathrm{bec}} \simeq 5 \times 10^3$ as we wish to use for the $\boldsymbol{k}/-\boldsymbol{k}$ correlations measurements.

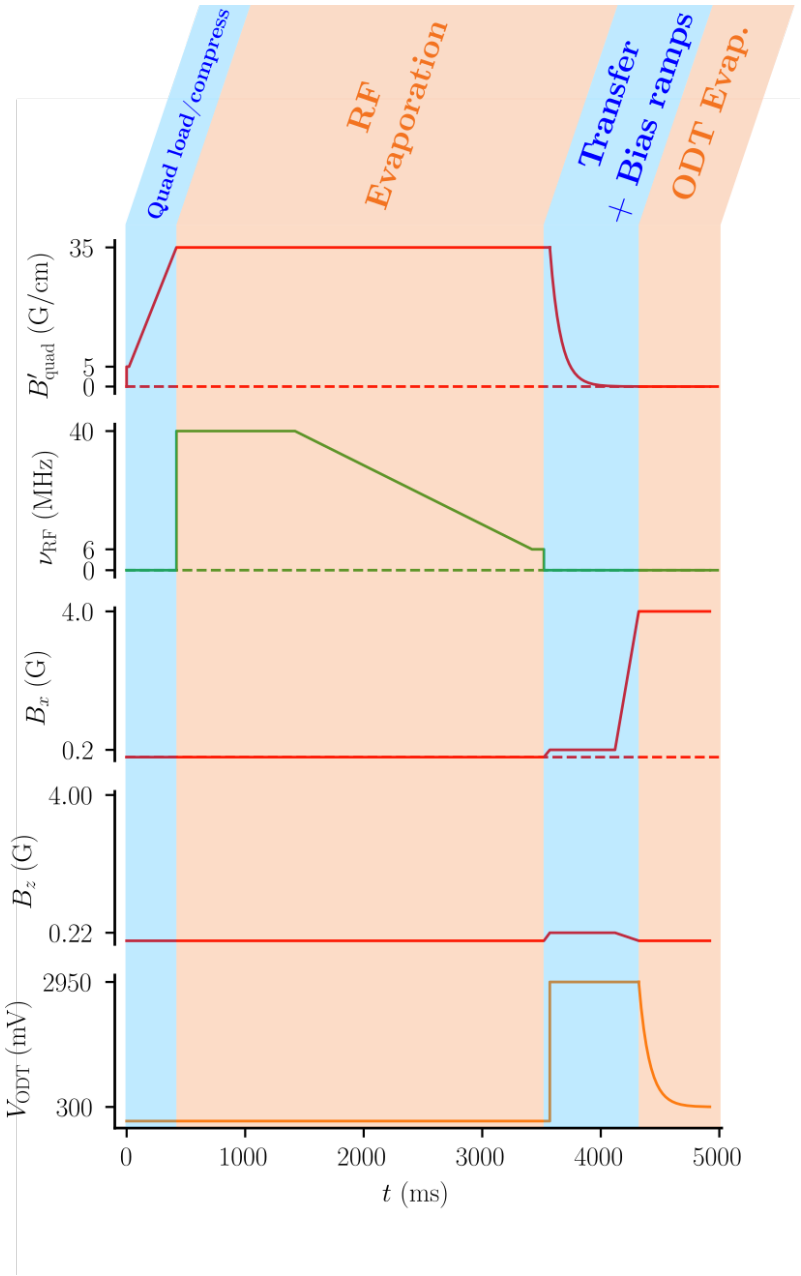

Figure 3.6: Condensation sequence. The red lines correspond to magnetic fields, *i.e* the quadrupole trap gradient and the x and z biases (no bias along y is used), the green line to the frequency of the RF wave used to peform the evaporation and the orange line to the ODT power, here expressed in terms of photodiode voltage V_{ODT}.

3.1.5 Optical imaging

While the specificity of our experiment is its electronic detection technique, we also use more usual optical imaging techniques that are way more convenient to observe and characterize the gas at the different steps of the experimental sequence.

Fluorescence imaging

The first kind of optical imaging technique that we use is fluorescence imaging. After a time of flight of a few milliseconds, we shine for 100 μs with the MOT beams resonant light on the atoms that absorbs the photons and re-emits them spontaneously in all directions of space. These photons can be detected with an InGaAs camera located on top of the science chamber with its optical axis oriented along the vertical z direction. Fluorescence imaging is mainly used to characterize all steps prior to the loading in the optical trap after which the gas becomes too small for the resolution of the imaging system.

Absorption imaging

To image the atoms in the ODT or the BEC itself, we use absorption imaging. We shine a probe beam of weak intensity on resonance with the $2\ ^3S_1 \rightarrow 2\ ^3P_2$ transition unto the atomic cloud and observe its "shadow" with a second InGaAs camera. The intensity of the detected light depends directly on the quantity of light absorbed by the atoms and therefore the density of the cloud. The camera is located on the side of the science chamber and its optical axis forms a small angle with the horizontal direction.

While the resolution of the camera of 12 μm in the image plane is not suited to make in-situ images, the BEC can be properly observed after a small time-of-flight of a few milliseconds. Interestingly, we can obtain from the absorption images the number of atoms in the BEC N_{bec} by measuring the Thomas-Fermi radius of the gas after a small TOF [15].

3.1.6 3D optical lattice

We now pursue the description of our experimental apparatus with one of the key ingredients of the physics we study, the 3D optical lattice. Its main characteristics are:

- The 3D lattice is made from a single narrow linewidth laser capable of delivering up to 15 W. Its wavelength is 1550 nm, *i.e* far from any atomic resonance just as for the Optical Dipole Trap, so that the atoms are trapped at the maximum values of intensity.
- The main beam is divided into 3 independent beams, one for each direction of space, that are sent on the science chamber to make the optical lattice as illustrated on Fig.-3.5. One of the beam is horizontal (named H) and perpendicular to the axis defined by the Zeeman slower, while the other two form a $\pm 45°$ angle with the horizontal direction, hence their name, +45 and -45. The waists of the beams are $(141, 151, 155)$ μm.
- Each beam is retro-reflected to create the interferences necessary for the lattice pattern, but detuned by 20 MHz from the other directions so they do not interfere with one another.

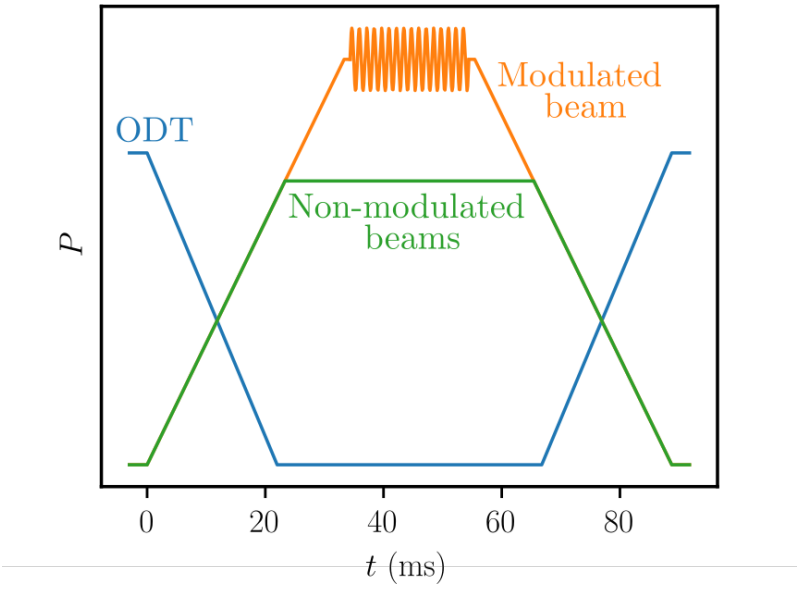

Figure 3.7: Calibration sequence of the lattice depth. The atoms are loaded in the lattice by ramping down the ODT power (blue) and ramping up the lattice power (orange and green). The beam to calibrate is then modulated while the power of the two other beams is set to be 30% smaller to avoid excitations in directions different from the one that is being calibrated. Finally, the atoms are loaded back in the ODT to measure the number of remaining atoms with absorption imaging.

- In this configuration, the lattice spacing d, *i.e* the distance between two lattice sites is $d = \lambda/2 = 775$ nm.
- A fraction of the power of each beam is sent on a photodiode whose signal is used for the feedback loop of a PID controller used to lock the power on the desired value.
- Because of the Gaussian shape of the beam, the atoms feel the same external trapping frequency $\omega_{\text{trap}} = 2\pi \times 140 \times \sqrt{s}\ \text{s}^{-1}$ in the three directions of space, with s the lattice depth in units of recoil energy (see 2.1).

3.1.7 Calibration of the lattice depth

As we have seen in Chapter 2, the depth of the lattice potential and hence the ratio U/J is a crucial parameter that determines the phase of the lattice gas. It is then necessary to precisely calibrate this value prior to any experiment. The idea of the calibration is to associate a given value of the lattice depth s to a command voltage for the PID controller. As the power of each of the three beams are independent, the calibration must be done for each of the three beams alike.

To do so, we modulate the amplitude of one of the lattice beam at frequency f_{mod} for a duration $t_{\text{mod}} = 20$ ms, adding two sidebands in the lattice light spectrum $f \pm f_{\text{mod}}$. When $2f_{\text{mod}}$ is close to the resonance frequency $f_{\text{res}} = (E_2(q=0) - E_0(q=0))/\hbar$, it is possible to excite the atoms from the lowest energy band to the second excited band with a resonant two-photon process. As f_{res} is dependent from the lattice depth, the idea is to

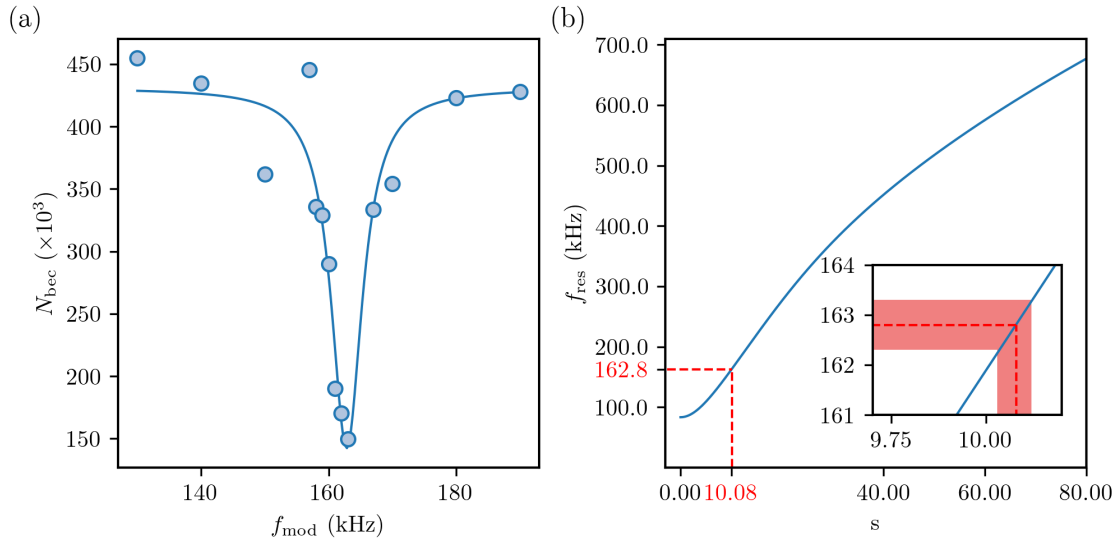

Figure 3.8: Calibration of the lattice depth. (a) Variation of the atom number after the calibration procedure as a function of the modulation frequency f_{mod}. A clear resonance of frequency $f_{\text{res}} = 162.8(5)$ kHz is observed. (b) Plot of the resonance frequency f_{res} as a function of the lattice depth s. The red dashed lines illustrates how the lattice depth $s = 10.08(5)$ is obtained from the measurement of f_{res} on the left panel. The inset shows a zoom on the region of interest with the red shaded area representing how the uncertainty on f_{res} translates to s.

scan the value of f_{mod} to find the resonance frequency from which we deduce the value of the lattice depth. If the amplitude of the lattice at which we perform the calibration is not too high (we use $s = 10$ in practice), atoms in the second excited band are not trapped and therefore lost. When we are perfectly at resonance, most atoms should then be lost, an effect that we can observe via absorption imaging. To make things more convenient, we load back the atoms into the ODT (see Fig.-3.7) before taking the absorption image to avoid the diffraction induced by the lattice beams and properly count the atoms. We therefore measure the number of remaining atoms in the BEC after this procedure as a function of f_{mod} and fit the data to find the minimum and so f_{res} as illustrated on Fig.-3.8. By calculating the energy bands, we obtain the relation between the lattice depth and the value of f_{res} that allows us to finally obtain the value of the lattice depth. We repeat this procedure for each lattice beams, where the power of the two non-modulated beams are lowered by 30% so that the cloud is not excited in the other directions.

3.2 Metastable Helium detection

Contrary to most cold atoms experiments that rely exclusively on optical detection techniques, our experiment revolves around a **single-atom resolved electronic** detection technique of which we will present the main features in this section. For a more thorough and technical description of the He* detector, we refer the reader to the manuscript of Hugo Cayla [28].

3.2.1 Micro-Channel Plates

The first main element of the He* detector is the **Micro-Channel Plate** (MCP). A Micro-Channel Plate is essentially a piece of metal in which an array of small holes, the micro channels, has been drilled. If a particle falls into one of the channels and hits its walls, it can extract one electron from the metal provided that the particle is energetic enough (work function of the metal $\sim$ a few eV) [81]. While MCPs cannot be used in most cold atoms experiment as the atoms are not energetic enough to extract this first electron, they are suited to detect He* thanks to the high energy of the metastable state $\simeq 19.8$ eV. An electric field is applied so that the electron is accelerated downwards and subsequently hits the walls of the channel to extract additional electrons, that will also extract more electrons and so on, just like an avalanche process. The MCP then works to amplify the initial discharge into a shower of a large number of electrons that can be properly detected.

Practically speaking, we use two MCPs in a z-stack configuration forming a herringbone pattern (see Fig.-3.9) to ensure the continuity of the electron shower [86]. They are polarized with a voltage of 2.4 kV. Using two plates is necessary to obtain a high enough amplification factor of 10^4. The channels are drilled with a 20° degree angle from the surface of the MCP in order to avoid that the atoms fall right through the channels without hitting the walls. Another important characteristics of the MCP is the **open-to-air ratio**, *i.e* the ratio between the holes surface and the total surface of the MCP. This must be as high as possible to avoid that atoms hit the MCP but not in a channel, thus losing the first electron. The new generation of MCPs we are using for the experiments conducted in this thesis (Hamamastu F9142-01 MOD6) implements a technology improving the open-to-air ratio to 90% for the top plate and 70% for the bottom one. The size of the MCPs allows us to detect momentum values up to 1.22 k_d in the plane MCPs plane.

The MCPs by themselves would be useless as we need something to detect the electron shower to know where a given atom has fallen. In high-energy particle physics experiments in which MCPs are the most widely used, this is done by putting behind the MCPs a phosphorus screen or photo-multipliers which are however not suited to our needs as they only record a 2D information. To measure the 3D momentum of the atom, we need to know the time of arrival of the atom in addition to the x and y coordinates at which it fell on the MCP. To this end, we use what we call **delay lines**.

3.2.2 Delay lines

The delay lines consists of two metallic wires of length $L_{x,y} = 20$ m wrapped around a hundred times around a holding board located beneath the MCPs. The electronic shower created by the MCPs couples into the delay lines, creating an electronic pulse that propagates at speed $v_g = 10^6$ m/s in the two directions of each delay lines as illustrated on Fig.-3.10. By recording the times of arrivals at each ends of the delay lines labelled $t_{x_1}, t_{x_2}, t_{y_1}$ and t_{y_2}, we reconstruct the coordinates and time of impact with:

$$x_{\text{det}} = \frac{1}{2}(t_{x_1} - t_{x_2})v_g \tag{3.3}$$

$$y_{\text{det}} = \frac{1}{2}(t_{y_1} - t_{y_2})v_g \tag{3.4}$$

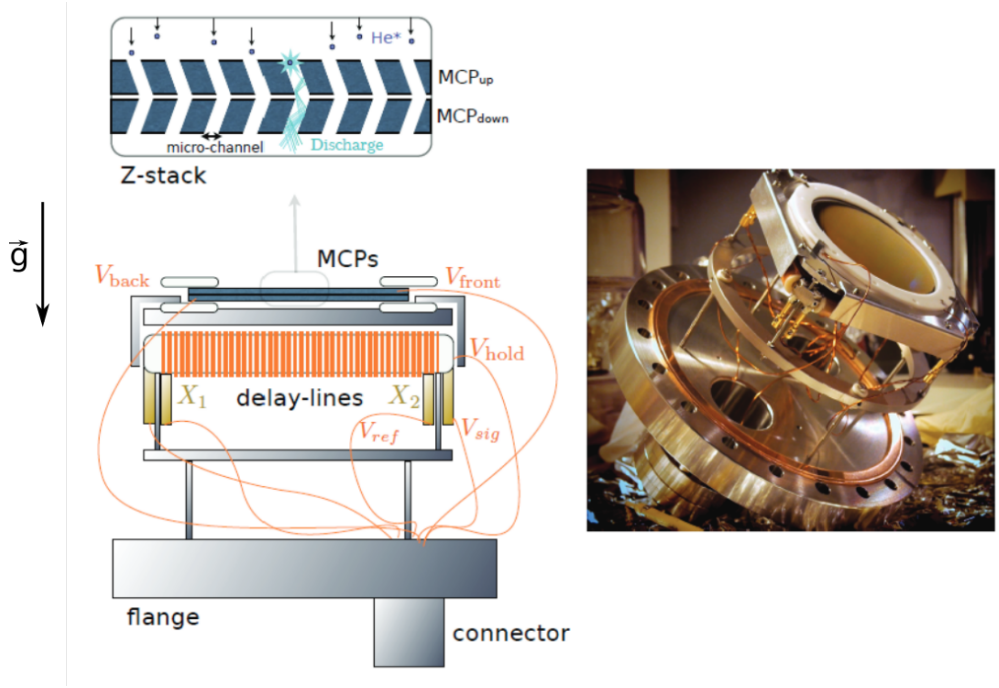

Figure 3.9: He* detector. The top left schematic illustrates how the MCP works, while the bottom left schematic shows the entirety of the He* detector with the delay-lines located underneath the two stacked MCPs. The right image is a photograph of the apparatus. Taken from [28].

$$t_{\text{det}} = t_{x_1} + t_{x_2} - \frac{L_x}{v_g} = t_{y_1} + t_{y_2} - \frac{L_y}{v_g} \tag{3.5}$$

We now need to understand how to use the values of x_{det}, y_{det} and t_{det} to obtain the 3D momentum $\boldsymbol{k}$ of the detected atoms. As detailled in Chapter 2, when there are no interactions between the atoms, the density $\rho_{\text{TOF}}(\boldsymbol{r}, t_{\text{TOF}})$ after a TOF t_{TOF} maps the in-trap momentum distribution with the simple ballistic relation $\hbar\boldsymbol{k} = m\boldsymbol{r}/t_{\text{TOF}}$ provided that the TOF is long enough to access the far-field regime.

To verify this condition, the MCPs are located at a distance $D_{\text{MCP}} = 43$ cm below the atom trap, corresponding to a TOF $t_{\text{TOF}} = 297$ ms for atoms with a zero vertical momentum to reach the detector. We remind that the far-field condition writes (see equation 2.39):

$$t_{\text{FF}} = \frac{mL^2}{2\hbar} \simeq 30 \text{ ms} \ll \text{t}_{\text{TOF}} \tag{3.6}$$

if we take the typical size of 40 lattice sites $L = 40d$, meaning that we are deep into the far-field regime. Note that this condition is made easier to fulfill thanks to the small mass of the Helium atom.

For now, we will assume that there are indeed no interactions during the TOF so that the ballistic relation is true. This hypothesis will be verified in the next sections. We thus need to know how to determine the position vector $\boldsymbol{r}$ where the atom is detected after the

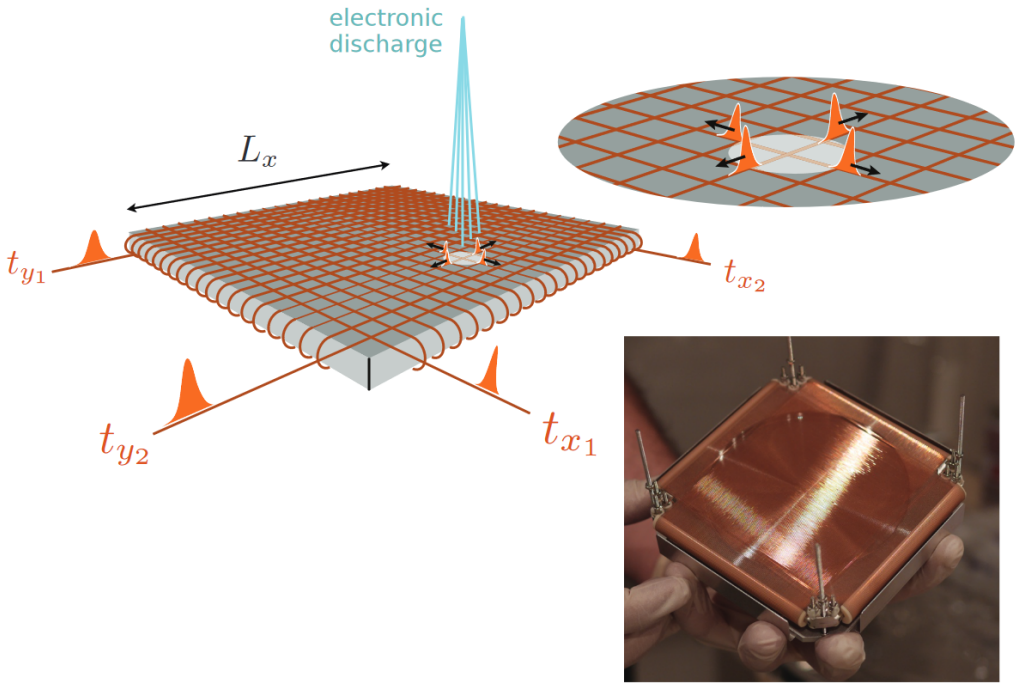

Figure 3.10: Schematic of the delay lines. The electronic discharge couples to the delay lines and propagates in the two directions of the delay lines. The times of arrival are recorded at each ends of the delay lines. Taken from [28].

TOF. While x and y are obtained directly from x_{det} and y_{det}, it is not so clear how to obtain z from what we measure with the delay lines.

When the trapping potential is turned off, the atoms experience a free fall under the sole effect of gravity. The vertical position z of an atom with an initial speed v_z after a time t is, taking the origin of the reference-frame at the center of the MCP and $t = 0$ when the trap is turned off:

$$z(t) = \frac{1}{2}gt^2 + v_z t - D_{\text{MCP}} \tag{3.7}$$

With t_{TOF} the time necessary for atoms with $v_z = 0$ to reach the detector, we can write:

$$D_{\text{MCP}} = \frac{1}{2}gt_{\text{TOF}}^2 \tag{3.8}$$

to obtain

$$z(t) = \frac{1}{2}g(t^2 - t_{\text{TOF}}^2) + v_z t \tag{3.9}$$

Finally, the time t_{det} at which an atom is detected on the detector at $z = 0$, which is the quantity we experimentally measure, verifies:

$$\frac{1}{2}g(t_{\mathrm{TOF}}^2 - t_{\mathrm{det}}^2) = v_z t_{\mathrm{det}} \tag{3.10}$$

To use the convenient ballistic relation $\hbar\boldsymbol{k} = m\boldsymbol{r}/t_{\mathrm{det}}$, we then define z so that $z = \frac{1}{2}g(t_{\mathrm{TOF}}^2 - t_{\mathrm{det}}^2)$.

3.2.3 Detection of the electronic pulses and accuracy of the detector

As we have seen in the last paragraph, the precision with which we measure the momentum of the atoms depends directly on the precision with which we measure the arrival times $(t_{x_1}, t_{x_2}, t_{y_1}, t_{y_2})$. It is therefore crucial to devise a procedure to attribute to a pulse an arrival time as precisely and reliably as possible. The main difficulty comes from the fact that the amplitude of the pulses varies as the different electronic showers do not couple with the same efficiency in the delay lines. If we were to attribute the arrival time by identifying when the signal goes above a given threshold voltage, a high amplitude pulse would be detected sooner than a low amplitude one. To circumvent this issue, we use a **constant fraction discriminator** (CFD) that produces the following signal:

$$V_{\mathrm{CFD}}(t) = V_{\mathrm{pulse}}\,(t) - f_c \times V_{\mathrm{pulse}}\,(t)\,(t-\tau) \tag{3.11}$$

where $f_c \in [0,1]$ and τ a delay. The resulting signal is therefore a bimodal pulse that crosses zero, setting the reference to trigger a 0-1V with sharp raising edge signal that is then fed to a FPGA-based Time to Digital Converter (TDC) to convert it to a digital time. The TDC coding step is $t_0 = 120$ ps defining an in-plane pixel of size:

$$x_0 = y_0 = \frac{1}{2}t_0 v_g = 60\ \mu\mathrm{m} \tag{3.12}$$

This defines an in-plane momentum pixel of size $1.4\times10^{-3}k_d$. The value of t_0 also defines a time pixel for the vertical direction that we can convert into a spatial pixel. As the velocity of the center-of-mass of the cloud after the TOF is roughly $v_{\mathrm{CM}} = 3$ m/s, the vertical spatial accuracy is then $z_0 = v_{\mathrm{CM}}t_0 \approx 0.4$ nm which is far better than the in-plane accuracy. However, as illustrated in Fig.-3.11, the vertical accuracy is actually limited by the angle θ of the micro-channels. Because of it, two atoms separated by a distance $l/\tan(\theta)$ where l is the diameter of the channel are actually detected simultaneously [28]. This leads to an effective accuracy on the measurement of the vertical position of $l/\tan(\theta) = 33\ \mu$m with $l = 12\ \mu$m and $\theta = 20°$, *i.e* twice better than the in-plane accuracy

The numbers discussed so far actually represent a lower bound for the accuracy that can be worsened because of the noise of the electronics or any experimental defect that we might overlook. One possible way to experimentally evaluate the resolution of the detector is to image on the detector an object with small structures as one would do in Optics. This method was actually implemented to measure the in-plane resolution of an older set of MCPs an electronics [115].

Actually, for our experimental purposes where we are detecting single atoms, we prefer to speak of the accuracy of the detector instead of its resolution, the accuracy being the

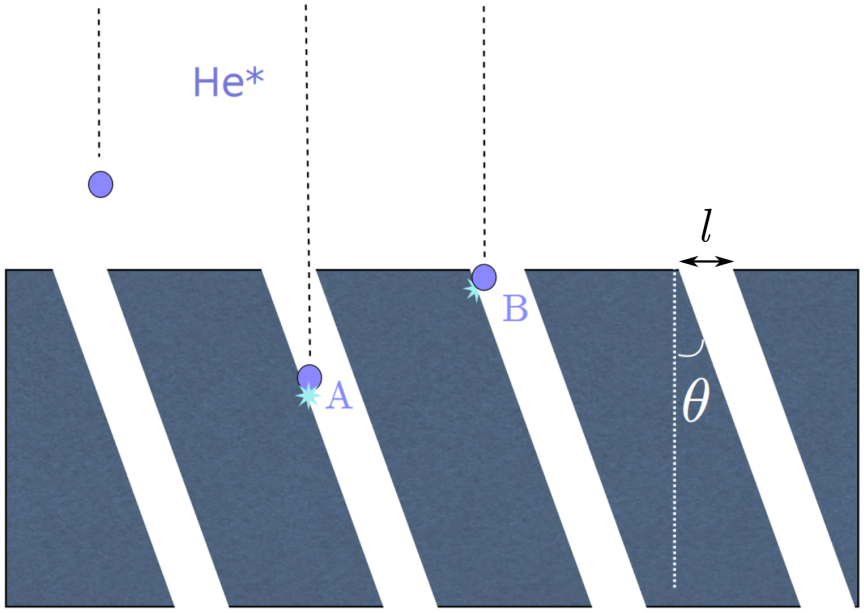

Figure 3.11: Vertical resolution of the detector. Because of the angle θ, the atoms A and B are detected at the same time even though they are separated by a distance $l/\tan(\theta)$ where l is the width of a channel. Taken from [28].

typical standard deviation of a set of measurements of a single atom momentum whose momentum is fixed. This is obviously very hard to implement in practice and we then need to devise an alternate method to access the accuracy of the detector. The solution is to make use of the Hanbury Brown and Twiss effect. As explained in Chapter 1, we expect to observe for a system with Gaussian statistics that the second-order correlation function goes to 2, $g^{(2)}(\boldsymbol{k},\boldsymbol{k}) = 2$, and decays on a typical scale $1/L$, L being the spatial size of the trapped gas. If however the width of the correlation function is not much larger than the accuracy of the detector, the second-order correlation function is broadened and the amplitude reduced. One can then create a large system so that the second-order correlation function is narrow enough so that the accuracy of the detector affects it, and deduce the value of the accuracy from the observed reduction of the amplitude.

This method was applied in Hugo Cayla's thesis [28] with a Mott insulator gas of 40×10^3 atoms to measure that the accuracy of the detector is isotropic and equal to $\sigma_{\mathrm{MCP}} = 2.5(1) \times 10^{-3}\ k_d$. However, in this case, the effect of the accuracy is not very strong as the spatial size of the gas is not very large. We then tried to complement these measurements by using thermal gases of $\sim 200 \times 10^3$ atoms produced in the ODT, taking advantage of the anistropy of the trap so that the gas is large in the direction where the trapping frequency is small. In this direction, the correlation function is then expected to be very narrow and thus heavily affected by the accuracy of the detector. We were indeed able to observe that the amplitude of the second-order correlation function is reduced down to 1.33(1) from which we deduced $\sigma_{\mathrm{MCP}} = 2.9(3) \times 10^{-3}\ k_d$ which is in fact quite consistent with the previous measurement. We note at this point that the correlation function measurements that we shall present in the next chapter are conducted with relatively low atom numbers for which the correlation functions are wide enough not to be affected by the accuracy of the detector that we will then neglect.

3.2.4 Reconstruction algorithm and saturation effects

As we have just seen, the position of the atoms are obtained from the quadruplet set of times $(t_{x_1}, t_{x_2}, t_{y_1}, t_{y_2})$ recorded at the end of the delay lines. The difficulty however is to correctly attribute each pulse to the correct atom. To do so, the pulses are then algorithmically sorted in quadruplets using the fact that if the arrival times of two pulses t_1 and t_2 are associated to the same atom, they must verify:

$$|t_1 - t_2| \leq \frac{L_{x,y}}{v_g} \tag{3.13}$$

For a detected pulse t_{x_1}, we thus conserve only the pulses on channels x_2, y_1 and y_2 that fall within the time window defined by equation 3.13. If there are still several possible quadruplets, we compute for each quadruplet the quantity:

$$D = t_{x_1} + t_{x_2} - (t_{y_1} + t_{y_2}) \tag{3.14}$$

that should be zero according to equation 3.5 if the times of the quadruplet correspond to the detection of an atom. We therefore select the quadruplet for which the quantity D is the closer to zero and remove the four times from the lists of arrival times and repeat the procedure. Note that we presented a simplified version of the algorithm for clarity sake, we refer the reader once again the thesis of Hugo Cayla [28] for a more thorough description accounting for the imperfections of the detector.

Saturation

One of the principal drawbacks of the He* detector is its high sensitivity to saturation effects for high flux of particles. Indeed, if two particles fall close-by in a time smaller than the time required for the electronic charges to reload the area depleted by the detection of the first particle, the amplification factor for the second particle is significantly reduced, meaning that the particle might not be detected. This is notably the case for the dense Bose-Einstein condensates. We will not spend too much describing the effects of this "physical" saturation that have been well studied in previous works [25, 28, 52, 115] and that will not be too much of a trouble for the experiments we wish to conduct of this thesis. Indeed, we want to look at the correlations in the depletion of a BEC for which the momentum density is quite low and thus not subject to saturation effects.

Our measurements might however be affected by another kind of saturation effect related to the reconstruction algorithm. Let's consider two atoms A and B falling on the detector at times t^A and t^B for which we record 8 arrival times. We have 7 possible combinations of these arrival times:

- $(t^A_{x_1}, t^A_{x_2}, t^A_{y_1}, t^A_{y_2})$ and $(t^B_{x_1}, t^B_{x_2}, t^B_{y_1}, t^B_{y_2})$, the proper one.
- $(t^B_{x_1}, t^A_{x_2}, t^A_{y_1}, t^A_{y_2})$ and $(t^A_{x_1}, t^B_{x_2}, t^B_{y_1}, t^B_{y_2})$
- $(t^A_{x_1}, t^B_{x_2}, t^A_{y_1}, t^A_{y_2})$ and $(t^B_{x_1}, t^A_{x_2}, t^B_{y_1}, t^B_{y_2})$
- $(t^A_{x_1}, t^A_{x_2}, t^B_{y_1}, t^A_{y_2})$ and $(t^B_{x_1}, t^B_{x_2}, t^A_{y_1}, t^B_{y_2})$
- $(t^A_{x_1}, t^A_{x_2}, t^A_{y_1}, t^B_{y_2})$ and $(t^B_{x_1}, t^B_{x_2}, t^B_{y_1}, t^A_{y_2})$
- $(t^A_{x_1}, t^B_{x_2}, t^B_{y_1}, t^A_{y_2})$ and $(t^B_{x_1}, t^A_{x_2}, t^A_{y_1}, t^B_{y_2})$

- $(t^A_{x_1}, t^B_{x_2}, t^A_{y_1}, t^B_{y_2})$ and $(t^B_{x_1}, t^A_{x_2}, t^B_{y_1}, t^A_{y_2})$

Let us now assume that the flux of particle is high so that t^A and t^B are very close so that equation 3.13 cannot be used to exclude any of the combinations. We are then only left with the calculation of D. The problem is that the two last combinations also give $D = 0$ and cannot be discriminated from the proper one. The coordinates reconstructed from these wrong combinations write:

$$X1 = \frac{t^A_{x1} - t^B_{x2}}{2v_g} = X + \frac{t^A - t^B}{2v_g} \quad Y1 = \frac{t^B_{y1} - t^A_{y2}}{2v_g} = Y + \frac{t^B - t^A}{2v_g} \quad T1 = \frac{t^A + t^B}{2}$$
$$\text{and} \tag{3.15}$$
$$X2 = \frac{t^B_{x1} - t^A_{x2}}{2v_g} = X + \frac{t^B - t^A}{2v_g} \quad Y2 = \frac{t^A_{y1} - t^B_{y2}}{2v_g} = Y + \frac{t^A - t^B}{2v_g} \quad T2 = \frac{t^A + t^B}{2}$$

or

$$X1 = \frac{t^A_{x1} - t^B_{x2}}{2v_g} = X + \frac{t^A - t^B}{2v_g} \quad Y1 = \frac{t^A_{y1} - t^B_{y2}}{2v_g} = Y + \frac{t^A - t^B}{2v_g} \quad T1 = \frac{t^A + t^B}{2}$$
$$\text{and} \tag{3.16}$$
$$X2 = \frac{t^B_{x1} - t^A_{x2}}{2v_g} = X + \frac{t^B - t^A}{2v_g} \quad Y2 = \frac{t^B_{y1} - t^A_{y2}}{2v_g} = Y + \frac{t^B - t^A}{2v_g} \quad T2 = \frac{t^A + t^B}{2}$$

There are therefore some wrongly reconstructed atoms that end up on $\pm 45°$ lines as illustrated on Fig.-3.12. Moreover, if we take $X \simeq 0$ and $Y \simeq 0$, $X1 \simeq -X2$ and $Y1 \simeq -Y2$. If the times $T1 = T2$ correspond to $k_z = 0$, the wrongly reconstructed pair of atoms looks exactly like a $\boldsymbol{k}/-\boldsymbol{k}$ pair! Even worse, the saturation occurs mainly for BEC atoms because of the high density, and the BEC corresponds exactly to momentum values close to $k = 0$, *i.e* $X \simeq 0$ and $Y \simeq 0$. This is then a problem as we can artificially create $\boldsymbol{k}/-\boldsymbol{k}$ pairs because of this indeterminacy in the reconstruction algorithm. This is something that we will need to keep in mind for the analysis of the experimental data.

3.2.5 Two-photon Raman transfer

As we have seen in the first sections of this chapter, the BEC is prepared in the magnetic-substate $m_J = 1$. To make a proper measurement of the in-trap momentum of the atoms, it is absolutely crucial that their TOF trajectories are not perturbed, notably by interactions with magnetic fields. In that respect, it would be quite hard to shield the science chamber from every unwanted magnetic field on the large distance of 43 cm on which we let the atoms fall to access the far-field regime of expansion. A solution to cancel these unwanted interactions is to transfer the atoms into the non-magnetic sub-state $m_J = 0$. All non-transferred atoms are then removed by applying a strong magnetic gradient so that they do not reach the MCPs.

When I started my PhD, we used a magnetic field bias to separate the different sub-states with the Zeeman effect and then drive the transition between $m_J = 1$ and $m_J = 0$

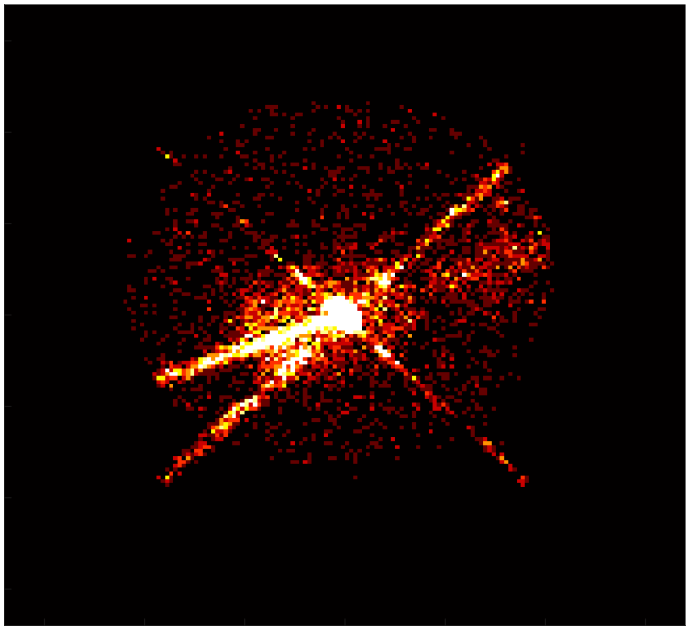

Figure 3.12: Time integrated 2D MCP image illustrating the presence of a saturation cross at $\pm 45°$. The third "line" is not related to saturation effects and corresponds to evaporated atoms that can fall on the MCP at the same time than the BEC.

with a RF wave within the lowest-energy manyfold [25, 28]. However, the energy difference between the sub-states $m_J = 1$ and $m_J = 0$ and $m_J = 0$ and $m_J = -1$ is the same. We therefore have a 3-level system with two resonant transitions and can only achieve a 50% population transfer to $m_J = 0$. This has a strong consequence: only half of the atoms at maximum can reach the detector, thus reducing the detection efficiency by at least a factor 2. Even worse, the effective Rabi frequencies were limited by the highest accessible RF powers in our experiment. The pulse duration corresponding to the maximum transfer efficiency was then too large so that the transfer was perturbed by fluctuations of the magnetic field, forcing us to work with shorter pulse and therefore lower detection efficiencies. This is particularly harmful for correlation measurements such as $\boldsymbol{k}/-\boldsymbol{k}$ pairing as we need to detect the two atoms of the pair: losing a factor α on the detection efficiency reduces the probability to detect a $\boldsymbol{k}/-\boldsymbol{k}$ pair by a factor α^2. This calls to change the transfer scheme to achieve a 100% (or close to) population transfer to the $m_J = 0$ state.

To do so, we use an optical transfer scheme, a two-photon Raman transfer. While this was used on our experiment a few years back on the $2\ ^3S_1 \rightarrow 2\ ^3P_1$, it was abandoned as spontaneous emission effects were perturbing the measured momentum distribution to sufficiently high levels, harming the measurements conducted at the time. Nevertheless, our goal to detect $\boldsymbol{k}/-\boldsymbol{k}$ pairs motivated us to build the required setup, with the notable addition of a third laser source allowing us to address the remaining transition $2\ ^3S_1 \rightarrow 2\ ^3P_0$, better suited for Raman transfer as we will later see.

Principle of the two-photon Raman transfer

To understand what two-photon Raman transfer is, let us consider a lambda level structure with two ground states $|g_1\rangle$,$|g_2\rangle$ and one excited state $|e\rangle$ (see Fig.-3.13). Raman scattering

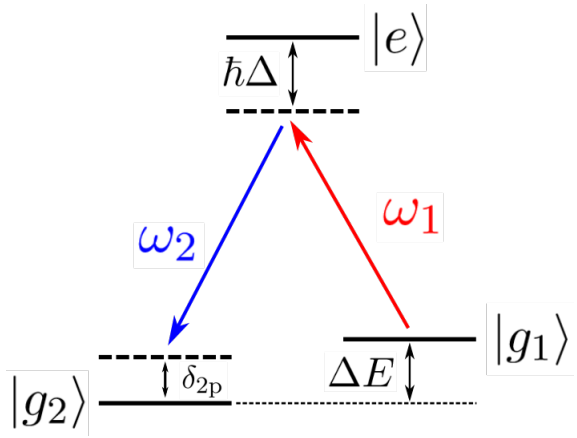

Figure 3.13: Lambda level structure in which a two-photon Raman transfer can be used to transfer atoms from $|g_1\rangle$ to $|g_2\rangle$.

is an inelastic process in which the atom absorbs a first photon of frequency ω_1 and re-emits a photon of frequency ω_2, changing its internal state from $|g_1\rangle$ to $|g_2\rangle$. The absorbed photon is called the **pump** photon and the emitted one the **Stokes** photon. This process is resonant when the energy difference between the absorbed and scattered photons corresponds to the energy difference ΔE between the two states $|g_1\rangle$ to $|g_2\rangle$. If the modes ω_1 and ω_2 are populated, for instance if we shine laser light on the atom at these two frequencies, the process can be stimulated as the probability to emit a photon in a given mode is more likely the more photons there are in the mode. It is therefore possible to exploit this effect to realize a population transfer from the state $|g_1\rangle$ to the state $|g_2\rangle$.

In the rotating wave approximation [144], the 3-level Hamiltonian can be written in the $\{|g_1\rangle, |g_2\rangle, |e\rangle\}$ basis as:

$$\hat{H}_{\text{3-level}} = \hbar \begin{pmatrix} 0 & 0 & \Omega_1/2 \\ 0 & -\delta_{2p} & \Omega_2/2 \\ \Omega_1/2 & \Omega_2/2 & -\Delta \end{pmatrix} \tag{3.17}$$

where Ω_1 and Ω_2 are the Rabi frequencies associated to laser fields 1 and 2, $\Delta = (\omega_e - \omega_{g_1}) - \omega_1$ and $\delta_{2p} = (\omega_{g_2} - \omega_{g_1}) - (\omega_2 - \omega_1)$ (see Fig.-3.13). Importantly, Δ must be large to avoid one photon absorption, *i.e.* population of the excited state and spontaneous emission. In these conditions, the excited level can be adiabatically eliminated to describe the two-photon transfer as an effective two-level coupling between $|g_1\rangle$ and $|g_2\rangle$. The corresponding Hamiltonian writes:

$$\hat{H}_{\text{eff}} = \begin{pmatrix} 0 & \Omega_{2p} \\ \Omega_{2p} & -\delta' \end{pmatrix} \tag{3.18}$$

with $\Omega_{2p} = \frac{\Omega_1\Omega_2}{2\Delta}$ and $\delta' = \delta_{2p} - (\Omega_1^2 + \Omega_2^2)/4\Delta \approx \delta_{2p}$.

From this expression, we use the well-known results of Rabi oscillations [41] to get the effective Rabi frequency

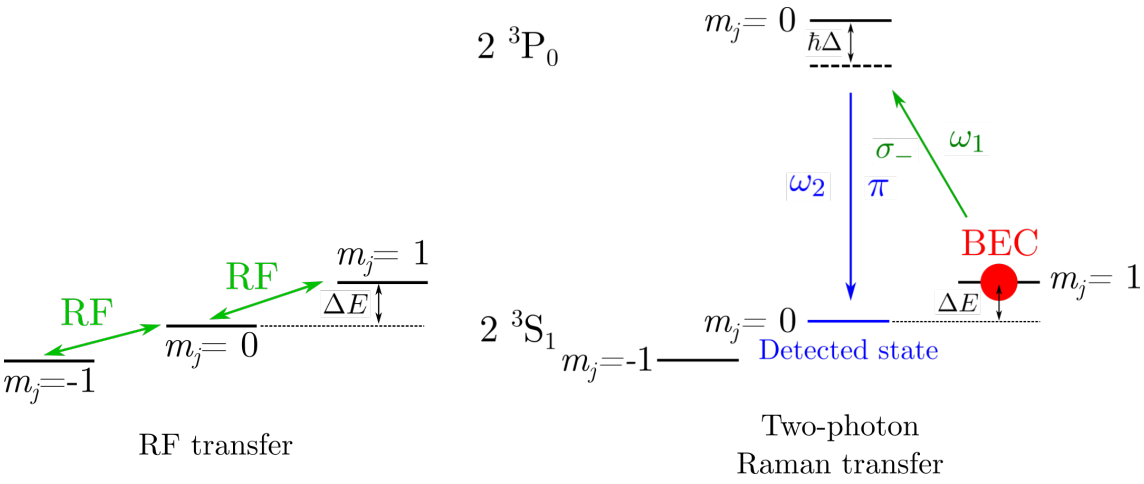

Figure 3.14: Implementation of the two-photon Raman transfer with ^{4}He* (right). The situation for the RF transfer is represented on the left for comparison.

$$\Omega_{\text{eff}} = \sqrt{\frac{\Omega_1^2\Omega_2^2}{4\Delta^2} + \delta_{2\text{p}}^2} \tag{3.19}$$

and that maximum transfer efficiency is the ratio $\eta_{2\text{p}} = \Omega_{2\text{p}}^2/\Omega_{\text{eff}}^2$. For $\delta_{2\text{p}} = 0$, we get $\eta_{2\text{p}} = 1$ meaning that it is possible to transfer the entire population of $|g_1\rangle$ to $|g_2\rangle$.

Experimental implementation

To implement the two-photon Raman transfer, we use the transition $2\ ^3S_1 \rightarrow 2\ ^3P_0$ that effectively realizes the lambda structure required for Raman transfer (see Fig.-3.14). Interestingly, the level $2\ ^3P_0$ has only one sub-state meaning that only the transitions of interest are possible, eliminating any risk of off-resonance excitations of other transitions as it could be the case when using $2\ ^3P_1$ for the excited level. The pump beam is σ_- polarized (actually linearly polarized in the experiment, see below) and the Stokes beam π polarized. Importantly, the momentum of the atom is modified because of the absorption of a pump photon and the emission of a Stokes photon. As we do not want to not want to change the momentum of the atoms during the TOF to properly measure the in-trap momentum, we opt for a configuration with co-propagating pump and Stokes beams.

The optical setup is represented in Fig.-3.15. In brief, the two beams are obtained from a single homemade External-Cavity Diode Laser [173], locked on the $2\ ^3S_1 \rightarrow 2\ ^3P_0$ of frequency ν_0 via saturated absorption spectroscopy. In the saturated absorption spectroscopy arm of the setup, the frequency of the laser is shifted by 400 MHz by a double pass Acousto-Optic Modulator (AOM) before locking, meaning that the frequency of the laser is $\nu = \nu_0 - 400$ MHz. The main beam is then split in two beams whose respective powers are controlled by rotating a half-wave plate in front of a polarizing beam-splitter cube. The frequencies of each beam is set by another double pass AOM. In the end, the frequencies are $\nu_{\text{Stokes}} = \nu_0 - 800$ MHz for the Stokes beam and $\nu_{\text{Pump}} = \nu_0 - 813$ MHz for the pump beam. The small difference of 13 MHz is set to match the energy difference ΔE between the sub-states $m_J = 0$ and $m_J = 1$ that we control by applying a magnetic bias field along the x direction. The detuning to the one-photon transition is then $|\Delta| = 800$ MHz which

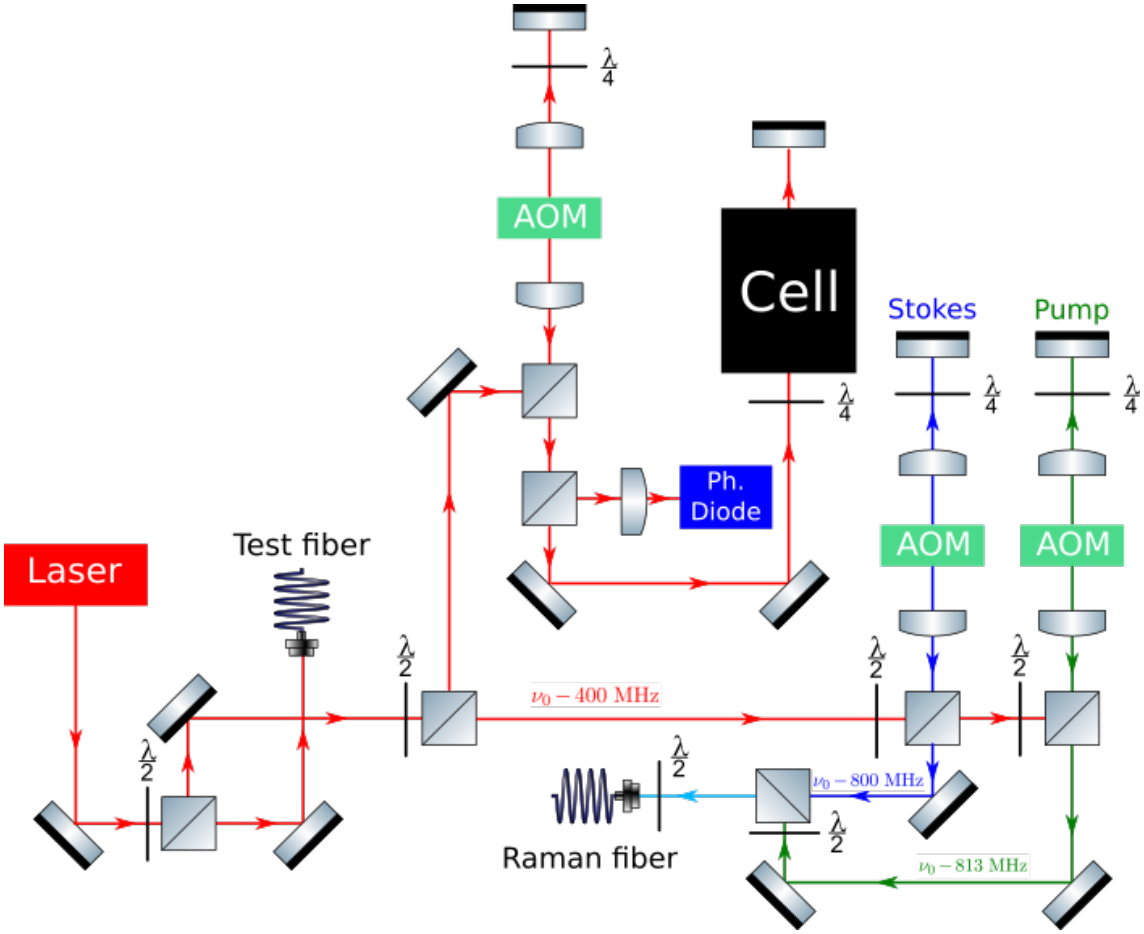

Figure 3.15: Optical setup for two-photon Raman transfer. After being frequency locked via saturated absorption spectroscopy, the laser beam is split to produce the Stokes and pump beam. The powers are controlled with half-wave plates and polarizing beam splitter, while the frequencies are controlled with Acousto-Optic Modulators.

is large enough to avoid spontaneous emission effects. An additional advantage of using the $2\ ^3S_1 \rightarrow 2\ ^3P_0$ transition is that the level $2\ ^3P_0$ is 29.9 GHz apart from the next level $2\ ^3P_1$, itself only separated by 2.3 GHz from $2\ ^3P_2$. Using a large detuning is then not a problem when adressing $2\ ^3S_1 \rightarrow 2\ ^3P_0$ compared to $2\ ^3S_1 \rightarrow 2\ ^3P_1$ where we could start exciting the $2\ ^3S_1 \rightarrow 2\ ^3P_2$ transition. The polarizations of the two beams are set to be linear and orthogonal. They are finally sent on two faces of a polarizing beam-splitter cube to be overlapped and coupled into a polarization-maintaining fiber bringing them to the science chamber as illustrated on Fig.-3.16.

The polarization at the exit of the fiber is set by a half-wave plate so that the Stokes beam is linearly polarized along the quantification axis x to have the π polarisation. The pump beam is linearly polarized as well but orthogonal to the Stokes beam polarisation. This decomposes as the sum of a σ_+ and σ_- polarisation for the atoms. Because of the energy levels structure, the σ_+ component does not interact with the atom, leaving only the effect of the wanted σ_- polarization. This means however than half of the power of the pump beam is useless, requiring to put twice more power for the pump beam than for the Stokes beam for a symmetric configuration.

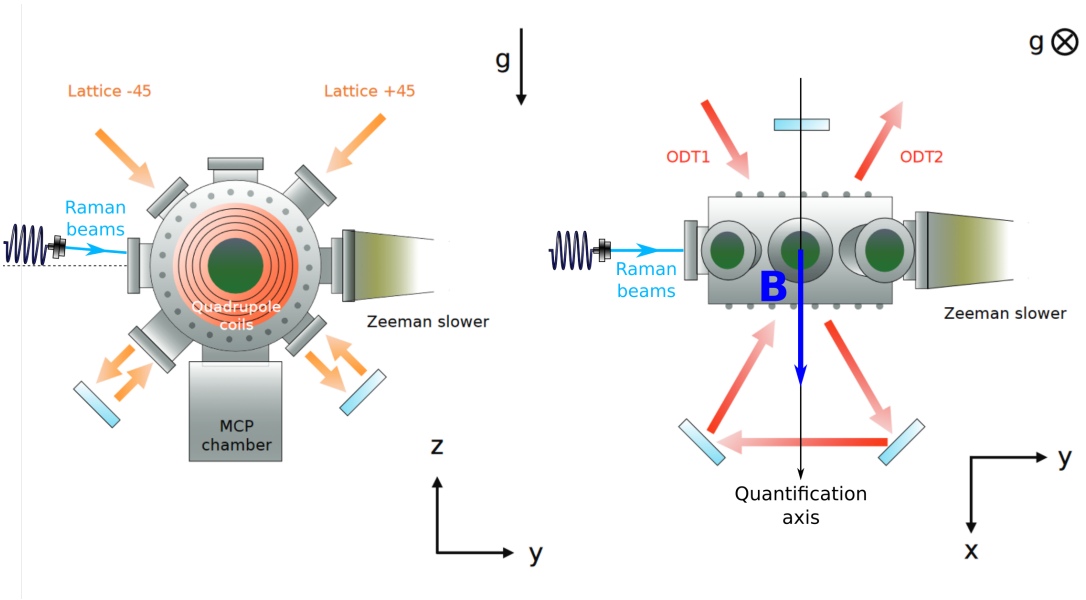

Figure 3.16: Orientation of the Raman beams in the experiment. On the right picture, the blue arrow denotes the orientation of the magnetic bias field, setting the quantification axis.

Measurement of the two-photon resonance

As previously discussed, the transfer efficiency is highly dependent from the detuning to the two-photon resonance condition set by the frequency difference $\Delta\nu = \nu_{\text{Stokes}} - \nu_{\text{Pump}}$ that we adjust thanks to the pump beam AOM. It is therefore important to scan $\Delta\nu$ prior to any use of two-photon Raman transfer to set it perfectly on resonance. The procedure is the following:

- We significantly reduce the power of the Raman beams (30 μW and 60 μW before the fiber for the Stokes and pump beams respectively) to avoid power broadening of the transition and to have a small Rabi frequency. The period of the Rabi oscillations is then large, we can therefore use a pulse long enough to obtain the necessary frequency resolution, but short enough so that we remain in the first linear increase of the transfer when the detuning changes. We chose a pulse duration of 60 μs while the Rabi oscillation period is ~ 200 μs.
- We prepare a Mott insulator whose large momentum distribution prevents saturation effects of the detector from happening.
- We perform two-photon Raman transfer for different values of $\Delta\nu$ and plot the number of detected atoms by the MCP as a function of $\Delta\nu$. We finally fit the data to find the position of the resonance as illustrated on Fig.-3.17.

Rabi oscillations

In order to check that the two-photon Raman transfer is working as intended, we measure Rabi oscillations for different powers and check that the square Rabi frequency indeed scales linearly with the product of the powers of the Stokes and pump beams (note that the scaling is different for a one photon transition). Like when we measure the two-photon resonance, we perform the measurement on a Mott insulator to avoid saturation. The

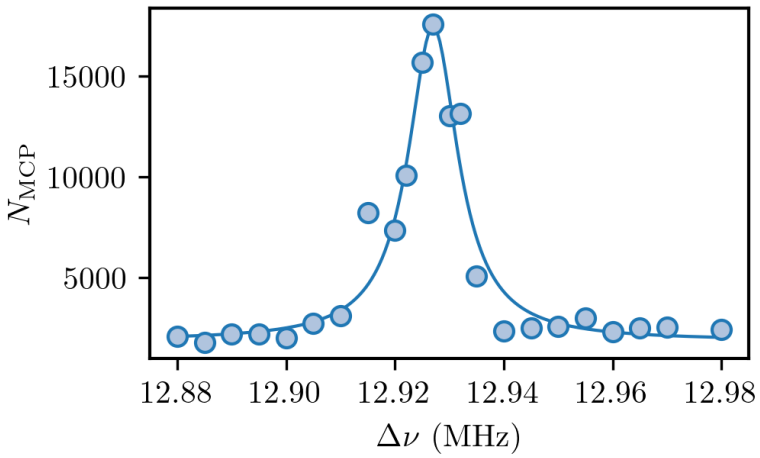

Figure 3.17: Number of detected atoms N_{MCP} (equivalent to the number of transferred atoms) as a function of the frequency difference between the Stokes and pump beams $\Delta\nu$. The maximum of N_{MCP} signals the two-photon resonance. The Lorentzian fit gives $\Delta\nu_{\mathrm{res}} = 12.927(1)$ MHz.

results are shown on Fig.-3.18 and are consistent with our expectations.

Measuring Rabi oscillations is the second part of the procedure to properly set up the two-photon Raman transfer prior to data taking. We set the power of the beams so that the maximum of the first Rabi oscillation corresponds to a pulse duration $t_{\mathrm{Rabi}} \simeq 10$ μs and measure a few Rabi oscillations to check it experimentally. This time is chosen to be as short as possible with respect to the elementary coding step of our sequencer for two purposes. First, the transfer is less sensitive to fluctuations of the magnetic field for shorter pulse times. Second, the bias field that we produce is not perfect, resulting in the presence of a small gradient of 0.17 G/cm. If the transfer takes too much time to complete, the atoms have time to travel on a significant distance so that they might see different values of the magnetic field, hence changing the two-photon resonance condition and reducing the overall transfer efficiency.

3.2.6 Measurement of the detection efficiency

We now look to determine the detection efficiency of the He* detector. In a first naive approach, we could simply produce a BEC, measure its number of atoms N_{bec} through the well-calibrated absorption imaging, use the two-photon Raman transfer to transfer all the atoms to the $m_J = 0$ state, perform the TOF and count the numbers of atoms detected on the MCP N_{MCP}. The detection efficiency is then simply the ratio $\alpha_{\mathrm{MCP}} = N_{\mathrm{MCP}}/N_{\mathrm{bec}}$. This method would however considerably underestimate the detection efficiency because of the saturation effects occuring with the high densities of the BEC. One could then think of using gases with more dilute distributions to avoid saturation, such as thermal gases or Mott insulators. This method is not so easy as well as it is practically difficult to obtain a momentum distribution wide enough so that the maximum densities values does not saturate the detector, but not too wide to avoid that a significant fraction of the atoms fall beyond the limits of the MCP.

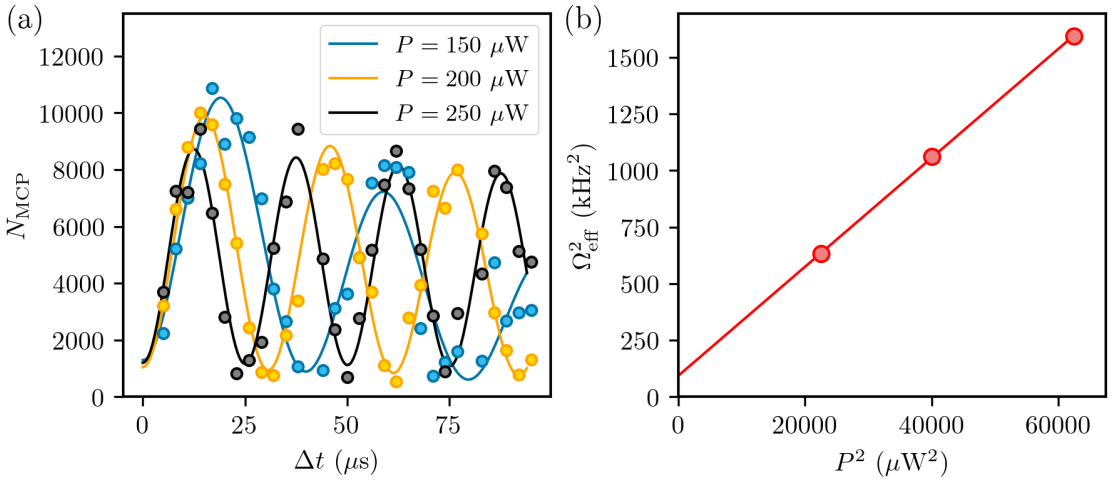

Figure 3.18: Rabi oscillations with two-photon Raman transfer. (a) Rabi oscillations at various beam power. P is the power of the Stokes beam measured before the fiber linking the optical table to the experiment. The solid fines correspond to a square sine function fit with an overall exponential decay. (b) Square Rabi frequencies Ω^2_{eff} as a function of the square power P (the power of the Stokes and pump beams are set to be the same). We obtain a linear relation with a small offset that might come from a slight miscalibration of the two-photon resonance.

To circumvent these issues, we will then work with a BEC but deliberately use the two-photon Raman transfer with a large detuning to the two-photon Raman transition to transfer only a very small fraction of the atoms and avoid saturation. Using the results of 3.2.5, the number of detected atoms on the MCP writes:

$$N_{\mathrm{MCP}} = N_{\mathrm{bec}} \left(\frac{\Omega_{2p}}{\Omega_{\mathrm{eff}}}\right)^2 \sin^2\left(\frac{\Omega_{\mathrm{eff}}\Delta t}{2}\right) \alpha_{\mathrm{MCP}} \tag{3.20}$$

with $\Omega_{\mathrm{eff}} = \sqrt{\Omega^2_{2p} + \delta^2_{2\mathrm{p}}}$ and Δt the duration of the Rabi pulse. If we measure N_{MCP}, N_{bec}, Ω_{2p} and the value of the detuning δ_{2p}, it is in principle possible to obtain the value α_{MCP}. We then devise the procedure to measure the detection efficiency to be as follows:

1. We first need to pinpoint very precisely where the two-photon resonance is. To do so, we measure the frequency of Rabi oscillations Ω_{eff} with a dilute gas for different values of the frequency difference $\Delta\nu$ between the Stokes and the pump beam close to the two-photon resonance condition. At this point, we do not care about the amplitude of the Rabi oscillations but only their frequency. Using $\Omega_{\mathrm{eff}} = \sqrt{\Omega^2_{2p} + \delta^2_{2\mathrm{p}}}$, we fit the experimental data to find the value of $\Delta\nu$ where Ω_{eff} is minimum which corresponds to the two-photon resonance as illustrated on Fig.-3.19 panel (a).
2. We prepare a BEC of $N_{\mathrm{bec}} = 2 \times 10^5$ atoms that we calibrate with absorption imaging.
3. We set the power of the Raman beams to have $\Omega_{2\mathrm{p}} = 20$ kHz.
4. We measure Rabi oscillations for various values of $\delta_{2\mathrm{p}} \in [300, 1000]$ kHz and extract the amplitude of the square sine function $N^{\mathrm{max}}_{\mathrm{MCP}}$. We typically transfer $\sim 1\%$ of the atoms.

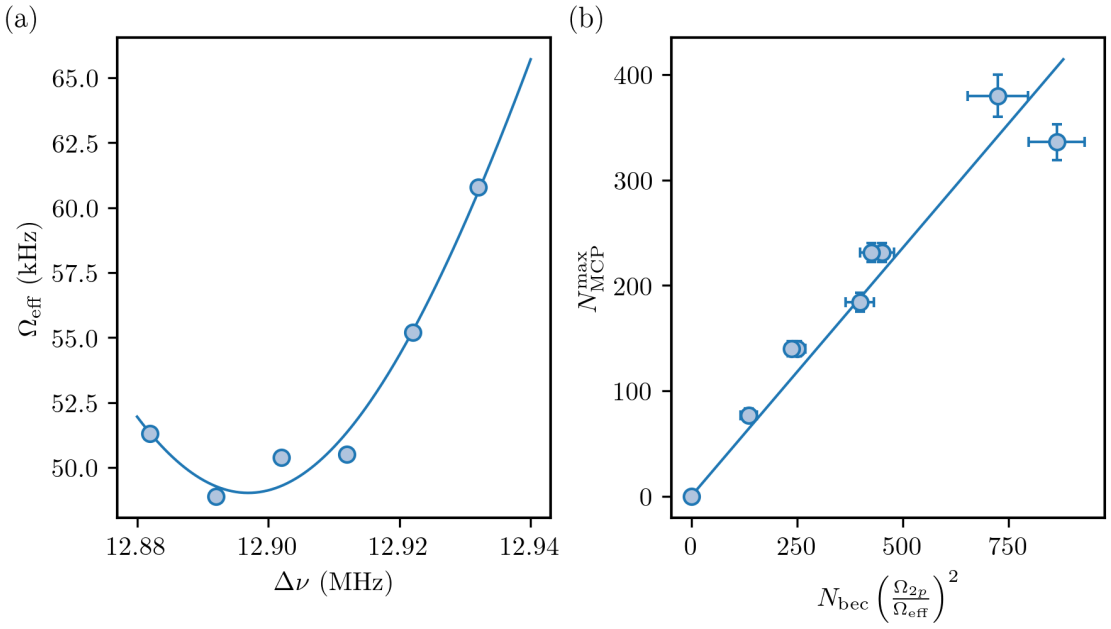

Figure 3.19: Measurement of the MCP detection efficiency. (a) Precise measurement of the two-photon resonance condition. The frequency difference between the Stokes and the pump beam is scanned to find where Ω_{eff} is minimum. The full line is a fit using $\Omega_{\text{eff}} = \sqrt{\Omega_{2p}^2 + \delta_{2\text{p}}^2}$. (b) Maximum detected number on the MCP for a given value of $\delta_{2\text{p}}$ as a function of the expected atom number $N_{\text{bec}} \left(\frac{\Omega_{2p}}{\Omega_{\text{eff}}}\right)^2$. The full line is the linear fit whose slope gives α_{MCP}.

5. We plot $N_{\text{MCP}}^{\text{max}}$ versus $N_{\text{bec}} \left(\frac{\Omega_{2p}}{\Omega_{\text{eff}}}\right)^2$. We fit the data with a linear function and deduce the value of α_{MCP} from the slope of the fit as illustrated on Fig.-3.19 panel (b).

The final measured value is $\boxed{\alpha_{\text{MCP}} = 0.53(2)}$. As mentioned earlier, the open-to-air ratio of the MCPs is around $\simeq$ 90%, meaning that almost all atoms fall in a channel, thus not limiting the detection efficiency. However, the first extracted electron has roughly a 1/2 probability to be ejected upwards outside of the channel, rendering the amplification process impossible, providing us with rough estimate of detection efficiency of the order of 50%.

3.3 Adiabatic preparation in the vicinity of the Mott transition

As developed in the first pages of this thesis, the general objective of our experiment is to simulate quantum interacting systems too complex to treat theoretically. More specifically, our experimental apparatus aims to simulate the equilibrium properties of the Bose-Hubbard model as described in Chapter 2. The standard procedure is to create a non-zero entropy state, the BEC, and progressively transform the Hamiltonian of the system by loading the atoms in the optical lattice to reach the desired Bose-Hubbard state. It is crucial that this transformation does not create excitations: in other terms, we want to keep the entropy of the system constant as we load the atoms in the optical lattice, *i.e*

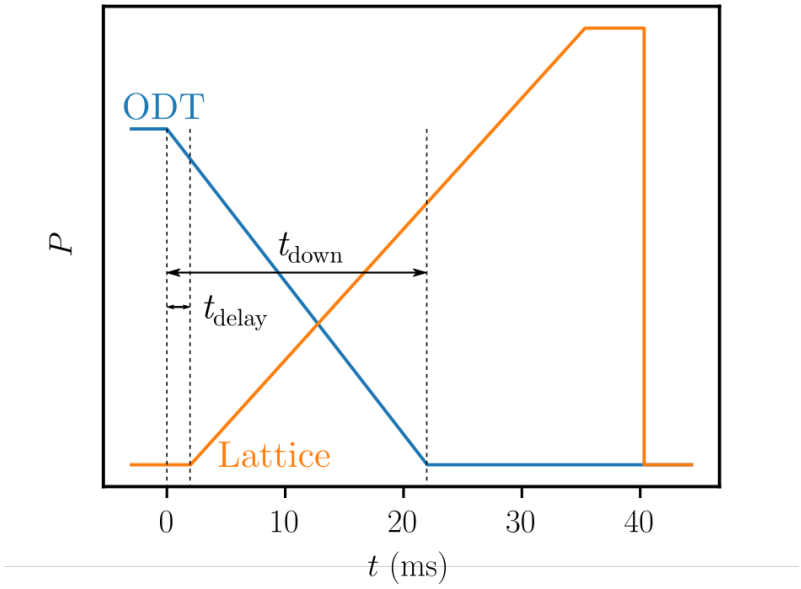

Figure 3.20: Loading sequence of the lattice.

ensure that the preparation of the target Hamiltonian is **adiabatic**. In this section, we will detail the procedure used to certify the adiabatic preparation of the Bose-Hubbard Hamiltonian in our experiment by exploiting the 3D single-atom momentum resolution of our apparatus as described in the beginning of this chapter.

3.3.1 Loading of the optical lattice

The crucial point of the preparation of an equilibrium state of the Bose-Hubbard Hamiltonian is the loading of the atoms in the optical lattice. This is done by ramping down the power of the ODT beams while ramping up the power of the lattice beams. We use several parameters to fine tune the loading sequence as represented on Fig.-3.20:

- The slope of the lattice ramp.
- t_{down} the time on which we ramp down the ODT power.
- t_{delay} the time delay between the beginning of the ramp of the optical lattice and the ramp of the ODT.

In order to optimize these parameters, the atoms are loaded back in the ODT with a symmetrical sequence to look for atom losses and heating effects to be minimized as illustrated on Fig-3.21. This technique has the advantage of being convenient and rather simple, but is not at all sufficient to prove that the loading is adiabatic. We tried using linear and exponential ramps and found that it did not make a difference [25]. We then settled for the simple linear ramps, corresponding to an almost exponential increase of s (see Fig-2.4). Their slope was set to 0.3 E_{r}/ms and remains constant no matter the final target value of s, only the ramp time changes. The optimal values of the other ramp parameters were found to be $t_{\text{down}} = 22$ ms and $t_{\text{delay}} = 0$ ms. With these parameters, we observe typical losses of 15% of the total atom number that we attribute to the not

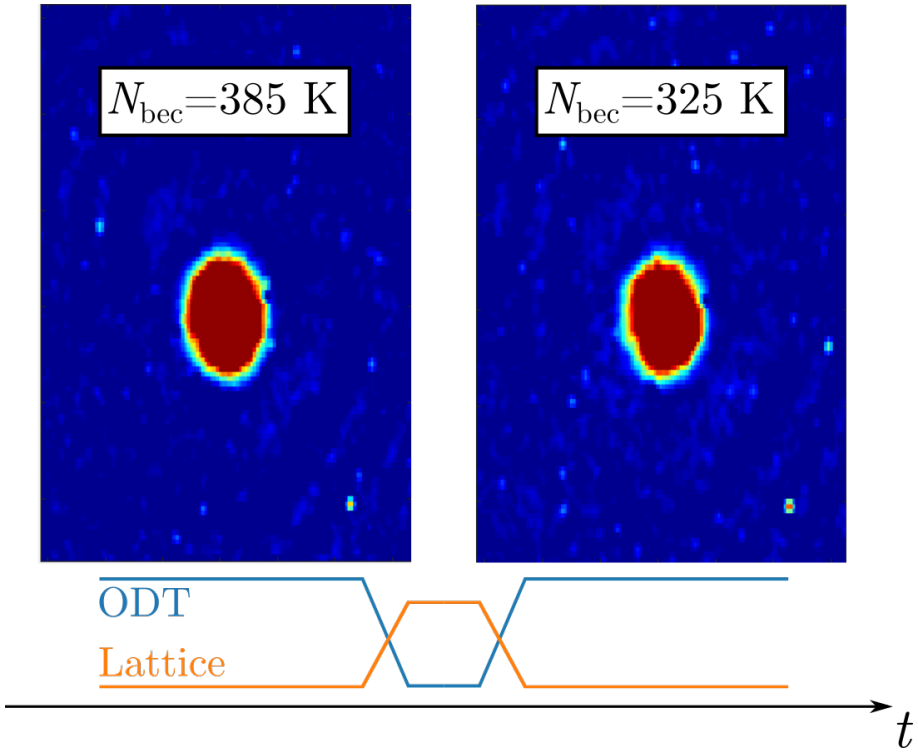

Figure 3.21: Absorption imaging of the BEC after a 10 ms TOF. The left image correspond to the BEC at the end of the evaporation sequence and the right image to the BEC loaded into the lattice and back to the ODT. No significant heating is observed, only a small loss of $\sim 15\%$ of the total atom number.

perfect overlap between the ODT and the lattice (the lost atoms carrying the extra kinetic energy obtained during the imperfect transfer), but no heating is detected.

3.3.2 Thermometry and entropy across the Mott transition

Now that we have experimentally optimized the parameters of the loading sequence, we verify its adiabaticity by extracting the temperature and the entropy from the momentum distribution [27].

Thermometry method

The temperature of the gas cannot be extracted directly from the density $\rho(\boldsymbol{k})$ as we do not have an analytical prediction for the trapped Bose-Hubbard model. The idea is then to use ab-initio Quantum Monte Carlo (QMC) calculations simulating the momentum distribution with the only adjustable parameter being the temperature (all other experimental parameters such as atom number, atom mass, scattering length or trapping frequencies are included in the QMC calculations). The QMC calculations were provided by Tommaso Roscilde from the Ecole Normale Supérieure de Lyon and were run for different temperature values. To get the temperature in the experiment, we select the QMC momentum distribution that best reproduces the experimental data as illustrated in Fig.-3.22. Formally speaking, we compare a cut of the normalized experimental density $\tilde{\rho}_{\mathrm{exp}}(k) = \rho(k,0,0)/\rho(0)$ to the QMC ones $\tilde{\rho}_{\mathrm{QMC}}(k,T) = \rho_{\mathrm{QMC}}(k,0,0,T)/\rho_{\mathrm{QMC}}(0)$. We

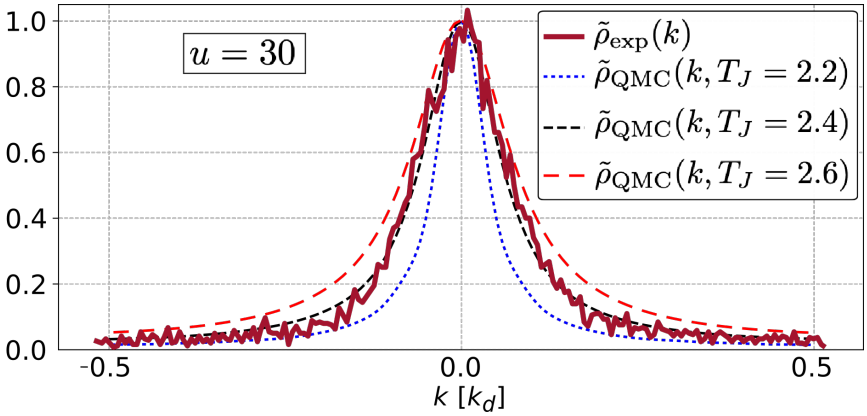

Figure 3.22: Comparison of experimental and QMC normalized 1D cuts of the momentum density for different temperatures. The ratio $u = 30$ corresponds roughly to the location of the critical point in the ground-state.

look to find the temperature value that minimizes the reduced chi-square quantity that we define as:

$$\chi^2_{\mathrm{r}}(T) = \frac{1}{N_p} \sum_{j=1}^{N_p} \frac{\left[\bar{\rho}_{\mathrm{exp}}(k_j) - \bar{\rho}_{\mathrm{QMC}}(k_j, T)\right]^2}{\sigma_{\mathrm{exp}}(k_j)^2} \tag{3.21}$$

We have discretized the first Brillouin zones with a uniform mesh of $N_p = 120$ points. The quantity $\sigma_{\mathrm{exp}}(k_j)$ is the error estimate on the experimental momentum density that is assumed to have Poissonian statistics, giving us $\sigma_{\mathrm{exp}}(k_j) = \sqrt{\tilde{\rho}_{\mathrm{exp}}(k_j)/N_{\mathrm{runs}}}$ with N_{runs} the number of experimental runs used to evaluate $\tilde{\rho}_{\mathrm{exp}}(k)$.

Importantly, these kind of measurements rely on two specific points of our experiment linked to our 3D single-atom resolution. Firstly, we can measure the full 3D momentum density $\rho(\boldsymbol{k})$ without any line-of-sight integration and thus characterize it with the finest level of details. Secondly, we are able to detect low densities signal and thus work with low atoms numbers $N_{\mathrm{bec}} \simeq 3,000$ for which QMC calculations are possible down to low temperatures.

We show on Fig.-3.23 plots of $\chi^2_{\mathrm{r}}(T_J)$ as a function of the temperature of the QMC calculations at $u = 30$ (see 2.1), where T_J is the reduced temperature $T_J = k_{\mathrm{B}}T/J$. We observe a clear minimum that indicates the temperature in the experiment. Interestingly, the minimum value $\chi^2_{\mathrm{r}}(T_J = 2.4) = 3.6 \pm 3.0$ is compatible with unity, meaning that the QMC calculations indeed reproduce the experimental data within the statistical uncertainty. We fit the data with a parabolic profile to identify the position of the minimum. The error on the fit gives us an estimate of the minimal error on the evaluation of the temperature with this technique that can be linked to the notion of Fisher information that we will see in the next paragraph. Note however that in order not to rely on a fit for every data sets, we will estimate the error bars by determining the temperature interval over which distinct values of χ^2_{r} are observed.

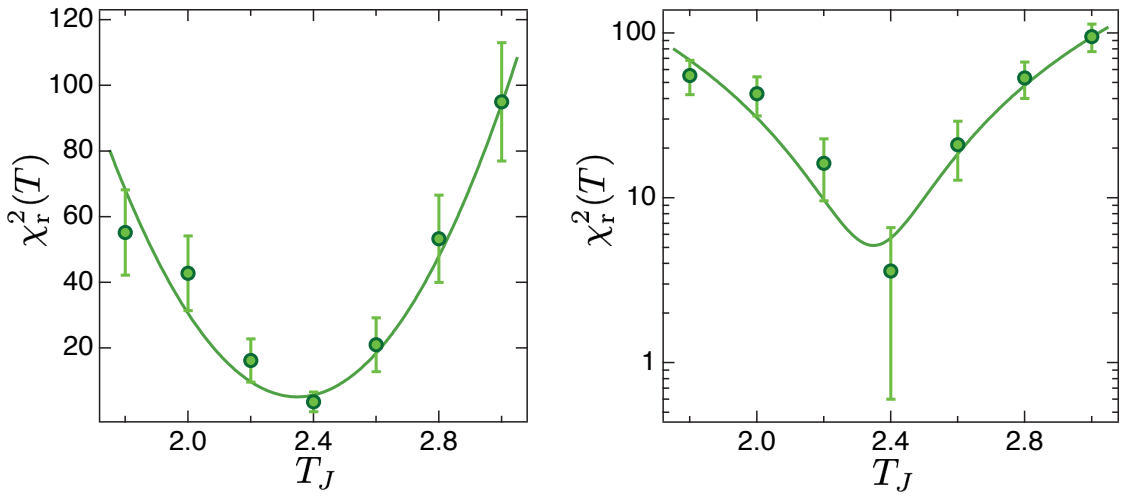

Figure 3.23: $\chi^2_r(T)$ as a function of temperature in linear and logscale. We clearly identify a minimum from which we deduce the value of T in the experiment.

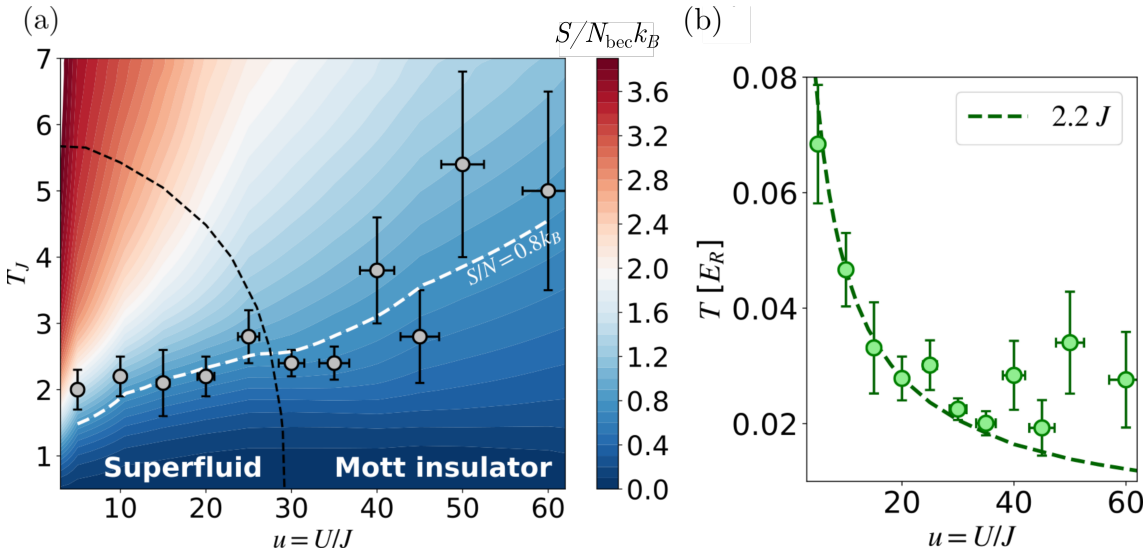

Figure 3.24: (a) Experimental reduced temperature $T_J = k_B T/J$ as a function of u. The underlying false color plot shows the theoretical map of the entropy per particle $S/N_{bec}k_B$ of the trapped 3D Bose-Hubbard model with the experimental parameters. The white dashed line is the isoentropic line $S/N_{bec} = 0.8\ k_B$. The black dashed line represents the line of critical temperatures for the uniform 3D Bose-Hubbard model at unit lattice filling [24]. (b) Absolute temperature in recoil units E_r as a function of u. The green dashed line corresponds to an energy $2.2J$ (in units of J) that best matches the experimental data in the range $u = 5 - 20$.

Temperature and entropy as a function of u

We plot on Fig-3.24 panel (a) the extracted values of T_J (T in units of J) as a function of u spanning the phase diagram of the Bose-Hubbard model. The experimental data is plotted alongside to the theoretical map of entropy. Note that we choose to plot the reduced temperature T_J to normalize the adiabatic cooling effect occurring when u increases as illustrated on Fig-3.24 panel (b). This effect comes from the fact that the isoentropic gas is contained in a Bloch band whose width is proportional to J and decreases with s (see Chapter 2). For this reason, the density of states increases with s, explaining why T goes down at constant entropy [171].

The value of the entropy is obtained from the QMC calculations giving the average energy by particle $e(T)$ for various values of the temperature. The energy is then fitted with a high-order polynomial function to compute the specific heat $c(T) = \mathrm{d}e(T)/\mathrm{d}T$ to finally obtain the entropy $S(T)/N_{\mathrm{bec}} = \int_0^T d\theta c(\theta)/\theta$ in a given QMC simulation. The values of the entropy are shown in Fig-3.24 in false colors. The light white lines represent isoentropic lines. We see that all experimental points are compatible with the isentropic curves spanning the entropy range $S/N_{\mathrm{bec}} = 0.8(1)\ k_{\mathrm{B}}$. These observations are consistent with our assumption that the lattice ramps create a series of thermal equilibrium states that we go through adiabatically conserving the entropy, thus certifying the experimental adiabatic preparation of equilibrium states of the 3D Bose-Hubbard model.

How can we understand the evolution of the isoentropic curve with u? For the moderate entropy values of the experiment, we observe two asymptotic regimes, the superfluid regime ($u \leq 25$) in which the isoentropic curves grow slowly with u, and the Mott insulator regime ($u \geq 35$) in which the isoentropic curves grow more rapidly. At low values of u, the growth can be understood with Bogoliubov theory. As seen in Chapter 1, the speed of sound depends on the strength of the interactions and therefore increases with u ($c \propto \sqrt{u}$), decreasing the density of states. The temperature dependence of the entropy is then $\sim T^3/u^2$ [84] so that the isoentropic curves $S/N_{\mathrm{bec}}k_{\mathrm{B}} = s_0$ should grow as $T \sim s_0^{1/3}u^{2/3}$ (this holds for the homogeneous case and low energies in which the dispersion relation is phononic). On the other hand, in the Mott insulator regime, the entropy writes $S/N_{\mathrm{bec}}k_{\mathrm{B}} \sim \exp(-\Delta/T)$ where $\Delta \sim u$ is the Mott Insulator gap, giving $T \sim u$ along the isoentropic curves [70]. Explaining the plateau linking the two asymptotic regimes would require a more detailled study that falls out of the scope of this thesis and will be the subject of future works.

In addition, we measured the entropy per particle $S_0/N_{\mathrm{bec}}k_{\mathrm{B}}$ in the BEC before loading it into the lattice to see if it matches the entropy measured in the lattice. To evaluate S_0, we use the relation for a non-interacting, partially-condensed Bose gas in a harmonic trap [129]:

$$S_0/N_{\mathrm{bec}}k_B = \frac{4g_4(1)}{\eta(3)}\,(1 - f_c) \tag{3.22}$$

with $g_4(1) \simeq 1.082$, $\eta(3) \simeq 1.2026$ and f_c the condensed fraction. In the ODT, the thermal energy significantly exceeds the interaction energy, $k_BT \sim h \times 2380$ Hz $\gg \mu \sim h \times 350$ Hz, meaning that interactions should be negligible, allowing us to use the above equation to find $\boxed{S_0/N_{\mathrm{bec}} = 0.72(7)\ k_B}$ with $f_c = 0.80(7)$. We compare on Fig.-3.25 the measured

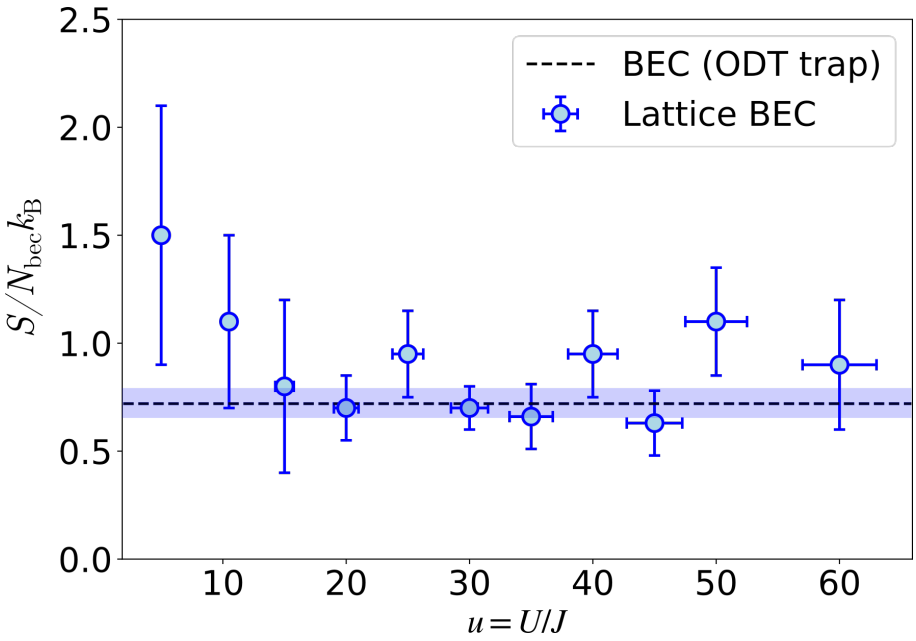

Figure 3.25: Entropy per particle for various values of u. Almost all points are compatible with the BEC entropy $S_0/N_{\rm bec} = 0.72(7)\ k_B$.

BEC entropy to the one measured at the various values of u in the lattice. In the region close to $u \simeq 30$ where the error bars are the smallest, we get an excellent agreement, confirming that the loading of the lattice is adiabatic.

3.3.3 Fischer information and Cramér-Rao bound

The attentive reader would have noticed on Fig.-3.24 that the vertical error bars on the experimental temperatures and entropies vary significantly with u and are smaller close to the quantum critical point. This comes from the fact that the momentum distribution is far less sensitive to the effect of the temperature deep in the Mott Insulator phase as the opening of the energy gap Δ in the excitation spectrum for excitations near the center of the trap supresses thermal effects for $T \leq \Delta$. The variation of the error bars is quantified by the concept of **Fisher information**. This quantity was introduced by Fisher [61] as a mean to quantify the amount of information carried by the distribution of a random variable about a given parameter. In our case, we want to know how well we can determine the parameter temperature by looking at the momentum distribution. The Fisher information writes [157]:

$$I(T) = \sum_k \frac{\tilde{\rho}_{\rm QMC}(k,T)}{\mathcal{N}_T} \left[\frac{\partial \log\left(\tilde{\rho}_{\rm QMC}(k,T)/\mathcal{N}_T\right)}{\partial T_J}\right]^2 \tag{3.23}$$

where $\mathcal{N}_T$ is the normalization of $\tilde{\rho}_{\rm QMC}(k,T)$ summed over all k.

The Fisher information tells us what is the minimum uncertainty δT with which we can evaluate the temperature through the **Cramér-Rao** bound that writes (valid when entanglement is not playing a role):

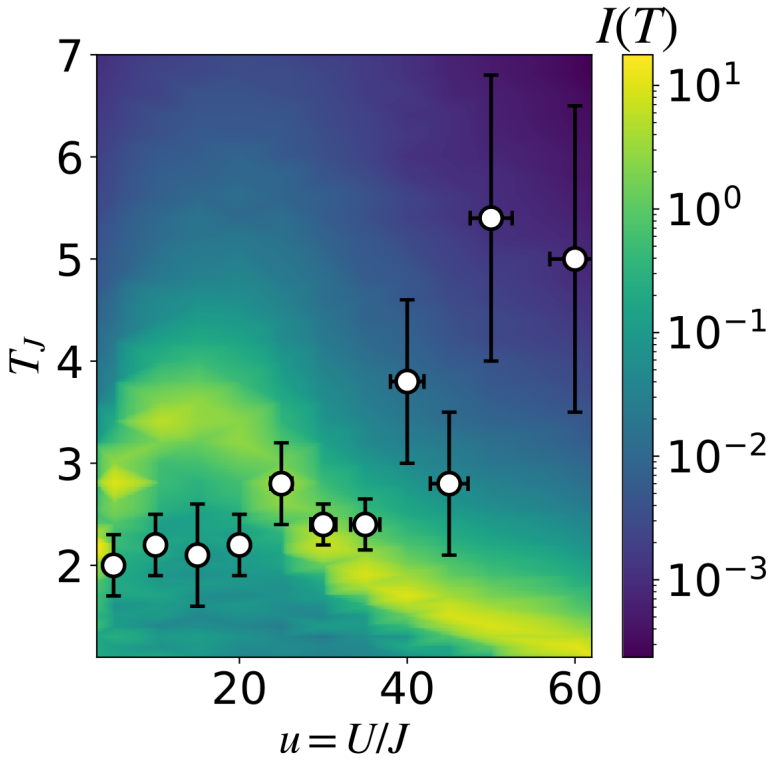

Figure 3.26: Fischer information as a function of the reduced temperature T_J and u plotted alongside the experimental temperatures. We observe that the size of the error bars is directly linked to the value of the Fischer information and minimum at the phase transition signaled by the yellow line.

$$\delta T_J = \frac{k_B \delta T}{J} \geq (\delta T_J)_{\min} = \frac{1}{\sqrt{I(T) N_{\text{runs}}}} \tag{3.24}$$

Translating the equations into words, the Fisher information tells us how sensitive the momentum density is to variations of the temperature and consequently how precisely we can estimate the temperature by measuring $\tilde{\rho}_{\text{QMC}}(k, T)$ with finite statistics. We computed the Fisher information across the phase diagram as shown in Fig.-3.26. We see that the Fisher information varies quite a lot, over 4 orders of magnitude. It takes its lower value in the deep Mott region, while it is at its maximum for temperatures where the gas undergoes its transition to a normal gas (yellow line), consistently with our error bars that we can now compare to the Cramér-Rao bound. We estimated that the typical uncertainty on the reduced temperature is $\delta T_J \sim 0.3$ in the superfluid regime and $\delta T_J \sim 1.5$ in the deep Mott regime. The former corresponds to $I(T) \sim 1$ and $(\delta T_J)_{\min} \sim 0.4$ and the latter to $I(T) \sim 10^{-3}$ and $(\delta T_J)_{\min} \sim 1.3$. Close to the Mott transition, $I(T) \sim 7$ and $(\delta T_J)_{\min} \sim 0.02$. With the parabolic fit method of Fig.3.23, we evaluate $(\delta T_J) = 0.03$ at $u = 30$, thus nearly reaching the Cramér-Rao bound. We are thus always close to saturating the limit set by the Fisher information, meaning that we essentially extract all the possible information on the temperature from the measurement of the momentum density.

3.4 Characterisation of two-body collisions in the time-of-flight dynamics

Before using our experimental setup to look for the $\boldsymbol{k}/-\boldsymbol{k}$ correlations of the quantum depletion, it is crucial to benchmark it and test whether the measured distribution $\rho_{\mathrm{TOF}}(\boldsymbol{r}, t_{\mathrm{TOF}})$ indeed maps the in-trap momentum distribution $\rho(\boldsymbol{k})$ or is perturbed by interactions effects occuring during the TOF. In Chapter 2, we have seen that the interactions can be conveniently treated thanks to the mean-field approximation. Under this approximation, the effects of interactions are expected to be negligible. This hypothesis was verified by comparing the experimental data to QMC calculations of the in-trap momentum distribution, obtaining a very good agreement [29]. For more details on this measurement, we refer the reader to the previous manuscripts [25, 28].

The precision set by this kind of benchmarking procedure is totally suited for experiments aiming to measure the in-trap momentum **density** of the gas, *e.g.* to extract the temperature of the gas as described in the previous section. However, to measure correlations between individual particles, we need to be more precise and look for interaction effects that cannot be described by the mean-field approximation. The only likely interaction effects of the kind in our experiment are **two-body collisions**. This section will detail how these collisions occur and how to experimentally characterize them to determine whether they perturb significantly the measured distribution or not.

3.4.1 Presentation of the problem

As we have seen in Chapter 2, the momentum distribution of the lattice gas in the superfluid region of the phase diagram is made of copies of the BEC of momentum $jk_d\boldsymbol{e}_i$ with $j \in \mathbb{Z}$ and $i = x, y, z$. During the TOF, it is possible to observe s-wave collisions between the atoms of these different BEC copies [76]. Let us then for instance consider the case of a collision between an atom in the copy $j = 0$ with initial momentum $\boldsymbol{k}_{i1} = \boldsymbol{0}$ and one in the x copy $j = 1$ with initial momentum $\boldsymbol{k}_{i2} = k_d\ \boldsymbol{e}_x$. If we write these momenta in the center-of-mass reference frame, we rather get $\boldsymbol{k}_{i1} = -k_d/2\ \boldsymbol{e}_x$ and $\boldsymbol{k}_{i2} = k_d/2\ \boldsymbol{e}_x$. As the collision is elastic, the momentum and kinetic energy are conserved so that the momenta of the atoms $\boldsymbol{k}_{f1}$ and $\boldsymbol{k}_{f2}$ after the collision write:

$$\boldsymbol{k}_{i1} + \boldsymbol{k}_{i2} = \boldsymbol{k}_{f1} + \boldsymbol{k}_{f2} = \boldsymbol{0} \tag{3.25}$$

$$\frac{\hbar^2 k_{1f}^2}{2m} + \frac{\hbar^2 k_{2f}^2}{2m} = \frac{\hbar^2 k_d^2}{2m} \tag{3.26}$$

This means that $\boldsymbol{k}_{1f}$ and $\boldsymbol{k}_{2f}$ must have equal norms $k_d/2$ and be antiparallel. Their direction is a priori random. After the collision, the atoms then end up on a sphere of diameter k_d in momentum-space as illustrated on Fig.-3.27. For a large number of collisions, all the atoms that underwent a collision form a spherical halo that we can observe experimentally.

We understand that this effect is detrimental to our measurement, as the collision process changes the momentum distribution of the gas during the TOF, meaning that we

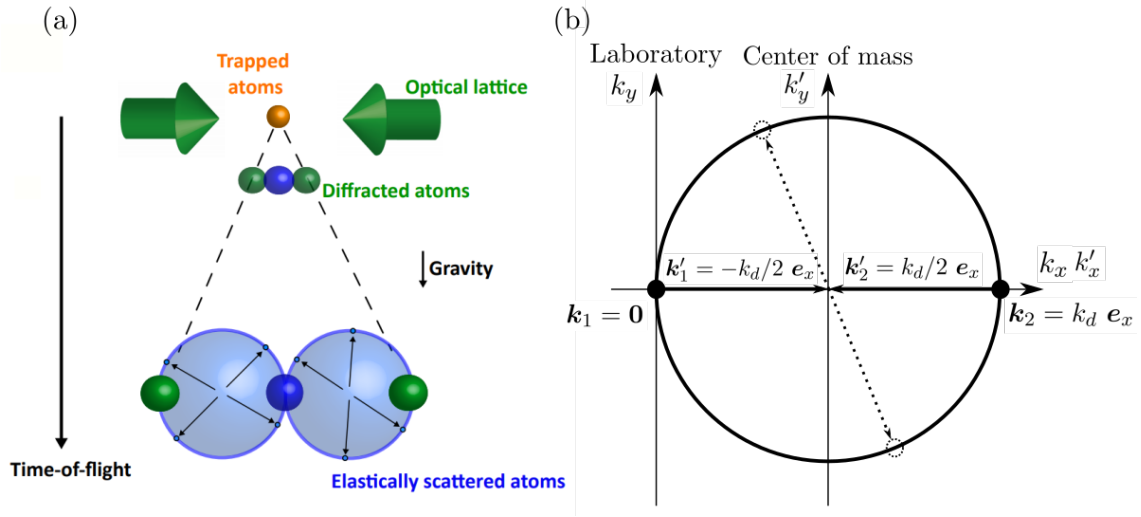

Figure 3.27: Elastic collisions between copies of the condensate. (a) Sketch of the experiment along one axis. During the TOF, diffracted copies of the BEC form as a result of the lattice trapping potential. Two-body collisions can occur between these different diffracted copies and manifest themselves as spherical halos. (b) Illustration of the momentum conservation rule explaining the spherical shape of the scattering halos.

do not measure the true in-trap momentum distribution. However, the scattering halos are not visible for the low atom numbers we wish to work with for the observation of the $\boldsymbol{k}/-\boldsymbol{k}$ pairs of the quantum depletion. While this is a good sign, we would like to know precisely how likely it is for a two-body collision to happen in these conditions so that we can safely apply the ballistic relation. We will then deliberately load a large number of atoms in the optical lattice to observe clear scattering halos and count the number of atoms inside of them in order to validate a simple classical model that we will use to predict the number of collisions at the low atom numbers we wish to use.

3.4.2 Classical model

We will start our study by devising a simple classical model to evaluate the number of collisions before checking its validity experimentally. To illustrate the idea behind it, we compute the number of collisions between the condensate copies $j = 0$ and $j = 1$. The first step is to evaluate the collision rate of one atom at position $\boldsymbol{r}$ at time t belonging to the $j = 0$ BEC copy with all the atoms in the copy $j = 1$. This rate writes [36, 122]:

$$\Gamma_{\text{coll}} = n_1(\boldsymbol{r}, t) \times \sigma \times v_{0,1} \tag{3.27}$$

where n_1 is density of the copy $j = 1$, $v_{0,1} = v_d = \hbar k_d/m$ the relative velocity of the two copies and $\sigma = 8\pi a_s^2$ the scattering cross-section, with a_s the s-wave scattering length (we remind that $a_s = 7.5$ nm for ^{4}He*). To obtain the total number of collisions, we integrate over all particles of the copy $j = 0$ and over the time interval during which the copies spatially overlap. If we wish to obtain the number of collisions for all first order copies, we can simply multiply this number by 6 to finally obtain:

$$N_{\text{coll}} = 6 \int dt \int d\boldsymbol{r}\ \sigma v_d n_0(\boldsymbol{r},t) n_1(\boldsymbol{r},t) \tag{3.28}$$

To evaluate this quantity, we need to determine the density profiles $n_j(\boldsymbol{r},t)$. While a full description of the TOF dynamics would be way too complicated in the frame set by this simple model, the densities can be evaluated by considering the different energies and time scales of the problem. The shortest time scale is set by the frequency of a lattice site ω_{site} to which we associate the corresponding harmonic oscillator length $a_{\text{h.o.}} = \sqrt{\hbar/m\omega_{\text{site}}}$. From this, we compute the time scale $t_0 \simeq mda_{\text{h.o.}}/h \simeq 1\ \mu$s on which the wave-functions of the different sites overlap. After a few t_0, the overall density profile is smoothed with a total size hardly larger than the in-trap size L and a lower density than that in the trap. In turn, the densities profile are then well described by the Thomas-Fermi parabolic profile of the BEC $n_{\text{BEC}}(\boldsymbol{r})$.

We also need to consider other timescales, much larger than t_0 and associated with:

- The spatial separation of two copies $t_{\text{sep}} \sim 2L/v_d \sim 0.1$ ms.
- The expansion of the BEC driven by its kinetic energy $t_{\text{kin}} \sim mL/\hbar\Delta k \sim 10$ ms where Δk is the momentum width of the BEC.
- The expansion of the BEC under the effect of the mean-field potential t_{MF}.

We note that when the size of the trapped gas is much larger than the lattice spacing $L \gg d$ (which is typically the case in our experiment), we get $\Delta k \ll k_d$ explaining why we obtain $t_{\text{sep}} \ll t_{\text{kin}}$. Things are more complicated for t_{MF} as it depends on the number of atoms and can be of the order of t_{sep}. From this, we consider two scenarios: one where the number of atoms is small enough so that mean-field effects can safely be neglected, and one where they must be accounted for.

Scenario 1: mean-field effects are negligible

In this scenario, the size of the BEC copies increases in time only through the effect of kinetic energy. As we have seen that $t_{\text{sep}} \ll t_{\text{kin}}$, we understand that the size of the density profiles hardly changes during the interaction time, *i.e* before separation of the different BEC copies. We can therefore safely assume that the shape of the density profiles does not change during the interaction time, allowing us to evaluate analytically equation 3.28 to obtain:

$$N_{\text{coll}} = \frac{48\alpha_0\alpha_1}{315}\left(\frac{15N_{\text{bec}}\, a_s}{L}\right)^2 \tag{3.29}$$

where we have introduced the coefficients α_j denoting the fraction of the total atom number in one of the copies j. The scaling $N_{\text{coll}} \propto a_s^2 N_{\text{bec}}^2/L^2$ is identical to what was found in previous works describing the collisions between two BECs [174, 175].

Scenario 2: mean-fields effects are not negligible

In this scenario, it is not possible anymore to assume that the shape of the density profiles does not change during the interaction time, making the calculation of equation 3.28 much

more complicated and beyond the scope of this thesis. This is however not really important as the goal of this experiment is to determine the number of collisions at low atom number. If we are able to find atom numbers for which the collisions spheres are visible while the mean-field effects are negligible, we will be able to validate our simple model and use it to predict the number of collisions at low atom numbers. We must however keep in mind that the analytical model of equation 3.29 should fail at high atom numbers. The expansion of the BEC copies induced by the mean-field effects implies a decrease of the density compared to Scenario 1, meaning that we should observe less collisions that what is predicted from equation 3.29.

Actually, it is possible to discriminate between the two scenarios by looking at the width of the collision spheres. When the expansion is ballistic, *i.e* in Scenario 1, the width of the collision sphere that we will note δk_s is equal to the in-trap momentum width $\Delta k \propto 1/L$ and should therefore decrease when the total number of atoms increases. On the contrary, δk_s is increased in Scenario 2 because of the additional kinetic energy resulting from the mean-field interaction potential, meaning that δk_s increases when the strength of mean-field effects increases, *i.e* when the atom number increases. We therefore expect the variations of δk_s with the total atom number N_{bec} to show a minimum that signals the crossover between Scenarios 1 and 2.

3.4.3 Data analysis

We show on Fig.-3.28 the typical detected momentum distribution on which we can see clear scattering halos. We produce a variety of data sets to test the effect of the atom number and of the lattice amplitude. The procedure to count the number of collisions is as follows:

1. For each scattering halo, we restrict the analysis to a small slice so that we exclude the region where the halo intersects with the condensate peaks or other scattering halos as illustrated on the inset of the Fig.-3.29.
2. We calculate for each atom in the slice the momentum distance to the center of the sphere k_r and compute the histogram $\mathcal{N}(k_r)$ of the number of atoms located at a distance k_r. The size of the bins is 0.01 k_d.
3. We account for the efficiency of our detection process α_D by multiplying the value of each bin of the histogram by $1/\alpha_D$. Careful, as this experiment was done before the implementation of the Raman transfer, the efficiency was lower than measured in 3.2.6. A full calibration as the one previously described was not possible as we could not observe clean Rabi oscillations because of the much smaller Rabi frequencies. We therefore measured α_D by recording diluted distributions of Mott insulators to avoid saturation effects and comparing them to absorption images for which we can precisely know the number of atoms. We obtained $1/\alpha_D = 15.5(1.0)$.
4. We obtain histograms such as represented on Fig.-3.29 in which we observe a peak at $k_r = 0.5\ k_d$ signalling the presence of the scattering halo. We remove the contribution of the background that corresponds to the quantum and thermal depletion and fit the peak with a Gaussian function to obtain the width of the halo δk_s and the number of atoms in the slice of scattering halo.
5. Assuming spherical symmetry, the total number of scattered atoms is obtained by integrating the value measured in the slice over the entire sphere.
6. We finally obtain the number of detected collisions $N_{\text{coll}}^{\text{exp}}$ by summing the number of

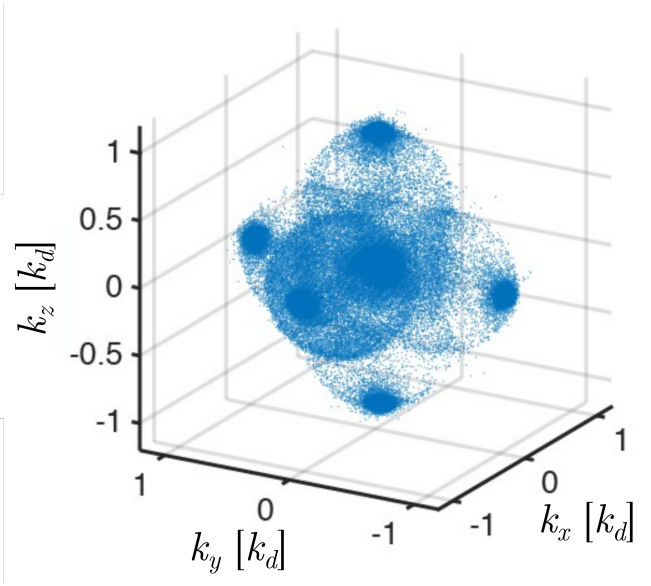

Figure 3.28: 3D momentum distribution of a superfluid lattice gas. The s-wave scattering halos are clearly visible (the BEC peaks are saturated for the scattering halos to be visible).

scattered atoms measured in the different halos. Note that we use only 5 of the 6 first order halos as one of them is partially falling out of the MCP.

Width of the scattering halos

We show on Fig.-3.30 the measured RMS widths of the scattering halos δ_s as a function of the atom number. The error bars are obtained from the error on the Gaussian fit. We observe a minimum around $N_0 \simeq 1.7 \times 10^5$ at which the mean-field effects start playing a significant role. This first result is consistent with the simple picture drawn previously where we identified two regimes distinguished by the different roles played by the mean-field potential during the TOF.

Evolution with total atom number

We plot on Fig.-3.31 panel (a) the evolution of the number of collisions with the total atom number at a fixed lattice amplitude $s = 5$. The vertical error bars account for the standard error of the mean on $N_{\text{coll}}^{\text{exp}}$ and the uncertainty on the detection efficiency. The horizontal error bars depict the standard deviation on N_{bec}. The dashed line represents the analytical model of equation 3.29 where the effect of the atom number is contained in the term $(N_{\text{bec}}/L)^2$ giving in the Thomas-Fermi approximation $N_{\text{coll}} \propto N_{\text{bec}}^{8/5}$. While we find a good agreement with the experimental data at low atom number and without any adjustable parameters, we find that the analytical model overestimates the number of collisions for $N_{\text{bec}} > N_0$. Once again, these results are in line with our simple model even at the quantitative level when the mean-field potential does not affect the TOF dynamics ($N_{\text{bec}} < 2 \times 10^5$). In addition, we plot the probability of collision per atom $\eta_1 = N_{\text{coll}}^{\text{exp}}/N_{\text{bec}}$ in panel (b) of Fig.-3.31.

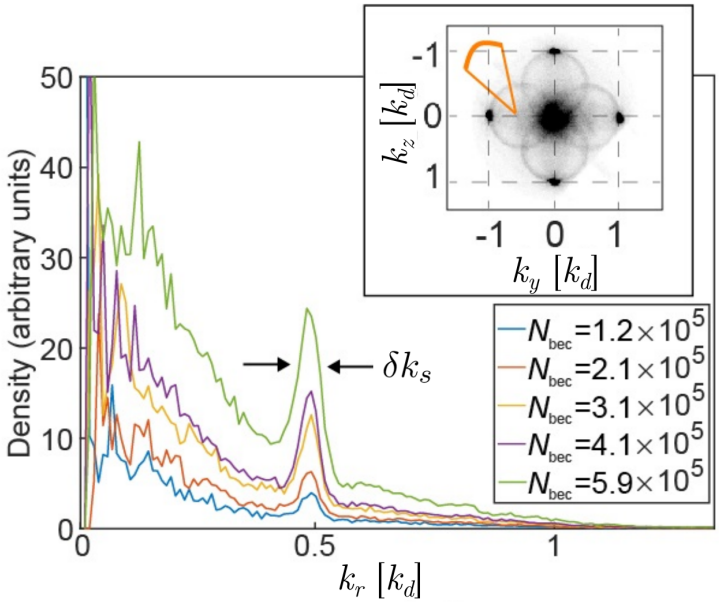

Figure 3.29: Atom numbers histograms as a function of the momentum distance k_r to the center of the scattering halo. We show histograms for different total atom numbers N_{bec} for a fixed lattice amplitude $s = 5$. Inset: two-dimensional cut at $k_x = 0$ through the 3D distribution. The orange region indicates where the number of scattered atoms is calculated.

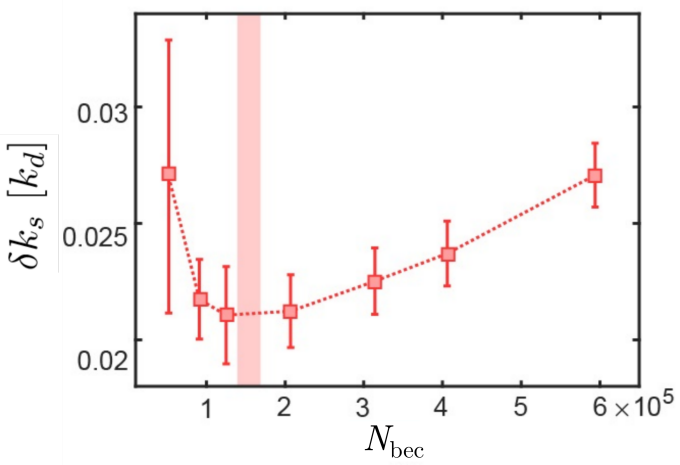

Figure 3.30: RMS width δk_s of the scattering halos as a function of N_{bec}. The red dashed line is a guide-to-the-eye. The red shaded area signals the crossover between the two scenarios described in the main text.

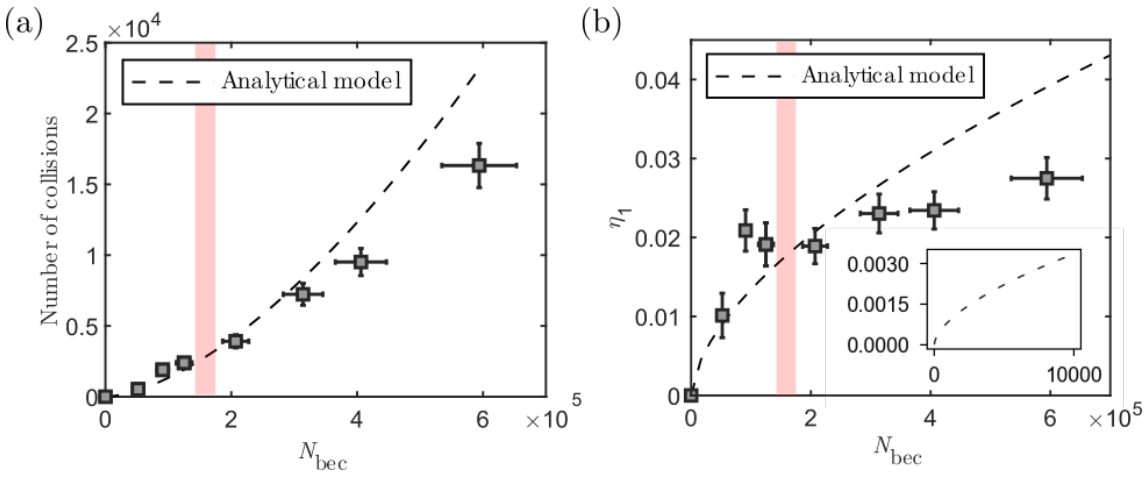

Figure 3.31: (a) Experimental number of collisions $N_{\text{coll}}^{\text{exp}}$ between the copies $j = 0$ and $j = 1$ as a function of the atom number N_{bec} at a fixed lattice amplitude $s = 5$. The dashed line is the analytical model of equation 3.29. (b) Probability of collision per atom $\eta_1 = N_{\text{coll}}^{\text{exp}}/N_{\text{bec}}$. The inset shows a zoom for low atom numbers.

Evolution with lattice depth

We plot on Fig.-3.32 the evolution of the probability of collision per atom η_1 with the lattice amplitude s at a fixed total number of atoms $N_{\text{bec}} = 3.9(4) \times 10^5$. As we have seen in Chapter 2, the lattice amplitude changes the population of the BEC copies and therefore the coefficients α_0 and α_1 appearing in 3.29. At very low lattice amplitudes, the population in the diffracted peaks is very small, $\alpha_0 \simeq 1$, $\alpha_1 \simeq 0$, meaning that the number of collisions is very low. As s increases, the number of collisions increases as α_1 increases. With $s > 5$, we start populating higher orders of diffraction, thus reducing the number of collisions between the copies $j = 0$ and $j = 1$. This explains the non-monotonic behavior of the analytical model that is well reproduced by the experimental data. Once again, the model overestimates the number of collisions as $N_{\text{bec}} > N_0$.

3.4.4 Conclusion

Now that we have validated that our simple model properly works for low atom number, we can extrapolate the probability of collision per atom for the typical atom numbers (a few 10^3) that we wish to use for the $\boldsymbol{k}/-\boldsymbol{k}$ correlation experiment. For $N_{\text{bec}} \sim 5 \times 10^3$, we find as shown on the inset of panel (b) of Fig-3.31 that the probability for an atom to collide during the TOF is $\eta_1 \sim 10^{-3}$ which is extremely low. Before reaching our final conclusion, we need to discuss the contribution of other possible scattering halos, such as the one involving higher order copies $j \geq 2$ or between two first order copies. These halos are more diluted because of a lower number of collisions and larger volume and are in turn not visible in the experiment, but might contribute significantly at high values of s. We can evaluate their contribution by setting the appropriate values of α_j in equation 3.29. We obtain an upper bound by considering the extreme situation where the number of copies would be as large as the number of atoms and find that this increases η_1 by only a factor 3, meaning that the measured probability η_1 gives a good estimate of the total probability of collisions. We can therefore safely conclude that two-body collisions will be negligible in our $\boldsymbol{k}/-\boldsymbol{k}$ pair experiment where only a few 10^3 atoms are loaded into the

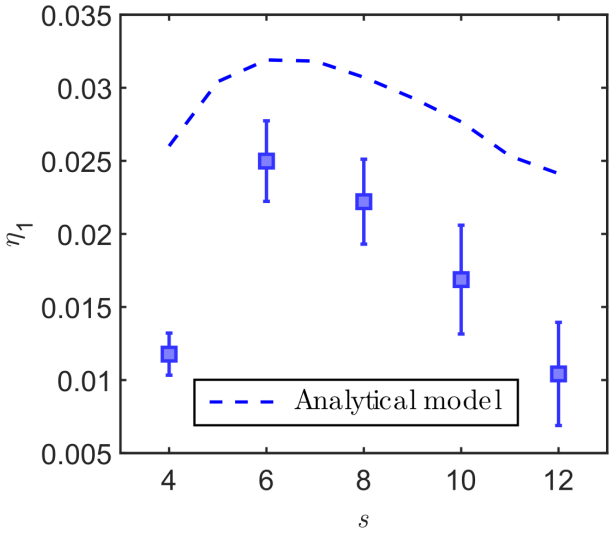

Figure 3.32: Probability of collision per atom η_1 as a function of the lattice depth s at a fixed atom number $N_{\mathrm{bec}} = 3.9(4) \times 10^5$. The blue dashed line is the analytical model of equation 3.29.

3D lattice. This results completes the previous benchmarking experiments [29], proving that the ballistic relation applies in our experiment.

3.5 Conclusion

We have seen in this chapter how metastable Helium ^{4}He* can be brought to quantum degeneracy and how to make use of the properties of the metastable state to implement a 3D single-atom resolved momentum detection technique. Importantly, the population transfer method to decouple the atoms from the magnetic field before the TOF was improved by replacing the former RF transfer by an optical two-photon Raman transfer with two advantages: (i) contrary to the RF transfer where the transfer efficiency is limited to 50% because of the three sub-levels structure of the 2^3S_1 state, we can achieve full population transfer with two-photon Raman transfer, (ii) we can reach much higher effective Rabi frequencies and use shorter pulse durations for which the transfer is unaffected by fluctuations of the magnetic field. We thus improved the detection efficiency by more than a factor ~ 4. This improvement is of primary importance for $\boldsymbol{k}/-\boldsymbol{k}$ correlations measurement as it enhances the probabilty to detect a $\boldsymbol{k}/-\boldsymbol{k}$ pair by a factor 16. Finally, we have certified our ability to adiabatically prepare the gas in the optical lattice in the vicinity of the Mott transition and studied the effects of TOF s-wave two body collisions to ensure that the momentum distribution is not perturbed during the TOF at the single atom level, so that the measured distribution indeed reveals the in-trap distribution. All the lights are then green to proceed with the actual measurement of $\boldsymbol{k}/-\boldsymbol{k}$ correlations as we will now see.

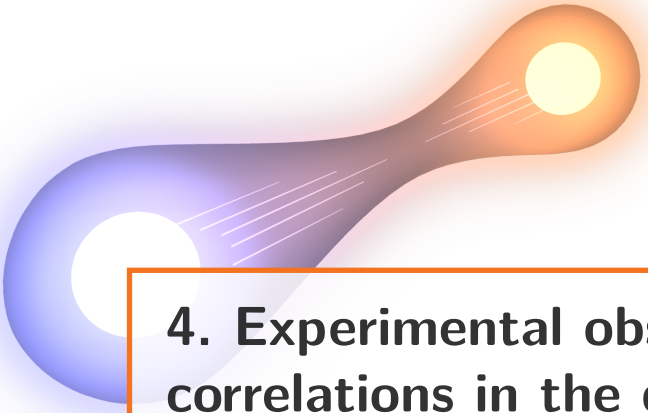

Chapter 4

4. Experimental observation of k/-k correlations in the depletion of a weakly-interacting Bose gas

The weakly interacting Bose gas has been the subject of a large variety of experimental studies, both aiming at measuring the Bogoliubov spectrum of excitations [63, 112, 119, 150] as well as the quantum depletion [33, 106, 166]. However, even though there have been experimental measurements of the Lee, Huang and Yang beyond-mean field correction to the ground-state energy [114, 145], an experimental study of the correlations in the many-body ground-state, and more precisely the observation of the $\boldsymbol{k}/-\boldsymbol{k}$ pairs, is yet to be done more than 60 years after their prediction [103]. As we have seen through the different chapters of this thesis, our experimental setup is perfectly suited for such an investigation.

We will present in this chapter the main result of this thesis, namely the observation of the $\boldsymbol{k}/-\boldsymbol{k}$ pairs of the quantum depletion [155]. We will detail the numerical procedure and the analysis method used to extract the correlation signals and present the experimental results. With the theoretical developments of Chapter 1, we will show how we can link the measured anomalous correlation signal to the $\boldsymbol{k}/-\boldsymbol{k}$ pairs of the quantum depletion by studying the effect of temperature, the widths and amplitudes of the correlation peaks, as well as the fluctuations of the atom number difference between modes $\boldsymbol{k}$ and $-\boldsymbol{k}$. In addition, we will show how our measurement constitutes a first step towards showing the presence of momentum-space entanglement in many-body equilibrium states. We will finally discuss some preliminary results on the evolution of the correlation signals with the region of momentum-space they are probed in.

4.1 Numerical procedure to extract two-body correlations

As seen in the previous chapter, we are capable for each experimental run of reconstructing the 3D momentum coordinates of every atom detected by the He* detector. We must now devise a numerical procedure to extract the two-body correlation signals from this raw data. Our goal is then to compute the general normalized second-order correlation function:

$$g^{(2)}(\boldsymbol{k},\boldsymbol{k'}) = \frac{\langle \hat{a}^\dagger_{\boldsymbol{k}} \hat{a}^\dagger_{\boldsymbol{k'}} \hat{a}_{\boldsymbol{k}} \hat{a}_{\boldsymbol{k'}} \rangle}{\langle \hat{a}^\dagger_{\boldsymbol{k}} \hat{a}_{\boldsymbol{k}} \rangle \langle \hat{a}^\dagger_{\boldsymbol{k'}} \hat{a}_{\boldsymbol{k'}} \rangle} \tag{4.1}$$

We recognize that $\langle \hat{a}^\dagger_{\boldsymbol{k}} \hat{a}_{\boldsymbol{k}} \rangle$ is the momentum density $\rho(\boldsymbol{k})$ in mode $\boldsymbol{k}$. We remind the result of Chapter 1 for weakly-interacting bosons that the $g^{(2)}$ function will take values different from 1 in two cases:

- For $\boldsymbol{k'} \simeq \boldsymbol{k}$, the **normal** correlations corresponding to the Hanbury Brown and Twiss effect also known as bosonic bunching.
- For $\boldsymbol{k'} \simeq -\boldsymbol{k}$, the **anomalous** correlations signalling $\boldsymbol{k}/-\boldsymbol{k}$ pairs in the quantum depletion.

In practice, plotting the $g^{(2)}$ function is not straightforward. On the one hand, the function here is 6D and thus hard to plot in an intelligible way. On the other hand, obtaining a sufficient signal-to-noise ratio for correlation measurements between single modes $\boldsymbol{k}$ and $\boldsymbol{k'}$ whose volume is typically $(1/L_{\mathrm{BEC}})^3$, with L_{BEC} the size of the BEC, is hardly possible. The idea is then to average the $g^{(2)}$ function over a large volume Ω_k of the momentum-space and introduce a new parameter $\delta\boldsymbol{k}$ to write:

$$g^{(2)}_A(\delta\boldsymbol{k}) = \frac{\int_{\Omega_k} \langle \hat{a}^\dagger_{\boldsymbol{k}} \hat{a}^\dagger_{\delta\boldsymbol{k}-\boldsymbol{k}} \hat{a}_{\boldsymbol{k}} \hat{a}_{\delta\boldsymbol{k}-\boldsymbol{k}} \rangle \mathrm{d}\boldsymbol{k}}{\int_{\Omega_k} \rho(\boldsymbol{k}) \rho(\delta\boldsymbol{k}-\boldsymbol{k}) \mathrm{d}\boldsymbol{k}} \tag{4.2}$$

$$g^{(2)}_N(\delta\boldsymbol{k}) = \frac{\int_{\Omega_k} \langle \hat{a}^\dagger_{\boldsymbol{k}} \hat{a}^\dagger_{\delta\boldsymbol{k}+\boldsymbol{k}} \hat{a}_{\boldsymbol{k}} \hat{a}_{\delta\boldsymbol{k}+\boldsymbol{k}} \rangle \mathrm{d}\boldsymbol{k}}{\int_{\Omega_k} \rho(\boldsymbol{k}) \rho(\delta\boldsymbol{k}+\boldsymbol{k}) \mathrm{d}\boldsymbol{k}} \tag{4.3}$$

With this definition, we see that for $\delta\boldsymbol{k} = \boldsymbol{0}$, we are either looking at **anomalous** $\boldsymbol{k}/-\boldsymbol{k}$ correlations (equation 4.2) or **normal** $\boldsymbol{k}/\boldsymbol{k}$ correlations (equation 4.3). Note that the absence of a subscript (N, A) in the following denotes a general calculation valid for both normal and anomalous correlation functions. We reduced the 6D function to a 3D function of the parameter $\delta\boldsymbol{k}$ which equals $\boldsymbol{0}$ when the correlation condition $\boldsymbol{k'} = \pm\boldsymbol{k}$ is fulfilled. This gives us a natural way to evaluate $g^{(2)}(\delta\boldsymbol{k})$ with the experimental data: we compute the values of the parameter $\delta\boldsymbol{k}$ for every detected atom pairs in an experimental run by calculating their momentum sum or difference for anomalous and normal correlations respectively. By computing the histogram of these values and averaging over many experimental runs, we evaluate the numerator of equation 4.2 or 4.3 respectively.

4.1.1 Description of the algorithm

The algorithm described here is similar to the one used in our previous works [26, 30] and detailed in [25, 28]. This previous version was mainly designed for the observation of bosonic bunching. I adapted the algorithm to make it suitable for the calculation of $\boldsymbol{k}/-\boldsymbol{k}$ correlations as well, as we will discuss now.

Numerator calculation

The first step is to compute the numerator of equations 4.2 or 4.3 that we denote $G^{(2)}(\delta\boldsymbol{k})$. We note N_{runs} the number of experimental runs and N_i the number of atoms in the i-th shot. The procedure is as follows:

Algorithm 1 $G^{(2)}$ calculation

```
for i = 1 : N_runs do
    for j = 1 : N_i do
        for p = 1 : N_i do
            Compute δk = k_j ± k_p
            Increment the corresponding voxel in 3D histogram G^(2)
        end for
    end for
end for
```

We end up with a 3D histogram where each voxel is associated to a value of $\delta\boldsymbol{k} = (\delta k_x, \delta k_y, \delta k_z)$ and records how many atom pairs have this specific momentum sum or difference, depending on the kind of the correlations probe. The voxels are set to be cubic of dimension $\Delta k_{\parallel}$. The value of $\Delta k_{\parallel}$ is adapted so that we can properly resolve the correlation peaks while ensuring a proper signal-to-noise ratio. In practice, we use $\Delta k_{\parallel} = 1.2 \times 10^{-2}\ k_d$ for $\boldsymbol{k}/-\boldsymbol{k}$ correlations and $\Delta k_{\parallel} = 6 \times 10^{-3}\ k_d$ for $\boldsymbol{k}/\boldsymbol{k}$ correlations as the correlation peak is narrower than the anomalous one (see 1.4).

The major difference with the previous version of the algorithm (see Appendix of [26]) is that we record here the full 3D histogram of calculated $\delta\boldsymbol{k}$ on every pair of atoms. The procedure was originally made simpler by calculating three one-dimensional histograms, one for each direction of space. Each of these histograms represents a one-dimensional cut of the general 3D correlation function $G^{(2)}(\delta\boldsymbol{k})$. For instance, to obtain the x direction histogram, for the atom j in run i, we calculate δk_x only for atoms p close enough in momentum-space to find a $\boldsymbol{k}/\boldsymbol{k}$ correlation, *i.e* with $|k_y^{(j)} - k_y^{(p)}| \leq \Delta k_{\perp}$ and $|k_z^{(j)} - k_z^{(p)}| \leq \Delta k_{\perp}$, where $\Delta k_{\perp}$ defines a transverse integration (see later). This method obviously saves computing time and RAM space, but is not suited to look for $\boldsymbol{k}/-\boldsymbol{k}$ correlations.

At this point, we record in the central voxels associated to $\delta\boldsymbol{k} \simeq \boldsymbol{0}$ what we call **true coincidences**, namely two atoms detected conjointly as a result of $\boldsymbol{k}/-\boldsymbol{k}$ pairing or bosonic bunching. However, we also record **accidental coincidences** that do not represent correlations but result from the momentum distribution of the atoms. We then need a normalization process to get rid of the contribution of accidental coincidences, *i.e* a method to compute the denominator of equation 4.2 or 4.3.

Denominator calculation

We now compute the denominator of equation 4.2 or 4.3, representing the effect of accidental coincidences. To perform this calculation, we would like to use a sample of uncorrelated atoms with the same momentum density than our experimental data. This can be done by merging all experimental shots together, each shot being uncorrelated with one another. We then apply the procedure we have just described to this data set. However, the correlations present within single shots remain in this large file. In the end, the total number of correlations in the numerator is $\sum_i N_i^2$ whereas the number of coincidences in

the merged file is $(\sum_i N_i)^2$. With $\bar{N}$ the mean number of atoms per shot, we see that:

$$\frac{\sum_i N_i^2}{(\sum_i N_i)^2} = \frac{N_{\text{runs}}\bar{N}^2}{N_{\text{runs}}^2\bar{N}^2} = \frac{1}{N_{\text{runs}}} \tag{4.4}$$

Therefore, with enough shots (we use $N_{\text{runs}} = 2 \times 10^3$ in the experiment), the contribution of residual coincidences is negligible and the normalization procedure valid.

In the end, the integrated $g^{(2)}$ function is obtained by dividing the numerator histogram by the denominator and multiplying by the normalization factor $\frac{(\sum_i N_i)^2}{\sum_i N_i^2}$ that takes into account the number of coincidences of the numerator and denominator. Note that it is possible to take a fraction of all atoms for the denominator calculation to avoid large computation time. This is particularly handy to have quick first results before launching longer calculations for a nicer signal-to-noise ratio.

4.1.2 Saturation of the detector and reconstruction errors

As we have seen in 3.2.4, the algorithm reconstructing the positions at which the atoms fall on the MCP can give wrong results when the atomic flux is too high, which is typically the case with the very dense condensed diffraction peaks. This effect is particularly detrimental to the measurements described in this chapter as it artificially creates $\boldsymbol{k}/-\boldsymbol{k}$ pairs. To circumvent this issue, we remove from the analysis the momentum region where $|k_z| < 0.05\ k_d$ which corresponds to the region where the wrongly reconstructed BEC atoms are, at the expense of losing some possible "true" pairs located in this region. We check that the wrongly reconstructed atoms have been correctly removed from the analysis by watching the saturation cross disappear as illustrated on Fig.-4.1.

4.1.3 Transverse integration

Now that we know how to numerically obtain the 3D histogram of the $g^{(2)}$ function, we must discuss how to represent the data. One of the most natural and intelligible way to do so is to plot 1D cuts of the $g^{(2)}$ function along the three direction of space to properly visualize the 3D correlation peak located in $\delta\boldsymbol{k} = \boldsymbol{0}$. To extract a 1D cut along the x direction for instance, we could simply take the line of voxels verifying $\delta k_y = \delta k_z = 0$. However, this is often not sufficient to have a proper signal-to-noise ratio. We therefore rather average the values of several voxels lines associated to $\delta\boldsymbol{k}$ values verifying $|\delta k_y, \delta k_z| \leq \Delta k_\perp$ as illustrated on Fig-4.2, where $\Delta k_\perp$ defines the transverse integration. Note that this procedure applies for both normal and anomalous correlation functions.

We now write what is the signal that is plotted when this process is applied. The theoretical, normalized and integrated two-body correlation function is well modelled in first approximation by a 3D Gaussian function:

$$g^{(2)}(\delta\boldsymbol{k}) = 1 + \eta_0 \prod_{i=x,y,z} \exp\left(\frac{-\delta k_i^2}{2\sigma_i^2}\right) \tag{4.5}$$

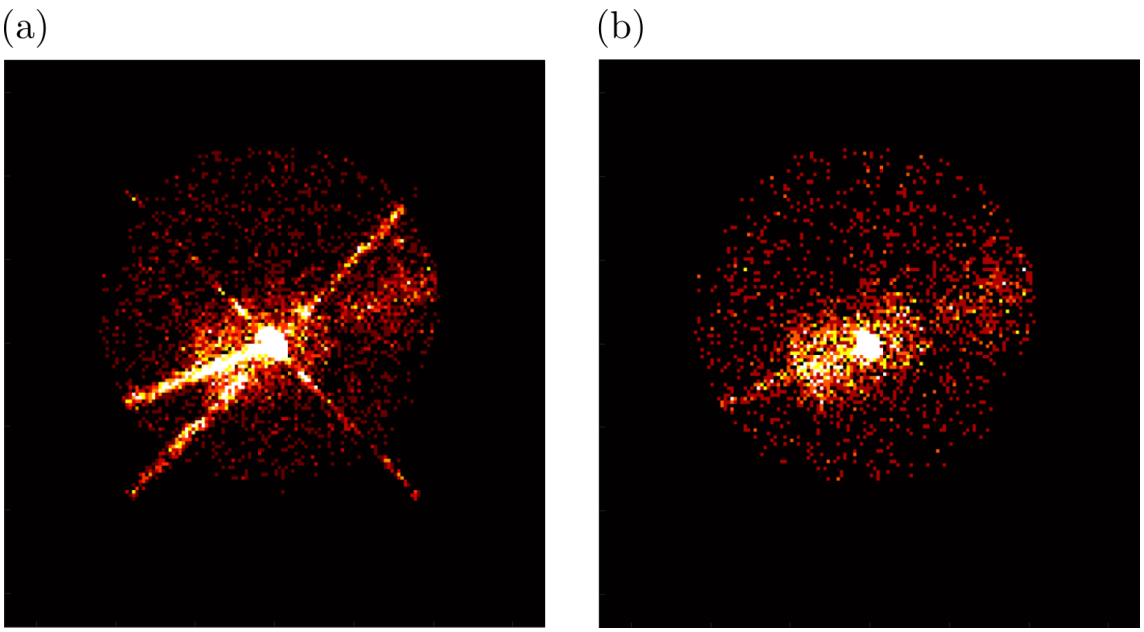

Figure 4.1: Correction of software saturation. (a) Time integrated 2D MCP image, uncorrected, with the saturation cross as already shown in 3.2.4. (b) Same image where the region $|k_z| < 0.05\ k_d$ has been removed. The saturation cross has disappeared.

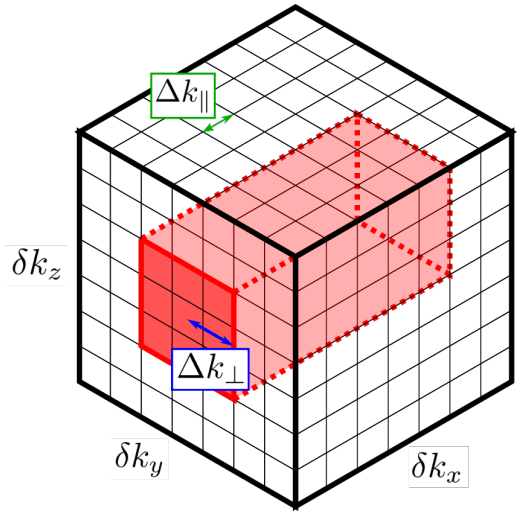

Figure 4.2: Illustration of the transverse integration. Every voxel contains the value of the $g^{(2)}$ function for a given value of $\delta\boldsymbol{k} = (\delta k_x, \delta k_y, \delta k_z)$. The figure illustrates the procedure to take a 1D cut in the x direction: we average over several pixel lines to increase the signal-to-noise ratio. This is the transverse integration $\Delta k_{\perp}$ as defined on the schematic.

where we introduce η_0 the amplitude of the correlation peak and σ_i the RMS width of the correlation peak in direction $i = x, y, z$. Importantly, we have assumed that the different correlation axes are separable. We re-write this equation to account for the transverse integration process, with the example of a cut along the x direction:

$$g^{(2)}\left(\delta k_x\right) = \frac{1}{\left(2\Delta k_\perp\right)^2} \iint_{-\Delta k_\perp}^{\Delta k_\perp} \left(1 + \eta_0 \prod_{i=x,y,z} \exp\left(\frac{-\delta k_i^2}{2\sigma_i^2}\right) \mathrm{d}\delta k_y \mathrm{d}\delta k_z\right) \tag{4.6}$$

This expression can be analytically evaluated and writes:

$$g^{(2)}\left(\delta k_x\right) = 1 + \eta_0 \frac{2\pi\sigma_y\sigma_z}{\left(2\Delta k_\perp\right)^2} \exp\left(\frac{-\delta k_x^2}{2\sigma_z^2}\right) \mathrm{erf}\left(\frac{\Delta k_\perp}{\sqrt{2}\sigma_y}\right) \mathrm{erf}\left(\frac{\Delta k_\perp}{\sqrt{2}\sigma_z}\right) \tag{4.7}$$

Note that we have here neglected the small longitudinal integration induced by the size of the voxel, which is typically 3 times smaller than the RMS width of the correlation peaks in our experimental data. In addition, we assume that the correlation peaks are isotropic as the lattice potential and then the spatial size of the gas are isotropic, giving $\sigma_x = \sigma_y = \sigma_z = \sigma$. We thus see that when measuring any correlation peak amplitude with a Gaussian fit on a 1D cut of the $g^{(2)}$ function, we get a reduced amplitude η that writes:

$$\eta(\Delta k_\perp) = \eta_0 \times \frac{2\pi\sigma^2}{(2\Delta k_\perp)^2} \left[\mathrm{erf}\left(\frac{\Delta \mathrm{k}_\perp}{\sqrt{2}\sigma}\right)\right]^2 \tag{4.8}$$

The idea is then to measure η for several values of $\Delta k_\perp$ and fit the data with equation 4.8 with η_0 and σ as free parameters. This is illustrated on Fig-4.3 and Fig.-4.4 for $\boldsymbol{k}/\boldsymbol{k}$ and $\boldsymbol{k}/-\boldsymbol{k}$ correlations respectively. For a single value of the transverse integration, η is obtained by averaging the 3 amplitudes fitted on the 1D cuts along the 3 directions of space. The uncertainty on the parameters of the fit defines the error bars on the amplitude.

In addition, we have checked that the transverse integration process does not significantly change the width of the correlation peak as shown on the inset of Fig.-4.4. The extracted width is therefore the fitted width at the lowest transverse integration for which we get a satisfactory signal to noise ratio.

4.1.4 Benchmarking of the algorithm with two-body scattering spheres

Before using the algorithm to look for $\boldsymbol{k}/-\boldsymbol{k}$ pairing signal in the depletion of a weakly-interacting Bose gas, it was crucial to test it on a data set with a large number of $\boldsymbol{k}/-\boldsymbol{k}$ pairs to certify that it was working properly. Luckily, we could re-use the data taken for measuring two-body collisions during the time-of flight described in Chapter 3. Indeed, because of the elastic character of the collision, every atom on a scattering sphere is correlated with a partner on the other side of the sphere, yielding $\boldsymbol{k}/-\boldsymbol{k}$ correlations in the reference frame of the center of mass of the colliding BECs [85, 123]. In addition to the 3D diffraction data that we already presented, we also acquired data in a single lattice beam configuration to induce 1D diffraction and obtain only two scattering spheres (see

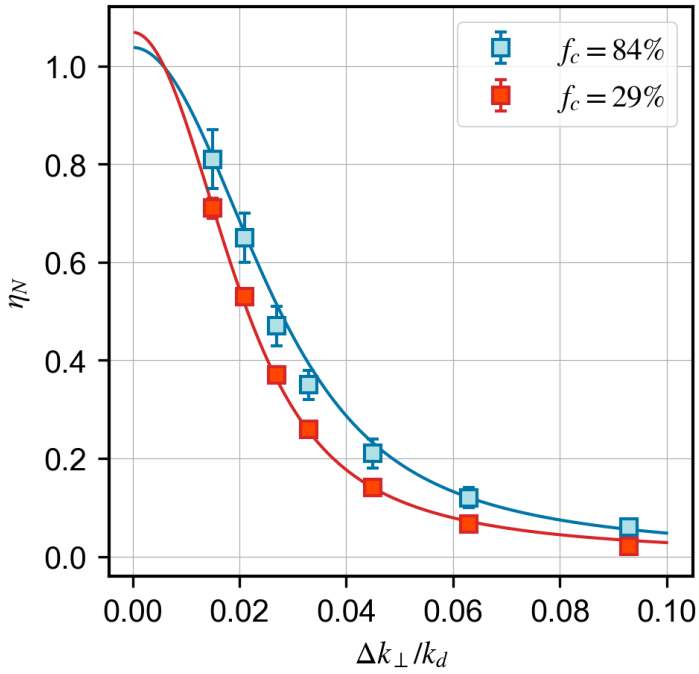

Figure 4.3: Fitted amplitude of the normal correlation peak η_N as a function of the transverse integration $\Delta k_\perp$ for data sets with different condensed fraction. The data is fitted with model defined in equation 4.8 with η_0 and σ as free parameters. This method allows us to extract the amplitude at zero transverse integration $\eta_{0,N}$.

Fig.-4.5). The advantage is that we have a large number of atoms in these scattering spheres, making the analysis easier.

Contrary to the $\boldsymbol{k}/-\boldsymbol{k}$ correlations of the quantum depletion, we de not expect a correlation peak at $\delta\boldsymbol{k} = \boldsymbol{0}$. If we consider for instance collisions between the 0th and 1st orders of diffraction along z, the overall momentum before and after the collision is $k_d\boldsymbol{e_z}$ ($\boldsymbol{e_z}$ is the unitary vector of the z axis), so that the sum of the momenta of the two correlated atoms after the collision must be $k_d\boldsymbol{e_z}$. We thus expect a correlation peak for each sphere, one at $\delta k = (0, 0, +1\ k_d)$ and one at $\delta k = (0, 0, -1\ k_d)$.

We run the algorithm on the experimental data and obtain the results shown in Fig.-4.6. We observe two correlation peaks at the expected locations! We can now extract the widths and amplitudes of the peaks with a Gaussian fit and see if they match with the results of [154] detailled in Chapter 3. We find RMS widths of $\sigma_A = 2.3(9) \times 10^{-2}\ k_d$ and $\sigma_A = 2.7(8) \times 10^{-2}\ k_d$ for the spheres centered on $-k_d$ and $+k_d$ respectively, the error bars being given by the uncertainty on the fit coefficients. This is consistent with the measured widths of the scattering halos presented in 3.4.3, namely $\delta k_s = 2.1(9) \times 10^{-2}$ for $N_{\mathrm{bec}} = 1.25 \times 10^5$ close to the total number of atoms used here. The prediction of the amplitude is rather straightforward in this configuration as we know that every atom on the sphere has a momentum correlated partner, allowing us to compare it to the experiment. To count the experimental number of detected pairs, we use the following procedure:

1. The voxel size is increased to $\Delta k_{\parallel} = 0.25\ k_d$ so that a single voxel contains the

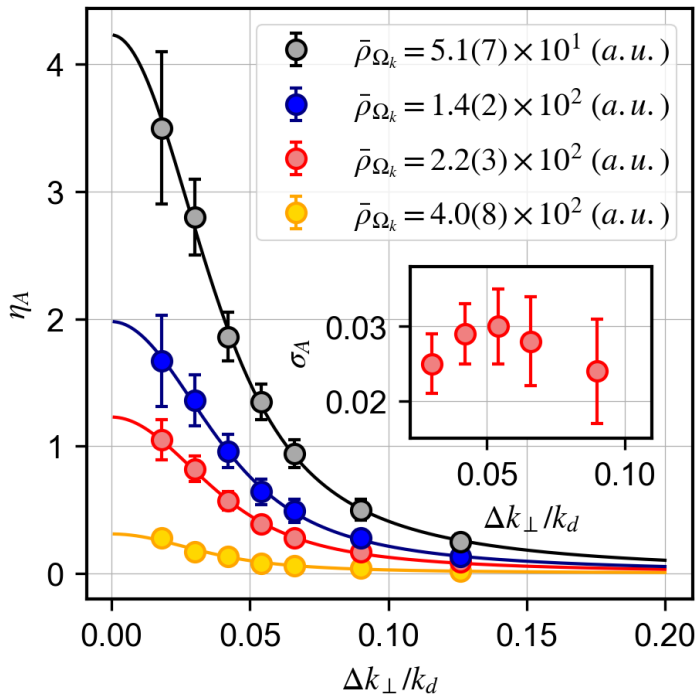

Figure 4.4: Fitted amplitude of the anomalous correlation peak η_A as a function of the transverse integration $\Delta k_\perp$ for data sets with various average densities $\bar{\rho}_{\Omega_k}$ (see later). The inset represents the fitted width σ_A as a function of the transverse integration $\Delta k_\perp$. No significant effect can be observed within the error bars.

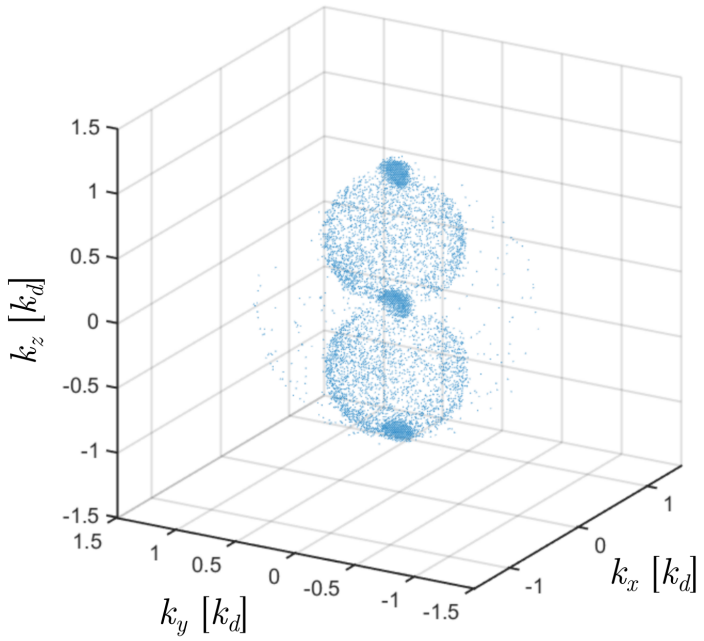

Figure 4.5: 1D diffraction and associated scattering spheres. Note that while the condensed peaks are shown here, they are removed before calculating the correlations.

correlation peak entirely to count all true correlations.

2. We count the number of coincidences $N_{\text{numerator}}$ in the voxel centered on a correlation peak of the numerator histogram of equation 4.2.
3. We count the number of coincidences $N_{\text{denominator}}$ in the same voxel of the denominator of equation 4.2 to evaluate the number of accidental coincidences.
4. As the numerator contains both true and accidental coincidences, we evaluate the number of true coincidences by subtracting the number of accidental coincidences and taking into account the normalization factor:

$$2N_{\text{pairs}} = \left(N_{\text{numerator}} - N_{\text{denominator}}\right) \times \frac{\sum_i N_i^2}{(\sum_i N_i)^2} \tag{4.9}$$

where the factor 2 is added as we define N_{pairs} as the number of pairs and we rather obtain the number of paired atoms with this formula.

We find that the average number of detected pairs per run is $N_{\text{pairs}}/N_{\text{runs}} = 6.25$. This number must be compared to the number of pairs that we expect from the number of atoms in the spheres that we evaluate using the following procedure:

- Writing N_{tot} the total atom number in a given sphere, we know that we should detect $N_{\text{tot}}\alpha_{\text{MCP}}^2/2$ correlated pairs, where α_{MCP} is the detection efficiency of the He* detector.
- The number of detected atoms in the considered sphere is simply $N_{\text{tot}}\alpha_{\text{MCP}}$. Multiplying this measured number by $\alpha_{\text{MCP}}/2$, we thus obtain the expected number of correlated pairs.

We find that we expect to detect 8.5(5) pairs per run which is rather consistent with the number of detected pairs per run. The uncertainty is given by the uncertainty on the detection efficiency. Note that as this experiment was done before the implemention the two-photon Raman transfer scheme, the detection efficiency was lower than what was calibrated in Chapter 3 and was equal to $\alpha_{\text{MCP}} = 6.5(4)\%$.

4.2 Observation of the pair correlation signal

Now that we have determined the numerical procedure to extract the correlation signals from the raw data, we look to apply it on our experimental data. In this section, we will present the measured $\boldsymbol{k}/-\boldsymbol{k}$ correlation signal of which we will try to understand the main features. Our goal is to first identify clear arguments linking this signal to the quantum depletion, before going into quantitative details that will be the subject of the next section.

4.2.1 Accessing the BEC depletion

In order to detect $\boldsymbol{k}/-\boldsymbol{k}$ pairs in the depletion, it is absolutely crucial to remove from the analysis all atoms belonging to the BEC and its diffracted copies as explained in Chapter 1 1.5.1. For each recorded data set and before running the algorithm, we remove all atoms outside the volume Ω_k that we design to exclude momentum regions with condensed atoms as illustrated on Fig-4.7. We set Ω_k to have a cubic symmetry that matches the symmetry of the momentum distribution in a cubic lattice. We remove all atoms with $|k_i| < k_{\text{min}}$

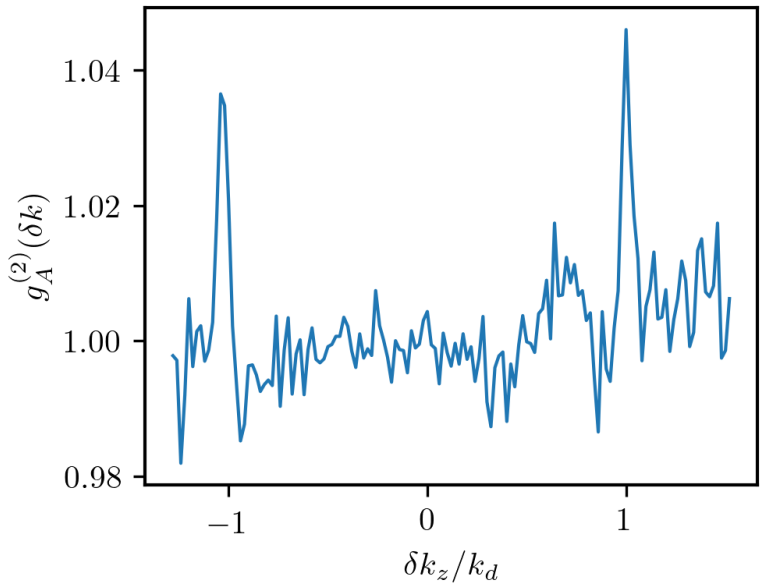

Figure 4.6: 1D cut of the anomalous correlation function $g_A^{(2)}$ along the z axis. We observe two correlation peaks, one for each correlation sphere. The longitudinal size of the voxels is $\Delta k_{\parallel} = 2 \times 10^{-2}$ and the transverse integration $\Delta k_{\perp} = 9 \times 10^{-2}$.

and $|k_i| > k_{\text{max}}$ where k_i is the momentum projection along an axis $i = x, y, z$. We use $k_{\text{min}} = 0.15\, k_d$, corresponding to ~ 6 times the RMS width of the BEC peaks, in order to ensure that all condensed atoms have been removed. The high limit is set to $k_{\text{max}} = 0.85\, k_d$ to exclude higher order peaks and is slightly smaller than the momentum range probed by the He* detector. In terms of healing length, this corresponds to $0.85 \leq |k|\xi \leq 1.15$, *i.e* the region where the phononic character of the Bogoliubov quasi-particles is negligible and thus where finite temperature excitations do not contribute to the anomalous correlations (see 1.3).

4.2.2 First characterization of the pair correlation signal

We now look to observe the $\boldsymbol{k}/-\boldsymbol{k}$ pairs of the quantum depletion. We prepare a BEC with a target number of $N_{\text{bec}} = 5 \times 10^3$ atoms in an optical lattice of amplitude $V = 7.75\ E_r$. With this lattice amplitude, we are in the superfluid regime of the phase diagram in which we expect the $\boldsymbol{k}/-\boldsymbol{k}$ correlations: we measure a condensed fraction of 84% corresponding to a depletion level for which the Bogoliubov theory is expected to hold (see Supp. Mat. of [106]). In order to have sufficient statistics, we repeat the experiment $\sim 4,000$ times. In practice, we cannot prepare BECs with the exact same number of atoms at each shot. Note that the atom number fluctuations of large BECs of $N_{\text{bec}} = 5 \times 10^5$ atoms are below 10% but when we attempt to work with only $N_{\text{bec}} = 5 \times 10^3$ atoms, shot-to-shot fluctuations are much larger. We then need to post-select the data and remove runs with a detected atom number falling too far from the target number. This is one of the strengths of our experiment: as each atom has the same probability of being detected, we can select shots with the good total atom number a posteriori with a precision unattainable with optical imaging measuring densities. This must however be mitigated by the fact that saturation effects reduce the number of detected atoms in a way that can be hard to

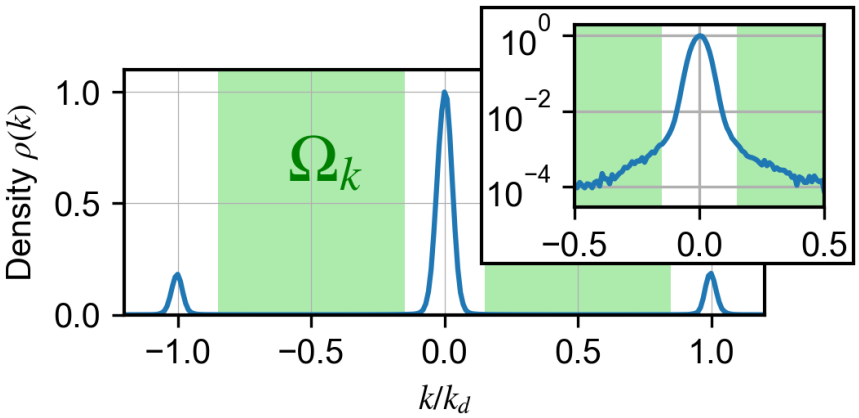

Figure 4.7: 1D cut of the momentum density illustrating the integration volume Ω_k. The central peak corresponds to the BEC and the lateral peaks at $\pm\ k_d$ to diffraction peaks induced by the presence of the optical lattice. The green area shows the volume Ω_k containing the depleted atoms selected for the correlation measurement. While barely visible in linear scale, they can be seen in the log scale plot shown in inset.

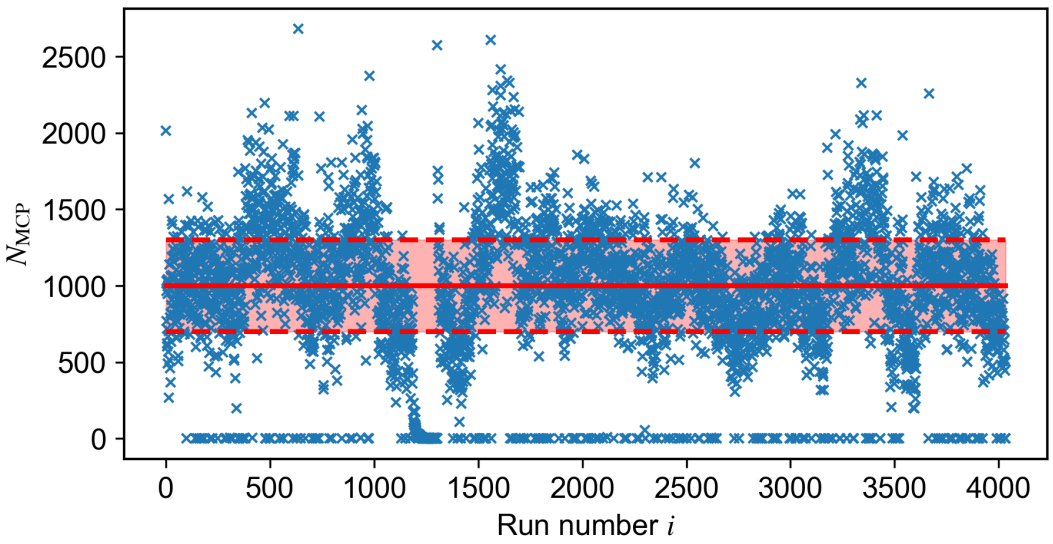

Figure 4.8: Number of detected atoms N_{MCP} for each experimental runs of a data set. The full red line represents the target detected atom number. The red shaded area between the dashed lines illustrate the allowed fluctuations of the detected atom number. All runs outside of the red area are rejected.

predict precisely. We allow for 30% fluctuations around the target number (see Fig.-4.8) and end up conserving around $\sim 2,000$ runs on which we run the algorithm.

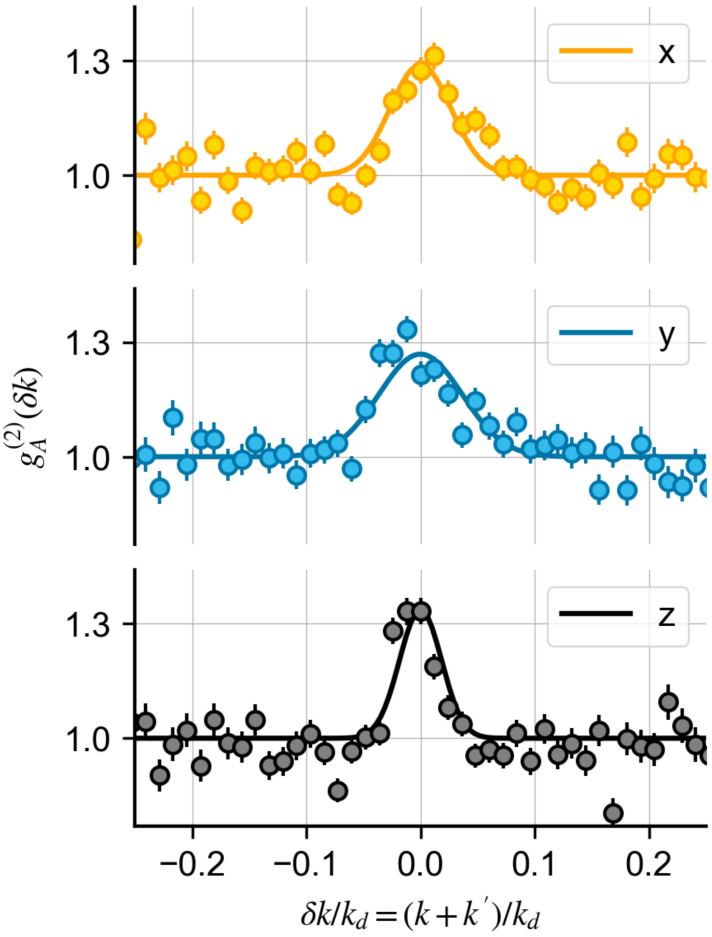

Figure 4.9: 1D cuts through the anomalous correlation function $g_A^{(2)}$ along the axis of the 3D optical lattice. The transverse integration is $\Delta k_\perp = 3 \times 10^{-2}\ k_d$ and the longitudinal voxel size is $\Delta k_\parallel = 1.2 \times 10^{-2}\ k_d$. The data is fitted by Gaussian functions (solid lines). The nice correlation peaks signal the presence of $\boldsymbol{k}/-\boldsymbol{k}$ pairs. The error bars are obtained from the inverse square root of the number of counts in the voxels.

We have plotted on Fig-4.9 1D cuts through the calculated $g_A^{(2)}$ function on which we see clear correlation peaks standing out from the noise! This is the kind of signal we were aiming to obtain and constitutes the central result of this thesis. Before analyzing the features of this correlation signal in more details, we conduct a first series of experimental checks. First, we extend the range of $\delta\boldsymbol{k}$ on which we plot the $g_A^{(2)}$ function to find correlation peaks at $\delta k = \pm k_d$ as shown on Fig.-4.10. This is something that we expected from Bloch theorem (see 2.1) as the lattice is a periodic potential.

Furthermore, we check that there are no correlations in the coherent BEC state. We do so by selecting atoms with $|k_i| < 0.04\ k_d$ with $i = x, y, z$. We show on Fig.-4.11 the calculated normal and anomalous correlation functions for the mode of the BEC. As expected, both correlation functions are flat, except for a small modulation of the order of

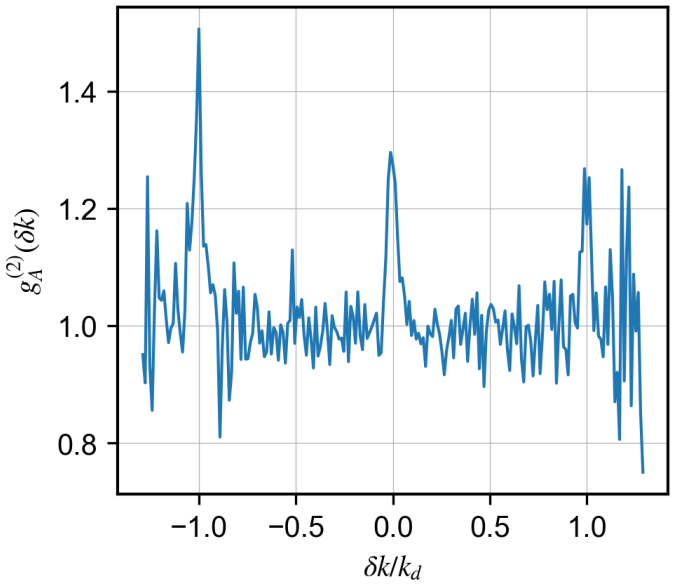

Figure 4.10: 1D cut of the anomalous correlation function $g_A^{(2)}$. Because of the lattice periodic potential, we observe additional correlation peaks at $\pm k_d$.

1% that is an artifact of the normalization procedure caused by shot-to-shot fluctuations of the width of the BEC (see [28]).

Now that we have observed an anomalous correlation signal, we must ask whether its origin is indeed the one we expect, namely $\boldsymbol{k}/-\boldsymbol{k}$ pairing in the quantum depletion as a result of the interplay between interactions and quantum fluctuations. For starters, one of the key specificity of the $\boldsymbol{k}/-\boldsymbol{k}$ pairs of the quantum depletion is that they exist in an **at-equilibrium** system. This is in strong contrast with **out-of-equilibrium** configurations where non-linearities efficiently drive resonant processes. In these cases, both momentum and energy are conserved. In fact, $\boldsymbol{k}/-\boldsymbol{k}$ pairing in such out-of-equilibrium systems has already been observed on various experimental platforms such as:

- Parametric down conversion in quantum optics [21].
- Dissociation of diatomic molecules in atomic physics [78].
- Elastic collisions in high energy physics [3] or with ultracold atoms [123] as we have seen earlier (see Fig.-4.6).

A main difference with the $\boldsymbol{k}/-\boldsymbol{k}$ correlation signal obtained in the scattering spheres is that we observe here a peak located at $\delta\boldsymbol{k} = \boldsymbol{0}$. This signals that the total momentum of the atom pair is $\boldsymbol{0}$. As our system consists of an at-rest BEC, the pairing process could not have resulted from an out-of-equilibrium effect. We remind here an important point of 1.2.5, which is that if we isolate a single collision, we find that the energy is not conserved as the two colliding atoms acquire momenta $\boldsymbol{k}$ and $-\boldsymbol{k}$ meaning that the total kinetic energy is $2(\hbar^2k^2/2m) \neq 0$. This shows that this effect cannot be explained classically because of the origin of the pairs, namely the quantum fluctuations. The pairs cannot be isolated as they form a single quantum state with the BEC, the many-body ground-state. This point constitutes the novelty of our experimental observation.

While these first observations seem to point towards the fact that we are indeed seeing

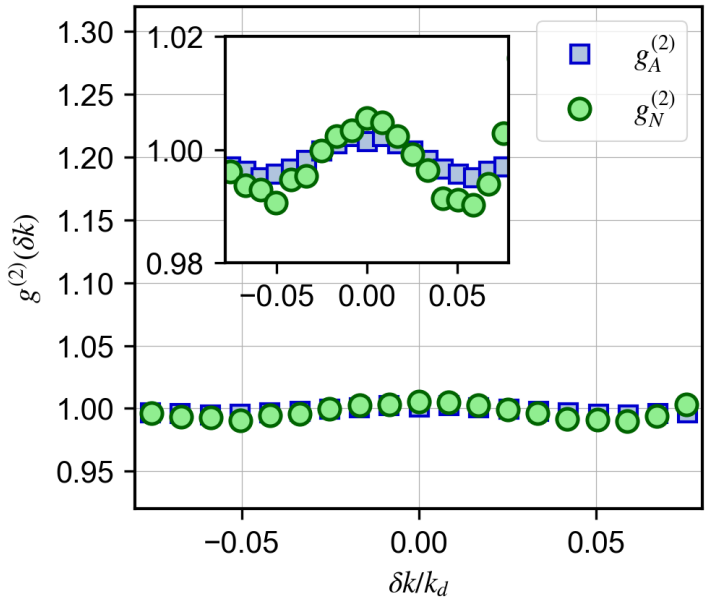

Figure 4.11: Normal and anomalous correlation functions in the BEC. The correlation functions are flat, except for a small-amplitude modulation that is due to normalisation issues induced by shot-to-shot fluctuations of the BEC width in momentum-space.

the $\boldsymbol{k}/-\boldsymbol{k}$ pairing of the quantum depletion, we look to further characterize the correlation signal and determine whether our observations are consistent with the results of the Bogoliubov theory to prove this point. To this end, we will first study the effect of temperature that is supposed to destroy the $\boldsymbol{k}/-\boldsymbol{k}$ correlation signal linked to $T = 0$ quantum coherences, as explained in Chapter 1 1.5.2.

4.2.3 Effect of temperature

The temperature can be increased in a rather simple manner by holding the atoms at the final amplitude of the lattice for a longer duration, the gas being continuously heated over time (attributed to imperfections such as spontaneous emission or mechanical vibrations). We repeat the experiment with a holding time of 500 ms corresponding to hundreds of tunneling times $225 \times h/J$. The increase in temperature can be seen by looking at the momentum density profile as shown in the panel (b) of Fig-4.12: the thermal depletion has increased, increasing the momentum density in the depletion region by a factor ~ 4. Note however that we did not increase the temperature too much to keep a significant condensed fraction of the order of $f_c = 29\%$ (in the absence of BEC there is no quantum depletion). As the thermally depleted atoms show no $\boldsymbol{k}/-\boldsymbol{k}$ correlations, only the denominator of equation 4.2 increases as both $\rho(\boldsymbol{k})$ and $\rho(-\boldsymbol{k})$ increases each by a factor 4, thus reducing the amplitude of the anomalous correlation function by at least a factor 16, bringing it under the experimental noise as we see on Fig-4.12 panel (a). Note that this reduction factor could in fact be even larger as the condensed fraction is small, meaning that the Bogoliubov approximation should not hold anymore.

We also repeated the experiment for an intermediate temperature obtained with a holding time of 200 ms corresponding to $90 \times h/J$ tunneling time. The condensed fraction

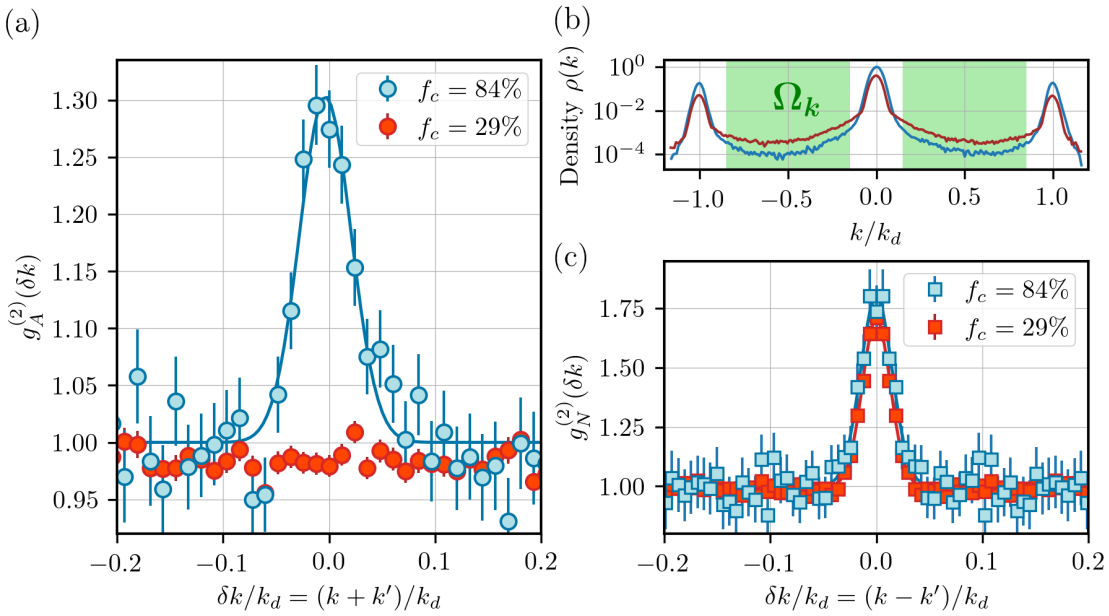

Figure 4.12: Atom-atom correlations in weakly-interacting BECs at two different temperatures. The data for the low-temperature BEC ($f_c = 84\%$), *resp.* for the heated BEC ($f_c = 29\%$), are depicted in blue, *resp.* in red. (a) Anomalous correlations $g_A^{(2)}(\delta k)$ at opposite momenta. The $\boldsymbol{k}/-\boldsymbol{k}$ peak disappears as the temperature increases. (b) 1D cut of the normalized density $\rho(k)$ in semilog scale. The depletion density increases with temperature. (c) Normal correlations $g_N^{(2)}(\delta k)$ for the same datasets and Ω_k. The peak amplitude shows no significant change as the temperature increases. Note that the transverse integration $\Delta k_\perp = 1.5 \times 10^{-2}\, k_d$ used here reduces the amplitude of the peaks.

is then $f_c = 55\%$ and we observe a peak of intermediate amplitude as shown on Fig-4.13.

We thus observe that the $\boldsymbol{k}/-\boldsymbol{k}$ correlation signal is extremely sensitive to temperature, hinting to the fact that it is related to a $T = 0$ ground-state effect. It is also quite illuminating to compare the $\boldsymbol{k}/-\boldsymbol{k}$ correlations to the bosonic bunching $\boldsymbol{k}/\boldsymbol{k}$ correlations. As explained in Chapter 1 1.3, the bosonic bunching effect is the consequence of the chaotic statistics of bosons, a property shared by the thermal and quantum depletion. Therefore, changing the temperature and thus the balance between thermal and quantum depletion should have no effect on bosonic bunching. This is what we observe experimentally as shown on Fig-4.12 panel (c).

In conclusion, we have on the same experimental data two very different behaviours with temperature that illustrate nicely the natures of the correlation signals. On the one hand, $\boldsymbol{k}/\boldsymbol{k}$ correlations unaffected by temperature, reveal the chaotic statistics of the system. On the other hand, $\boldsymbol{k}/-\boldsymbol{k}$ correlations are lost when temperature increases and reveal the quantum coherences in the many-body equilibrium state. These observations constitute a rather convincing argument that we are indeed observing a $\boldsymbol{k}/-\boldsymbol{k}$ correlation signal caused by the quantum depletion and not some other effect that we could have overlooked.

In the following, we study in quantitative details these correlation signals.

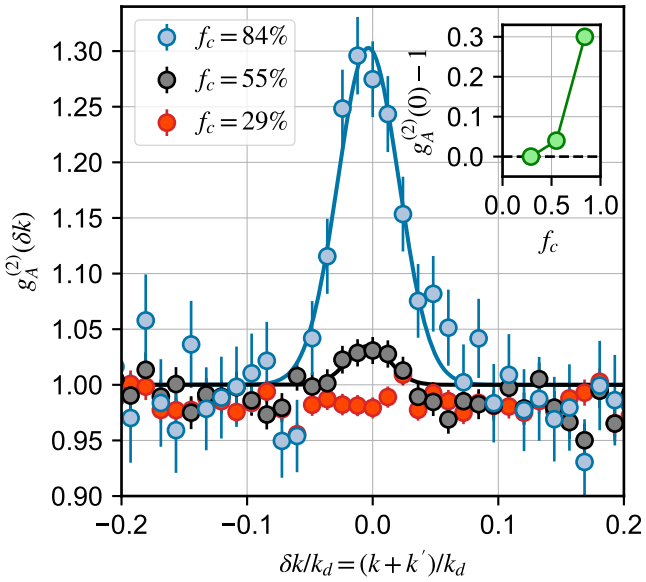

Figure 4.13: Anomalous correlation function for data sets with different temperatures and condensed fractions. The amplitude of the $\boldsymbol{k}/-\boldsymbol{k}$ correlation signal is progressively lost as the temperature rises and the condensed fraction diminishes. Inset: amplitude of the correlation peak $g_A^{(2}(\mathbf{0})$ as a function of the condensed fraction f_c.

4.3 Study of the width of the correlation peaks

In a first stage, we study the width of the correlation peak, a quantity that actually contains meaningful information about the many-body equilibrium state. The key aspect is the same used by Hanbury Brown and Twiss in their seminal paper to measure the size of Sirius through the measurement of the second order correlation function in far-field, namely the width of the correlation peak is inversely proportional to the spatial size of the source.

This subject has been discussed in 1.4 in light of the results of the theoretical work [23]. We remind that as the anomalous correlations are exclusively caused by quantum depleted atoms whose spatial extent is the one of the BEC, the width of the anomalous correlation peak σ_A is inversely proportional to the size of the BEC L_{BEC}. On the other hand, the normal correlations are caused by quantum depleted atoms but also thermally depleted atoms whose spatial size extends beyond the BEC because of the increased kinetic energy. This tells us that the width of the normal correlations peak σ_N should be smaller than that for anomalous correlations.

We plot on Fig.-4.14 the experimental correlation peaks widths for different total atom numbers. The horizontal error bars correspond to the standard deviation of the total atom number, while the vertical error bars correspond to the standard deviation of the mean over the three directions of the momentum-space. With this first analysis, we observe that for all atom numbers, $\sigma_A > \sigma_N$. In addition, one would expect to see both widths decrease with the total atom number as the size of the system grows with N_{bec}. This is more or less what the experimental data suggests but the error bar are too large to make a definite statement on this point. Note that in the Thomas-Fermi regime, the size of the

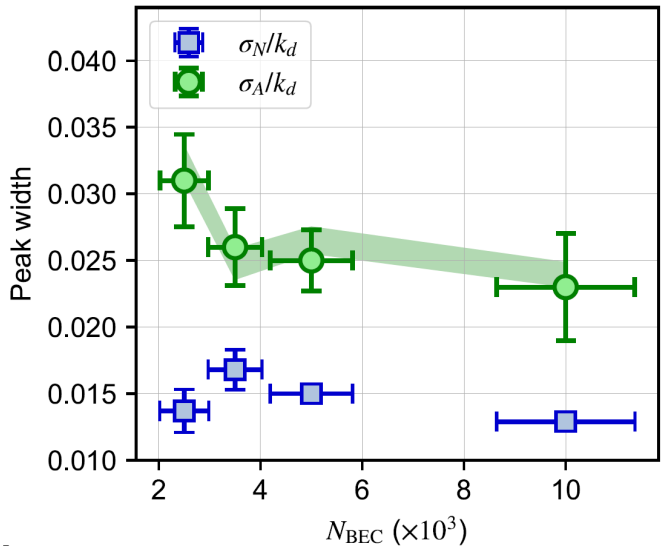

Figure 4.14: RMS widths of the anomalous (green) and normal (blue) correlation peaks. As expected from Bogoliubov theory, we get $\sigma_A > \sigma_N$ for each data set. The green area represents an estimation from the BEC width σ_{BEC} (see main text).

BEC changes slowly with the total atom number $L_{\mathrm{BEC}} \propto N_{\mathrm{bec}}^{1/5}$, translating in a change of $\sim$ 30% of the width of the correlation peaks from the data with $N = 2.5 \times 10^3$ to $N = 10 \times 10^3$ that is hard to resolve within our error bars.

We now look at the quantitative value of σ_A that can be numerically evaluated. The calculations have been performed by S. Butera and I. Carusotto from the BEC center in Trento, Italy, with the Bogoliubov theory for a trapped 1D system [23]. They evaluate $\sigma_{A,\mathrm{theo}} = 0.94\sigma_{\mathrm{BEC}}$, with σ_{BEC} the RMS width in momentum-space of the condensate. This relation is not modified in presence of a lattice as the size L_{BEC} does not change when the ratio $\mu/\hbar\omega$ is fixed. This is explained by the equality $m\omega^2 = m^*\omega^{*2}$ with m^* the effective mass in the lattice and ω^* the corresponding effective frequency as defined in 2.4.3.

We can therefore measure σ_{BEC} to exploit this result. To do so, we need to account for deviations induced by the saturation of the detector. Indeed, the BEC is very dense resulting in a high flux of atoms saturating the detector. If we plot 1D cuts of the momentum density, the BEC momentum profile is then flattened at the top and fitting with a Gaussian function over-evaluates the momentum width of the condensate. To circumvent this issue, we adapt the parameters of the Raman transfer (see 3.2.5) to reduce drastically the flux of detected atoms and avoid saturating the detector to ensure proper fitting.

Center-of-mass fluctuations

During our first analysis, we noticed that the anomalous correlation peak was larger than that of the BEC, contrary to what we would have expected. We also noticed that the momentum width of the BEC was larger than what we obtained applying the Gutzwiller variational approach (see 2.2.5) with our calibrated atom numbers. We attribute this to an imperfection in our experiment, the shot-to-shot fluctuations of the center-of-mass of the atomic distribution. When averaging over many experimental runs, these fluctuations

enlarge artificially the measured width of the BEC, as well as the width of the anomalous correlation peak. These fluctuations can nevertheless be characterized by comparing the experimental momentum width of the BEC to the one predicted by the Gutzwiller variational approach.

When accounting for center-of-mass fluctuations, the measured momentum density results from the convolution with the distribution of center-of-mass displacements and has a RMS width:

$$\sigma_{\mathrm{BEC}} = \sqrt{\sigma_{\mathrm{BEC},0}^2 + \Delta k_{\mathrm{com}}^2} \tag{4.10}$$

where $\sigma_{\mathrm{BEC},0}$ is the "true" BEC momentum width with $\sigma_{\mathrm{BEC},0} \propto 1/L_{\mathrm{BEC}}$. For instance, the Gutzwiller variational approach gives $\sigma_{\mathrm{BEC},0} \simeq 1.7 \times 10^{-2}\ k_d$ for a total atom number $N_{\mathrm{bec}} = 5 \times 10^5$ and we measure $\sigma_{\mathrm{BEC}} = 2.00(4) \times 10^{-2}\ k_d$. From this we deduce $\Delta k_{\mathrm{com}} = 1.05(2) \times 10^{-2}\ k_d$. Note that such fluctuations are small, corresponding to 1% of the distance between the diffraction peaks. We repeat the procedure to evaluate Δk_{com} for all of the data sets of Fig.-4.14.

For a $\boldsymbol{k}/-\boldsymbol{k}$ pair of atoms, a center-of-mass displacement $\mathrm{d}\boldsymbol{k}$ induces a momentum difference $\delta\boldsymbol{k} = 2\mathrm{d}\boldsymbol{k}$. The effect of the fluctuations are thus twice larger for the width of the anomalous correlations peak than for the BEC momentum width:

$$\sigma_A = \sqrt{\sigma_{A,0}^2 + 4\Delta k_{\mathrm{com}}^2} \tag{4.11}$$

Combining this with the numerical evaluation and the measured values of Δk_{com}, we obtain a corrected estimate of σ_A that is represented as the green area in Fig.-4.14. The width of the area represent the uncertainty given by the uncertainty on the measurement of σ_{BEC} and the uncertainty on the determination of L_{BEC} caused by fluctuations of the total atom number. We find that our experimental data matches the numerical calculations of [23], even if our experimental configuration is different (3D with an optical lattice contrary to 1D with a regular harmonic trap [23]).

We note that the fluctuations of the center-of-mass have however no effect on the normal correlation signal. Within a given shot, the center-of-mass fluctuations simply manifest as a global displacement of all the atoms of this shot by a quantity that we note $\boldsymbol{k}_{\mathrm{COM}}$. As a result, the momentum difference $\delta\boldsymbol{k} = \boldsymbol{k}_1 - \boldsymbol{k}_2$ between two atoms of this shot is not affected by the center-of-mass fluctuations, $(\boldsymbol{k}_1 + \boldsymbol{k}_{\mathrm{COM}}) - (\boldsymbol{k}_2 + \boldsymbol{k}_{\mathrm{COM}}) = \boldsymbol{k}_1 - \boldsymbol{k}_2$. In turn, the normal correlation function $g_N^{(2)}(\delta\boldsymbol{k})$ remains unchanged.

We then plot again the data of Fig.-4.14 accounting for the effect of center-of-mass fluctuations on Fig.-4.15. We observe that we cannot clearly state that $\sigma_A > \sigma_N$ with the experimental error bars, contrary to what we observed with our first incomplete analysis. This is most likely due to the fact that the temperature is too low to impact the width of the normal correlation function in a way that can be resolved in our experiment.

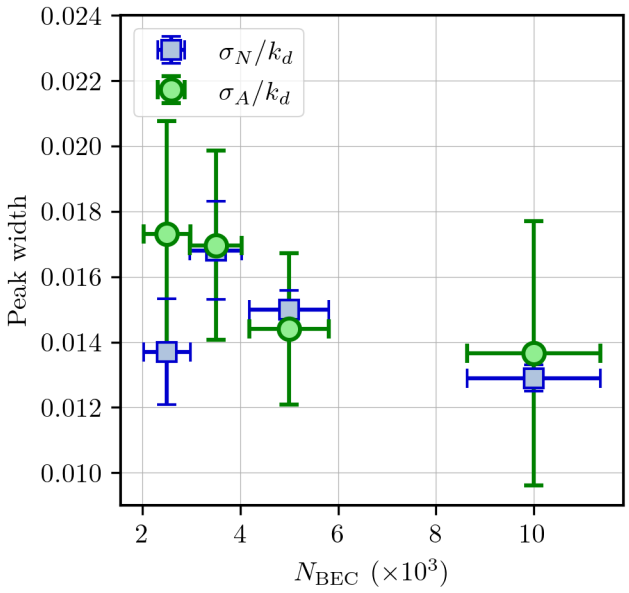

Figure 4.15: RMS widths of the anomalous (green) and normal (blue) correlation peaks corrected of the center-of-mass fluctuations. The widths σ_A and σ_N are no longer distinguishable within error bars, indicating that the temperature is too low to observe a clear separation of the anomalous and normal widths.

4.4 Study of the amplitude of the correlation peaks

We now move on to the study of the amplitude of the correlation peaks. Our objective will be to test how the predictions of Bogoliubov theory for the homogeneous case detailled in Chapter 1 hold for our experimental system with an optical lattice, as well as to provide further evidence of the quantum nature of the anomalous correlation signal.

4.4.1 Normal correlations

The prediction of the amplitude of the normal correlation peak is straightforward: as the statistics of the system are chaotic, we should observe a perfect bunching $g_N^{(2)}(\mathbf{0}) = 2$. Coming back to the normal correlations plot of Fig-4.12, we observe that the amplitude is around 1.8, *i.e* slightly lower than 2. This is because of the transverse integration effects described in 4.1.3. We fit the dependency of the observed amplitude with transverse integration to extract the corrected amplitude value as explained in 4.1.3 and illustrated in Fig.-4.3. We obtain $g_N^{(2)}(\mathbf{0}) = 2.05(6)$ and $g_N^{(2)}(\mathbf{0}) = 2.09(5)$ for the high and low condensed fraction data sets respectively, consistently with Bogoliubov theory showing that the statistics of the system are chaotic. Note that our team conducted a thorough study of $\boldsymbol{k}/\boldsymbol{k}$ correlations in the depletion of a lattice gas in [30], notably showing that we observe perfect bunching independently of the value of temperature as illustrated on Fig.-4.16.

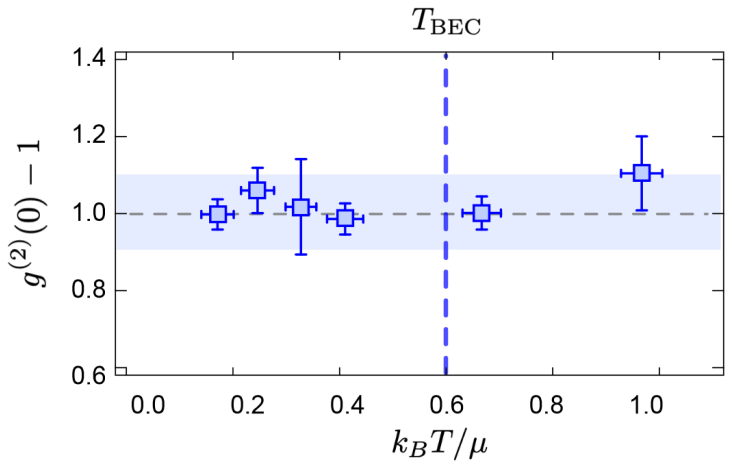

Figure 4.16: Bunching amplitude $g^{(2)}(0) - 1$ as a function of the reduced temperature $k_{\mathrm{B}}T/\mu$. The measurements are consistent with $g^{(2)}(0) = 2$ at any temperature. The blue dashed line signals the temperature of the BEC T_{BEC}.

4.4.2 Anomalous correlations

We now turn to analyzing the amplitude of the anomalous correlation peaks. As we have seen with the calculations developed in section 1.1.4, we can draw an analogy between the Bogoliubov weakly-interacting Bose gas and the non-degenerate parametric amplifier in Quantum Optics. While this analogy is direct if we were to work at zero temperature and have a fully quantum depletion where all atoms are correlated, we expect in our case that the amplitude of the anomalous correlation peak is reduced because of the presence of uncorrelated thermally depleted atoms.

We showed in 1.1.4 that the amplitude of the anomalous correlation peak of the non-degenerate parametric amplifier is expected to scale linearly with the inverse of what is called the average mode occupancy, *i.e.* the average number of photons per mode. In atomic physics, the analog to the average mode occupancy is the momentum density, *i.e.* the average number of atoms in a certain mode $\boldsymbol{k}$ that we can control by changing the total number of atoms N_{bec}. As changing N_{bec} should not significantly affect the balance between the quantum and thermal depletion, we should be able to observe that the amplitude of the anomalous correlation peak scales linearly with the inverse momentum density, despite not being at $T = 0$.

Actually, as explained in 4.2.1, we measure correlation functions averaged over many modes in the momentum volume Ω_k. The parameter setting the amplitude we observe is then the average momentum density $\bar{\rho}_{\Omega_k}$ defined as:

$$\bar{\rho}_{\Omega_k} = \int_{\Omega_k} \rho(\boldsymbol{k}) \mathrm{d}\boldsymbol{k} \tag{4.12}$$

We have several possibilities to change the value of $\bar{\rho}_{\Omega_k}$:

- Change the experimental parameters to load a different target total atom number N_{bec} in the optical lattice.

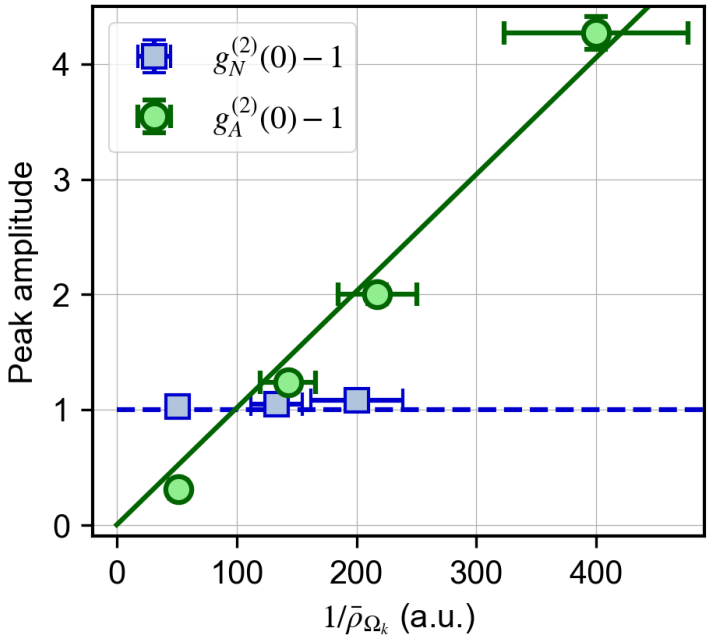

Figure 4.17: Amplitude of the correlation peaks versus the inverse average density $\bar{\rho}_{\Omega_k}$. We observe a linear scaling for anomalous correlations, while normal correlations stay constant and compatible with $g_N^{(2)}(\mathbf{0}) = 2$.

- Change the total atom number N_{bec} in the post-selection (see 4.2.2).
- Change the bounds of the integration volume Ω_k.

We prepare 4 data sets using a combination of these 3 possibilities. We perform the experiment with a target loaded atom number $N_{\text{bec}} = [2.5, 5, 10] \times 10^3$, and extract an additional set with $N_{\text{bec}} = 3.5 \times 10^3$ from the data intended for $N_{\text{bec}} = 5 \times 10^3$ by changing the post-selection criterion. We also reduce Ω_k to momenta between $k_{\min} = 0.3\ k_d$ and $k_{\max} = 0.7\ k_d$, *i.e.* to a region where the depletion is lower. We thus reduce $\bar{\rho}_{\Omega_k}$ to observe higher amplitude values in hope of observing a clear violation of the Cauchy-Schwarz inequality (see 1.1.5).

The results are plotted on Fig.-4.17 alongside the normal correlations amplitude for comparison. The horizontal error bars are the same as for Fig.-4.14 while the vertical error bars are obtained from the fit error. We observe a linear scaling of the anomalous amplitude with the inverse average momentum density. On the other side, changing $1/\bar{\rho}_{\Omega_k}$ does not change the chaotic nature of the system statistics, we thus observe $g_N^{(2)}(\mathbf{0}) = 2$ independently of the value of $\bar{\rho}_{\Omega_k}$. Once again, the amplitudes were corrected of transverse integration effects as shown on Fig.-4.4. Note that the normal correlations amplitude is not shown for the point at the lowest average density as the amplitude does not increase at lower densities, resulting in a decrease of the signal-to-noise ratio.

If we were at $T = 0$, we remind from 1.1.4 that the absolute value of the amplitude of the anomalous correlation peak should be $g_A^{(2)}(\mathbf{0}) = 2+1/\bar{\rho}_{\Omega_k}$. Because of the temperature, we rather expect that the limit of $g_A^{(2)}(\mathbf{0})$ when $\bar{\rho}_{\Omega_k}$ goes to infinity is a number between 1 and 2 whose value is determined by the balance between the quantum and thermal

depletion. In the experiment, we found that a linear fit of $g_A^{(2)}(\mathbf{0}) - 1$ versus $1/\bar{\rho}_{\Omega_k}$ with a zero intercept well matches the data, suggesting that the fraction of quantum depletion is actually very small. In fact, this quantity can be determined more precisely as we will now see.

Discussion on the detected number of atom pairs

The absolute value of the amplitude can be used to extract the number of detected $\boldsymbol{k}/-\boldsymbol{k}$ pairs, following the procedure previously described in 4.1.4. For the data set $N_{\text{bec}} = 5\times10^3$, $f_c = 84\%$, we find that we detect on average 0.5 pairs per shot, for roughly $N_{\Omega_k} = 100$ atoms detected in Ω_k. This number can be used to calculate the fraction of quantum depleted atoms in the overall depletion condensate that we will write α_Q. We first assume that all atoms in the quantum depletion form a $\boldsymbol{k}/-\boldsymbol{k}$ pair and that atoms forming a $\boldsymbol{k}/-\boldsymbol{k}$ pair necessarily belong to the quantum depletion. We then have:

$$2N_{\text{pairs}} = N_{\Omega_k}\alpha_{\text{MCP}}\alpha_Q \tag{4.13}$$

This equation can be understood as follows. We initially have a given number of depleted atoms in Ω_k that we detect only a fraction of because of the MCP detection efficiency. This number is N_{Ω_k} which already includes the detection efficiency per atom α_{MCP}. In all these atoms, only the fraction of quantum depleted ones α_Q will be $\boldsymbol{k}/-\boldsymbol{k}$ paired. In addition, we miss some pairs when detecting only one atom of the pair because of the detection efficiency, hence the addition of α_{MCP} in the formula.

We use equation 4.13 to evaluate α_Q and find $\alpha_Q \simeq 1.6\%$. Using a $T = 0$ Gutzwiller approach (see 2.2.5), we estimate the quantum depletion to be 5% and infer that the thermal depletion must then be $\simeq 10\%$ as the overall condensed fraction is $f_c = 84\%$. This would mean that we should rather have $\alpha_Q \simeq 33\%$, so more than an order of magnitude larger than our experimental measurement. We perform the same measurements for data sets with different total atom numbers with the results shown in Table-4.1, and observe that the value of α_Q does not significantly change. While this is consistent with the fact that we are able to observe a linear scaling of $g_A^{(2)}(\mathbf{0}) - 1$ with $1/\bar{\rho}_{\Omega_k}$ and that $g_A^{(2)}(\mathbf{0}) - 1$ tends to almost zero when $\bar{\rho}_{\Omega_k}$ goes to infinity, there is significant discrepancy with the estimation of the Gutzwiller approach. Finding a clear explanation for this discrepancy remains an open question and would require an extensive theoretical work far beyond the scope of this thesis. We can however suggests a few possible explanations:

- While we estimate the total quantum depletion, we cannot count all the pairs as some of them are located in the region of the BEC removed from the analysis. At the moment, we do not have the theoretical tools necessary to determine how many pairs are removed that way.
- Some of the pairs that we detect are located close to the edge of the first Brillouin where the relation dispersion becomes flat (see 2.4.2). It is then not so clear whether Bogoliubov's theory predictions for an homogeneous gas should quantitatively hold, as the Bogoliubov dispersion relation is an increasing function of the momentum.

In conclusion, the observed linear scaling is consistent with what is predicted by Bogoliubov theory and gives us another argument showing that the observed anomalous correlation signal is linked to the quantum depletion. The absolute value of the amplitude

N_{bec}	$N_{\mathrm{pairs}}/N_{\mathrm{runs}}$	α_Q
2.5×10^3	0.15	1.5%
5×10^3	0.5	1.6%
10×10^3	0.9	1.2%

Table 4.1: Average number of detected $\boldsymbol{k}/-\boldsymbol{k}$ pairs per experimental run and fraction of quantum depleted atoms in the depletion for different total atom numbers.

cannot however be understood in the framework of the Bogoliubov theory [23] that does not account for all the specificities of our experiment, such as the presence of the lattice. In fact, evaluating this number is currently beyond what is possible to calculate, making our experiment an example of quantum simulation.

4.5 Towards measuring entanglement

As we underlined in the first chapter of this thesis, it would be of great interest to characterize how entanglement emerges in at-equilibrium many-body systems such as the one we are working with here. Although we do not have all the experimental tools to claim that we are indeed seeing entanglement in our experiment yet, we nevertheless observe clear signatures of quantum phenomena that hints towards it as we will discuss now.

4.5.1 Relative number squeezing

If we were in the perfect situation $T = 0$ were the depletion is fully quantum, the populations in modes $\boldsymbol{k}$ and $-\boldsymbol{k}$ would be totally correlated so that the quantity $N(\boldsymbol{k}) - N(-\boldsymbol{k})$ is non-fluctuating and always equal to 0. This is obviously not the case in our finite temperature experiment where a significant fraction of the depletion is thermal and thus uncorrelated. However, we expect the $\boldsymbol{k}/-\boldsymbol{k}$ correlations to reduce the fluctuations of $N(\boldsymbol{k}) - N(-\boldsymbol{k})$. This is what we call **relative number squeezing**, similar to –but not to be confused with– regular squeezing [161] that denotes the reduction of the fluctuations of an operator (*e.g* momentum) under the Heisenberg limit at the expense of increased fluctuations for the conjugate operator (*e.g* position).

The idea is then to measure the statistics of the difference of atom numbers in modes $\boldsymbol{k}$ and $-\boldsymbol{k}$ that we will refer to as $N(\boldsymbol{k})$ and $N(-\boldsymbol{k})$. For one of the modes, the fluctuations of the number of atoms are set by the **shot noise** and follow a Poisson law. The particularity of the Poisson law for a random variable is that the variance of the variable is equal to its mean, giving for instance for mode $\boldsymbol{k}$:

$$\sigma^2_{N(\boldsymbol{k})} = \langle N(\boldsymbol{k})^2 \rangle - \langle N(\boldsymbol{k}) \rangle^2 = \langle N(\boldsymbol{k}) \rangle \tag{4.14}$$

What can we tell of the statistics of the number difference in two modes $\boldsymbol{k}$ and $\boldsymbol{k}'$, $N(\boldsymbol{k}) - N(\boldsymbol{k}')$? If the populations in the two modes are totally uncorrelated, the difference of two independent Poissonian random variables is Poissonian as well and we then get:

$$\sigma^2_{N(\boldsymbol{k})-N(\boldsymbol{k}')} = \langle N(\boldsymbol{k}) - N(\boldsymbol{k}')\rangle \tag{4.15}$$

If we now chose $\boldsymbol{k}' = -\boldsymbol{k}$, we expect the $\boldsymbol{k}/-\boldsymbol{k}$ correlations present in the depletion to reduce the fluctuations of the number difference, yielding what is called a **sub-Poissonian** law. Just like the $\boldsymbol{k}/-\boldsymbol{k}$ correlation signal is lost with temperature, we expect that the reduction of the number difference fluctuations becomes smaller and smaller as temperature increases, increasing the fraction of thermally, uncorrelated, depleted atoms.

Our goal is then to measure $\sigma_{N(\boldsymbol{k})-N(-\boldsymbol{k})}$ and see whether it is smaller than the expected value for a Poisson law. To this end, we define a convenient quantity that we call the squeezing parameter ξ:

$$\xi^2_{\boldsymbol{k},\boldsymbol{k}'} = \frac{\langle (N_{\boldsymbol{k}} - N_{\boldsymbol{k}'})^2\rangle - \langle N_{\boldsymbol{k}} - N_{\boldsymbol{k}'}\rangle^2}{\langle N_{\boldsymbol{k}}\rangle + \langle N_{\boldsymbol{k}'}\rangle} \tag{4.16}$$

This squeezing parameter to the square is simply the standard deviation of the number difference normalized by the expected standard deviation for uncorrelated variables. Therefore, we expect $\xi^2_{\boldsymbol{k},\boldsymbol{k}'} = 1$ if there are no correlations between modes $\boldsymbol{k}$ and $\boldsymbol{k}'$, and $\xi^2_{\boldsymbol{k},\boldsymbol{k}'} < 1$ if the modes populations are correlated.

To evaluate ξ^2, we record for each experimental shots the number of detected atoms in cubic boxes paving the entire integration volume Ω_k. Intuitively, we could set the size of the boxes to match that of a mode. If we define the volume of a mode as the volume of a sphere whose radius is the two-particle correlation length l_c obtained from the normal correlation function width with $l_c = \sqrt{2}\sigma_N$ [26], we obtain that there are $N_{\text{mode}} = 1.5 \times 10^4$ modes in Ω_k, *i.e* on average ~ 0.01 atoms/mode/run (for $N_{\text{bec}} = 5 \times 10^3$) which is way too small to have proper statistics to evaluate ξ^2. We then chose a size of $(0.3\ k_d)^3$ for a total number of $5^3 = 125$ boxes paving the volume Ω_k, minus the central box corresponding to the BEC leaving us with 124 boxes. The average numbers of detected atoms per shot are ~ 100, ~ 240 and ~ 360 for the data sets with $f_c = 84\%$, $f_c = 55\%$ and $f_c = 29\%$ respectively, meaning that the average number of atom per box are 0.8, 1.92 and 2.88 respectively. Having access to the atom number for each of the ~ 2000 runs at various values of $\boldsymbol{k}$, we compute the squeezing parameter between different pairs of boxes as illustrated on Fig.-4.18, either correlated or uncorrelated for reference. The measured values of ξ^2 are averaged over all possible pairs of boxes for a given configuration. The uncertainty on ξ^2 is evaluated statistically on all the ξ^2 values obtained on the 62 different pairs of boxes and defined as the standard error.

The results are summarized in Table 4.2 and Fig.-4.19. For the low-temperature, high condensed fraction data, we are indeed able to observe a small relative number squeezing within the errorbars. Note that this number squeezing is small compared to that found in discrete (spin) variables experiments [20, 54, 126] as it is inherently limited by the uncorrelated thermally depleted atoms and the detection efficiency. For uncorrelated modes, the squeezing parameter is very slightly above 1, highlighting that the correlations indeed reduce the fluctuations of the number difference. For higher temperatures (lower condensed fraction), no relative number squeezing is observed as the correlations are drowned out. In addition, we see that the squeezing parameter increases as we increase the temperature. This is due to global atom number fluctuations of the order of 15% in our experiment. At

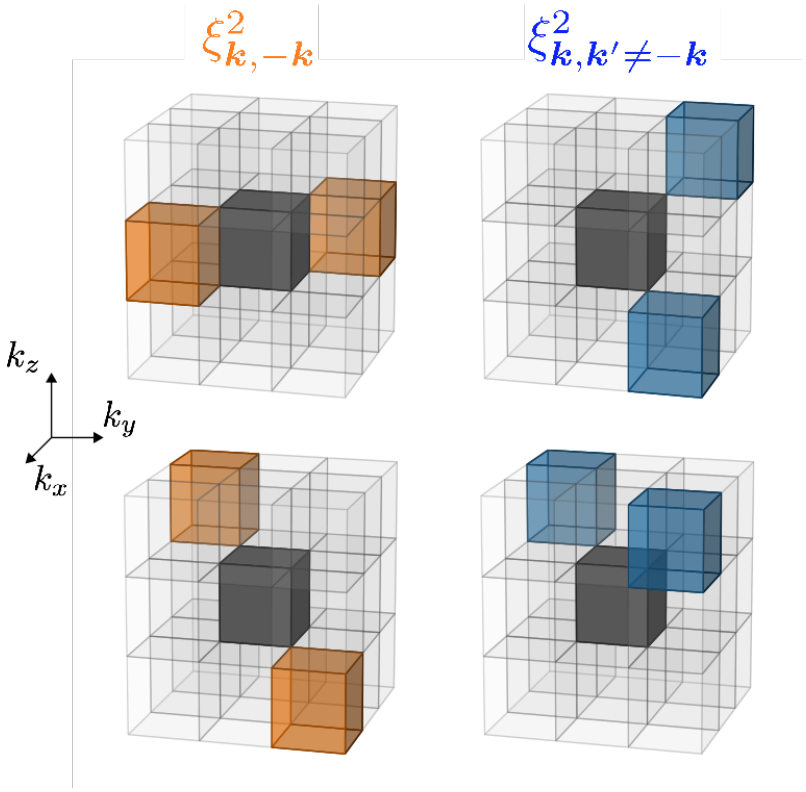

Figure 4.18: Relative number squeezing measurement. The number of detected atoms in cubic boxes are recorded for each experimental run. We compute the squeezing parameter ξ between correlated (orange) boxes as illustrated on the right, or uncorrelated (blue) boxes on the left. The central black box corresponds to the BEC, removed from the analysis.

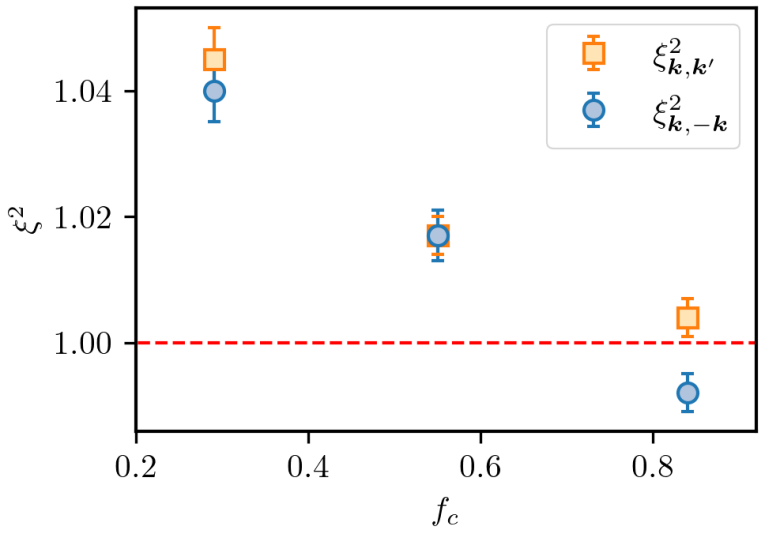

Figure 4.19: Squeezing parameter ξ^2 as a function of the condensed fraction f_c for correlated and uncorrelated modes. The red line indicates the expected value $\xi^2 = 1$ for Poissonian number difference fluctuations. At $f_c = 0.84$, a clear difference is observed between $\xi^2_{\boldsymbol{k},-\boldsymbol{k}}$ and $\xi^2_{\boldsymbol{k},\boldsymbol{k}'}$ and relative number squeezing is observed as $\xi^2_{\boldsymbol{k},-\boldsymbol{k}} < 1$. The difference between $\xi^2_{\boldsymbol{k},-\boldsymbol{k}}$ and $\xi^2_{\boldsymbol{k},\boldsymbol{k}'}$ disappears as f_c decreases as the effect of $\boldsymbol{k}/-\boldsymbol{k}$ correlations gets drowned out. The global increase in the value of ξ^2 when f_c decreases is caused by total atom number fluctuations (see main text).

low temperature, there are few detected atoms per box and the shot noise is thus large and dominating the total atom number fluctuations. On the opposite, at higher temperatures, the number of depleted atoms increases, reducing the shot noise. The contribution of total atom number fluctuations is then not negligible anymore and increase the fluctuations of the number difference, higher than what is expected for a Poisson law, explaining why we observe $\xi^2 > 1$.

f_c	$\xi^2_{\boldsymbol{k},-\boldsymbol{k}}$	$\xi^2_{\boldsymbol{k},\boldsymbol{k}'}$
0.84	0.992(3)	1.004(3)
0.55	1.017(4)	1.017(3)
0.29	1.040(5)	1.045(5)

Table 4.2: Experimental values of the squeezing parameter for correlated and uncorrelated modes and different condensed fractions.

4.5.2 Experimental violation of the Cauchy-Schwarz inequality

We have previously shown in 1.1.5 how the Cauchy-Schwarz inequality writes with creation and annihilation operators and translated it in terms of correlation functions. Translated to anomalous and normal correlations function discussed in this chapter, the Cauchy-Schwarz inequality writes:

$$g^{(2)}_A(\boldsymbol{k},-\boldsymbol{k}) \leq g^{(2)}_N(\boldsymbol{k},\boldsymbol{k}) \tag{4.17}$$

We thus have a clear violation of the Cauchy-Schwarz inequality with our experimental data on 3 different data points, with a maximum violation of $5.27(8) > 2.09(5)$ (Fig.-4.17). This adds up to the list of quantum signatures in the anomalous correlation signal.

As discussed in 1.1.5, violating the Cauchy-Schwarz inequality equals fulfilling the Busch-Parentani criterion to prove entanglement, provided that certain conditions are fulfilled. The first one is that the statistics of the system must be thermal chaotic. This is something that we have experimentally verified by measuring $g_N^{(2)}(\mathbf{0}) = 2$. The second condition is to have $\langle a_{\boldsymbol{k}}^\dagger a_{-\boldsymbol{k}} \rangle = 0$. While this is true in Bogoliubov theory and would be reasonable to assume in our experiment, this is not something that we have experimentally measured and that therefore forbids us to claim that we observe entanglement in momentum-space. This correlator could be measured using an atomic inteferometer setup [51, 90, 105] using Bragg diffraction [109] to produce atom mirrors and beam splitters. This would however require that we upgrade our experimental apparatus to have the required lattice beam to implement the proper Bragg diffraction scheme. Nevertheless, proving the presence of entanglement in momentum-space in many-body equilibrium systems would be a significant result that motivates such experimental work in the near future.

4.6 Preliminary study: dependency of the correlation signals with k

As we have seen throughout this chapter, the balance between the quantum and thermal depletion and thus the temperature plays an important role in both the amplitude of the anomalous correlation function (see 4.2.3) as well as the width of the normal correlation function (see 1.4). Interestingly, the ratio of the quantum and thermal depletion changes with the momentum value k as they have different momentum scales set by the strength of the interactions and the temperature respectively. Whereas we have until now kept the integration volume Ω_k as large as possible, it would be then be interesting to reduce it and move it around momentum-space to see whether we can observe variations of the characteristics of the correlation signals depending on the momentum value around which Ω_k is centered. Note that the study presented in this section is preliminary and still an on-going work.

4.6.1 Evolution of the amplitude of the anomalous correlations with k

As far as the amplitudes of the correlation signals are concerned, there is not much too learn studying the dependency of the amplitude of the normal correlation signal with k as it only reveals the chaotic statistics of the system that are unaffected by temperature and are thus independent of k. We will then focus solely on the amplitude of the anomalous correlation function.

We repeat the analysis procedure described before for various integration volumes Ω_k that we set by changing its boundaries k_{min} and k_{max} (see 4.2.1). In practice, we chose the couples $[k_{\text{min}}, k_{\text{max}}] = [0.15, 0.3], [0.2, 0.35], ..., [0.35, 0.5]$ k_d, scanning the first Brillouin zone. As Ω_k is smaller than for previous analyses showed in this chapter, the signal-to-noise ratio is not sufficient to extract a value of the amplitude for a large panel of transverse integration values to extract the amplitude corrected from transverse integration as described in 4.1.3. We will then rather plot the raw amplitude η_A for a fixed transverse

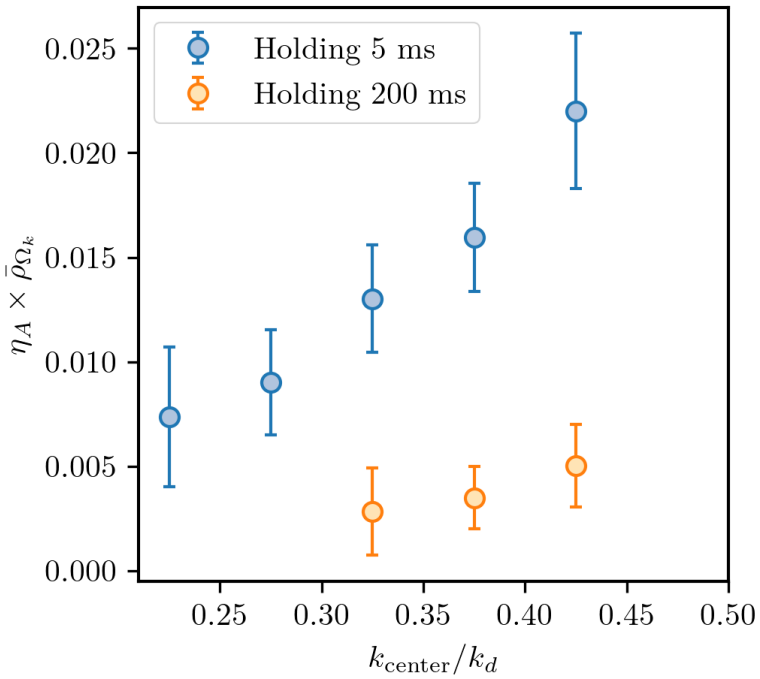

Figure 4.20: Raw amplitude η_A mutiplied by the average density $\bar{\rho}_{\Omega_k}$ as a function of k_{center} for two data sets at different temperatures.

integration $\Delta k_\perp = 3 \times 10^{-2}\ k_d$. In addition, when changing Ω_k, we also change the value of $\bar{\rho}_{\Omega_k}$ that affects the amplitude of the anomalous correlation peak. We therefore "normalize" this effect by plotting the quantity $\eta_A \times \bar{\rho}_{\Omega_k}$ that should only reveal the effect of the variations of the balance between the quantum and the thermal depletion.

We plot on Fig.-4.20 $\eta_A \times \bar{\rho}_{\Omega_k}$ as a function of $k_{\mathrm{center}} = (k_{\mathrm{min}} + k_{\mathrm{max}})/2$ for the data sets with $N_{\mathrm{bec}} = 5 \times 10^3$ and holding times 5 ms and 200 ms. We observe that for the coldest data set, $\eta_A \times \bar{\rho}_{\Omega_k}$ increases with k, indicating that the ratio of the quantum depletion to the thermal depletion increases with k in the momentum range that we probe. When the temperature increases (orange points of Fig.-4.20), the thermal depletion increases and populates higher momentum modes, meaning that the ratio of the quantum depletion to thermal depletion should not increase as fast or even possibly decrease with k if the temperature is high enough. This is what we observe on the experimental data for which $\eta_A \times \bar{\rho}_{\Omega_k}$ increases much slower for the heated data. We note that as the overall density of the depletion is higher at low k reducing the amplitude of the anomalous correlation function, we were not able to observe the correlation signal for $[k_{\mathrm{min}}, k_{\mathrm{max}}] = [0.15, 0.3], [0.2, 0.35]$ with the 200 ms holding data.

While this kind of data could in principle be used to find the temperature of the experiment, we must for the moment only restrict ourselves to the qualitative description we have just given for lack of a precise theory of the correlations in an optical lattice.

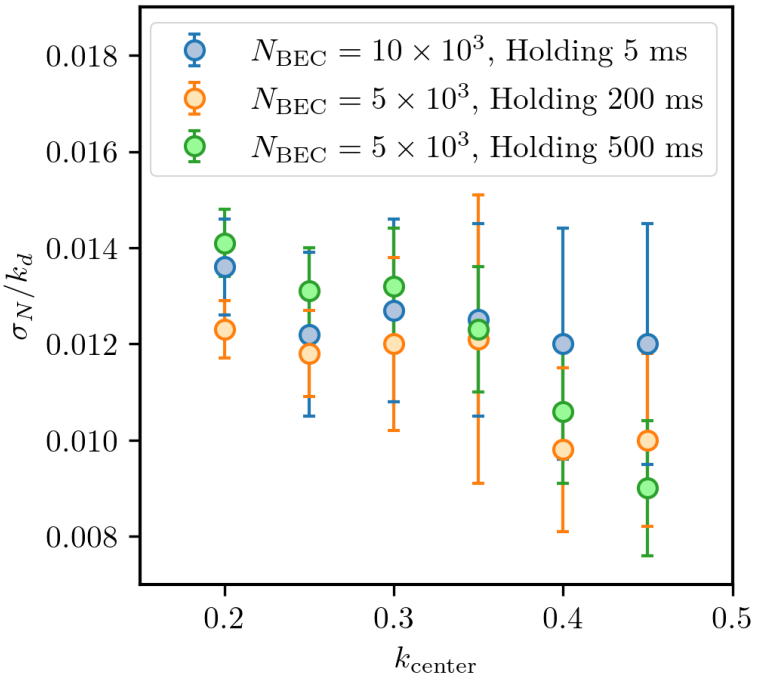

Figure 4.21: Normal correlation peak width σ_N as a function of k_{center} for various data sets at different temperatures.

4.6.2 Evolution of the width of the normal correlations with k

As seen in 1.4.2, the width of the anomalous correlation peak is essentially constant with k and therefore does not bring much additional information. On the contrary, in analogy with the amplitude of the anomalous correlation peak, the width of the **normal** correlation peak σ_N is strongly dependent from the balance between the quantum and thermal depletion (see 1.4.1). As described in the previous paragraph, we measure σ_N for different integration volumes Ω_k. This time, we choose $[k_{\mathrm{min}}, k_{\mathrm{max}}] = [0.15, 0.25], [0.2, 0.3], ..., [0.4, 0.5]$ k_d.

We plot on Fig.-4.21 σ_N as a function of k_{center} for 3 data sets: the first one with $N_{\mathrm{bec}} = 10 \times 10^3$ and a holding time of 5 ms and the other two with $N_{\mathrm{bec}} = 5 \times 10^3$ and holding times 200 ms and 500 ms respectively to increase the temperature. We note that we deliberately chose a data set with a higher atom number for the lowest holding times to increase the number of depleted atoms and have a proper signal to noise ratio. Unfortunately, we observe that the error bars are too large to capture any possible variations of σ_N. It then seems after this preliminary that $g_A^{(2)}(\mathbf{0})$ is a better suited probe than σ_N to understand the variations of the balance between the quantum and thermal depletion with k in our experiment.

As mentioned in the introduction to this section, the results presented here are still quite preliminary and there are quite a few points that need further investigation, notably why the number of detected pair is lower than expected which is directly connected to the balance between the quantum and the thermal depletion, constituting an interesting prospect for the near future.

4.7 Conclusion

We have reached the end of our investigation of two-body correlations in the depletion of weakly interacting Bose gases. To sum things up, let us remind the main steps of the work conducted during this thesis and its main results.

- We decided to try to detect experimentally the $\boldsymbol{k}/-\boldsymbol{k}$ pairs of the quantum depletion predicted by the Bogoliubov theory of the weakly-interacting Bose gas, as this phenomenon is one of the conceptually simplest non-trivial, many-body, quantum correlation effect. By conducting this study, we hope to better understand the physics of many-body equilibrium states and how correlations and entanglement emerge through the combined effects of interactions and quantum fluctuations.
- We based our experimental procedure on an experimental setup producing He* BECs implementing a 3D single-atom resolved electronic detection technique. We decided to use an optical lattice to enter the low-temperature regime dominated by interactions to ensure a sufficient level of quantum depletion so that the $\boldsymbol{k}/-\boldsymbol{k}$ pairs can be properly detected.
- We completed previous benchmarking measurements [29] by measuring two-body time-of-flight collisions with large number of atoms in the lattice. From this, we were able to conclude that two-body collisions are negligible for the typical number of atoms used in our correlation measurement experiments. This validates the ballistic relation linking the momentum of the in-trap to their detected position after the TOF.
- We measured the temperature of the gas at different amplitudes of the lattice potential to certify the adiabatic preparation of the system.
- We implemented a two-photon Raman transfer scheme to replace the previous RF transfer, improving the detection efficiency by a factor ~ 4.
- We adapted an existing algorithm to make it suited to extract the $\boldsymbol{k}/-\boldsymbol{k}$ correlation signal from the experimental data and benchmarked it with scattering spheres data.
- We were able to successfully observe anomalous and normal correlation signals in various data sets with different total atom numbers. We validated that the observed anomalous correlation signal is linked to the $\boldsymbol{k}/-\boldsymbol{k}$ pairs of the quantum depletion with the following points:
  - The signal is lost with temperature, contrary to the normal correlation signal that reveal the chaotic statistics of the system, unaffected by temperature.
  - The width of the anomalous correlation peak matches the numerical calculations of [23] when accounting for center-of-mass fluctuations.
  - $g_A^{(2)}(\mathbf{0})$ scales linearly with the inverse average momentum density $\bar{\rho}_{\Omega_k}$, while $g_N^{(2)}(\mathbf{0})$ remains constant.
  - Relative number squeezing between correlated boxes at opposite momenta is observed.
  - A violation of the Cauchy-Schwarz inequality $g_A^{(2)}(\mathbf{0}) \gg g_N^{(2)}(\mathbf{0})$ is reported.

This experimental observations are an encouraging first step towards more ambitious correlation measurements. One of our short term objective is to study the Mott transition and look for complex correlation patterns involving several particles not predicted by simple theoretical treatment such as Bogoliubov theory. As there is currently no theory describing this kind of physics, this represents quite a fascinating prospect that would really put our experiment in the field of quantum simulation. In addition, a more long term

prospect would be to improve our experimental setup to bring the fermionic isotope $^3He^*$ to quantum degeneracy to perform momentum correlations measurements with fermions and study BEC-BCS crossover physics. A notably important result would be to observe the $\boldsymbol{k}/-\boldsymbol{k}$ pairing of a Cooper pair [42]. Observing the $\boldsymbol{k}/-\boldsymbol{k}$ pairing of the quantum depletion shows us that we are indeed capable of seeing $\boldsymbol{k}/-\boldsymbol{k}$ pairing with our experiment and constitutes a small step towards this result.

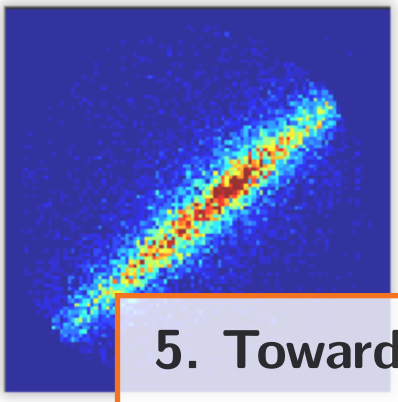

Chapter 5

5. Towards measuring Tan's contact in 1D gases

For the last chapter of this thesis, we will depart from the main line set by the $\boldsymbol{k}/-\boldsymbol{k}$ correlations of the quantum depletion and shift our attention to a different topic that exploits another feature of the single-atom resolution of our experiment. While we have used it so far to look for correlations between individual particles, another strong advantage of our apparatus is the possibility to detect very low densities signals inaccessible with optical measurements. An example of such a signal is the k^{-4} tails in the momentum density of 1D gases, also known as Tan's contact [153].

As we will see in the first section of this chapter, Tan's contact is a fascinating and promising universal quantity that can be used to characterize many different systems, especially 1D gases, in level of details inaccessible with more common experimental techniques. We will then quickly summarize the main points of the theoretical work [170] on which we will rely to interpret our experimental data. We will next explain how 1D physics can be effectively implemented with our experimental apparatus and detail the procedure used to measure Tan's contact, before discussing the first preliminary results.

5.1 Tan's contact

5.1.1 Definition from the large momentum tails

To understand what Tan's contact is, we consider two atoms with contact interactions in the ultracold regime in 1D. The two-body wave-function then only depends from the inter-particle distance r and the s-wave scattering length a_s [160]:

$$\psi(r) = -\frac{r}{a_s}\, e^{-r/a_s} \tag{5.1}$$

The Fourier transform of this expression is rather easy to compute and writes:

$$\tilde{\psi}(k) = \int_0^\infty \psi(r)\, e^{2\pi i k r}\, dr \propto \frac{1}{(i2\pi k - 1/a_s)^2} \tag{5.2}$$

from which we obtain the momentum density:

$$\rho(k) = |\tilde{\psi}(k)|^2 \propto \frac{1}{2(2\pi k a_s)^4 - 2(2\pi k a_s)^2 + 1} \tag{5.3}$$

Interestingly, if we look at the asymptotic behavior at large k we find that:

$$\rho(k) \underset{k\to\infty}{\sim} \frac{1}{k^4} \tag{5.4}$$

The presence of contact interactions translates into a k^{-4} scaling of the momentum distribution at large k. Importantly, this signature holds for higher dimensions, independently of temperature, interaction strength or quantum statistics making it a **universal relation**. From equation 5.4, we define the Tan's Contact C as:

$$C = \lim_{k\to\infty} k^4 \rho(k) \tag{5.5}$$

Importantly, we will take in this chapter the convention:

$$\int \frac{dk}{2\pi} \rho(k) = N_{\text{bec}} \tag{5.6}$$

where N_{bec} is the total number of atoms, with the notable addition of the factor $1/2\pi$ to match the definition of the theoretical work [170] to which we will compare the experimental data.

5.1.2 Connection to thermodynamic quantities

While the k^{-4} scaling is universal, the value of C depends on the physical characteristics of the system such as the number of particles, temperature, dimension etc. and thus contains meaningful information that would otherwise be hard to measure with standard experimental techniques. This was first theorized by Shina Tan in 2008 [153] who showed that C is a thermodynamic quantity revealing how the total energy of a two component Fermi gas changes when adiabatically tuning the inverse scattering length a_s:

$$-\frac{dE}{d(1/a_s)} = \frac{h^2 C}{2\pi m} \tag{5.7}$$

This result is known as Tan's adiabatic sweep theorem and can be adapted to the 1D bosonic case [10] to obtain:

$$C = \frac{4m}{\hbar^2}\frac{\partial\Omega}{\partial a_{1D}}\bigg|_{T,\mu} \tag{5.8}$$

with Ω the grand potential and $a_{1\mathrm{D}}$ the 1D scattering length whose expression will be discussed later. This result can also be rewritten [169] to include the interaction energy of the system $\langle H_{\mathrm{int}}\rangle$ that we have often encountered throughout this thesis and that is usually hard to measure separately from the total energy:

$$C = \frac{2g_{1\mathrm{D}}m^2}{\hbar^4}\langle H_{\mathrm{int}}\rangle \tag{5.9}$$

with $g_{1\mathrm{D}}$ the 1D coupling constant that is defined from the 1D scattering length by [116]:

$$g_{1\mathrm{D}} = -\frac{2\hbar^2}{ma_{1\mathrm{D}}} \tag{5.10}$$

5.1.3 Characterization of 1D Lieb-Liniger regimes

Another significant motivation to measure Tan's contact is to characterize the different regimes of Lieb-Liniger 1D systems of interacting bosons as a function of temperature and of the strength of the interactions. Tan's contact is indeed particularly suited to study the Lieb-Liniger model [104] as it revolves around the approximation that the interactions between the atoms are repulsive, contact interactions:

$$\hat{H} = \sum_j \left[-\frac{\hbar^2}{2m}\frac{\partial^2}{\partial^2 {x_j}^2} + V(x_j)\right] + g_{1\mathrm{D}}\sum_{j<l}\delta(x_j - x_l) \tag{5.11}$$

with V an external trapping potential.

These different regimes have been widely investigated [125] and are illustrated on the state diagram of Fig.5.1. The lower right part of the diagram corresponds to the strongly interacting or Tonks-Girardeau regime where the repulsive interactions are so strong that they mimic the Pauli exclusion principle for fermions. The gas is then said to fermionize. As the strength of the interactions decreases, the gas progressively goes to a weakly-interacting quasi-condensate phase characterized by suppressed density fluctuations but fluctuating phase, contrary to the true condensate. The weakly-degenerate ideal bosons region refers to the region where the effect of interactions are negligible compared to temperature.

The main difficulty to experimentally characterize those regimes resides in the fact that most quantities show a smooth and monotonic behavior when crossing the transition points between the different regimes. This motivated theoretical studies of the dependency of the Tan's contact with the strength of interactions and temperature to determine if C can be used as a probe to characterize these different regimes. Previous works have conducted such studies for homogeneous bosons at finite temperature [96, 97], trapped bosons at zero temperature [113, 117] or for the trapped finite temperature Tonks-Girardeau regime

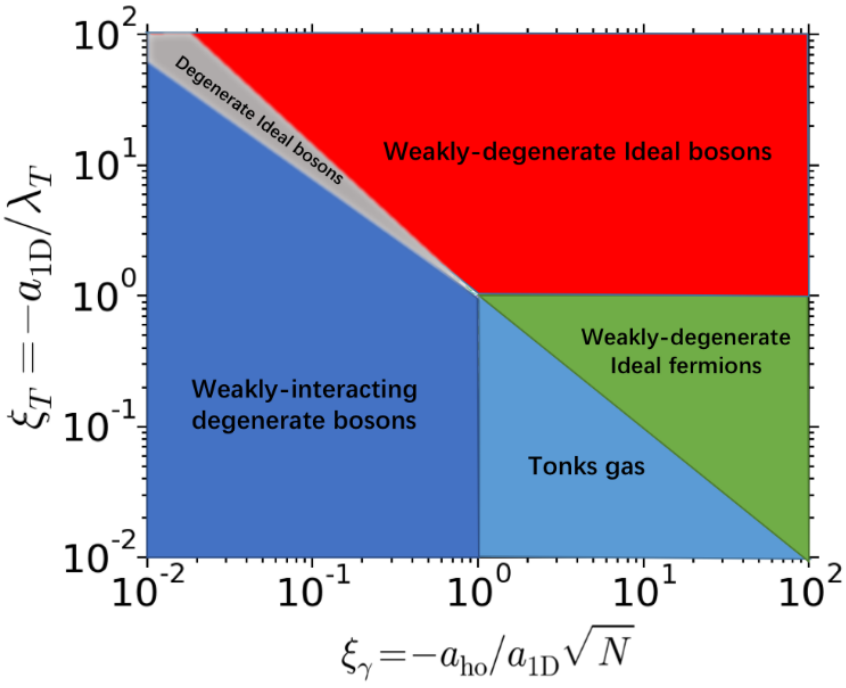

Figure 5.1: State diagram of trapped 1D Bose gases with repulsive interactions as a function of the reduced temperature ξ_T and the reduced interaction strength ξ_γ for trapped 1D gases. The solid lines indicate smooth crossovers between the different regimes. Taken from [169].

[158]. They were recently completed by [170], characterizing trapped Lieb-Liniger bosons for arbitrary values of the temperature and the interaction parameter.

There have been many experiments aiming at measuring Tan's contact in strongly interacting systems for both bosons and fermions, using a variety of methods such as RF spectroscopy [136, 165], Ramsey interferometry [62, 176], structure factor measurement with Bragg spectroscopy [99] or measurements of the momentum distribution [107, 152]. One of the main experimental difficulties for measuring Tan's contact from the momentum density $\rho(k)$ when the gas is not strongly interacting comes from the fact that the high momentum k^{-4} tails correspond to very low density values that are hard to detect with usual optical imaging techniques. This problem is however solved with the He^* detector thanks to his large dynamic momentum range. Interestingly, our experimental apparatus can be adapted to study 1D physics by transforming our 3D optical lattice into a 2D one as we will see in 5.3, making it a good candidate to verify the predictions of [170].

5.2 Theoretical study

Before going into the experimental details, we start our discussion by summarizing the main results of [170]. In this theoretical work, the external trapping potential V of equation 5.11 is taken to be harmonic like in most experiment, including ours. We will write the trapping frequency ω_{1D}.

5.2.1 Two-parameter scaling

At first glance, the physics of the system and in turn Tan's contact should depend from 4 parameters:

- The total number of particles N_{bec}.
- The temperature T.
- The trapping frequency $\omega_{1\mathrm{D}}$.
- The coupling constant $g_{1\mathrm{D}}$.

The first result of [170] is to show that C actually depends from only two parameters, the first one being the reduced interaction strength:

$$\xi_\gamma = -a_{\mathrm{ho}}/a_{1\mathrm{D}}\sqrt{N} \tag{5.12}$$

with $a_{\mathrm{ho}} = \sqrt{\hbar/m\omega_{1\mathrm{D}}}$ the harmonic oscillator length and $a_{1\mathrm{D}}$ the 1D scattering length. The second one is the reduced temperature:

$$\xi_T = -a_{1\mathrm{D}}/\lambda_T \tag{5.13}$$

with $\lambda_T = \sqrt{2\pi\hbar^2/mk_{\mathrm{B}}T}$. The contact can then be written as a function of ξ_γ and ξ_T:

$$C = \frac{N^{5/2}}{a_{\mathrm{ho}}^3} f(\xi_\gamma, \xi_T) \tag{5.14}$$

The goal is then to determine the variations of $f(\xi_\gamma, \xi_T)$. To do so, the authors of [170] follow two complementary approaches. The first one consists in using the Bethe Ansatz which is the exact solution of the Yang-Yang equations [168] of the 1D homogeneous gas. The results are then adapted to the trapped case by using the Local Density Approximation (LDA) in the same fashion of what we did in 2.2.3. The validity of this approach is checked by comparing its prediction to *ab-initio* QMC calculations as shown on Fig-5.2.

5.2.2 Maximum contact versus temperature

A striking and unexpected feature of Fig.-5.2 panel (b) is that the contact shows a non-monotonous dependency with ξ_T with a maximum, contrary to the monotonous increase in the Tonks-Girardeau regime predicted by [158]. While the maximum exists for any value of ξ_γ, the effect is more pronounced in the strongly-interacting regime.

Strongly-interacting regime

In this regime, the contact can be determined analytically via a virial expansion [158] and writes:

$$C = \frac{2N^{5/2}}{\pi a_{\mathrm{ho}}^3}\frac{\xi_\gamma}{\xi_T}\left(\sqrt{2} - \frac{e^{1/2\pi\xi_T^2}}{\xi_T}\mathrm{Erfc}(1/\sqrt{2\pi}\xi_T)\right) \tag{5.15}$$

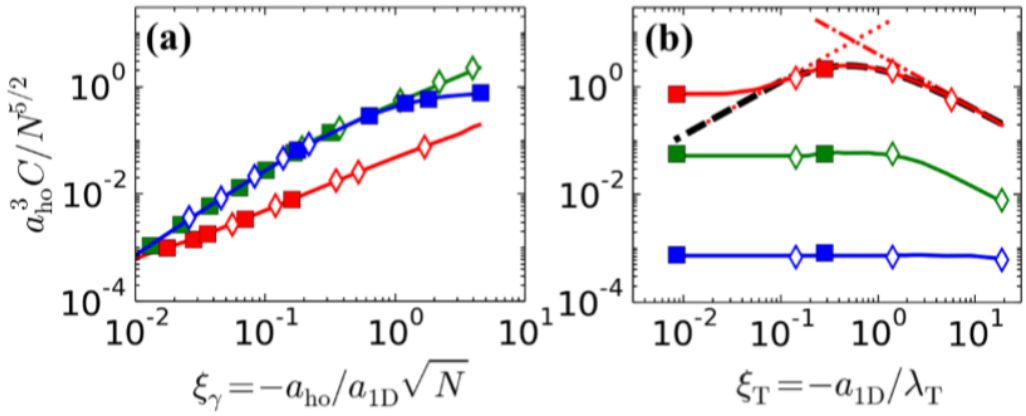

Figure 5.2: Reduced contact $a_{ho}^3 C/N^{5/2}$ as a function of ξ_T and ξ_γ as predicted from the LDA approach (solid lines) and QMC calculations (points). The different symbols correspond to various parameters for the QMC calculations (see [170] for further details). (a) Reduced contact versus ξ_γ at fixed temperatures corresponding to $\xi_T = 0.0085$ (blue), 0.28 (green), and 18.8 (red). (b) Reduced contact versus ξ_T at fixed interaction strengths corresponding to $\xi_\gamma = 10^{-2}$ (blue), 1.58×10^{-1} (green), and 4.47 (red). The black dashed, red dotted, and red dash-dotted lines correspond to equations 5.15, 5.16 and 5.17 respectively.

In the asymptotic regime of low-temperature limit $\xi_\gamma^{-1} \leq \xi_T \leq 1$, this expression simplifies to:

$$C = 2\sqrt{2}\,\frac{N^{5/2}}{a_{ho}^3}\,\xi_\gamma\,\xi_T \tag{5.16}$$

In the opposite regime of high-temperature $(\xi_\gamma^{-1},\, 1) \leq \sqrt{\xi_T}$, we rather get:

$$C \simeq 2\sqrt{2}\,\frac{N^{5/2}}{\pi a_{\rm ho}^3}\,\frac{\xi_\gamma}{\xi_T} \tag{5.17}$$

We thus clearly see the non-monotonic behavior of the contact with temperature. These 3 expressions are plotted on Fig-5.2. We see that the full analytical expression of 5.15 (black dashed line) well matches the LDA predictions, except for low-temperatures for which the virial expansion is not suited.

The existence of a maximum value of the contact can be understood by the competition between the effect of temperature and interactions. While interaction dominates, the gas is fermionized and the contact increases with temperature [158], whereas it decreases as thermal fluctuations take over and fermionization disappears. The location of the maximum of the contact thus provides a way to characterize the crossover to fermionization.

Weakly-interacting regime

In the weakly-interacting regime, the interactions are not strong enough to fermionize the gas. In the low-temperature regime $(1,\, \xi_T) \leq \xi_\gamma^{-1}$, the gas forms a quasi-condensate and

the contact is obtained from equation 5.9 with the mean-field expression of $\langle H_{\text{int}} \rangle$ and writes:

$$C = \eta \frac{N^{5/2}}{a_{\text{ho}}^3} \xi_\gamma^{5/3} \tag{5.18}$$

with $\eta = 4 \times 3^{2/3}/5$. We see that C does not depend from temperature here. At high temperatures $\xi_\gamma^{-1} \leq \xi_T \leq \xi_\gamma^{-2}$, interactions become negligible so that the gas is nearly ideal and the contact writes:

$$C = \left(16\sqrt{\pi} \frac{N^{5/2}}{a_{ho}^3} \xi_\gamma^5 \xi_T^3 \right) G(\alpha) \,, \tag{5.19}$$

with $G(\alpha)$ decreasing at least in λ_T^4 (see [170] for the explicit expression), making C decrease with temperature. Once again, identifying the temperature at which C starts to decay allows to characterize the crossover between the quasi-condensate regime and the nearly ideal Bose gas regime.

5.3 Experimental realisation of 1D gases with the optical lattice

5.3.1 2D Lattice

Now that we have seen what Tan's contact is and how it could be used to characterize the regimes of Lieb-Liniger 1D gases, we show how our experimental apparatus can be adapted to study 1D physics with the objective of testing experimentally the predictions of [170]. The main idea to obtain an experimental 1D system is to "freeze" the degrees of freedom of the atoms in two directions of space. To do so, the easiest solution is to use a harmonic trapping potential with trapping frequencies $\omega_\perp$ large enough so that the energy difference $\Delta E = \hbar\omega_\perp$ between the ground-state and the first excited state is much larger than the typical energy of the atoms $\Delta E \gg k_{\text{B}}T, \mu$ as illustrated on Fig-5.3. Such high trapping frequencies are accessible in our experiment thanks to the optical lattice. Instead of using the 3 pairs of countra-propagating beam as we did so far, we use only 2 such pairs to produce a 2D lattice. Interestingly, the total laser power is divided amongst 2 pair of beams instead of 3, meaning that we can reach much higher values of the lattice depth, typically up to $s = 30$. In the direction where there is no lattice, the trapping potential results from the Gaussian shape of the beams and has a trapping frequency $\omega_{1\text{D}} = 2\pi \times 140\sqrt{s} = 2\pi \times 713$ Hz for $s = 26$. In the other 2 directions, the trapping frequency is on the contrary very large as a result of the lattice interference pattern $\omega_\perp \simeq 2\pi \times 200$ kHz, which is much larger than the energy of the atoms $k_{\text{B}}T, \mu \simeq h \times 25$ kHz with typical experimental parameters.

Using the optical lattice in this configuration then allows us to emulate 1D physics. The main drawback of this method is that we end up with an array of 1D gases rather than a single one, complicating the comparison with theory.

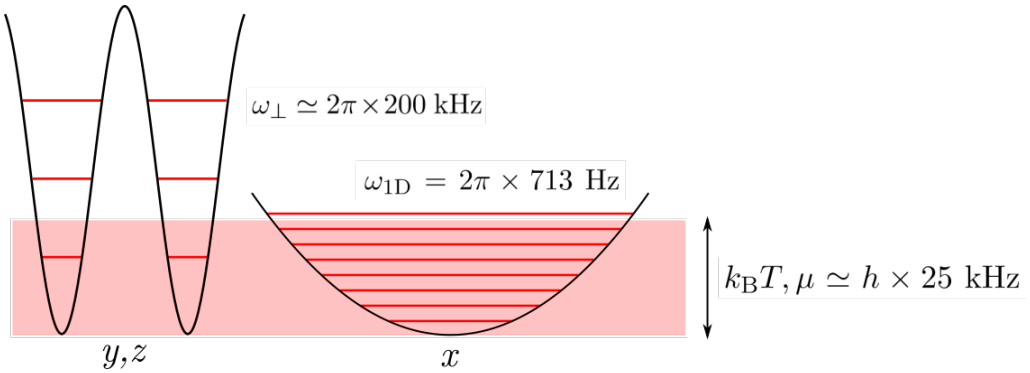

Figure 5.3: Configuration of the optical lattice to produce 1D tubes. In the transverse direction, the lattice interference pattern creates a confining potential that can be approximated to a harmonic potential near the center of the site. The trapping frequency is high enough so that the degree of freedom of the atoms in these directions is "frozen". On the other hand, the lattice is absent in the longitudinal direction and the trapping frequency only results from the Gaussian shape of the beams. This is the 1D direction.

5.3.2 Characterization of the 1D tubes

Number of atoms

One major difficulty of working with our array of 1D gases comes from the fact the atom number varies from one 1D tube to another. To determine the atom number distribution, we first need to determine the density profile of the cloud in the 2D lattice.

To do so, we first remind that under the Thomas-Fermi approximation [124], the density profile of a BEC in a 3D harmonic potential writes:

$$n(\boldsymbol{r}) = \frac{\mu}{g}\left[1 - \left(\frac{x}{R_x}\right)^2 - \left(\frac{y}{R_y}\right)^2 - \left(\frac{z}{R_z}\right)^2\right] \tag{5.20}$$

where $R_i = \sqrt{\frac{2\mu}{m\omega_i^2}}$ is the Thomas-Fermi radius in direction i and g the 3D coupling constant already encountered a few times in this manuscript. Under the mean-field approximation, the chemical potential is:

$$\mu = \frac{\hbar\bar{\omega}}{2}\left(15 N_{\text{bec}} \frac{a_s}{a_{\text{ho}}^{\text{3D}}}\right)^{2/5} \tag{5.21}$$

with $\bar{\omega} = \omega_x\omega_y\omega_z/3$ the average trapping frequency with $a_{\text{ho}}^{\text{3D}} = \sqrt{\hbar/m\bar{\omega}}$

Similarly to the method developed in 2.4.3, we rescale the coupling constant g [98] to account for the presence of the 2D lattice:

$$g' = g\left(\frac{\sqrt{\pi/2}s^{1/4}}{\text{Erf}\left[\pi s^{1/4}/2\right]}\right)^2 \tag{5.22}$$

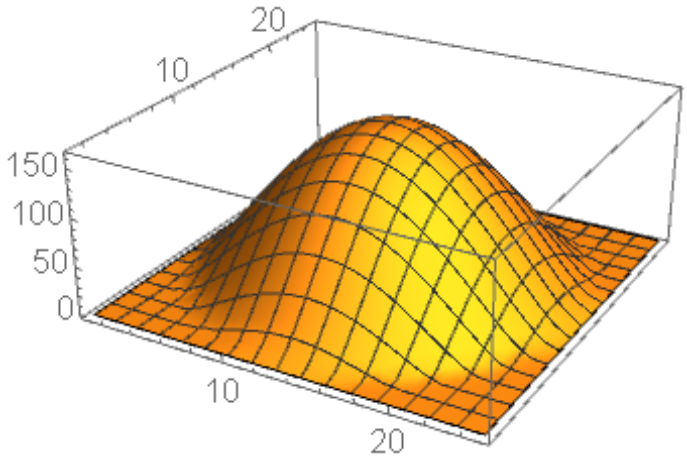

Figure 5.4: Atom number distribution in a 2D lattice of amplitude $s = 26$ for $N_{\text{bec}} = 30 \times 10^3$.

with the notable difference that we are using here a power 2 instead of power 3 in 2.4.3 as we use here a 2D lattice. We then obtain the rescaled chemical potential:

$$\mu' = \frac{\hbar\omega_{1D}}{2}\left(15N_{tot}\frac{a_s}{a_{\text{ho}}}g'^2\right)^{2/5} \tag{5.23}$$

from which we finally obtain the new Thomas-Fermi radius in the transverse directions:

$$R_{\text{TF}} = \frac{1}{d}\sqrt{\frac{2\mu'}{m\omega_\perp^2}} \tag{5.24}$$

that we express in units of lattice spacing d for convenience. The number of atoms in the tube indexed j, l then writes (see Fig.-5.4 and Fig.-5.5):

$$N_{j,l} = N_{00}\left(1 - \frac{j^2 + l^2}{R_{\text{TF}}^2}\right). \tag{5.25}$$

where N_{00} is the number of atoms in the central tube. We deduce N_{00} from the total atom number N_{bec} with the normalization condition $N_{\text{bec}} = \sum_{j,l} N_{j,l}$ giving:

$$N_{00} = \frac{5}{2\pi}\frac{N_{\text{bec}}}{R_{\text{TF}^2}} \tag{5.26}$$

Density and interaction parameter

Knowing the number of atom in each tube, it is interesting to determine the density and reduced interaction strength parameter ξ_γ in each of the tubes. To do so, we first rewrite the 1D interaction strength $g_{1\text{D}} = 2\hbar\omega_\perp a_s$ [116] from the transverse trapping frequency and the 3D scattering length which are our known experimental parameters. We then

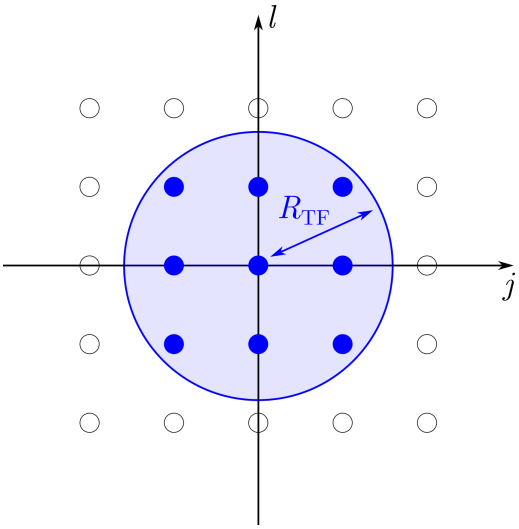

Figure 5.5: Schematic of the array of 1D tubes. The large blue circle denotes the parabolic density profile of the BEC that determines which of the lattice sites contain atoms (blue dots).

write the 1D chemical potential and 1D density for the different tubes, both functions of the number of atoms in the tube:

$$\mu_{1D}^{j,l} = \left(\frac{3}{4\sqrt{2}}\, N_{j,l}\, g_{1D}\, \omega_{1D}\, \sqrt{m}\right)^{2/3} \tag{5.27}$$

$$\rho_{1D}^{j,l}(x) = \frac{\mu_{1D}}{g_{1D}} - \frac{1}{2}\, m\, \omega_{1D}^2\, x^2 \tag{5.28}$$

In practice, the second term of equation 5.28 can be neglected because of the small size of the 1D gases $\sim \mu$m and the weak confinement $\omega_{1D} \approx 2\pi \times 700$Hz so that $\rho_{1D}^{j,l}(x)$ is constant and well approximated by its value at the center of the trap $\rho_{1D}^{j,l}(0)$. We then simply write $\rho_{1D}^{j,l}$.

The reduced interaction strength ξ_γ is rather straightforward to obtain from the atom number distribution:

$$\xi_\gamma^{j,l} = -a_{\mathrm{ho}}/a_{1\mathrm{D}}\sqrt{N_{j,l}} \tag{5.29}$$

with $a_{1\mathrm{D}}$ that can be written from the 3D scattering length a_s with $a_{1\mathrm{D}} = \hbar/m\omega_\perp a_s$.

Weighted average

The values of $\xi_\gamma^{j,l}$ for each of the 1D tubes are however not very meaningful in practice as the distribution that we measure results from the contribution of every lattice tubes. It is therefore more convenient to define a single averaged value of $\bar{\xi}_\gamma$ to approximately describe the entire ensemble of 1D gases. One could first simply think of using a simple average:

$$\bar{\xi}_\gamma = \frac{1}{N_{\text{tubes}}} \sum_{j,l} \xi_\gamma^{j,l} \tag{5.30}$$

This kind of averaging is however too strong of an approximation as it assumes that each of the tubes contribute equally to the total measured distribution which is wrong as the contribution of the tubes with more atoms will be more significant. We then choose to weight the contribution of each of the tubes in the average by its fraction of the total atom number:

$$\bar{\xi}_\gamma = \sum_{j,l} \frac{N_{j,l}}{N_{\text{bec}}} \xi_\gamma^{j,l} \tag{5.31}$$

Note that this kind of weighted averaging can be done for all relevant quantities that vary from one 1D tube to another.

Temperature

We have proven in 3.3 that the loading of the 3D lattice is adiabatic up to lattice depths of $s = 18$. As we keep the same loading sequence for the 2D lattice preparing the 1D tubes, it is rather reasonable to assume that the loading is here adiabatic as well even though we go to higher amplitudes and the geometry of the lattice is different. Under this assumption, we then expect the temperature to be the same amongst all the 1D tubes. We will see later how information on the temperature can be obtained from the measured momentum distribution.

Independence of the tubes

In order to properly observe 1D physics, it is crucial that all the 1D tubes are independent from one another, *i.e* no coherence subsists in the transverse directions. This is in principle true when the typical loading time of the lattice set by the slope of the lattice ramps of 0.3 E_r/ms (see 3.3.1) is longer that the decoherence time of the cloud. Practically speaking, we can determine whether the 1D tubes are indeed incoherent or not by looking for diffraction peaks in the transverse directions, as their presence reveals coherent interferences between the different tubes. While we indeed observed no diffraction peaks in most data sets, there were a few occasions where they could be seen, especially for the coldest data sets and lower lattice amplitudes $s \simeq 22$. This calls for a proper study of the decoherence mechanisms happening during the loading of the lattice that has not yet been conducted at the moment where this manuscript is being written. We will for the remainder of this chapter assume that the tubes are indeed independent as the data was taken for relatively high lattice amplitudes $s = 26$ at which we observed no diffraction peaks in the transverse direction.

5.4 Detection of large momentum components

While the great sensitivity of the He* detector is perfectly suited to detect the very low density k^{-4} momentum tails, its range is inherently limited by the size of the MCPs. This

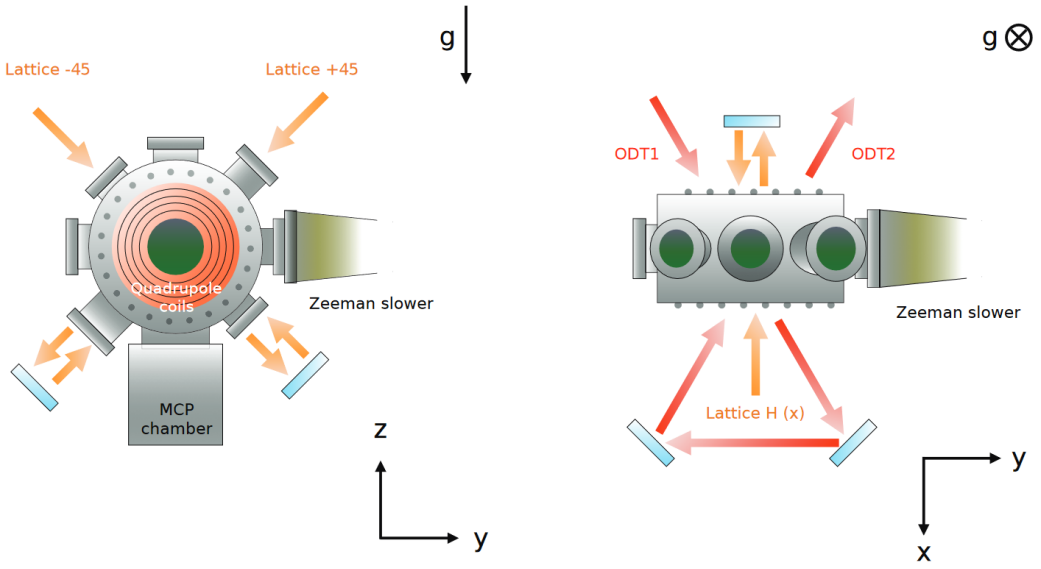

Figure 5.6: Orientation of the lattice beams in the experiment, illustrating the possible 1D directions. Taken from [28].

is a major drawback as the k^{-4} decay only happens for large values of k that might fall out of the range of the He* detector. One solution could be to have the 1D direction vertical as the He* detector range is not limited in this direction, but this is not possible due to the layout of the lattice beams (see 5.6). The most advantageous solution is then to set the 1D direction along the direction set by the $+45°$ beam (the 2D lattice is then made by the $-45°$ and horizontal beams), increasing the effective range of the detector by a factor $\sqrt{2}$. The maximum detectable momentum is then $k_{\mathrm{max}} \simeq 14\ \mu\mathrm{m}^{-1}$.

Actually, we can use the results of [167] that show that the k^{-4} decay should start around $k_0 \sim 1.6 \times \bar{\rho}_{1\mathrm{D}}$ to determine whether the tails should be detectable or not. For $N_{\mathrm{bec}} \simeq 100 \times 10^3$, we find that $k_0 \simeq 10\ \mu\mathrm{m}^{-1}$, meaning that even though we could see the beginning of the k^{-4} decay, the range is too small to observe it on a sufficiently large momentum range. We therefore need a solution to effectively increase the momentum range of the He* detector.

5.4.1 Magnetic gradient and displacement procedure

One solution to this issue is to give the entire cloud a momentum kick in the first instants of the TOF to artificially shift the momentum range of the He* detector towards high momenta. With our experimental setup, the easiest way to do so is to create a magnetic gradient to apply a magnetic force on the atoms during a time t_{grad} before transferring them to the $m_j = 0$ sub-state.

New population transfer technique

This technique however brings some experimental complications as the population transfer cannot be done immediately after turning off the trap. As a matter of fact, the atoms starts moving during the time t_{grad} and will therefore be at different positions when the transfer

is performed. The problem comes from the fact that there is a slight inhomogeneity in the bias field along direction x used to set the energy difference between the sub-states $m_J = 0$ and $m_J = 1$, resulting in a small gradient of 0.17 G/cm as already mentioned in 3.2.5. This means that the resonance condition for a Raman or RF transfer depends on the initial momentum of the atoms, with the consequence that we cannot properly transfer the whole cloud to $m_J = 0$ with a simple single frequency Rabi pulse.

To solve this issue, we make use of the Landau-Zener effect that describes the probability for a transition between two levels to occur when the coupling frequency varies linearly in time. As the experiments described in this chapter were performed before the implementation of the two-photon Raman transfer described in Chapter 3, this was done by linearly sweeping the frequency ν_{RF} of a RF wave with a span $\Delta\nu_{\mathrm{RF}}$ around the central resonance frequency $\nu_{\mathrm{res}} \simeq 12.93$ MHz (see 3.2.5) in a time $\Delta t_{\mathrm{sweep}}$. The values of $\Delta\nu_{\mathrm{RF}}$ and $\Delta t_{\mathrm{sweep}}$ are set according to three constraints.

- The initial and final detunings must be much larger than the RF Rabi frequency Ω_{RF} so that $\Delta\nu_{\mathrm{RF}} \gg 2\Omega_{\mathrm{RF}} \simeq 20$kHz
- The fraction of transferred atom depends from the rate $\alpha = \Delta\nu_{\mathrm{RF}}/\Delta t_{\mathrm{sweep}}$ at which $\nu_{\mathrm{RF}}(t)$ changes. The transfer is more efficient as α is low.
- $\Delta\nu_{\mathrm{RF}}$ must be large enough to encapsulate all resonance frequencies shifted because of the residual magnetic gradient to properly transfer all relevant momentum classes. For an initial momentum $k = -k_d = -8.1\ \mu\mathrm{m}^{-1}$, the resonance shift with respect to $k = 0$ atoms is around 75 kHz with $t_{\mathrm{grad}} = 13$ ms.

We then decide to set $\Delta\nu_{\mathrm{RF}} = 2$MHz to make sure that no momentum class is excluded, and set $t_{\mathrm{sweep}} = 3$ ms so that $\alpha/\Omega_{\mathrm{RF}}^2 = 6.7$, yielding a total detection efficiency $\eta_{\mathrm{sweep}} = 0.10(1)$. We remind that this number accounts for the transfer efficiency which is limited to 50% because of the three level structure of 2^3S_1 and the efficiency of the detector itself.

Generation of the magnetic gradient

The procedure to create the magnetic gradient was mainly designed to fit the constraints set by the design of our experimental apparatus. As a matter of fact, the geometry of the science chamber makes it quite hard to install coils capable of producing a strong enough gradient along the direction of the $+45°$ or $-45°$ beams which are the best choice for the 1D direction in terms of momentum range of the detector. On the other hand, there is a gradient coil quite close to the atoms capable of producing a strong enough gradient along the horizontal beam direction that we will denote as the x direction, as well as the MOT coils capable of producing a strong gradient 4 times stronger along x. We then decided to set the 1D direction along x. While this reduces the momentum range by a factor $\sqrt{2}$, this is not a big issue as we will use the gradient to compensate for it.

After quite a bit of testing, we decided to use the MOT coils instead of the x gradient coils as the former is capable of producing a stronger gradient, effectively reducing the time during which the gradient must be applied. This has the advantage of reducing the spatial spread of the atoms before the transfer to $m_J = 0$ and thus the inhomogeneity in resonance frequencies because of the residual gradient.

Displacement procedure

The procedure is represented on Fig.-5.7. Right after the lattice is turned off, we increase the current in the MOT coils to produce the magnetic gradient. However, the current in the MOT coils typically needs around 10 ms to reach the highest possible values, which is already quite long. We then set the command voltage V_c to be close to the highest possible value, let the current increase for $t_1 = 1$ ms and then set the command to 0 and let the current decay for $t_2 - t_1 = 13$ ms until it is fully turned off. After that, we finally perform the population transfer and let the atoms fall unto the MCP. The momentum displacement of the cloud can be set by changing the command voltage V_c.

Calculation of the induced displacement

The effect of the magnetic gradient on the TOF trajectories of the atoms can be calculated rather easily. For simplicity sake, we will assume that the gradient is constant in time and write B' its value along the x axis. The atoms feel a force $F_x = 2\mu_B B'$ for the time t_{grad} during which the gradient is on, with μ_B the Bohr magneton and the factor 2 being the Landé factor. Taking $t = 0$ when we start turning on the gradient, the speed of atoms with a zero initial velocity at the center of the trap after t_{grad} writes:

$$v_x(t_{\text{grad}}) = \frac{2\mu_B B'}{m} t_{\text{grad}} \tag{5.32}$$

In turn, their position writes:

$$x(t_{\text{grad}}) = \frac{\mu_B B'}{m} t_{\text{grad}}^2 \tag{5.33}$$

The final position after the full TOF is linked to $x(t_{\text{grad}})$ by

$$x(t_{\text{TOF}}) - x(t_{\text{grad}}) = v_x(t_{\text{grad}})(t_{\text{TOF}} - t_{\text{grad}}) \tag{5.34}$$

The calculations can be simplified by considering that (i) $t_{\text{grad}} = 13$ ms $\ll$ $t_{\text{TOF}} = 296$ ms and consequently (ii) $x(t_{\text{grad}}) \ll x(t_{\text{TOF}})$. As a result, the position at the end of the TOF is simply:

$$x(t_{\text{TOF}}) = \frac{2\mu_B B'}{m} t_{\text{grad}} t_{\text{TOF}} \tag{5.35}$$

The effect of the gradient is then simply to shift the position of the entire cloud at the end of the TOF without distorting it, with a simple linear relation between the intensity of the gradient and the value of the position shift.

5.4.2 Transverse integration effects and range limitations

As in 4.1.3, the transverse size of the voxels that we will use to compute the momentum density (see 5.5.2) defines a transverse integration $\Delta k_\perp$ that needs to be sufficiently large $\simeq$

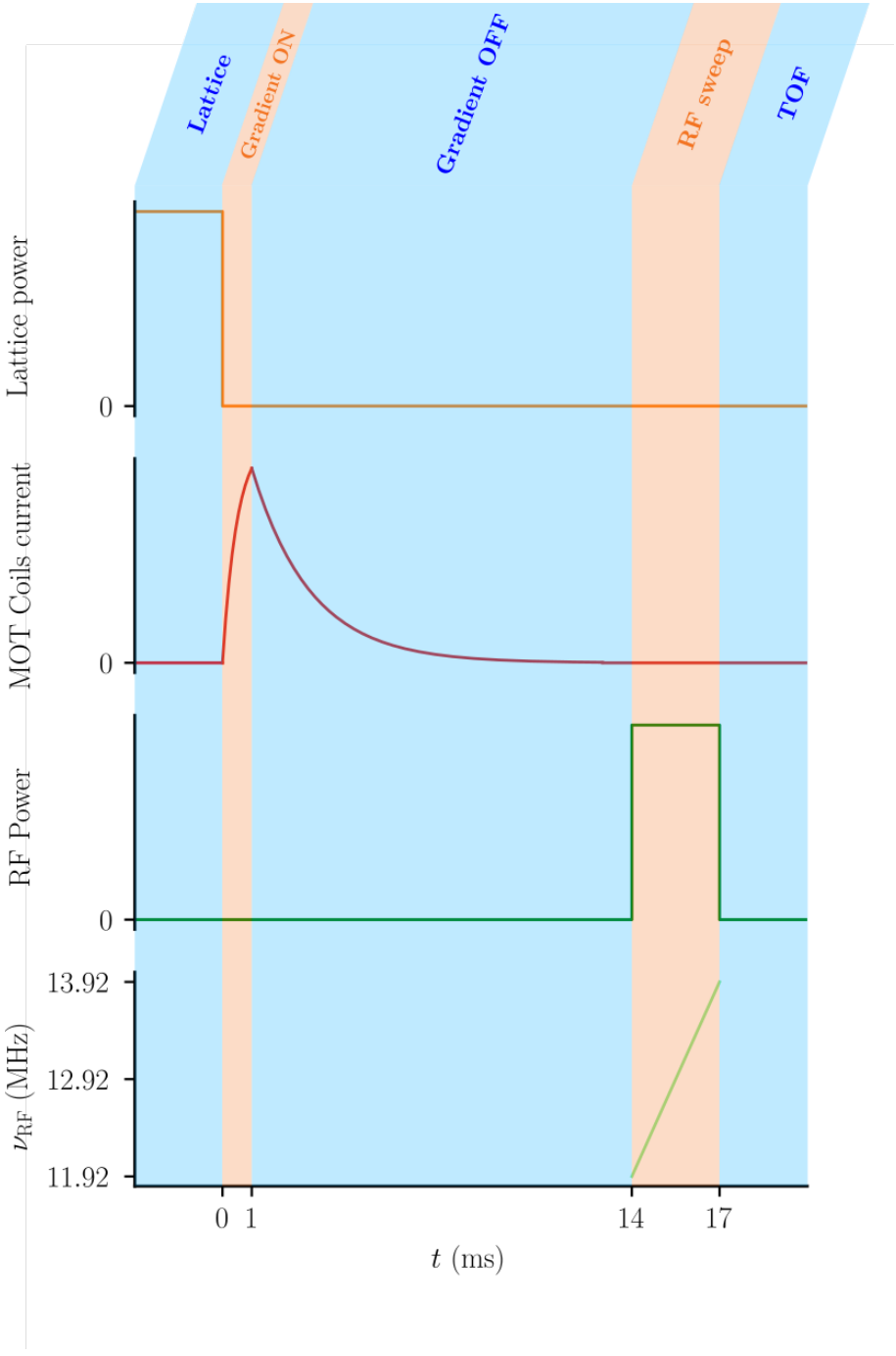

Figure 5.7: Experimental sequence to shift the entire momentum distribution so that the k^{-4} tails fall onto the He* detector. The lattice power is represented in orange, the MOT coils current in red and the RF wave power and frequency in green and light green respectively.

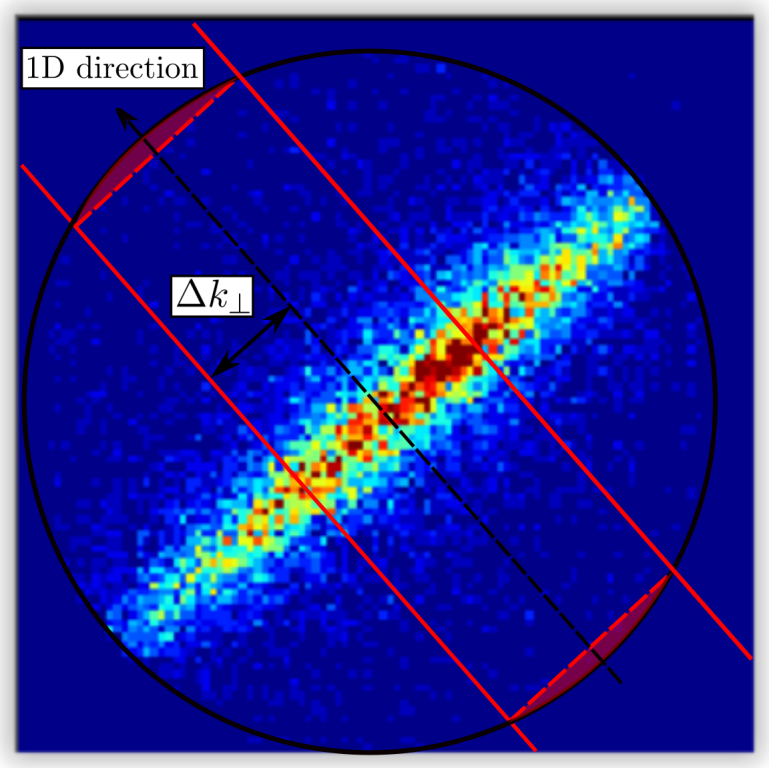

Figure 5.8: Gravity integrated 2D image of the distribution of the 1D lattice gas illustrating the effect of the transverse integration. The red shaded area indicated the region where the geometry of the detector affects the measurement of $n_{1D}(k)$.

0.8 μm^{-1} to ensure a proper signal-to-noise ratio. As illustrated on Fig.5.8, the transverse integration however effectively reduces the momentum range in the 1D direction because of the circular shape of the detector that cuts out a part of the integration volume. The transverse integration must then be kept as low as possible and the distorted edges of the distribution ignored in the analysis.

5.4.3 Benchmarking with 3D lattice gases momentum distribution

To check that our method does not induce any distortion of the momentum distribution, we benchmark it with 3D lattice gas momentum distribution for different displacements. The lattice amplitude is set to $s = 15$, *i.e* high enough so that the momentum distribution has a wide background but still sharp diffraction peaks. We can check the overlap of the data sets for different displacements with the wide background while precisely characterizing distortion effects by looking at the location of the diffraction peaks.

The data is plotted on Fig-5.9 and Fig-5.10. These two figures illustrate several crucial points:

- Even though we get an almost perfect agreement between the blue (non-displaced) and the orange curve on Fig.-5.9, the orange peak at $k = k_d$ is lower than expected. This is an effect that we attribute to the transverse integration that causes the measured distribution to decay faster than we would expect on the edges of the MCPs

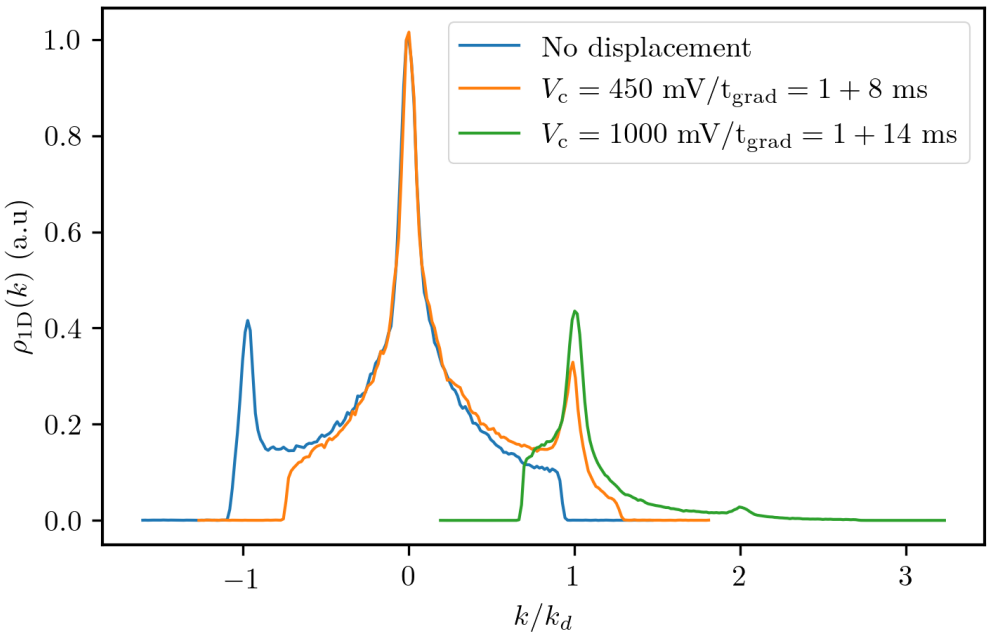

Figure 5.9: Test of the displacement sequence on a 3D lattice $s = 15$ momentum distribution. The blue curve corresponds to no displacement gradient, while the orange, and green curves corresponds to displaced data with a command voltage $V_c = 450$ mV for the orange curve and $V_c = 1000$ mV for the green one. The time t_{grad} before the RF transfer consists 1 ms during which the current in the MOT coils is set to increase, and 8 ms where it is left to decrease for the orange curve. This time is extended to 14 ms for the green curve.

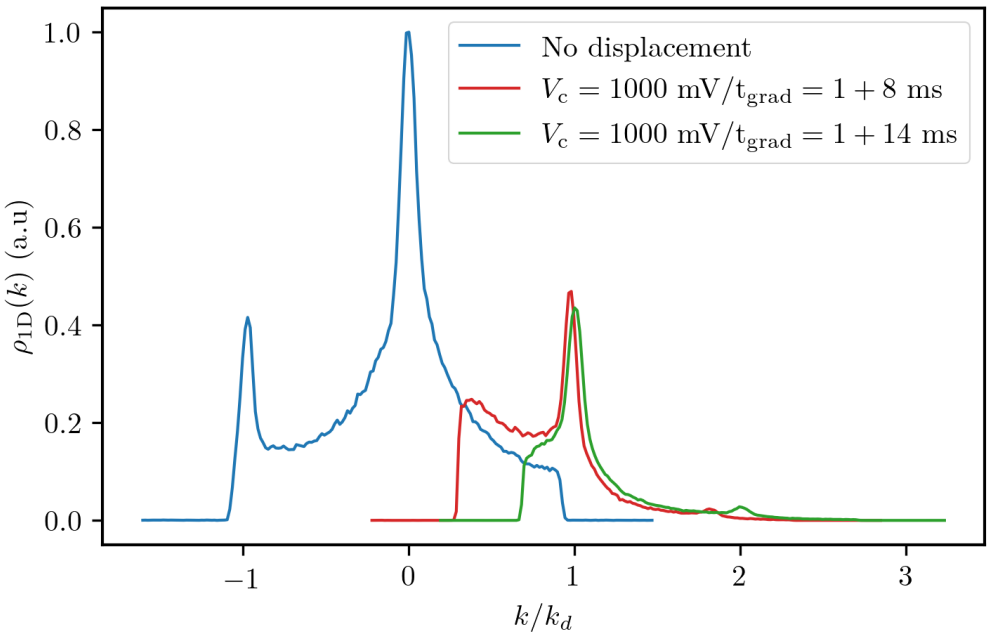

Figure 5.10: Distortion of the distribution. The parameters are the same than for Fig.-5.9 with the addition of the red curve corresponding to a command voltage $V_c = 1000$ mV and t_{grad} of 1 ms during which the current in the MOT coils is set to increase and 8 ms where it is left to decrease. As this time is too small for the strong gradient too be properly turned off, the distribution is distorted explaining why the diffraction peak appears at lower k value.

as explained in the previous paragraph. The green curve however well reproduces the shape of the -1 k_d peak.

- The red curve of Fig-5.10 illustrates an important caveat of the displacement procedure. While we still let the current in the MOT coils increase for 1 ms, we perform the RF transfer only 8 ms after this step which is too short for the gradient to properly turn off, contrary to the green curve where this time is increased to 14 ms. Because of the distance travelled by the atoms before the RF sweep and the presence of a gradient, the atoms see different magnetic fields and thus have different resonance frequencies depending on their initial momentum. When the RF sweep is performed, some atoms will then be transferred later than others and will thus interact longer with the magnetic field, resulting in a larger displacement and a distortion of the distribution. This effect is striking on the red curve for which the diffraction peak appears at a lower k than expected. On the other hand, if we wait long enough for the displacement gradient to be turned off, this effect disappear as illustrated by the diffraction peak of the green curve well centered on $k = k_d$.

Overall, we get a nice overlap between the different properly displaced data sets and therefore conclude that our displacement method does not induce any distortion of the measured momentum distribution.

5.5 Experimental study

Having described the experimental procedure to collect the data, we detail in this section the techniques and crucial points to properly analyze the experimental data.

5.5.1 Analysis of the transverse shape

The first point that we need to check is the transverse shape of the 3D distribution to know whether we can fully decouple what is happening in the 1D direction from what is happening in the other two transverse directions. The transverse momentum distribution is supposed to be a Gaussian distribution whose width depends on the transverse trapping frequency. If the atoms are in the harmonic oscillator ground state of the transverse direction, the RMS width of the distribution in momentum-space is $\sigma_{\text{theo}} = \sqrt{\frac{m\omega_\perp}{2\hbar(1+4a_s\rho_{1D})}}$ [69].

On Fig.-5.11, we plot the transverse distribution along gravity at different positions along the 1D direction and normalize it to 1. We observe that we get the same RMS size for every k_{1D} at which the cut is done meaning that the 1D direction is fully decoupled from what is happening in the transverse direction. We extract its RMS width $\sigma_{\text{exp}} = 5.96(2)\ \mu\text{m}^{-1}$. This data set was taken with $s = 26$, meaning that $\omega_\perp = 1.33(3) \times 10^6\ \text{s}^{-1}$ (see 2.3.1 for the detailled formula), giving $\sigma_{\text{theo}} = 5.8(1)\ \mu\text{m}^{-1}$ in agreement with the experimental value.

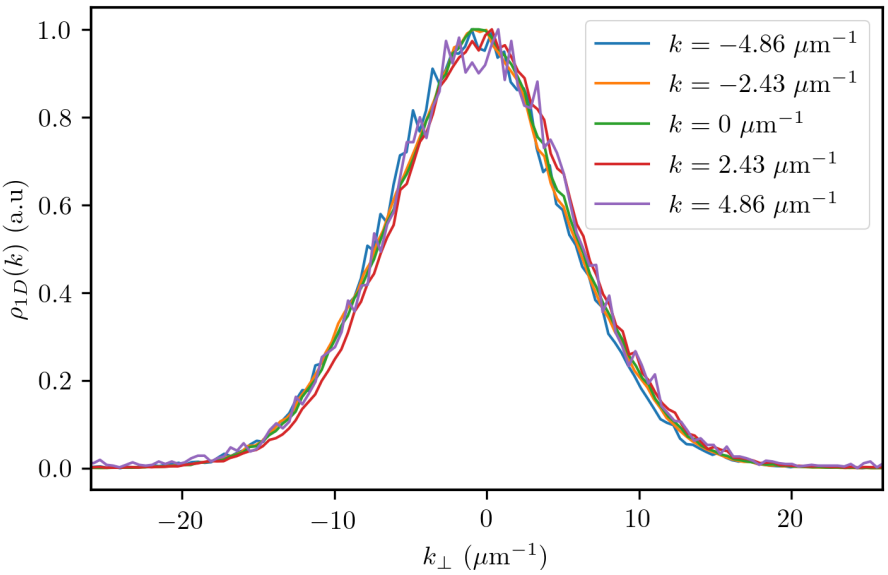

Figure 5.11: Normalized 1D cut along gravity of the experimental distribution at various k along the 1D direction. The Gaussian shape remains unchanged, meaning that the 1D direction is fully decoupled from the transverse directions.

5.5.2 Calculation of the momentum density

In order to compare the experimental values of the Tan's contact to theory, it is crucial to obtain the absolute value of the 1D density $\rho_{1D}(k)$ from the experimental data. To do so, we exploit the fact that the transverse distribution shape is the same along the 1D direction as we have just seen. Under the effect of the fast transverse expansion, some atoms fall beyond the MCPs and are therefore not detected. However, knowing the transverse profile, we can do as if everything was only happening in one direction and integrate over the transverse profile. The procedure is the following:

- We plot the transverse distribution $\rho_\perp(k)$ (in the vertical direction where it is not cut out by the finite size of the He* detector) and extract its RMS width σ_{exp}.
- For one voxel of size $\Delta k_{1D} \times \Delta k_\perp^2$, we have (keeping in mind normalization condition with the factor 2π):

$$\rho_{1D}(k) = 2\pi \times \frac{N_{\text{vox}}(k)}{\eta_{\text{sweep}} \Delta k_{1D} \Delta k_\perp^2} \left(\int \rho_\perp(k_\perp) dk_\perp \right)^2 \tag{5.36}$$

$$\tag{5.37}$$

η_{sweep} being the detection efficiency and $N_{\text{vox}}(k)$ the number of atoms in the voxel at a given k. From this, we obtain the expression of $\rho_{1D}(k)$ that depends only on measured experimental values:

$$\rho_{1D}(k) = 4\pi^2 \times \frac{N_{\text{vox}}(k)}{\eta_{\text{sweep}} \Delta k_{1D} \Delta k_\perp^2} \sigma_{\text{exp}}^2 \tag{5.38}$$

5.5.3 Measurement of the temperature

As we want to study the dependency of the Tan's contact with temperature and compare with *ab-initio* QMC calculations, we first need to extract the temperature from the experimental data. Actually, the width of the momentum distribution contains information about the temperature under certain conditions that we will now discuss.

We need to look at the properties of the first order spatial correlation function which are directly reflected in the momentum distribution. In 1D gases at $T = 0$, the interactions induce an algebraic decay of the first order correlation function that translates into an algebraic decay of the momentum distribution [65, 128]. However, at $T \neq 0$, the temperature creates phase fluctuations that induce an exponential decay of the first order correlation function. In the weakly-interacting regime where $(1, \xi_T) \leq \xi_\gamma^{-1}$, this decay happens on shorter length scales than the one induced by interactions. This means that at low k, the momentum distribution is Lorentzian (Fourier transform of a damped exponential) [31, 55, 68]:

$$\rho_{1\mathrm{D}}(k) = \frac{2\bar{\rho}_{1\mathrm{D}}(0)/\delta k}{1 + (k/\delta k)^2} \tag{5.39}$$

with $\bar{\rho}_{1\mathrm{D}}(0)$ the average central density over the tubes weighted by the number of atoms in the tube. Its width δk is linked to the coherence length of the gas L_ϕ:

$$\delta k = \frac{\alpha_{\mathrm{fit}}}{L_\phi} \tag{5.40}$$

itself linked to temperature by:

$$L_\phi = \frac{\hbar^2 \bar{\rho}_{1\mathrm{D}}(0)}{m k_{\mathrm{B}} T} \tag{5.41}$$

where α_{fit} is a coefficient that depends from the 1D trapping frequency $\omega_{1\mathrm{D}}$ and the interaction parameter. It is not entirely clear whether this picture should hold for our typical experimental parameters putting us near the frontier between the weakly-interacting and strongly interacting regimes. However, numerical QMC calculations performed by Hepeng Yao from Centre de Physique Théorique at Ecole Polytechnique have shown that this description works, provided that the proper α_{fit} is used. Its value has been calibrated with the QMC calculations and is typically equal to $\alpha_{\mathrm{fit}} = [0.78, 0.79]$ for the data sets presented here. The temperature of the system can then easily be extracted with a Lorentzian fit of the measured momentum distribution at low k as illustrated on Fig-5.12.

In practice, the temperature can be increased in the same fashion than described in 4.2.3 by increasing the holding time in the lattice. This effect is clearly visible in Fig-5.12 where we see that the width of the Lorenztian increases when the holding time is increased. Table 5.1 shows the temperatures, lattice holding times and reduced temperatures of the 3 data sets presented in this chapter.

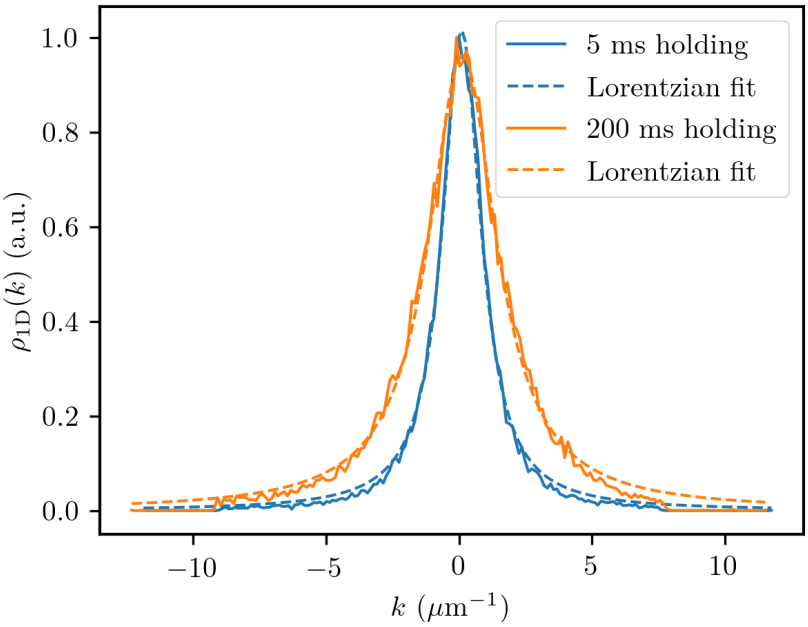

Figure 5.12: Normalized 1D momentum distribution $\rho_{1D}(k)$ for lattice holding times $t_{\text{hold}} = 5$ ms and $t_{\text{hold}} = 200$ ms. The Lorentzian fit well matches the data at low k. The increase in the width of the distribution signals the increase in temperature induced by the increased holding time in the lattice. We measure $T = 800$ nK for $t_{\text{hold}} = 5$ ms and $T = 1.5$ μK for $t_{\text{hold}} = 200$ ms.

t_{hold} (ms)	T (μK)	ξ_T
5	0.8	1.57
200	1.5	2.09
600	2.9	2.91

Table 5.1: Temperature of the system for 3 lattice holding times t_{hold} and corresponding reduced temperature ξ_T.

5.5.4 Interaction parameter

The other relevant parameter affecting the value of Tan's contact besides temperature is the reduced interaction strength as defined in equation 5.12 which we control by changing the total number of atoms N_{bec} loaded in the 2D optical lattice. Table 5.2 shows its weighted average values versus the total atom number N_{bec} for the 3 data sets that will be discussed here.

N_{bec}	$\bar{N}$	$\bar{\xi}_\gamma$
3.1×10^4	58	0.167
1.1×10^5	125	0.113
2.3×10^5	192	0.092

Table 5.2: Weighted average number of atoms per tube and average reduced interaction strength for 3 different total atom numbers N_{bec}.

5.5.5 Experimental procedure and first extracted values of the Tan's contact

The procedure to measure Tan's contact for a given data set is as follows:

- We prepare the parameters of the experiment to reach the desired values of temperature and atom number. The latter is calibrated via absorption imaging while the former is set by changing the holding time in the lattice and checking that the width of the 1D distribution increases.
- We start by taking ~ 100 experimental shots with no gradient to measure the low k distribution from which we can extract the temperature as explained in 5.5.3. We do not need to take a large number of shots as the signal is quite high and we do not require a very high signal-to-noise ratio to obtain the temperature.
- We set the gradient to shift the momentum distribution to access the momentum region where the k^{-4} tails are supposed to be present as explained in 5.4. Usually, the displacement is not too high so that the momentum range overlaps the natural momentum range of the He* detector where no gradient is used, allowing to check that the displaced data matches nicely the non-displaced data in the region of the overlap as shown on Fig.-5.13 panels (a) and (b). In the following for clarity sake, we will plot one single curve obtained by merging the low and high momentum data.
- After computing the 1D distribution $\rho_{1\text{D}}(k)$ with the method detailed in 5.5.2, we plot the quantity $\rho_{1\text{D}}(k) \times k^4$. The presence of k^{-4} tails is signaled by a flat zone that we can fit with a constant function to extract the bare value of the contact C as illustrated on Fig.-5.13.

Coming back to the predictions of [170], we have already seen that the contact can be

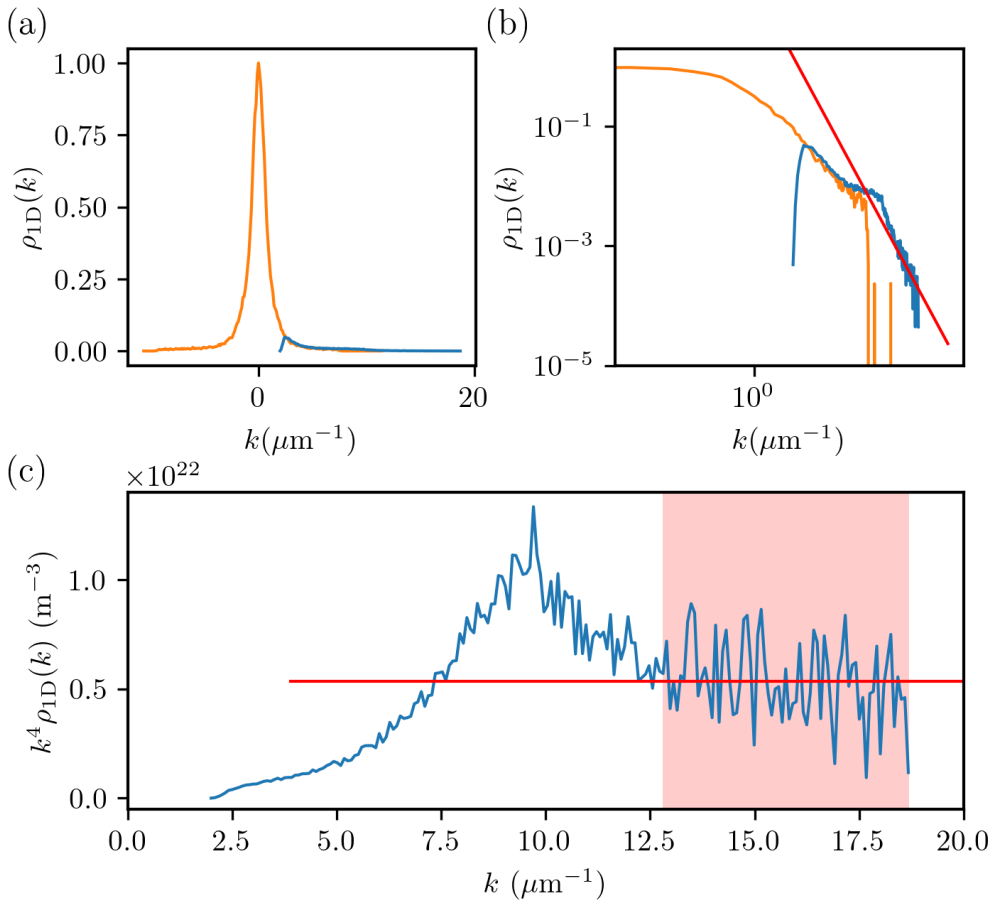

Figure 5.13: Plots of $\rho_{1D}(k)$ for $s = 26$, $N = 3.1(3) \times 10^4$ and $t_{hold} = 5$ ms. (a) Linear scale plot of the normalized $\rho_{1D}(k)$ for two momentum ranges. (b) Same data in log scale. The red line indicates a k^{-4} fit. (c) $k^4\rho_{1D}(k)$ at high momentum. The red shaded area indicates the flat zone of the k^{-4} tail.

written:

$$C = \frac{N^{5/2}}{a_{\mathrm{ho}}^3} f(\xi_\gamma, \xi_T) \tag{5.42}$$

We can then define a rescaled contact:

$$\tilde{C} = C \frac{a_{\mathrm{ho}}^3}{N^{5/2}} \tag{5.43}$$

as plotted on Fig-5.2. In the following, we will then plot $\tilde{C}$ instead of the bare value C for convenience.

5.6 Discussion of the preliminary results

5.6.1 Qualitative evolution with temperature

We plot on Fig.-5.14 the experimental rescaled contact $\tilde{C}$ as a function of ξ_T for a fixed atom number $N = 1.1(1) \times 10^5$ corresponding to $\xi_\gamma = 0.113$. The error bars corresponds to the standard deviation over the data points averaged to obtain the value of the contact. As we only have 3 data points at the moment, it is rather hard to see a clear trend appearing, but the point at high temperature is clearly lower than the other 2. This qualitative behavior is consistent with the predictions of [170]: with the reduced interaction strength $\xi_\gamma = 0.113$, we should be somewhere close to the green curve of 5.2 panel (b) in the region of ξ_T where $\tilde{C}$ is decreasing. It seems however that we should increase ξ_γ to observe the non-monotonic behavior of the contact with the current error bars of the experiment.

5.6.2 Qualitative evolution with the interaction strength

We plot on Fig.-5.15 the experimental bare contact C as a function of $\bar{N}$ and the experimental rescaled contact $\tilde{C}$ as a function of ξ_γ for a fixed temperature $T = 0.8$ μK corresponding to $\xi_T = 1.57$. Interestingly, C and $\tilde{C}$ behave very differently: while C increases by roughly an order of magnitude because of the dependency in $N^{5/2}$, $\tilde{C}$ is found to be close to constant. This is rather reassuring as we are able to observe strong variations of the bare experimental contact that nevertheless look to be qualitatively consistent with theory. According to Fig.-5.2, $\tilde{C}$ should indeed be slowly increasing with ξ_γ as we may observe here.

5.6.3 Comparison with QMC calculations

So far, we have only discussed the qualitative evolution of $\tilde{C}$ with ξ_T and ξ_γ which seems encouraging and consistent with theory. We now push our study one step further by comparing the experimental data to *ab-initio* QMC calculations simulating our experiment. The calculations were once again performed by Hepeng Yao and simulate the distribution

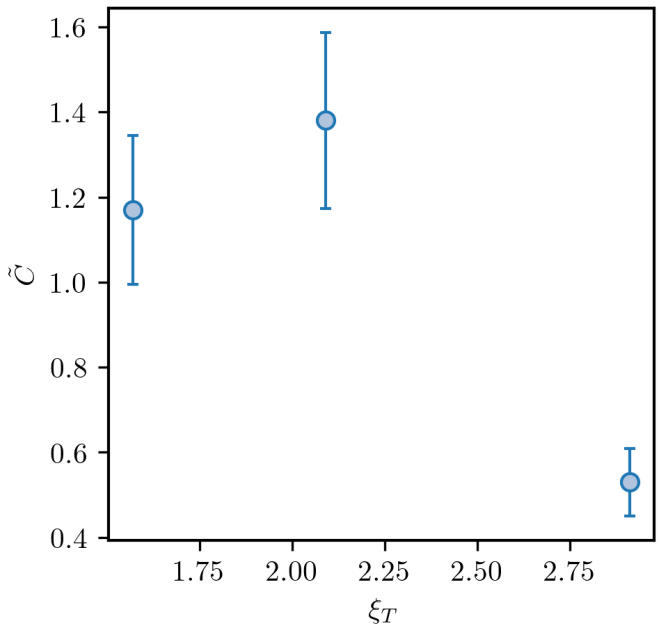

Figure 5.14: Rescaled contact $\tilde{C}$ as a function ξ_T for a fixed $\xi_\gamma = 0.113$. The qualitative behavior is consistent with the predictions of [170] as $\tilde{C}$ decreases with λ_T.

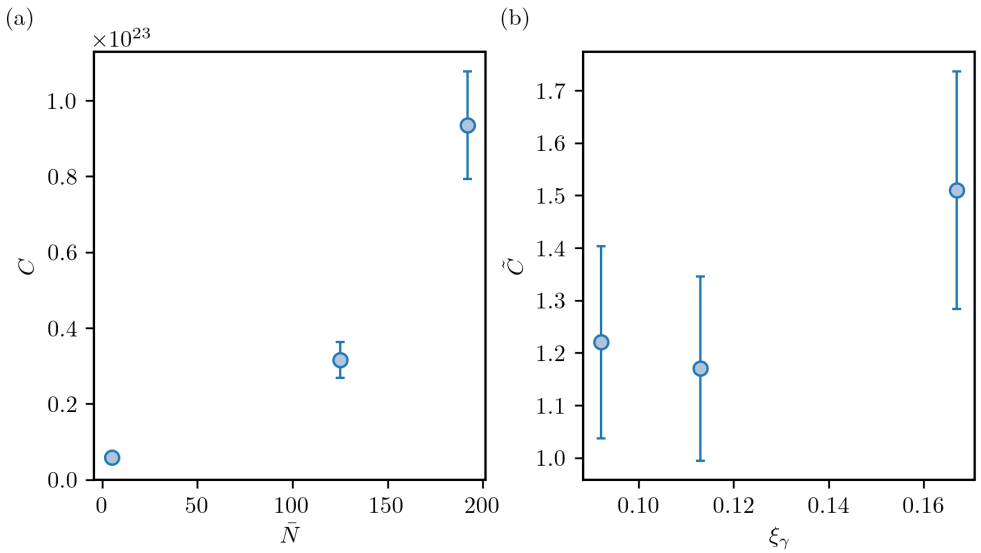

Figure 5.15: Contact for various interaction strengths at a fixed temperature $\xi_T = 1.57$ (a) Bare contact as a function of the weighted average number of atoms per tube $\bar{N}$. (b) Rescaled contact $\tilde{C}$ as a function of the reduced temperature ξ_T.

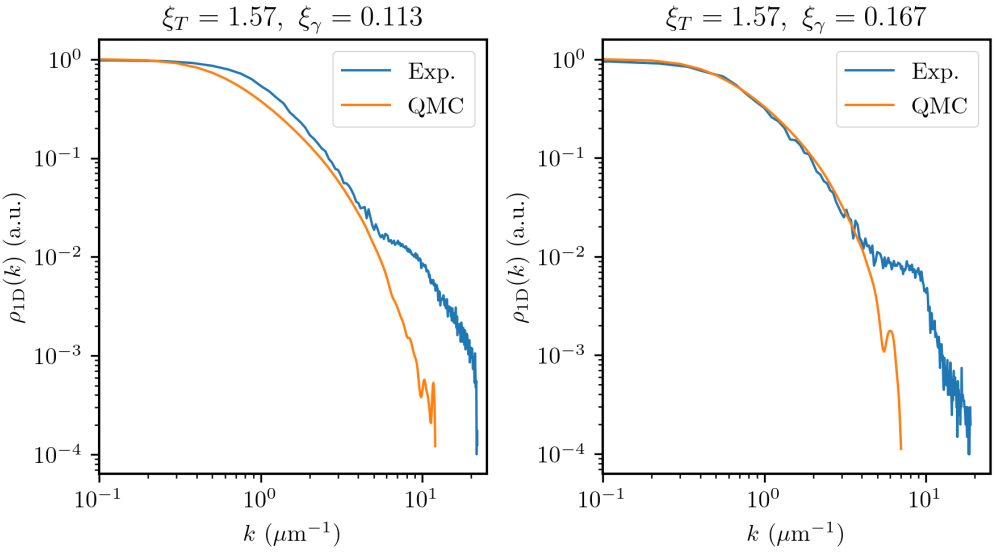

Figure 5.16: Comparison between the normalized experimental data and QMC calculations for two different total atom numbers $N_{\mathrm{bec}} = 110 \times 10^3$ (left) and $N_{\mathrm{bec}} = 31 \times 10^3$ (right).

of tubes to match the experiment as precisely as possible. The results are plotted on Fig.-5.16 for two interaction parameters $\xi_\gamma = 0.113$ and $\xi_\gamma = 0.167$ corresponding to $N_{\mathrm{bec}} = 1.1(1) \times 10^5$ and $N_{\mathrm{bec}} = 3.1(3) \times 10^4$ for a fixed temperature $\xi_T = 1.57$. The agreement for the low k part is slightly off for the $N_{\mathrm{bec}} = 1.1(1) \times 10^5$ data set, possibly due to a slight misevaluation of the temperature, but very good for the $N_{\mathrm{bec}} = 3.1(3) \times 10^4$ data set, meaning that the method we use to describe the entire 2D array of 1D tubes and to determine the temperature is rather accurate, at least for low atom numbers. There is however a very clear disagreement by two orders of magnitude in the high k part where the k^{-4} tails are supposed to be.

Possible explanations

It is actually not the first time that our team tried to measure a k^{-4} scaling as we already attempted to measure this kind of scaling in the quantum depletion of a Bose-Einstein condensate. In [34], we actually measured a k^{-4} scaling that was first attributed to Tan's contact but with too high of an amplitude, like in the case of the data presented here. Further investigations [28] revealed that this scaling was in fact caused by $m_J = 0$ impurities in the condensate that cannot be prevented from falling unto the MCPs as they do not interact with magnetic fields. It was then the first hypothesis that we thought of to explain this discrepancy with the QMC calculations.

We then decided to characterize the effect of these $m_J = 0$ atoms as well as the non-transferred $m_J = 1$ that are not properly kicked that we will name "background" atoms by preparing the gases as we usually would and using the same displacement sequence, but not performing the population transfer in the beginning of the TOF. We performed a first test of the kind by preparing a gas with a deliberately low atom number $N_{\mathrm{bec}} = 26(3) \times 10^3$, taking low and high momentum data as usual, and then measuring the distribution of $m_J = 0$ for the same experimental sequence than used for the high momentum data. Even though the $m_J = 0$ are unaffected by the magnetic field, we plot the distribution as if

it were displaced to clearly compare it to the "true" displaced 1D distribution plotted in log-scale, as shown on Fig-5.17. We repeated this experiment for two different methods of removing the remaining non-transferred $m_J = 1$ atoms, the first one being the usual method of using the x gradient coil and the second one consisting in abruptly ramping up the current in the y and z bias coils to effectively create a gradient in time and push the atoms by doing so. We learn several things from these measurements:

- The background density is higher when using the y and z bias coils than the x gradient coil for the magnetic removal kick. This is rather reassuring has it had always been our preferred method so far. However, the shape of the two profiles are also slightly different. As these two data sets have been taken on the same day, this cannot be explained by day-to-day fluctuations of the state of the experiment. This could then mean that the $m_J = 0$ atoms are not fully decoupled from the $m_J = 1$ atoms during the TOF and that there could be some interactions affecting the shape of the background density. In addition, as the magnetic bias used to separate the magnetic sub-levels for the population transfer is along the x direction, the kick using the y and z bias coils is not oriented along the quantification axis. This could result in some uncontrolled population transfer between the $m_J = 1$ and the $m_J = 0$ sub-states.
- The background density is however very close to the measured 1D distribution, especially with the y, z removal kick where they overlap. Even worse, the background density seems to show a k^{-4} decay as observed in the past.
- Contrary to the background density, the magnetic removal kick method does not affect the 1D momentum distribution. This could be explained using the argument stated earlier that using the y and z bias coils for the magnetic kick induces some population transfer from $m_J = 1$ and $m_J = 0$. While this effect is significant when no RF sweep population transfer is performed, we can expect that it does not play any role when a large portion of the atoms have already been transferred to $m_J = 0$ with the RF sweep.
- The plateau region that does not appear in the QMC data cannot however be explained by the effect of the background density which is roughly one order of magnitude lower in this momentum region.

Unfortunately, these first tests seem to indicate that the $m_J = 0$ impurities could indeed be playing a role, at least for low total atom numbers. We reproduced the same kind of experiment (this time leaving out the y, z removal kick method) for a higher number of atoms $N = 1.1(1) \times 10^5$ with the results show in Fig-5.18. The data is strikingly different as the 1D density is about one order of magnitude higher than the background density in the k^{-4} decay region! The $m_J = 0$ impurities cannot then explain the discrepancy between the experimental and QMC data of the right panel of Fig-5.16 where the total atom number is similar.

5.7 Conclusion

In conclusion, we observed qualitative behaviors of the amplitude of the k^{-4} tails that seem to point towards the fact that we are measuring Tan's contact. However, the discrepancy with theory and QMC calculations is large and remains so far unexplained and an open question. While the first tests to quantify the effect of the $m_J = 0$ impurities seem

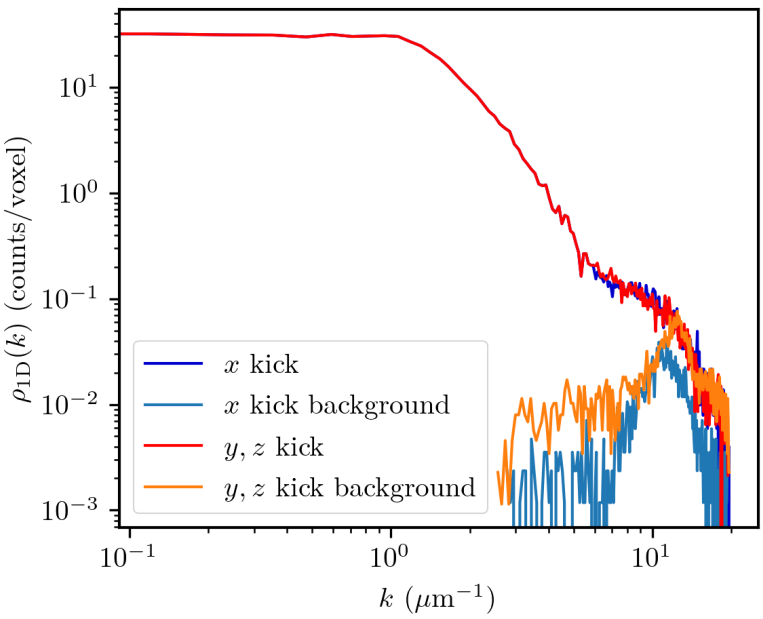

Figure 5.17: Effect of the background $m_J = 0$ impurities for a total atom number $N_{\text{bec}} = 26(3) \times 10^3$. The experiment is done twice with two different methods of removing the non-transferred $m_J = 1$ atoms in the beginning of the TOF, one using a gradient along x (labelled as x kick), one abruptly ramping up the current in the y and z bias coils (labelled as y, z kick).

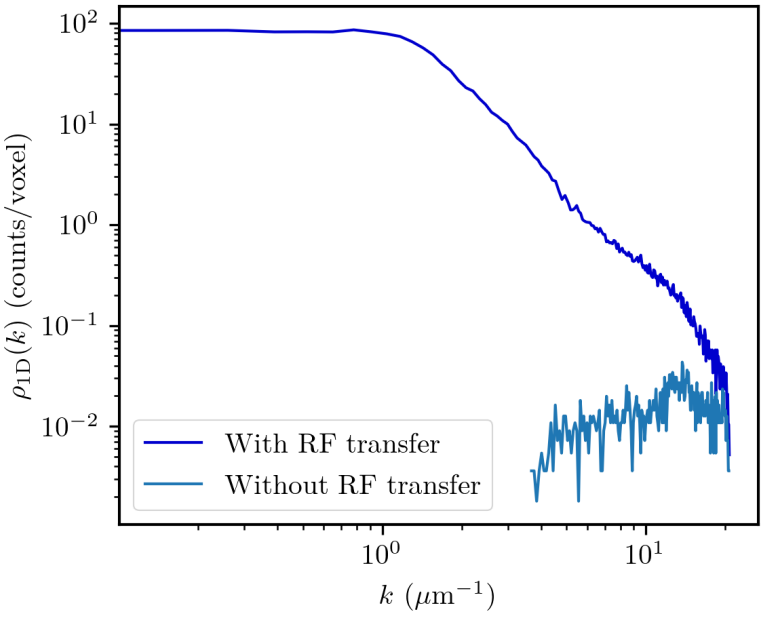

Figure 5.18: Effect of the background $m_J = 0$ impurities for a total atom number $N_{\text{bec}} = 1.1(1) \times 10^5$

to indicate that they could partly explain the discrepancy at low atom numbers, this explanation does not hold for higher atom numbers. One of the principal questions to elucidate would be to understand what the intermediate algebraically decaying region means. We could indeed think that this is a physical feature related to the algebraic decay of the first order correlation function under the effect of interactions as explained in 5.5.3, but this is contradicted by the QMC calculations. We could however imagine that there is something that we did not properly understand in the way that the different 1D tubes contribute to the total distribution that the QMC calculations fail to reproduce. On the contrary, this could be the signature of some experimental defect that we have overlooked.

In the near future, we plan to reproduce these experiments using the newly implemented two-photon Raman transfer. We hope that the increased detection efficiency will help us to separate more clearly the signal from the background effects and maybe help us identify more clearly what the problem sources are to find new paths to explore.

Conclusion

The central result of this thesis is the observation of $\boldsymbol{k}/-\boldsymbol{k}$ pairs in the quantum depletion of a weakly-interacting lattice Bose gas. Most of the work I did during my PhD was oriented towards that goal. This measurement was the next step in our task of fully characterizing the correlations across the superfluid to Mott insulator transition after the first two works [26, 30] conducted by the former PhD students Hugo Cayla and Cécile Carcy that focused on the local correlations, respectively deep in the Mott regime and in the superfluid region.

The first work that I conducted during my PhD is the study the two-body scattering halos [154] as a means to complete the previous benchmarking work [29] to certify that the measured atomic distribution faithfully represents the in-trap momentum distribution at the level of individual atoms. We devised a simple theoretical model predicting the number of atoms in the collision halos that we validated experimentally by measuring this number for large number of atoms loaded in the lattice. Extrapolating the predictions of the simple model to the low atom numbers usually used in our experiments, we could show that two-body collisions can be safely neglected, proving that our experiment is suited to probe correlations between individual particles. A second work aimed at studying the adiabatic preparation of the gas in the vicinity of the Mott transition [27]. Led by Cécile Carcy in collaboration with the theoretician Tommaso Roscilde, it has been completed around the middle of my PhD, concluding the series of experiments aiming to prove that our experiment properly simulates the Bose-Hubbard model. In particular, this work showed that it is possible to adiabatically approach the Quantum Critical Point of the superfluid to Mott insulator transition at finite entropy, *i.e* without creating excitations, contrary to the $T = 0$ case where this is expected to be impossible. This work then sets the ground for the study of correlations across the superfluid to Mott insulator transition that we defined as one of our main point of interest in the introduction to this manuscript.

Our team had attempted before at revealing the pairing mechanism associated to the quantum depletion without success. We identified the low detection efficiency ($\sim 10-15\%$) as a central issue and thus we decided to implement a two-photon Raman transfer to improve it. Building and testing the Raman transfer was the second main project of my PhD.

It was more or less at this time that the Covid-19 pandemic hit, forcing us to leave the lab and stay at home. I used this period away from the lab room to develop the algorithm to compute the anomalous correlation function $g_A^{(2)}$ (to look for the $\boldsymbol{k}/-\boldsymbol{k}$ correlations). I tested and troubleshot this algorithm at first with simulated data and in a second time with the data from the earlier project on the scattering halos (in which classical $\boldsymbol{k}/-\boldsymbol{k}$ correlations can be observed in the frame of the center of mass of each halo).

We started the measurement campaign for the $\boldsymbol{k}/-\boldsymbol{k}$ correlations a few months after the end of first lockdown and were able to observe first experimental signals. We then performed experiments to investigate the role of temperature and of atoms number on the pairing signal and to compare pair correlations with the bunching effect. These measurements provided strong evidences that the observed $\boldsymbol{k}/-\boldsymbol{k}$ correlations were the expected signature of quantum coherences built by atom pairs as a result of interactions. Several features associated with $T = 0$ quantum coherences induced by the pairs could be observed and we propose an interpretation in analogy with two-mode squeezed states in Quantum Optics.

In addition, we observed $g_A^{(2)}(\mathbf{0}) \gg g_N^{(2)}(\mathbf{0})$, violating the Cauchy-Schwarz inequality, once again signaling the quantum nature of the correlation signal, and finally measured relative number squeezing between modes $\boldsymbol{k}$ and $-\boldsymbol{k}$. These last two measurements constitute a first step towards demonstrating the presence of entanglement in the many-body equilibrium state of our system. This notably opens the way to characterizing squeezing and entanglement with **continuous** variables (here the momentum), extending such studies beyond **discrete** spin variables as mostly done so far.

In a nutshell, we were able to report the first observation of $\boldsymbol{k}/-\boldsymbol{k}$ correlations in an **at-equilibrium** system, resulting from the interplay between quantum fluctuations and interactions, confirming the 60 years old prediction of Bogoliubov and Lee-Huang-Yang. Interestingly, one of the motivations to observe this signal laid in its conceptual simplicity and the existence of the well-rounded Bogoliubov theory describing it, giving us a general frame to interpret the experimental data. However, the presence of the optical lattice represents an already significant change from the homogeneous Bogoliubov theory and makes theoretical approaches much more complicated and to this day missing. While many of our observations are consistent with Bogoliubov theory, we observed that it notably fails to quantitatively explain the number of detected pairs. This means that our experiment starts to qualify as a quantum simulator as defined in the introduction, even though new theories might emerge in the near future to explain these results as the complexity of the system is still manageable.

Building up on the quantum simulation aspect, this result is also of great importance for our future experiments as it shows that our experiment is capable of detecting non-local $\boldsymbol{k}/-\boldsymbol{k}$ correlations (we had only observed close-by $\boldsymbol{k}/\boldsymbol{k}$ correlations before), hinting at a possible detection of more complex and hard to predict correlation patterns, notably close the Quantum Critical Point of the Mott transition, that would be a big step towards understanding the physics of strongly interacting many-body systems. This also confirms that we could detect $\boldsymbol{k}/-\boldsymbol{k}$ correlations in Cooper pairs and help understanding the physics of superconductivity with future experiments with fermionic $^3\mathrm{He}^*$.

In parallel, I also spent a significant amount of time working on the project of measuring Tan's contact in 1D gases, in collaboration with Hepeng Yao and his supervisor

Laurent–Sanchez Palencia from Centre de Physique Théorique at Ecole Polytechnique. This work also falls into the general goal of studying many-body interacting systems with a complementary approach to correlation functions, *i.e* measuring high momentum tails revealing the presence of contact interactions. We implemented a solution to increase the momentum range of the detector by using a magnetic gradient to shift the entire momentum distribution and access the high momentum region, and were able to observe a k^{-4} decay on various data sets. While the qualitative evolution of the contact with temperature and interaction strength is consistent with theory, there is a large discrepancy with the QMC calculations that remains to this day unexplained and should be the subject of future experiments. Obtaining an agreement with theory would be of primary importance to show that the momentum density at high k can be used to properly characterize the different regimes and crossovers between them in interacting 1D gases.

Outlooks

Our measurements of $\boldsymbol{k}/-\boldsymbol{k}$ correlations have voluntarily left constant the lattice depth. An immediate way of pushing these measurements further (that we have already started working on) is to monitor the pairing while progressively increasing the lattice depth. As U/J increases, and with it the strength of the interactions, we should reach a point at which the Bogoliubov approximation is not valid anymore. It would then be interesting to see how this effect translates to the $\boldsymbol{k}/-\boldsymbol{k}$ correlation signal. As mentioned earlier, we notably expect that more complex correlation patterns may appear as the strength of the interactions increases, effectively involving more than 2 particles. These kind of complex correlations are expected to be particularly important at the Quantum Critical Point of the superfluid-to-Mott insulator transition. A short-mid range prospect would then be to develop new data analysis techniques to measure higher order correlation functions, test them in simple cases like by measuring bosononic bunching with more than 2 particles, and finally use them in experimental data progressively closer to the Quantum Critical Point. As obtaining a good enough signal to noise ratio to measure a n-th order correlation function gets increasingly difficult as n increases, we would need to take large amount of data at the Quantum Critical Point. This prospect is particularly exciting as no theory predicts what should happen in terms of momentum-space correlations at the Quantum Critical Point, making this measurement a true quantum simulation.

In addition, our observation of the violation of the Cauchy-Schwarz inequality would be enough to obtain the important result of proving the presence of entanglement in momentum-space in many-body equilibrium systems if we were able to measure the correlator $\langle a^\dagger_{\boldsymbol{k}} a_{-\boldsymbol{k}} \rangle$ and show that it is negligible, as in Bogoliubov theory. Improving our experimental setup to have the lattice beams required to perform atomic interferometry and measure this correlator then constitutes another interesting outlook.

Another short term objective is to further investigate the discrepancy between the experimental data and the QMC calculations for the measurement of Tan's contact, notably by taking additional data using the newly added two-photon Raman transfer. We hope that the increased detection efficiency would help us being less sensitive to possible effects of the $m_J = 0$ impurities while reducing the number of non-transferred $m_J = 1$ atoms. While these atoms are supposed to be prevented from falling on the detector thanks to a strong magnetic gradient kick, we observed that there could be unwanted dynamics such

as uncontrolled transfer to the $m_J = 0$ state that could perturb our measurement. This measurements might then help us to identify eventual problems in the experiment or in the way that we compare our data to the theory.

Finally, a more long term prospect would be to improve the experimental setup to bring the fermionic isotope of Helium, ^{3}He*, to quantum degeneracy. This would open the way to study a whole new kind of physics with the great momentum-space resolution of our detector. It would be particularly interesting to study the physics of the BEC-BCS transition and directly measure $\boldsymbol{k}/-\boldsymbol{k}$ correlations in a Cooper pair. To do so, we would first need to identify a usable Feshbach resonance to create the Cooper pairs as there have currently not been a proper investigation of the existence of Feshbach resonance in ^{3}He*.

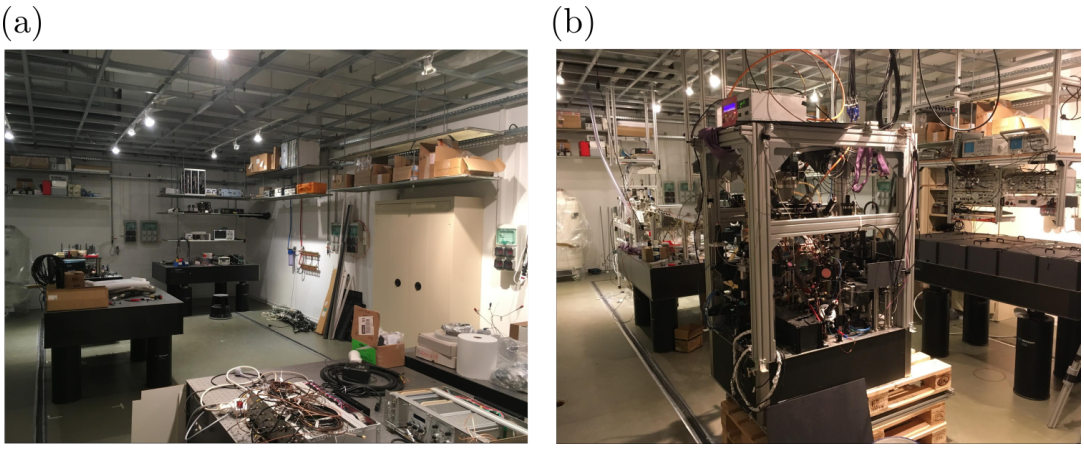

Figure 1: The new experiment room. (a) Before moving in, with only a few optical tables left by the previous occupants of the room. (b) After moving in.

Actually, the lab room in which all the experiments of this thesis were conducted was starting to get packed, and adding the new equipment to cool down a new atomic species would have barely left enough space in the room for a PhD student. This last year, we took a first (but big!) step towards the installation of ^{3}He* in our experiment by moving the entire apparatus to a new bigger room a few steps down the corridor (see Fig.-1), giving us plenty of additional space. At the moment that I am writing this manuscript, we managed to get the experiment back to its working state and were able to produce BECs and should be able to resume taking data soon. I would like to end this manuscript with one last figure (2) which is one of my favorite picture of my time as a PhD student, showing the Helium Lattice team in the perilous process of moving the science chamber to the new room, in which I hope it will serve to make many beautiful experiments in the years to come.

Figure 2: The Helium Lattice team with the Science Chamber, moving from the old room to the new one.

List of Figures

List of Tables

Publications

- C. Carcy, H. Cayla, A. Tenart, A. Aspect, M. Mancini, and D. Clément. **Momentum-space atom correlations in a mott insulator**. *Physical Review X*, 9(4):041028, 2019. Used as reference [26] in this manuscript.

- A. Tenart, C. Carcy, H. Cayla, T. Bourdel, M. Mancini, and D. Clément. **Two-body collisions in the time-of-flight dynamics of lattice bose superfluids**. *Physical Review Research*, 2(1):013017, 2020. Used as reference [154] in this manuscript.

- H. Cayla, S. Butera, C. Carcy, A. Tenart, G. Hercé, M. Mancini, A. Aspect, I. Carusotto, and D. Clément. **Hanbury-brown and twiss bunching of phonons and of the quantum depletion in a strongly-interacting bose gas**. *Physical Review Letters*, 125:165301, 2020. Used as reference [30] in this manuscript.

- C. Carcy, G. Hercé, A. Tenart, T. Roscilde, and D. Clément. **Certifying the adiabatic preparation of ultracold lattice bosons in the vicinity of the mott transition**. *Physical Review Letters*, 126(4):045301, 2021. Used as reference [27] in this manuscript.

- G. Hercé, C. Carcy, A. Tenart, J.-P. Bureik, A. Dareau, D. Clément, and T. Roscilde. **Studying the low-entropy mott transition of bosons in a three-dimensional optical lattice by measuring the full momentum-space density**. *Physical Review A*, 104, 2021. Used as reference [83] in this manuscript.

- A. Tenart, G. Hercé, J.-P. Bureik, A. Dareau, and D. Clément. **Observation of pairs of atoms at opposite momenta in an equilibrium interacting bose gas**. *Nature Physics*, 17(12):1364-1368, 2021. Used as reference [155] in this manuscript.

Bibliography

[1] A. Abbas, X. Meng, R. Patil, J. Ross, A. Truscott, and S. Hodgman. Rapid generation of metastable helium bose-einstein condensates. *Physical Review A*, 103(5): 053317, 2021.

[2] M. H. Anderson, J. R. Ensher, M. R. Matthews, C. E. Wieman, and E. A. Cornell. Observation of bose-einstein condensation in a dilute atomic vapor. *Science*, 269 (5221):198–201, 1995.

[3] G. Arnison and al. First observation of correlations between high transverse-momentum charged-particules in events from the cern proton and anti-proton collider. *Physical letters*, 118:173, 1982.

[4] N. W. Ashcroft, N. D. Mermin, et al. Solid state physics, 1976.

[5] A. Aspect, E. Arimondo, R. e. a. Kaiser, N. Vansteenkiste, and C. Cohen-Tannoudji. Laser cooling below the one-photon recoil energy by velocity-selective coherent population trapping. *Physical Review Letters*, 61(7):826, 1988.

[6] W. S. Bakr, J. I. Gillen, A. Peng, S. Fölling, and M. Greiner. A quantum gas microscope for detecting single atoms in a hubbard-regime optical lattice. *Nature*, 462(7269):74–77, 2009.

[7] J. Bardeen, L. N. Cooper, and J. R. Schrieffer. Theory of superconductivity. *Physical review*, 108(5):1175, 1957.

[8] F. Bardou, O. Emile, J.-M. Courty, C. Westbrook, and A. Aspect. Magneto-optical trapping of metastable helium: collisions in the presence of resonant light. *EPL (Europhysics Letters)*, 20(8):681, 1992.

[9] M. Barrett, J. Sauer, and M. Chapman. All-optical formation of an atomic bose-einstein condensate. *Physical review letters*, 87(1):010404, 2001.

[10] M. Barth and W. Zwerger. Tan relations in one dimension. *Annals of Physics*, 326 (10):2544–2565, 2011.

[11] S. Bergkvist, P. Henelius, and A. Rosengren. Local-density approximation for confined bosons in an optical lattice. *Physical Review A*, 70(5):053601, 2004.

[12] I. Bloch. Ultracold quantum gases in optical lattices. *Nature physics*, 1(1):23–30, 2005.

[13] I. Bloch, J. Dalibard, and W. Zwerger. Many-body physics with ultracold gases. *Reviews of modern physics*, 80(3):885, 2008.

[14] N. Bogoliubov. On the theory of superfluidity. *Journal of Physics (USSR)*, 11(1): 23, 1947.

[15] Q. Bouton. *Etude miscroscopique de la distibution en impulsion de condensats de Bose-Eintein d'Hélium métastable*. Theses, Université Paris Saclay (COmUE), Nov. 2016.

[16] Q. Bouton, R. Chang, A. Hoendervanger, F. Nogrette, A. Aspect, C. Westbrook, and D. Clément. Fast production of bose-einstein condensates of metastable helium. *Physical Review A*, 91(6):061402, 2015.

[17] R. H. Brown and R. Twiss. A test of a new type of stellar interferometer on sirius. *Nature*, 178(4541):1046–1048, 1956.

[18] R. H. Brown and R. Q. Twiss. Lxxiv. a new type of interferometer for use in radio astronomy. *The London, Edinburgh, and Dublin Philosophical Magazine and Journal of Science*, 45(366):663–682, 1954.

[19] R. Bücker, A. Perrin, S. Manz, T. Betz, C. Koller, T. Plisson, J. Rottmann, T. Schumm, and J. Schmiedmayer. Single-particle-sensitive imaging of freely propagating ultracold atoms. *New Journal of Physics*, 11(10):103039, 2009.

[20] R. Bücker, J. Grond, S. Manz, T. Berrada, T. Betz, C. Koller, U. Hohenester, T. Schumm, A. Perrin, and J. Schmiedmayer. Twin-atom beams. *Nature Physics*, 7:608 – 611, 2011.

[21] D. C. Burnham and D. L. Weinberg. Observation of simultaneity in parametric production of optical photon pairs. *Physical Review Letters*, 25(2):84, 1970.

[22] X. Busch and R. Parentani. Quantum entanglement in analogue hawking radiation: When is the final state nonseparable? *Physical Review D*, 89(10):105024, 2014.

[23] S. Butera, D. Clément, and I. Carusotto. Position-and momentum-space two-body correlations in a weakly interacting trapped condensate. *Physical Review A*, 103: 013302, 2021.

[24] B. Capogrosso-Sansone, N. Prokof'Ev, and B. Svistunov. Phase diagram and thermodynamics of the three-dimensional bose-hubbard model. *Physical Review B*, 75 (13):134302, 2007.

[25] C. Carcy. *Investigation of the Mott transition with metastable Helium atoms*. Theses, Université Paris Saclay (COmUE), Nov. 2019.

[26] C. Carcy, H. Cayla, A. Tenart, A. Aspect, M. Mancini, and D. Clément. Momentum-space atom correlations in a mott insulator. *Physical Review X*, 9(4):041028, 2019.

[27] C. Carcy, G. Hercé, A. Tenart, T. Roscilde, and D. Clément. Certifying the adiabatic preparation of ultracold lattice bosons in the vicinity of the mott transition. *Physical Review Letters*, 126(4):045301, 2021.

[28] H. Cayla. *Measuring the momentum distribution of a lattice gas at the single-atom level*. Theses, Université Paris Saclay (COmUE), Nov. 2018.

[29] H. Cayla, C. Carcy, Q. Bouton, R. Chang, G. Carleo, M. Mancini, and D. Clément. Single-atom-resolved probing of lattice gases in momentum space. *Physical Review A*, 97(6):061609, 2018.

[30] H. Cayla, S. Butera, C. Carcy, A. Tenart, G. Hercé, M. Mancini, A. Aspect, I. Carusotto, and D. Clément. Hanbury-brown and twiss bunching of phonons and of the quantum depletion in a strongly-interacting bose gas. *Physical Review Letters*, 125: 165301, 2020.

[31] M. Cazalilla. Bosonizing one-dimensional cold atomic gases. *Journal of Physics B: Atomic, Molecular and Optical Physics*, 37(7):S1, 2004.

[32] R. Chang, A. Hoendervanger, Q. Bouton, Y. Fang, T. Klafka, K. Audo, A. Aspect, C. I. Westbrook, and D. Clément. Three-dimensional laser cooling at the doppler limit. *Physical Review A*, 90(6):063407, 2014.

[33] R. Chang, Q. Bouton, H. Cayla, C. Qu, A. Aspect, C. Westbrook, and D. Clément. Fast production of bose-einstein condensates of metastable helium. *Physical Review Letters*, 117:235303, 2016.

[34] R. Chang, Q. Bouton, H. Cayla, C. Qu, A. Aspect, C. Westbrook, and D. Clément. Momentum-resolved observation of thermal and quantum depletion in a bose gas. *Physical review letters*, 117(23):235303, 2016.

[35] L. W. Cheuk, M. A. Nichols, M. Okan, T. Gersdorf, V. V. Ramasesh, W. S. Bakr, T. Lompe, and M. W. Zwierlein. Quantum-gas microscope for fermionic atoms. *Physical review letters*, 114(19):193001, 2015.

[36] A. Chikkatur, A. Görlitz, D. Stamper-Kurn, S. Inouye, S. Gupta, and W. Ketterle. Suppression and enhancement of impurity scattering in a bose-einstein condensate. *Physical review letters*, 85(3):483, 2000.

[37] C. Chin, R. Grimm, P. Julienne, and E. Tiesinga. Feshbach resonances in ultracold gases. *Reviews of Modern Physics*, 82(2):1225, 2010.

[38] S. Chu, L. Hollberg, J. E. Bjorkholm, A. Cable, and A. Ashkin. Three-dimensional viscous confinement and cooling of atoms by resonance radiation pressure. *Physical review letters*, 55(1):48, 1985.

[39] D. Clément, N. Fabbri, L. Fallani, C. Fort, and M. Inguscio. Exploring correlated 1d bose gases from the superfluid to the mott-insulator state by inelastic light scattering. *Physical review letters*, 102(15):155301, 2009.

[40] C. Cohen-Tannoudji. Atomic motion in laser light. *Fundamental systems in quantum optics*, (53):1–164, 1990.

[41] C. Cohen-Tannoudji, B. Diu, and F. Laloë. *Mécanique quantique*. Centre de Publications Universitaire, Téhéran, 1986.

[42] L. N. Cooper. Bound electron pairs in a degenerate fermi gas. *Physical Review*, 104 (4):1189, 1956.

[43] J. Dalibard. Des cages de lumière pour les atomes: la physique des pièges et des réseaux optiques. *Cours du Collège de France*, 2013.

[44] J. Dalibard and C. Cohen-Tannoudji. Laser cooling below the doppler limit by polarization gradients: simple theoretical models. *JOSA B*, 6(11):2023–2045, 1989.

[45] A. Damascelli, Z. Hussain, and Z.-X. Shen. Angle-resolved photoemission studies of the cuprate superconductors. *Reviews of modern physics*, 75(2):473, 2003.

[46] T.-L. Dao, A. Georges, J. Dalibard, C. Salomon, and I. Carusotto. Measuring the one-particle excitations of ultracold fermionic atoms by stimulated raman spectroscopy. *Physical review letters*, 98(24):240402, 2007.

[47] K. B. Davis, M.-O. Mewes, M. R. Andrews, N. J. van Druten, D. S. Durfee, D. Kurn, and W. Ketterle. Bose-einstein condensation in a gas of sodium atoms. *Physical review letters*, 75(22):3969, 1995.

[48] L. De Broglie. *Recherches sur la théorie des Quanta*. Theses, Nov. 1924.

[49] F. P. Dos Santos, J. Léonard, J. Wang, C. Barrelet, F. Perales, E. Rasel, C. Unnikrishnan, M. Leduc, and C. Cohen-Tannoudji. Bose-einstein condensation of metastable helium. *Physical Review Letters*, 86(16):3459, 2001.

[50] F. P. Dos Santos, F. Perales, J. Léonard, A. Sinatra, J. Wang, F. S. Pavone, E. Rasel, C. Unnikrishnan, and M. Leduc. Penning collisions of laser-cooled metastable helium atoms. *The European Physical Journal D-Atomic, Molecular, Optical and Plasma Physics*, 14(1):15–22, 2001.

[51] P. Dussarrat, M. Perrier, A. Imanaliev, R. Lopes, A. Aspect, M. Cheneau, D. Boiron, and C. I. Westbrook. Two-particle four-mode interferometer for atoms. *Physical review letters*, 119(17):173202, 2017.

[52] M. L. Edgar, J. Lapington, and A. Smith. The spatial extent of gain depression for mcp-based photon detectors. *Review of scientific instruments*, 63(1):816–819, 1992.

[53] M. Endres, T. Fukuhara, D. Pekker, M. Cheneau, P. Schauβ, C. Gross, E. Demler, S. Kuhr, and I. Bloch. The 'higgs' amplitude mode at the two-dimensional superfluid/mott insulator transition. *Nature*, 487(7408):454–458, 2012.

[54] J. Esteve, C. Gross, A. Weller, S. Giovanazzi, and M. Oberthaler. Squeezing and entanglement in a bose–einstein condensate. *Nature*, 455(7217):1216–1219, 2008.

[55] N. Fabbri, D. Clément, L. Fallani, C. Fort, and M. Inguscio. Momentum-resolved study of an array of one-dimensional strongly phase-fluctuating bose gases. *Physical Review A*, 83(3):031604, 2011.

[56] U. Fano. Quantum theory of interference effects in the mixing of light from phase-independent sources. *American Journal of Physics*, 29(8):539–545, 1961.

[57] P. Fedichev, M. Reynolds, U. Rahmanov, and G. Shlyapnikov. Inelastic decay processes in a gas of spin-polarized triplet helium. *Physical Review A*, 53(3):1447, 1996.

[58] H. Feshbach. Unified theory of nuclear reactions. *Annals of Physics*, 5(4):357–390, 1958.

[59] R. Feynman. Simulating physics with computers. *International Journal of Theoretical Physics*, 21(6-7):467–488, 1982.

[60] M. P. Fisher, P. B. Weichman, G. Grinstein, and D. S. Fisher. Boson localization and the superfluid-insulator transition. *Physical Review B*, 40(1):546, 1989.

[61] R. A. Fisher. On the mathematical foundations of theoretical statistics. *Philosophical Transactions of the Royal Society of London. Series A, Containing Papers of a Mathematical or Physical Character*, 222(594-604):309–368, 1922.

[62] R. J. Fletcher, R. Lopes, J. Man, N. Navon, R. P. Smith, M. W. Zwierlein, and Z. Hadzibabic. Two-and three-body contacts in the unitary bose gas. *Science*, 355 (6323):377–380, 2017.

[63] Q. Fontaine, T. Bienaimé, S. Pigeon, E. Giacobino, A. Bramati, and Q. Glorieux. Observation of the bogoliubov dispersion in a fluid of light. *Physical Review Letters*, 121:183604, 2018.

[64] I. Frérot and T. Roscilde. Reconstructing the quantum critical fan of strongly correlated systems using quantum correlations. *Nature communications*, 10(1):1–7, 2019.

[65] D. Gangardt and G. Shlyapnikov. Stability and phase coherence of trapped 1d bose gases. *Physical review letters*, 90(1):010401, 2003.

[66] C. Gardiner and P. Zoller. *Quantum noise: a handbook of Markovian and non-Markovian quantum stochastic methods with applications to quantum optics*. Springer Science & Business Media, 2004.

[67] A. L. Gaunt, T. F. Schmidutz, I. Gotlibovych, R. P. Smith, and Z. Hadzibabic. Bose-einstein condensation of atoms in a uniform potential. *Physical review letters*, 110(20):200406, 2013.

[68] F. Gerbier. Condensat de bose-einstein dans un piège anisotrope. cohérence en phase et propriétés thermodynamiques. In *Annales de Physique*, volume 29, pages 1–183. EDP Sciences, 2004.

[69] F. Gerbier. Quasi-1d bose-einstein condensates in the dimensional crossover regime. *EPL (Europhysics Letters)*, 66(6):771, 2004.

[70] F. Gerbier. Boson mott insulators at finite temperatures. *Physical Review Letters*, 99(12):120405, 2007.

[71] F. Gerbier. Quantum gas in optical lattices. *Lecture notes*, 2015.

[72] F. Gerbier, S. Trotzky, S. Fölling, U. Schnorrberger, J. Thompson, A. Widera, I. Bloch, L. Pollet, M. Troyer, B. Capogrosso-Sansone, et al. Expansion of a quantum gas released from an optical lattice. *Physical review letters*, 101(15):155303, 2008.

[73] R. J. Glauber. Coherent and incoherent states of the radiation field. *Physical Review*, 131(6):2766, 1963.

[74] R. J. Glauber. The quantum theory of optical coherence. *Physical Review*, 130(6): 2529, 1963.

[75] J. W. Goodman. *Speckle phenomena in optics: theory and applications*. Roberts and Company Publishers, 2007.

[76] M. Greiner, I. Bloch, O. Mandel, T. W. Hänsch, and T. Esslinger. Exploring phase coherence in a 2d lattice of bose-einstein condensates. *Physical Review Letters*, 87 (16):160405, 2001.

[77] M. Greiner, O. Mandel, T. Esslinger, T. W. Hänsch, and I. Bloch. Quantum phase transition from a superfluid to a mott insulator in a gas of ultracold atoms. *Nature*, 415(6867):39–44, 2002.

[78] M. Greiner, C. A. Regal, J. T. Stewart, and D. S. Jin. Probing pair-correlated fermionic atoms through correlations in atom shot noise. *Physical Review Letters*, 94:110401, 2005.

[79] R. Grimm, M. Weidemüller, and Y. B. Ovchinnikov. Optical dipole traps for neutral atoms. *Advances in atomic, molecular, and optical physics*, 42:95–170, 2000.

[80] M. C. Gutzwiller. Effect of correlation on the ferromagnetism of transition metals. *Physical Review Letters*, 10(5):159, 1963.

[81] Y. Harada, S. Masuda, and H. Ozaki. Electron spectroscopy using metastable atoms as probes for solid surfaces. *Chemical reviews*, 97(6):1897–1952, 1997.

[82] A. Heidmann, R. Horowicz, S. Reynaud, E. Giacobino, C. Fabre, and G. Camy. Observation of quantum noise reduction on twin laser beams. *Physical review letters*, 59(22):2555, 1987.

[83] G. Hercé, C. Carcy, A. Tenart, J.-P. Bureik, A. Dareau, D. Clément, and T. Roscilde. Studying the low-entropy mott transition of bosons in a three-dimensional optical lattice by measuring the full momentum-space density. *Physical Review A*, 104, 2021.

[84] T.-L. Ho and Q. Zhou. Intrinsic heating and cooling in adiabatic processes for bosons in optical lattices. *Physical Review Letters*, 99(12):120404, 2007.

[85] S. S. Hodgman, R. I. Khakimov, R. J. Lewis-Swan, A. G. Truscott, and K. V. Kheruntsyan. Solving the quantum many-body problem via correlations measured with a momentum microscope. *Physical review letters*, 118(24):240402, 2017.

[86] A. Hoendervanger, D. Clément, A. Aspect, C. I. Westbrook, D. Dowek, Y. Picard, and D. Boiron. Influence of gold coating and interplate voltage on the performance of chevron micro-channel plates for temporally and spatially resolved single particle detection. *Review of Scientific Instruments*, 84(2):023307, 2013.

[87] L. Hoendervanger. *A New Metastable Helium Machine : An Investigation into the Attributes of Trapping, Cooling and Detecting Metastable Helium*. PhD thesis, 2014. Thèse de doctorat dirigée par Westbrook, Chris Physique Palaiseau, Institut d'optique théorique et appliquée 2014.

[88] D. Jacob, E. Mimoun, L. De Sarlo, M. Weitz, J. Dalibard, and F. Gerbier. Production of sodium bose–einstein condensates in an optical dimple trap. *New Journal of Physics*, 13(6):065022, 2011.

[89] D. Jaksch, C. Bruder, J. I. Cirac, C. W. Gardiner, and P. Zoller. Cold bosonic atoms in optical lattices. *Physical Review Letters*, 81(15):3108, 1998.

[90] M. Kasevich and S. Chu. Atomic interferometry using stimulated raman transitions. *Physical review letters*, 67(2):181, 1991.

[91] H. Katori and F. Shimizu. Laser cooling and trapping of argon and krypton using diode lasers. *Japanese journal of applied physics*, 29(11A):L2124, 1990.

[92] A. Keesling, A. Omran, H. Levine, H. Bernien, H. Pichler, S. Choi, R. Samajdar, S. Schwartz, P. Silvi, S. Sachdev, et al. Quantum kibble–zurek mechanism and critical dynamics on a programmable rydberg simulator. *Nature*, 568(7751):207–211, 2019.

[93] M. Keller, M. Kotyrba, F. Leupold, M. Singh, M. Ebner, and A. Zeilinger. Bose-einstein condensate of metastable helium for quantum correlation experiments. *Physical Review A*, 90(6):063607, 2014.

[94] W. Ketterle and N. Van Druten. Evaporative cooling of trapped atoms. *Advances in atomic, molecular, and optical physics*, 37:181–236, 1996.

[95] R. I. Khakimov, B. Henson, D. Shin, S. Hodgman, R. Dall, K. Baldwin, and A. Truscott. Ghost imaging with atoms. *Nature*, 540(7631):100–103, 2016.

[96] K. Kheruntsyan, D. Gangardt, P. Drummond, and G. Shlyapnikov. Pair correlations in a finite-temperature 1d bose gas. *Physical review letters*, 91(4):040403, 2003.

[97] M. Kormos, G. Mussardo, and A. Trombettoni. Expectation values in the lieb-liniger bose gas. *Physical review letters*, 103(21):210404, 2009.

[98] M. Krämer, L. Pitaevskii, and S. Stringari. Macroscopic dynamics of a trapped bose-einstein condensate in the presence of 1d and 2d optical lattices. *Physical review letters*, 88(18):180404, 2002.

[99] E. Kuhnle, H. Hu, X.-J. Liu, P. Dyke, M. Mark, P. Drummond, P. Hannaford, and C. Vale. Universal behavior of pair correlations in a strongly interacting fermi gas. *Physical Review Letters*, 105(7):070402, 2010.

[100] J. N. Kupferschmidt and E. J. Mueller. Role of interactions in time-of-flight expansion of atomic clouds from optical lattices. *Physical Review A*, 82(2):023618, 2010.

[101] L. D. Landau and E. M. Lifshitz. *Quantum mechanics: non-relativistic theory*, volume 3. Elsevier, 2013.

[102] L. Lavoine and T. Bourdel. Beyond-mean-field crossover from one dimension to three dimensions in quantum droplets of binary mixtures. *Phys. Rev. A*, 103:033312, 2021.

[103] T. D. Lee, K. Huang, and C. N. Yang. Eigenvalues and eigenfunctions of a bose system of hard spheres and its low-temperature properties. *Physical Review*, 106(6): 1135, 1957.

[104] E. H. Lieb and W. Liniger. Exact analysis of an interacting bose gas. i. the general solution and the ground state. *Physical Review*, 130(4):1605, 1963.

[105] R. Lopes, A. Imanaliev, A. Aspect, M. Cheneau, D. Boiron, and C. I. Westbrook. Atomic hong–ou–mandel experiment. *Nature*, 520(7545):66–68, 2015.

[106] R. Lopes, C. Eigen, N. Navon, D. Clément, R. P. Smith, and Z. Hadzibabic. Quantum depletion of a homogeneous bose-einstein condensate. *Physical Review Letters*, 119:190404, 2017.

[107] C. Luciuk, S. Trotzky, S. Smale, Z. Yu, S. Zhang, and J. H. Thywissen. Evidence for universal relations describing a gas with p-wave interactions. *Nature Physics*, 12 (6):599–605, 2016.

[108] L. Mandel and E. Wolf. *Optical coherence and quantum optics*. Cambridge university press, 1995.

[109] P. J. Martin, B. G. Oldaker, A. H. Miklich, and D. E. Pritchard. Bragg scattering of atoms from a standing light wave. *Physical review letters*, 60(6):515, 1988.

[110] L. Mathey, A. Vishwanath, and E. Altman. Noise correlations in low-dimensional systems of ultracold atoms. *Physical Review A*, 79(1):013609, 2009.

[111] J. McNamara, T. Jeltes, A. Tychkov, W. Hogervorst, and W. Vassen. Degenerate bose-fermi mixture of metastable atoms. *Physical Review Letters*, 97(8):080404, 2006.

[112] A. Miller, D. Pines, and P. Nozières. Elementary excitations in liquid helium. *Physical Review*, 127:1452–1464, 1962.

[113] A. Minguzzi, P. Vignolo, and M. Tosi. High-momentum tail in the tonks gas under harmonic confinement. *Physics Letters A*, 294(3-4):222–226, 2002.

[114] N. Navon, S. Nascimbene, F. Chevy, and C. Salomon. The equation of state of a low-temperature fermi gas with tunable interactions. *Science*, 328(5979):729–732, 2010.

[115] F. Nogrette, D. Heurteau, R. Chang, Q. Bouton, C. Westbrook, R. Sellem, and D. Clément. Characterization of a detector chain using a fpga-based time-to-digital converter to reconstruct the three-dimensional coordinates of single particles at high flux. *Review of Scientific Instruments*, 86(11):113105, 2015.

[116] M. Olshanii. Atomic scattering in the presence of an external confinement and a gas of impenetrable bosons. *Physical review letters*, 81(5):938, 1998.

[117] M. Olshanii and V. Dunjko. Short-distance correlation properties of the lieb-liniger system and momentum distributions of trapped one-dimensional atomic gases. *Physical review letters*, 91(9):090401, 2003.

[118] H. Ott. Single atom detection in ultracold quantum gases: a review of current progress. *Reports on Progress in Physics*, 79(5):054401, 2016.

[119] R. Ozeri, N. Katz, J. Steinhauer, and N. Davidson. Colloquium: Bulk bogoliubov excitations in a bose-einstein condensate. *Reviews of Modern Physics*, 77:187–205, 2005.

[120] R. Ozeri, N. Katz, J. Steinhauer, and N. Davidson. Colloquium: Bulk bogoliubov excitations in a bose-einstein condensate. *Reviews of Modern Physics*, 77(1):187, 2005.

[121] S. Papp, J. Pino, R. Wild, S. Ronen, C. E. Wieman, D. S. Jin, and E. A. Cornell. Bragg spectroscopy of a strongly interacting rb 85 bose-einstein condensate. *Physical review letters*, 101(13):135301, 2008.

[122] A. Perrin. *Observation de paires d'atomes corrélés au travers de la collision de deux condensats de Bose-Einstein*. Theses, Université Pierre et Marie Curie - Paris VI, Nov. 2007.

[123] A. Perrin, H. Chang, V. Krachmalnicoff, M. Schellekens, D. Boiron, A. Aspect, and C. I. Westbrook. Observation of atom pairs in spontaneous four-wave mixing of two colliding bose-einstein condensates. *Physical Review Letters*, 99(15):150405, 2007.

[124] C. J. Pethick and H. Smith. *Bose–Einstein condensation in dilute gases*. Cambridge university press, 2008.

[125] D. Petrov, G. Shlyapnikov, and J. Walraven. Regimes of quantum degeneracy in trapped 1d gases. *Physical Review Letters*, 85(18):3745, 2000.

[126] L. Pezzè, A. Smerzi, M. K. Oberthaler, R. Schmied, and P. Treutlein. Quantum metrology with nonclassical states of atomic ensembles. *Reviews of Modern Physics*, 90(3):035005, 2018.

[127] W. D. Phillips and H. Metcalf. Laser deceleration of an atomic beam. *Physical Review Letters*, 48(9):596, 1982.

[128] L. Pitaevskii and S. Stringari. Uncertainty principle, quantum fluctuations, and broken symmetries. *Journal of low temperature physics*, 85(5-6):377–388, 1991.

[129] L. Pitaevskii and S. Stringari. *Bose-Einstein condensation and superfluidity*, volume 164. Oxford University Press, 2016.

[130] L. Pollet. Recent developments in quantum monte carlo simulations with applications for cold gases. *Reports on progress in physics*, 75(9):094501, 2012.

[131] J. Rarity and P. Tapster. Experimental violation of bell's inequality based on phase and momentum. *Physical Review Letters*, 64(21):2495, 1990.

[132] M. Reid and D. Walls. Violations of classical inequalities in quantum optics. *Physical Review A*, 34(2):1260, 1986.

[133] A. Robert, O. Sirjean, A. Browaeys, J. Poupard, S. Nowak, D. Boiron, C. I. Westbrook, and A. Aspect. A bose-einstein condensate of metastable atoms. *Science*, 292(5516):461–464, 2001.

[134] D. S. Rokhsar and B. Kotliar. Gutzwiller projection for bosons. *Physical Review B*, 44(18):10328, 1991.

[135] S. Sachdev. *Quantum phase transitions*. Cambridge university press, 2011.

[136] Y. Sagi, T. E. Drake, R. Paudel, and D. S. Jin. Measurement of the homogeneous contact of a unitary fermi gas. *Physical review letters*, 109(22):220402, 2012.

[137] G. Salomon, L. Fouché, S. Lepoutre, A. Aspect, and T. Bourdel. All-optical cooling of k 39 to bose-einstein condensation. *Physical Review A*, 90(3):033405, 2014.

[138] B. L. Schumaker and C. M. Caves. New formalism for two-photon quantum optics. ii. mathematical foundation and compact notation. *Physical Review A*, 31(5):3093, 1985.

[139] T. Schweigler, V. Kasper, S. Erne, I. Mazets, B. Rauer, F. Cataldini, T. Langen, T. Gasenzer, J. Berges, and J. Schmiedmayer. Experimental characterization of a quantum many-body system via higher-order correlations. *Nature*, 545(7654):323–326, 2017.

[140] F. Serwane, G. Zürn, T. Lompe, T. Ottenstein, A. Wenz, and S. Jochim. Deterministic preparation of a tunable few-fermion system. *Science*, 332(6027):336–338, 2011.

[141] J. F. Sherson, C. Weitenberg, M. Endres, M. Cheneau, I. Bloch, and S. Kuhr. Single-atom-resolved fluorescence imaging of an atomic mott insulator. *Nature*, 467(7311): 68–72, 2010.

[142] F. Shimizu, K. Shimizu, and H. Takuma. Laser cooling and trapping of ne metastable atoms. *Physical Review A*, 39(5):2758, 1989.

[143] G. Shlyapnikov, J. Walraven, U. Rahmanov, and M. Reynolds. Decay kinetics and bose condensation in a gas of spin-polarized triplet helium. *Physical review letters*, 73(24):3247, 1994.

[144] B. W. Shore. *The theory of coherent atomic excitation*. 1996.

[145] T. G. Skov, M. G. Skou, N. B. Jørgensen, and J. J. Arlt. Observation of a lee-huang-yang fluid. *Physical Review Letters*, 126(23):230404, 2021.

[146] L. Sobirey, N. Luick, M. Bohlen, H. Biss, H. Moritz, and T. Lompe. Observation of superfluidity in a strongly correlated two-dimensional fermi gas. *Science*, 372(6544): 844–846, 2021.

[147] I. Spielman, W. Phillips, and J. Porto. Condensate fraction in a 2d bose gas measured across the mott-insulator transition. *Physical Review Letters*, 100(12):120402, 2008.

[148] J. Steinhauer, R. Ozeri, N. Katz, and N. Davidson. Excitation spectrum of a bose-einstein condensate. *Physical review letters*, 88(12):120407, 2002.

[149] J. Stenger, S. Inouye, A. P. Chikkatur, D. Stamper-Kurn, D. Pritchard, and W. Ketterle. Bragg spectroscopy of a bose-einstein condensate. *Physical Review Letters*, 82 (23):4569, 1999.

[150] P. Stepanov, I. Amelio, J.-G. Rousset, J. Bloch, A. Lemaître, A. Amo, A. Minguzzi, I. Carusotto, and M. Richard. Dispersion relation of the collective excitations in a resonantly driven polariton fluid. *Nature Communications*, 10:3869, 2019.

[151] J. Stewart, J. Gaebler, and D. Jin. Using photoemission spectroscopy to probe a strongly interacting fermi gas. *Nature*, 454(7205):744–747, 2008.

[152] J. Stewart, J. Gaebler, T. Drake, and D. Jin. Verification of universal relations in a strongly interacting fermi gas. *Physical Review Letters*, 104(23):235301, 2010.

[153] S. Tan. Large momentum part of a strongly correlated fermi gas. *Annals of Physics*, 323(12):2971–2986, 2008.

[154] A. Tenart, C. Carcy, H. Cayla, T. Bourdel, M. Mancini, and D. Clément. Two-body collisions in the time-of-flight dynamics of lattice bose superfluids. *Physical Review Research*, 2(1):013017, 2020.

[155] A. Tenart, G. Hercé, J.-P. Bureik, A. Dareau, and D. Clément. Observation of pairs of atoms at opposite momenta in an equilibrium interacting bose gas. *Nature Physics*, 17(12):1364–1368, 2021.

[156] E. Toth, A. Rey, and P. Blakie. Theory of correlations between ultracold bosons released from an optical lattice. *Physical Review A*, 78(1):013627, 2008.

[157] A. Van den Bos. *Parameter estimation for scientists and engineers*. John Wiley & Sons, 2007.

[158] P. Vignolo and A. Minguzzi. Universal contact for a tonks-girardeau gas at finite temperature. *Physical review letters*, 110(2):020403, 2013.

[159] L. Villa, J. Despres, and L. Sanchez-Palencia. Unraveling the excitation spectrum of many-body systems from quantum quenches. *Physical Review A*, 100(6):063632, 2019.

[160] L. Viverit, S. Giorgini, L. Pitaevskii, and S. Stringari. Momentum distribution of a trapped fermi gas with large scattering length. *Physical Review A*, 69(1):013607, 2004.

[161] D. F. Walls. Squeezed states of light. *Nature*, 306(5939):141–146, 1983.

[162] D. F. Walls and G. J. Milburn. *Quantum Optics*. Springer-Verlag, Berlin, 2008.

[163] G. H. Wannier. The structure of electronic excitation levels in insulating crystals. *Physical Review*, 52(3):191, 1937.

[164] A. Wenz, G. Zürn, S. Murmann, I. Brouzos, T. Lompe, and S. Jochim. From few to many: Observing the formation of a fermi sea one atom at a time. *Science*, 342 (6157):457–460, 2013.

[165] R. Wild, P. Makotyn, J. Pino, E. Cornell, and D. Jin. Measurements of tan's contact in an atomic bose-einstein condensate. *Physical review letters*, 108(14):145305, 2012.

[166] K. Xu, Y. Liu, D. Miller, J. Chin, W. Setiawan, and W. Ketterle. Observation of strong quantum depletion in a gaseous bose-einstein condensate. *Physical review letters*, 96(18):180405, 2006.

[167] W. Xu and M. Rigol. Universal scaling of density and momentum distributions in lieb-liniger gases. *Physical Review A*, 92(6):063623, 2015.

[168] C.-N. Yang and C. P. Yang. Thermodynamics of a one-dimensional system of bosons with repulsive delta-function interaction. *Journal of Mathematical Physics*, 10(7): 1115–1122, 1969.

[169] H. Yao. *Strongly-correlated one-dimensional bosons in continuous and quasiperiodic potentials*. Theses, Institut Polytechnique de Paris, Oct. 2020.

[170] H. Yao, D. Clément, A. Minguzzi, P. Vignolo, and L. Sanchez-Palencia. Tan's contact for trapped lieb-liniger bosons at finite temperature. *Physical review letters*, 121(22): 220402, 2018.

[171] S. Yoshimura, S. Konabe, and T. Nikuni. Adiabatic cooling and heating of cold bosons in three-dimensional optical lattices and the superfluid-normal phase transition. *Physical Review A*, 78(1):015602, 2008.

[172] B. Yurke and M. Potasek. Obtainment of thermal noise from a pure quantum state. *Physical Review A*, 36(7):3464, 1987.

[173] C. Zhang. Building and characterizing an external cavity laser at 1083 nm, 2019. Internship report.

[174] P. Ziń, J. Chwedeńczuk, A. Veitia, K. Rzażewski, and M. Trippenbach. Quantum multimode model of elastic scattering from bose-einstein condensates. *Physical review letters*, 94(20):200401, 2005.

[175] P. Ziń, J. Chwedeńczuk, and M. Trippenbach. Elastic scattering losses from colliding bose-einstein condensates. *Physical Review A*, 73(3):033602, 2006.

[176] X. Zou, L. Wang, and L. Mandel. Violation of classical probability in parametric down-conversion. *Optics communications*, 84(5-6):351–354, 1991.

Résumé

Ce manuscrit a pour objectif général l'étude de systèmes quantiques composés de nombreuses particules en interaction, plus connus sous le nom de systèmes à N-corps. La difficulté majeure dans l'étude de ces systèmes réside dans la présence d'un très grand nombre de degrés de liberté, rendant très difficile toute approche théorique exacte. Néanmoins, diverses méthodes approchées ont pu être utilisées pour étudier ces systèmes à N-corps. C'est notamment le cas de la thermodynamique qui consiste à étudier des propriétés moyennes d'ensemble du système, ainsi que de l'approche dite de champ moyen qui considère que les particules du systèmes sont indépendantes les unes des autres mais plongées dans un potentiel représentant l'action moyennée des autres particules du système. Bien qu'ayant fourni de nombreux résultats importants, ces approches ne sont pas adaptées à l'étude de systèmes fortement interagissants. Dans ce cas, il est alors nécessaires de prendre un compte les **corrélations** présentes entre les composantes individuelles du système, non décrites par les approches champ moyen.

Ces travaux de thèses se sont concentrés sur un exemple emblématique et conceptuellement simple de système à N-corps, le gaz de Bose homogène en interaction faible. Malgré son apparente simplicité, ce système présente en effet des phénomènes quantiques non triviaux ne pouvant être décrits par des approches champ moyen. C'est le cas de la **déplétion quantique**. A température nulle et pour un système non interagissant, la statistique de Bose-Einstein prédit que tous les bosons du système occupent l'état fondamental du système. C'est ce qu'on appelle un condensat de Bose-Einstein. Si l'on ajoute maintenant des interactions de contact entre particules, l'effet conjoint de ces interactions et des fluctuations quantiques va promouvoir des particules en dehors du condensat vers des états excités. Le terme **déplétion quantique** désigne la fraction d'atomes retirés du condensat de la sorte.

Il est possible de former une image microscopique de la déplétion quantique en s'appuyant sur la théorie de Bogoliubov dont l'idée centrale est de faire l'approximation que les interactions sont faibles pour les traiter de manière perturbative. La fraction d'atomes retirés du condensat par les interactions est considérée comme faible et l'on ne considère donc que les processus d'interactions impliquant deux particules du condensat. Comme l'impulsion des particules du condensat est nulle, l'impulsion initiale totale est nulle et doit l'être après le processus d'interaction en vertu de la conservation de l'impulsion. De ce fait, les impulsions des deux particules retirées du condensat doivent être de mêmes normes, mêmes

directions, mais de sens opposés. On observe donc la formation de paires d'atomes corrélés d'impulsions opposées $\boldsymbol{k}/\text{-}\boldsymbol{k}$. La particularité de ce phénomène vient du fait que les paires d'atomes d'impulsions opposées sont ici produites à partir d'un système **à l'équilibre** et ne peut ainsi être expliqué que dans le cadre d'une théorie quantique. Bien que prédit en 1957 par Lee, Huang et Yang, la signature microscopique de ce phénomène n'avait jamais été observée auparavant. En utilisant les capacités de détection à l'atome unique dans l'espace des impulsions du dispositif expérimental utilisé dans ces travaux de thèse, nous avons pu observer pour la première fois ce signal de corrélation.

Chapitre 1
Le premier chapitre présente le formalisme nécessaire à l'étude des corrélations quantiques. Il est introduit au travers du prisme de l'optique quantique pour lequel il a été initialement développé, avant d'être étendu à la physique atomique. Nous détaillons ensuite les éléments essentiels de la théorie de Bogoliubov du gaz de Bose homogène faiblement interagissant pour comprendre les caractéristiques principales du signal de corrélation $\boldsymbol{k}/\text{-}\boldsymbol{k}$ de la déplétion quantique et mettre en évidence les contraintes expérimentales pour son observation.

Chapitre 2
Afin de s'assurer que l'effet des interaction est suffisant par rapport à celui de la température dans notre expérience, il est nécessaire d'utiliser un réseau optique de façon à augmenter la force des interactions. Ce chapitre présente le modèle de Bose-Hubbard décrivant la physique de bosons sur réseaux et comment une mesure en temps de vol permet d'accéder expérimentalement à la distribution en impulsion du système.

Chapitre 3
Ce chapitre décrit le dispositif expérimental utilisé et comment l'utilisation d'hélium métastable et de détecteur à micro-canaux permet une détection résolue à l'atome unique. Nous présentons également plusieurs expériences visant à certifier l'exactitude de notre mesure.

Chapitre 4
Ce chapitre détaille l'observation expérimentale du signal de corrélation $\boldsymbol{k}/\text{-}\boldsymbol{k}$. Nous étudions ses principales caractéristiques : largeur, amplitude et dépendance à la température, interprétées au regard de la théorie de Bogoliubov. Nous démontrons également l'observation de la violation de l'inégalité de Cauchy-Schwarz classique et une réduction des fluctuations du nombre d'atomes entre mode d'impulsions opposés, prouvant la nature quantique de notre signal de corrélation.

Chapitre 5
Nous présentons dans ce chapitre un autre projet conduit pendant cette thèse, à savoir la mesure du contact de Tan dans un gaz de bosons uni-dimensionnel. Après une introduction théorique, nous présentons la procédure expérimentale utilisée pour extraire le valeur du contact de Tan des données expérimentales avant de discuter des premiers résultats et de leur désaccord avec la théorie.

université PARIS-SACLAY

ÉCOLE DOCTORALE
Ondes et Matière (EDOM)

Titre: Corrélations en impulsion dans la déplétion de gaz de Bose sur réseaux faiblement interagissant

Mots clés: Détection d'atomes uniques, Réseau optique, Corrélation en vitesse, Gaz quantique, Problème à N corps, Déplétion quantique

Résumé: Ce travail de thèse est centré sur l'étude d'un exemple emblématique de système quantique en interaction, le gaz de Bose en interaction faible. A température nulle, la théorie de Bogoliubov prévoit que l'effet conjoint des interactions et des fluctuations quantiques retire une fraction des atomes du condensat de Bose-Einstein. Cette fraction est nommée déplétion quantique. Elle consiste en une superposition cohérente de paires d'atomes à impulsions opposées. La présence de ces paires découle du processus microscopique d'interaction à deux particules. Bien que cette prédiction date de 60 ans, ce manuscrit rapporte la première observation de ces corrélations entre impulsions opposées dans la déplétion d'un gaz de Bose en interaction faible. Pour ce faire, nous produisons des condensats de Bose-Einstein d'Hélium-4 métastable chargés dans des réseaux optiques. L'utilisation d'Hélium métastable rend possible la détection d'atomes individuels en trois dimensions après un long temps de vol, aspect essentiel à la mesure des corrélations entre particules individuelles dans l'espace des impulsions. Après avoir exposé plusieurs résultats visant à démontrer que notre technique de détection mesure fidèlement l'impulsion d'atomes individuels, nous présentons nos signaux de corrélations. Nous en étudions les principales caractéristiques (amplitude, largeur, évolution avec la température) afin d'illustrer la nature quantique du mécanisme de paire. Au delà de confirmer une prédiction théorique, ces résultats constituent un premier pas dans l'étude des systèmes quantiques à N corps à l'équilibre au travers des corrélations en impulsion et ouvrent la voie à des études de systèmes plus fortement corrélés. Pour finir, nous présentons des résultats préliminaires sur un sujet différent, la mesure du contact de Tan via la densité en impulsion dans des gaz de Bose unidimensionnels.

Title: Momentum-space correlations in the depletion of weakly interacting lattice Bose gases

Keywords: Single-atom detection, Optical lattice, Momentum correlation, Quantum gas, Many-body problem, Quantum depletion

Abstract: This thesis work is focused on the study of the emblematic example of an interacting quantum system, the weakly-interacting Bose gas. At zero temperature, a fraction of the atoms is removed from the Bose-Einstein condensate through the interplay between the inter-particle interactions and the quantum fluctuations. This fraction is called the quantum depletion. It consists in a coherent superposition of pairs of atoms with opposite momenta, or put in other words momentum correlated atom pairs. The presence of these pairs is explained by the microscopic process of interaction between two particles. While this prediction is more than 60 years old, this manuscript reports the first observation of these opposite momentum correlations in the depletion of a weakly-interacting Bose gas. To do so, we produce metastable Helium-4 condensates loaded in optical lattices. Using metastable Helium makes possible the detection of individual atoms in three dimensions after a long time-of-flight, an essential aspect to measure correlations between individual particles in momentum space. After exposing several results proving that our detection technique faithfully measures the the momentum of individual atoms, we present our correlation signals. We study their main characteristics (amplitude, width, evolution with temperature) to illustrate the quantum nature of the pairing mechanism. More than confirming a theoretical prediction, these results constitute a first step in the study of many-body quantum systems at equilibrium and open the way to the study of more strongly correlated systems. In addition, we also present some preliminary results on a different project, namely the measure of Tan's contact using the momentum density in 1D Bose gases.

Université Paris-Saclay
Espace Technologique / Immeuble Discovery
Route de l'Orme aux Merisiers RD 128 / 91190 Saint-Aubin, France